Sodium sulphate crystallisation, water transport and stone decay.

Andrea Hamilton

A thesis submitted to the University of Edinburgh
for the Degree of Doctor of Philosophy

September 2005

Centre for Materials Science & Engineering in the School of Engineering and Electronics

Acknowledgments

I would like to thank many people for their help and assistance throughout this PhD with particular thanks to my supervisor, Professor Christopher Hall for his wise advice. Many members of this School and others within the University have been kind and helpful throughout this study, especially Dr Vasileios Koutsos, Dr John E. Dixon, Dr John Craven, Dr Nicola Cayzer and Dr David Allen. Members of other institutions in Edinburgh have also provided me with valuable time and assistance, in particular Dr Ewan K. Hyslop at the British Geological Survey and Dr Lyall I. Anderson at the National Museums of Scotland. Historic Scotland made the fieldwork section of this thesis possible, for which I am forever grateful.

For funding, many thanks go to the EPSRC and ARUP.

I would like to thank Andrew Girdwood, Lyall Anderson, Ellie Greenhalgh, Graeme Duncan, Barry Martin, Iain MacLennan, David-John Pitts, my parents; Kenneth and Janet and my sister Kirsteen for being there for me.

Andrea Hamilton

Abstract

Sodium sulphate is widely regarded as one of the most damaging salts to attack masonry, yet comparatively little is known about it in this context. There are still unanswered questions concerning its ability to change from the decahydrate form to the anhydrous and vice versa, which is crucial to understanding crystallisation pressure and stone decay. This work presents new information on the crystallisation of sodium sulphate, examines water transport through porous media, which is essential for understanding stone damage and examines a practical real world example of stone decay.

Sodium sulphate exists as an anhydrate named thenardite or a decahydrate named mirabilite. Mirabilite converts easily to thenardite at room temperature and RH <75 % although mirabilite is the stable phase at temperatures below 32.4 °C. In terms of destruction to a porous body, the generation of high supersaturations is critical which can be linked to the solubility relationship of mirabilite and thenardite. Chapter 3 explores this relationship through an insitu temperature controlled dynamic XRD study which discusses the supersaturation attainable with respect to mirabilite by cooling a sample of thenardite in aqueous solution formed from the dehydration of mirabilite in a 'closed' system. As the system cools from 32.4 °C it follows the metastable thenardite solubility curve until the reformation of mirabilite. This provides some insight into the possible supersaturation of the system with respect to the stable phase, mirabilite.

Also of practical interest is the behaviour of sodium sulphate in the presence of other commonly occurring cations. Calcium was used for this study due to the wide spread occurrence of gypsum in relation to stone damage. A synchrotron experiment conducted on beam line 16.4 at Daresbury Laboratory, shows for the first time the precipitation and dissolution of labile salt ($Na_4Ca(SO_4)_3.2H_2O$) from the starting materials of solid mirabilite and gypsum, cycled up and down in temperature using a glycol cold cell in the path of the beam.

Crystallisation by evaporation of aqueous solution was also used as another method of investigating the effect of calcium on the crystallisation of sodium sulphate at a single temperature above the mirabilite-thenardite transition temperature of 32.4 °C. A series of samples, produced at 40 °C, with increasing calcium concentration was examined. This indicated the formation of labile salt in a sodium rich solution at higher calcium concentrations in the series but also the formation of Na_2SO_4 (III). Phase III is a polymorph of anhydrous sodium sulphate which is metastable at 40 °C, but can be stabilised by cation substitution. A definite relationship was found to exist between the amount of calcium in solution, the formation of phase III and the eventual formation of labile salt.

Although stone decay from salt crystallisation is often seen under idealised lab conditions as the dramatic breaking apart of stone test samples, the real world often presents a different set of rules. Part of the Skara Brae settlement in Orkney, a site of cultural importance and showing extreme weathering in places, was investigated for signs of salt decay. Many different methods, including water transport analysis, were used to investigate the samples from the site itself and representative samples taken from close to the site to asses the relative importance of the decay mechanisms found to exist.

The final experimental section of this thesis deals more rigorously with the analysis of water transport through porous materials. For this study, three commonly used building materials were investigated as part of an E.U. funded round robin experiment. Characterisation of the materials using a variety of methods is given to explain their strong variation in water transport properties. Results from this laboratory and four different international laboratories are compared and contrasted providing an insight into the comparison of inter-laboratory results.

Tables

Figures

Figures

Abbreviations

AAC	Autoclaved aerated concrete
CB	Ceramic brick
CS	Calcium silicate
DSC	Differential Scanning Calorimetery
DTA	Differential Thermal Analysis
ESEM	Environmental Scanning Electron Microscope
IC	Ion Chromatography
ICP-OES	Inductively Coupled Plasma Optical Emission Spectrometer
MIP	Mercury Intrusion Porosimetery
NMR	Nuclear Magnetic Resonance
ppm	parts per million
SEM	Scanning Electron Microscope
XRD	X-ray diffraction

Contents

Chapter 6 – Fluid transport and materials characterisation

Chapter 7 – Conclusions

1. Introduction

The general aim of this work was to develop a greater understanding of the factors behind stone decay by soluble salts, in particular, sodium sulphate. Sodium sulphate was chosen because it is known to be amongst the most damaging of salts [1] and has been routinely used by the BRE (Building Research Establishment, UK) when assessing a stone for resistance to salt crystallisation. A greater understanding of sodium sulphate was therefore considered important. This relates to the way in which sodium sulphate transforms with temperature between the anhydrous form (thenardite) and the decahydrate (mirabilite) and vice versa. Mirabilite dehydrates to form thenardite easily at room temperature and RH <75 % as is well known, but re-crystallisation of mirabilite has received less attention. Hydration pressure, as thenardite hydrates to form mirabilite was often thought to be behind the dramatic damage caused to stone work by sodium sulphate crystallisation. Recent experimental evidence has shown that thenardite converts to mirabilite in the presence of moisture through dissolution and re-crystallisation [2], effectively ruling out hydration pressure, and pointing towards crystallisation pressure. The conversion of mirabilite to thenardite in a 'closed' system occurs at 32.4 °C as is well known, but there is scant information available on the conversion of thenardite back to mirabilite in a 'closed system', which is potentially very important in understanding the kinetics of this salts behaviour. As salts rarely occur in isolation in nature, it is important to understand the effect of other salts on the crystallisation and phase transitions of sodium sulphate. Calcium salts, such as gypsum (calcium sulphate dihydrate) were mainly used for this study of sodium sulphate crystallisation, due to their widespread occurrence in nature.

Ions move in solution, so the next logical step in investigating the role of salt decay is in understanding water transport through a porous material. While knowledge of salts is important to understanding stone decay, a real world study of a decaying site was conducted to gain an insight into the mechanisms present outside the laboratory. This is important, as real world conditions are often very complex with several decay mechanisms working together and as such provides a valuable insight into the role of salts in the real world.

1.1 Thesis preview

Although much is known about mirabilite and thenardite, comparatively little is known about the dynamic conversion of thenardite to mirabilite which is principally the subject of chapter 3, investigated using powder X-ray diffraction (XRD). The conversion of mirabilite to thenardite and back to mirabilite in a closed system is discussed in chapter 3 with reference to the concentration of the solution phase and the limitations of the equipment used. This work is potentially important in understanding the role of sodium sulphate in stone decay as discussed in chapter 2 with reference to the recent work of Scherer [3, 4] and Flatt [5].

The crystallisation of sodium sulphate in the presence of calcium sulphate is discussed in chapter 4 where two different experimental approaches were taken. The first examines the formation of labile salt ($Na_4Ca(SO_4)_3.2H_2O$) from the starting materials of solid mirabilite ($Na_2SO_4.10H_2O$) and gypsum ($CaSO_4.2H_2O$) in a 'closed' system using synchrotron radiation at Daresbury Laboratory, beamline 16.4 and highlights the formation of a double salt from the dehydration of mirabilite. The second examines the formation of Na_2SO_4 III, a higher temperature sodium sulphate polymorph by evaporation of aqueous solutions of Na_2SO_4 and $CaSO_4.2H_2O$, amongst others, at 40 °C. The stabilisation of metastable Na_2SO_4 III by ion substitution has been previously reported [6-8] but not from aqueous solution at low temperatures. This temperature range was chosen to be sympathetic to real world conditions in the region of thenardite stability and provides new information on the interaction of sodium sulphate with other commonly occurring cations in aqueous solution.

Chapter 5 is an example of real world stone decay from House 7, Skara Brae, Orkney. Articles of stone 'furniture' in House 7 are spalling and flaking quite rapidly. The purpose of this chapter was to examine the site for salt decay and with a view to understanding what decay mechanisms are present. This work examines the problem in detail using many different techniques such as XRD, ICP-OES and Ion Chromatography to examine salts present in stone spall fragments from the site. Thin section analysis coupled with XRD provides information on rock types present on the site. Further analysis was conducted on samples chosen from close to the site (E.

K. Hyslop, British Geological Survey, Edinburgh) to be representative of the stone articles on site as it was not possible to sample enough material from the site for extensive testing. Water transport analysis with HYDRUS 2D modelling and mechanical properties testing for swelling/contraction analysis (carried out at Princeton University, USA) were used to examine how water flows through the articles on site and if swelling/contraction damage is likely to contribute to the decay. Chapter 6 is a more detailed examination of water transport techniques, which expands on some of the water transport points raised in chapter 5. Chapter 7 is conclusions and ideas for future work.

1.2 References

1. Goudie, A.S. and H.S. Viles, *Salt Weathering Hazards*. 1997, Chichester: John Wiley and Sons Ltd.

2. Rodriguez-Navarro, C. and E. Doehne, *Salt weathering: Influence of evaporation rate, supersaturation, and crystallization pattern.* Earth Surface Processes and Landforms, 1999. **24**: p. 191-209.

3. Scherer, G.W., *Crystallization in pores.* Cement and Concrete Research, 1999. **29**: p. 1347 - 1358.

4. Scherer, G.W., *Stress from crystallization of a salt.* Cement and Concrete Research, 2004. **34**: p. 1613 - 1624.

5. Flatt, R.J., *Salt damage in porous materials: how high supersaturations are generated.* Journal of Crystal Growth, 2002. **242**: p. 435-454.

6. Dharmasena, G. and R. Frech, *The stabilization of phase III and phase I in sodium sulfate by aliovalent cation substitution.* Journal of Chemical Physics, 1993. **99**(11): p. 8929-8935.

7. Freyer, D., S. Fischer, K. Köhnke, and W. Voigt, *Formation of double salt hydrates. I - hydration of quenched Na_2SO_4-$CaSO_4$ phases.* Solid State Ionics, 1997. **96**: p. 29-33.

8. Freyer, D., W. Voigt, and K. Köhnke, *The phase diagram of the system Na_2SO_4-$CaSO_4$.* European Journal of Solid State Inorganic Chemistry, 1998. **35**(10-11): p. 595-606.

2. Literature review

The purpose of this chapter is to give an overview of current, classic and important literature relating to the subjects covered in this thesis. The intention is to provide a framework for comparative assessment of this work.

2.1 Sodium sulphate and stone decay

Sodium sulphate is a well known salt, primarily in the fields of stone decay, architectural conservation and ionic conductivity measurements. It is often regarded as the most damaging of soluble salts to attack masonry (see figure 2.1) and yet it is still not well understood. Hydration pressure, caused by the 'hydration' of the anhydrous salt into the larger decahydrate in the presence of moisture, was originally assumed to be the reason why sodium sulphate was so damaging to masonry. However, ESEM (Environmental Scanning Electron Microscope) investigations indicate that this is unlikely to be the case, as thenardite (Na_2SO_4) dissolves then precipitates as mirabilite ($Na_2SO_4.10H_2O$) rather than a direct conversion from the solid anhydrate to the hydrate [1]. Crystallisation pressure is thought to be the reason behind the spectacular damage caused to porous substrates from sodium sulphate, which results in damage when the pressure caused by the growing crystal exceeds the tensile strength of the stone [1-4] which is typically 3 – 9 MPa. The theory behind the crystallisation pressure is originally credited to the classic paper of Correns [5] and has been expanded more recently by Scherer and Flatt [2-4] who believe there must be a repulsive force between the growing crystal and the confining pore. The crystallisation pressure is given by Scherer [4] to be:

$$P_w = \kappa_{CL}^E - \kappa_{CL}^S = \frac{R_g T}{V_C} \ln\left(\frac{Q^E}{Q^S}\right) \qquad \textbf{(2.1)}$$

where P_w is the crystallisation pressure of the growing salt crystal on the surrounding pore, κ_{CL}^E is the curvature of the end of the crystal, κ_{CL}^S is the curvature of the sides of the crystal, R_g is the universal gas constant, T is the absolute temperature, V_c is the

molar volume of the crystal and Q^E/Q^S is the supersaturation of the surrounding solution. At this point a short explanation of solubility should be given:

The equilibrium between a solid ionic salt and its solution in water is governed by the solubility-product expression [6]. For an equilibrium constant, activity is a more accurate term than concentration, as $a_i = m_i\gamma_i$ where a_i is the ion activity, m_i is the ion molality and γ_i is the ion activity coefficient, which takes into account ionic strength and departure from ideality of the solution. The activity coefficient is often set to unity for insoluble salts as the solution is extremely dilute, but becomes increasingly significant for more soluble salts and the value decreases from unity. This leads to an expression for K_{sp}, for the dissolution of thenardite in pure water. The activity of the pure solid being equal to unity is neglected after equation 2.2. The ion activity product equals the equilibrium solubility product at equilibrium.

$$K_{sp} = \frac{a_{Na^+}^2 a_{SO_4^{2-}}}{a_{Na_2SO_4}} \qquad \textbf{(2.2)}$$

$$K_{sp} = \frac{m_{Na^+}^2 m_{SO_4^{2-}}}{(m^o)^3}\gamma_{Na^+}^2\gamma_{SO_4^{2-}} \qquad \textbf{(2.3)}$$

$$K_{sp} = m_{Na^+}^2 m_{SO_4^{2-}}\gamma_{\pm}^3 \qquad \textbf{(2.4)}$$

Where $\gamma_{\pm}$ is the mean activity coefficient of Na_2SO_4 and m^o is the standard concentration of 1 molal. Activity coefficients are never measured individually, which is why the mean expression is given here. Ion activity product (*IAP*) otherwise known as the reaction quotient (Q) requires an explanation. The K_{sp} refers to the activities at equilibrium; the *IAP* takes the same form as the K_{sp}, but involves the actual activities rather than the equilibrium values. The saturation index (*SI*) is defined as:

$$SI = \log\left(\frac{IAP}{K_{sp}}\right) \tag{2.5}$$

when $SI = 0$ the system is at equilibrium ($IAP = K_{sp}$), when $SI > 0$, the solution is supersaturated with respect to the thenardite and when $SI < 0$ the solution is undersaturated with respect to thenardite.

The most damaging scenario of maximum pressures for crystal growth in a pore is given by Scherer as the case when a large crystal is growing in a pore with small entries. This scenario can occur when, due to evaporation, pockets of liquid become trapped in pores with small entries, which require a low RH before the meniscus can travel through the opening. The concentration of the solution is increased by evaporation. Assuming that there are many crystals nucleating throughout these solution pockets formed in a piece of stone, then as the available material in solution is consumed by the growing crystals, the smaller ones will dissolve in favour of the continued growth of the larger crystals [4] as smaller crystals are more soluble in accordance with:

$$p = \gamma_{CL}\frac{dA}{dV} = \frac{2\gamma_{CL}}{r} \tag{2.6}$$

This assumes a spherical crystal. Where p is the amount of pressure required to inhibit growth as much as the surface energy does, which in effect is the pressure expression of the surface energy retardation effect on growth and γ_{CL} is the crystal-liquid interfacial free energy. As the pressure is dependent on the curvature of the crystal ($\frac{dA}{dV} = \kappa_{CL}$) it has a larger effect on smaller crystals. The end result is the diffusion of ions from the sites of higher concentration (where the smaller crystals have nucleated) to the sites of lower concentration feeding the growth of the larger crystals. This is thought to result in a high transient stress as crystals grow under a high supersaturation and then some relaxation as the solution relocates to the larger pores. Damage to materials with larger pores is a key question here and Scherer describes it as occurring under non-equilibrium conditions: when low RH drives the

solution concentration up faster than it can be reduced by diffusion. Scherer presents an illustration of the growth of a crystal in a spherical pore with an entry point on either side (left-right) of the pore. If the solution is allowed to evaporate at both sides the end result is a film of liquid separating the crystal from the pore wall where the meniscus has retreated to between the crystal and the pore wall, with further evaporation increasing the concentration of the available liquid film. This is a non-equilibrium condition and is thought to result in damage to either the crystal or the pore. As the yield strength of the crystal is in the region of 200 – 350 MPa, the pore structure will give way first [4]. The generation of high supersaturations is also important to understand. The interesting solubility of sodium sulphate is discussed in the next section, but here the salient point in the generation of high supersaturations comes from the observation that damage can occur during wetting cycles [4]. It is intuitive that as a material containing a salt solution is dried that the crystallisation damage occurs then, however, crystallisation damage can occur during the wetting cycle (stones are wetted and dried with sodium sulphate solution continuously to destruction [7]) and this is due to the slightly odd solubility of sodium sulphate. Thenardite forms at temperatures above 32.4 °C, but it can form directly at lower temperatures during fast evaporation conditions (low RH) as well as from the dehydration of mirabilite. As thenardite has a higher solubility than mirabilite below the transition temperature, any wetting cycle (at temperatures below 32.4 °C) will dissolve thenardite to produce a solution highly supersaturated with respect to mirabilite [2, 4], this supersaturation is thought to provide the driving force for damage to the porous network from crystallisation pressure.

a)

b)

c)

Figure 2.1: Cordova limestone exposed to routine sodium sulphate laboratory testing (samples are 5 x 5 x 25 cm). a) after 8 days there is no sign of efflorescence but the sample has began to crack. b) after 47 days a layer of stone has separated from all over the surface. c) a closer view of the sample shows columnar salt crystals growing from the surface under the separated layer. Images and caption courtesy of G. W. Scherer, Princeton University, USA.

2.2 Solubility and solid phases

The solubility of sodium sulphate in pure water has been measured many times. Three well known sources [8-10] are used throughout this work. Figure 2.2 is a plot of the two main phases, thenardite and mirabilite plus the metastable heptahydrate.

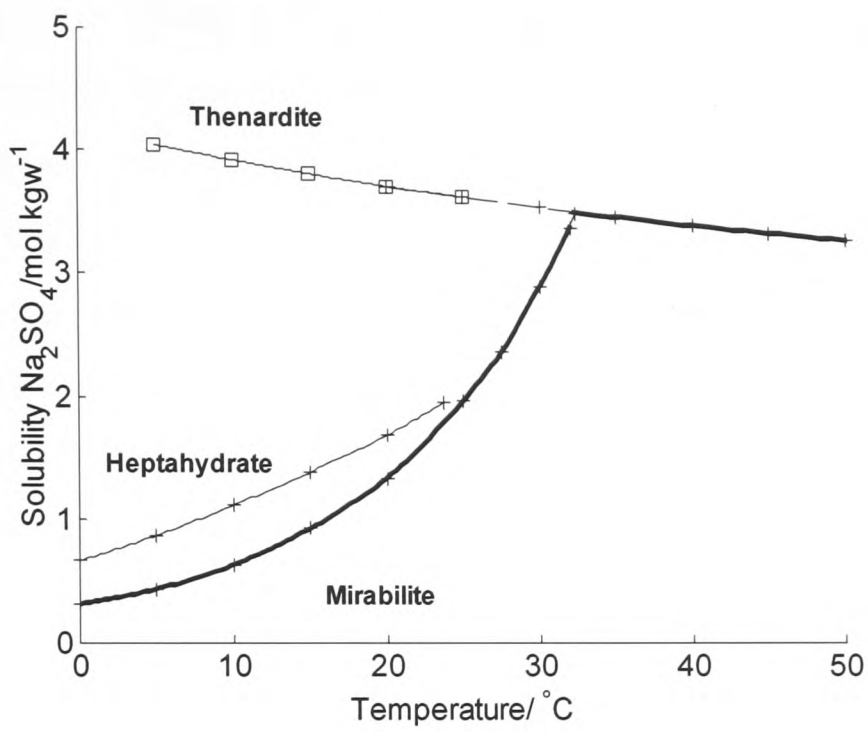

Figure 2.2: The solubility of thenardite [9, 10], heptahydrate [10] and mirabilite [10] in pure water. The bold lines indicate the stable phase with respect to temperature; the crosses are experimental data points from the sources listed. The squares are predicted metastable thenardite solubility points calculated using PHRQPITZ [11]. PHRQPITZ simulations, C. Hall, unpublished.

The high and temperature sensitive solubility of mirabilite ($Na_2SO_4.10H_2O$) contrasted with the retrograde and notably less temperature sensitive thenardite (Na_2SO_4) has often been thought to be part of the reason behind the severe damage caused by this salt during routine laboratory testing of stone samples. A metastable lower hydrate, simply known as a heptahydrate ($Na_2SO_4.7H_2O$) is metastable and rarely observed. The phases encountered by researchers in the field are mirabilite and thenardite. The fast dehydration of mirabilite to thenardite is also well known amongst researchers as mirabilite stability at temperatures below 32.4 °C is also regulated by RH. This leads to a stability zone for mirabilite with respect to RH in its stable temperature zone. According to Flatt [2] solid mirabilite, assuming a

temperature of 25 °C, is only stable within a narrow RH band of 75% to 94%, above 94 %, which is the ERH (equilibrium relative humidity), a saturated solution with respect to mirabilite forms. Therefore it is not surprising that in the field, thenardite is more commonly found. Mirabilite dehydrates quickly at RH values less than 75% at 20 °C [2] to form thenardite. Thenardite formed directly from solution and from the dehydration of mirabilite are texturally different [1] as discussed further in chapter 3. Many researchers have also noted the high supersaturations that can be sustained in solution before the crystallisation of mirabilite takes place as many attribute this as partly responsible for the damage caused by sodium sulphate crystallisation. These high supersaturations are the subject of chapter 3 and would benefit from further confirmation, provided by an insitu synchrotron X-ray experiment. Thenardite can also form directly at low RH values from solution evaporation [1]. The dissolution of the more soluble thenardite can result in the generation of high supersaturations with respect to mirabilite [2] if thenardite is dissolved at temperatures within the mirabilite stability region. Changes in temperature can also result in large amounts of mirabilite crystallising out of solution as the solubility varies strongly with temperature. The solubility of sodium sulphate and its equilibrium solid phases has many distinctive features:

- Strong variation in the solubility of mirabilite with temperature
- The narrow region of solid mirabilite stability with respect to RH
- The retrograde, higher solubility of thenardite
- The direct crystallisation of thenardite from solution (by evaporation) at low RH values and temperatures below 32.4 °C (in the mirabilite region of the solubility diagram).
- The existence of a metastable lower hydrate known as the heptahydrate

2.3 Double salts of sodium sulphate

2.3.1 Solubility measurements

Double salts of sodium sulphate have been investigated by a few researchers as part of the solubility of double or multi component systems. More frequently, these salts have been researched or encountered in Pitzer style [12] theoretical investigations of seawater chemistry. For the purposes of this work, the salts of interest are calcium-sodium-sulphates in the temperature region of 5 – 45 °C. Block and Waters [13] investigated the $CaSO_4$ – Na_2SO_4 – NaCl – H_2O system from 25 °C to 100 °C by adding set amounts of $Na_2SO_4.10H_2O$ and $CaSO_4.2H_2O$ to 35 ml of water or NaCl solution. The samples were allowed to come to equilibrium at the set temperature of the experiment then the composition of the solution and the 'wet residue' at equilibrium were analysed. The main points to note are that the transition temperature of mirabilite to thenardite at 32.4 °C is lowered to less than 25 °C in the presence of a concentrated NaCl solution (3.5 and 4.0 molal NaCl) and the double salts of $CaSO_4$ and Na_2SO_4 cannot be obtained unless thenardite is the stable sodium sulphate phase. The 'wet residue' at 25 °C (no NaCl) is analysed as being $CaSO_4.2H_2O$ until the Na_2SO_4 molality approached saturation with respect to mirabilite. Table 2.1 presents the pertinent data from Block et al. at 25 °C, which shows that the presence of Na_2SO_4 decreases the solubility of $CaSO_4$ then increases it as the concentration of Na_2SO_4 rises.

Na_2SO_4 Molality [13]	$CaSO_4$ Molality [13]	Solid phase [13]
0.000	0.0161	gypsum
0.032	0.0119	gypsum
0.104	0.0110	gypsum
0.109	0.0104	gypsum
0.262	0.0112	gypsum
0.462	0.0127	gypsum
0.821	0.0154	gypsum
1.307	0.0177	gypsum
1.753	0.0182	gypsum
1.784	0.0185	gypsum
1.912	0.0185	gypsum +mirabilite
1.885	0.0082	mirabilite
1.919	0.0055	mirabilite
1.852	0.0000	mirabilite

Table 2.1: Data from Block et al. [13] at 25 °C. The solubility of mirabilite ($Na_2SO_4.10H_2O$) is given by Gmelin [8] in g of Na_2SO_4 per 100g of water, the molality is therefore expressed as 1.968 m. For comparison, the solubility of gypsum in pure water is 0.01537 m [14].

Interpretation of table 2.1 requires an understanding of the solubility of gypsum in a sodium sulphate solution. This is shown at 25 °C in figure 2.3.

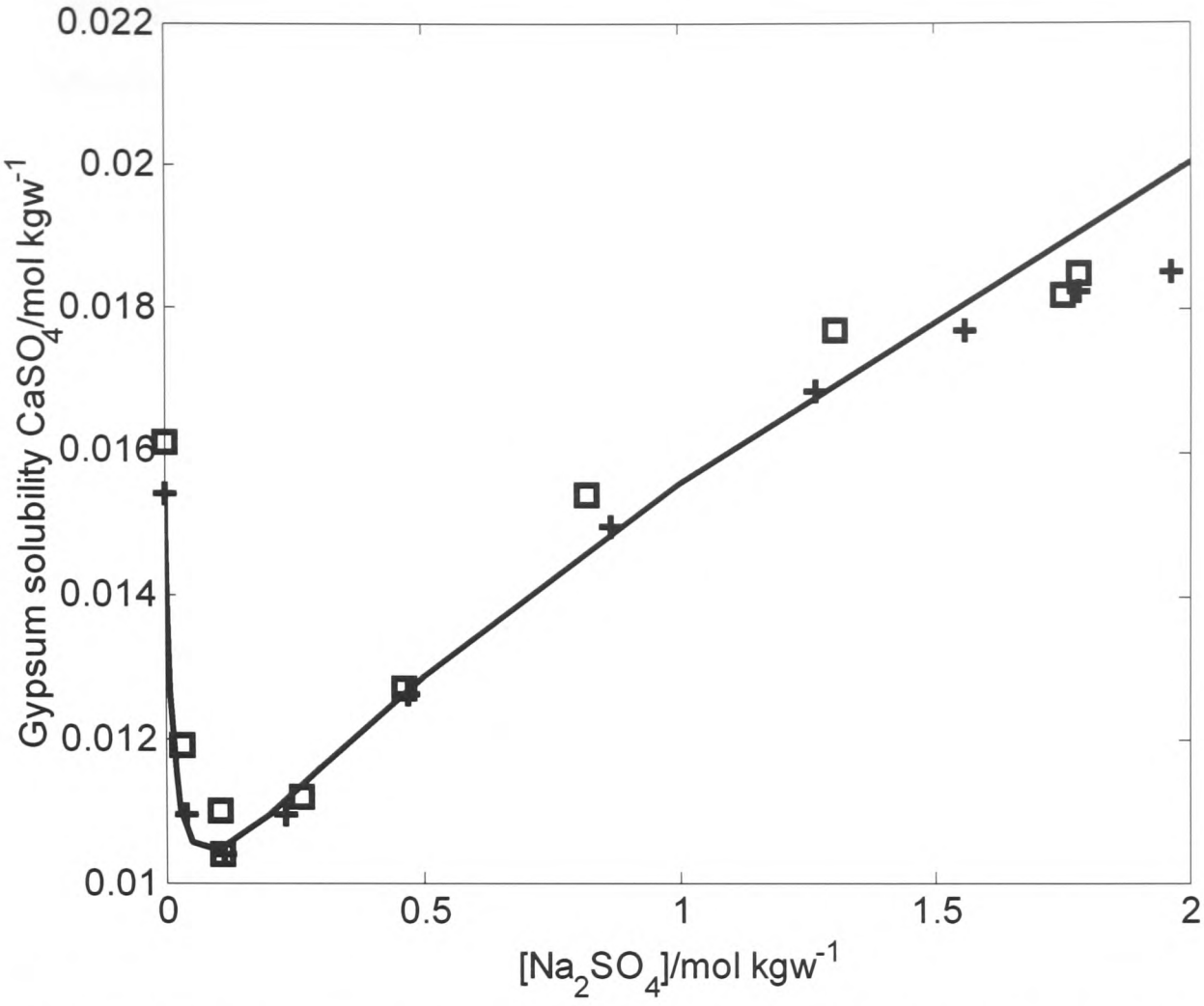

Figure 2.3: The solubility of gypsum (expressed as $CaSO_4$) in a sodium sulphate solution at 25 °C. Experimental data points from two literature sources: squares from Block et al. [13] and crosses from Hill et al. [15]. The solid line represents the solubility prediction from PHRQPITZ [11]. PHRQPITZ simulation, C. Hall, unpublished.

The solubility data for 40 °C are presented in table 2.2.

Na_2SO_4 Molality [13]	$CaSO_4$ Molality [13]	Solid phase [13]
0.0000	0.0158	gypsum
0.0370	0.0126	gypsum
0.1180	0.0108	gypsum
0.1230	0.0104	gypsum
0.2760	0.0123	gypsum
0.5600	0.0154	gypsum
1.0900	0.0165	gypsum
1.4340	0.0189	gypsum
2.0060	0.0202	gypsum
2.0380	0.0202	gypsum
2.1150	0.0199	gypsum and glauberite
2.2880	0.0144	glauberite
2.4740	0.0118	glauberite
2.9070	0.0082	glauberite
2.9930	0.0100	glauberite and labile salt
3.0230	0.0086	labile salt
3.2900	0.0070	labile salt
3.3860	0.0065	labile salt and thenardite
3.3800	0.0000	thenardite

Table 2.2: The solubility of gypsum, expressed as $CaSO_4$ in a sodium sulphate solution at 40 °C. Data from Block et al. [13]. The solubility of Na_2SO_4 in pure water [8] at 40 °C is 3.4127 moles per kgw. For comparison the solubility of gypsum in at 40 °C is 0.01553 moles $CaSO_4$ per kg water [14].

It is clear from table 2.1 and figure 2.2 that the solubility of gypsum decreases due to the common ion effect and then increases probably due to complex formation.

It is a notable fact that although the solubility of gypsum is markedly changed by the concentration of the sodium sulphate solution, the solubility of the more soluble sodium sulphate is little affected [13, 15]. This can be seen from a comparison of the last four lines from table 2.1, which shows that the sodium sulphate concentration and resulting solid phase of mirabilite is little affected by the

amount of gypsum added within the confines of that data set. It should be noted that the solubility of mirabilite and thenardite (last line of tables 2.1 and 2.2 respectively) is a little lower than the main literature sources used for this work [8, 10], for which there is no explanation.

The double salts of interest are glauberite and eugsterite (also called labile salt) [16]. Labile salt ($2Na_2SO_4.CaSO_4.2H_2O$) is metastable with respect to glauberite ($CaSO_4.Na_2SO_4$), but can remain unchanged in contact with its solutions for long periods of time [13, 15], changing to glauberite only at 75 °C. A decrease in the solubility of labile salt and glauberite has also been noted with increasing sodium sulphate concentration [13]. Possibly one of the most curious facts about labile salt precipitation was discovered by Hill et al., who conclude that there was no spontaneous precipitation of double salts up to a concentration of 30 % sodium sulphate. "In the presence however of solid thenardite at the invariant point, 32.85 %, the formation of labile salt begins immediately and the system becomes constant at the invariant concentration for labile salt and thenardite."

The change to the stable phase (glauberite) is very slow under all conditions of concentration [15] with labile salt always forming first at temperatures below 75 °C. The data supplied by Hill et al. is very interesting and useful as they give the composition of the starting mix, the composition of the solution at equilibrium and the solid phase. Table 2.3 contains the data they obtained at 35 °C with labile salt only as the stable phase.

Original complex		**Saturated solution**		
Wt % Na_2SO_4	**Wt % $CaSO_4$**	**Wt % Na_2SO_4**	**Wt % $CaSO_4$**	**Solid phase**
33.79	2.498	31.66	0.078	Labile salt
31.73	0.751	31.18	0.088	Labile salt
31.73	1.583	30.48	0.102	Labile salt

Table 2.3: Data obtained at 35 °C from Hill et al. [15].

In the temperature range of interest (5 – 45 °C) the stable $CaSO_4 – Na_2SO_4 – H_2O$ phases are gypsum ($CaSO_4.2H_2O$), anhydrite ($CaSO_4$), mirabilite ($Na_2SO_4.10H_2O$), thenardite (Na_2SO_4) and glauberite ($Na_2SO_4.CaSO_4$). Metastable phases are labile

salt and heptahydrate ($Na_2SO_4.7H_2O$). Of these metastable phases, the most common is labile salt. The heptahydrate of sodium sulphate is reported by researchers [8, 10] but has never been detected by the author.

Labile salt, although metastable with respect to glauberite forms readily in the presence of excess solid thenardite and can remain present for many months. The transformation towards glauberite is very slow at 35 °C according to the experiments of Block et al. [13] who do not find labile salt from 55 °C onwards. However, Hill et al. [15] record labile salt with regularity at temperatures up to 75 °C, which is the highest temperature they investigate, they note that only at 75 °C and above does the change to glauberite begin at once. However, there are differences in the experimental method used by both groups. Hill et al. examine (at 25 °C) the region of supersaturation with respect to mirabilite and obtained the points on the labile salt curve by "allowing the compound to form from gypsum after seeding with labile salt". They note that the reaction required one to two weeks for completion, except in the presence of excess thenardite, in which case the reaction was rapid. They also discover that glauberite does not form at all at 25 °C and that the points on the glauberite curve were obtained by the addition of glauberite prepared at higher temperatures, which reached equilibrium in one day.

In contrast, Block et al. did not seed the solutions at all and Hill et al. note that at 50 °C when they attempted to form labile salt from gypsum (and sodium sulphate), the formation of glauberite began before the formation of the labile salt was complete, it can therefore be understood that labile salt will not spontaneously form at temperatures above 50 °C. Both Block and Hill make mention of penta salt ($Na_2SO_4.5CaSO_4.3H_2O$), which is not discussed here as it is does not form of its own accord through the temperature range of interest (5 – 45 °C), forming at 70 °C according to the results of Block et al. (excluding the data using NaCl solutions). The main salts of interest for this work are gypsum, mirabilite, thenardite and labile salt. The following discoveries were made by Hill et al. and Block et al.:

- Labile salt is metastable with respect to glauberite in the range 25 – 75 °C [15] and will not form of its own accord at 55 °C and above [13]. Labile salt can form by seeding the solution up to 75 °C, at which point the change

towards glauberite begins at once [15]. At 50 °C the same authors note that when attempting direct formation of labile salt through seeding from gypsum and sodium sulphate, the formation of glauberite began before the formation of labile salt was complete. Glauberite, it seems, often forms via labile salt.

- The solubility of labile salt in water is described as 'explosive' in terms of its speed and the unexpectedly high $CaSO_4$ concentration found in solution, which exceeded the solubility of gypsum, anhydrite and bassanite [15].

- Labile salt will only form (without seeding the solution) when the stable phase is thenardite [13, 15].

- Labile salt will only spontaneously form in the presence of solid thenardite [15].

- The transition point of mirabilite to thenardite (32.4 °C) is lowered to below 25 °C in the presence of 3.5 and 4.0 molal NaCl solutions.

- The solubility of gypsum in a sodium sulphate solution dips then increases with increasing sodium sulphate concentration.

2.3.2 Natural waters and electrolyte mixtures

The composition of natural waters and modelling of solute concentrations is of great importance in the field of Geochemistry. As the salts of interest to this work are part of these systems, this field of literature will be touched on, albeit briefly. The solubility modelling of these aqueous systems is based round the equations developed by Pitzer [12] which expresses the molality dependence of the excess Gibbs free energy of the solution. Expressions for the activity and osmotic coefficients which are the quantities of interest in these non-ideal solutions are obtained by derivation of the Gibbs free energy.

The Pitzer equations are presented in many publications [12, 17-20]. To give a brief outline here, Pitzer developed the Guggenheim-Scatchard equations for calculating the activity and osmotic coefficients in dilute solutions. Guggenheims work fitted the experimental data up to 0.1 M solutions; Pitzer began the expansion by examining the component parts of the equation for improvement. Guggenheim included the original form of the Debye-Hückel law and added short range interaction terms, known as β_{MX} which represent the net effect of short range forces between M (cation) and X (anion) of a salt of form M_yX_x. These β_{MX} values were considered constants, but Pitzer considered them to vary slowly with solution concentration [12]. The main stem form of the Pitzer equation is the expression for the Gibbs excess energy (the difference between the actual Gibbs free energy of a solution and that of an ideal solution at the same conditions of concentration, temperature and pressure) which is differentiated to yield expressions for the osmotic and activity coefficients. Ionic strength, short range and long range electrostatic interaction terms are added. Solute specific parameters (such as β_{MX}) are added as ion interaction parameters with tables of these values given by Pitzer. The estimation of the ion interaction parameters for various systems has been the subject of many publications [21-26] and is of great interest in accurately modelling osmotic and activity coefficients.

There are six empirical parameters ($\beta_{MX}^{(0)}, \beta_{MX}^{(1)}, \beta_{MX}^{(2)}, C_{MX}^{\phi}, \theta_{ij} and \psi_{ijk}$) and A_ϕ which is the Debye-Hückel electrical term. The $\beta_{MX}^{(2)}$ term is important only for 2-2 or higher valence electrolytes that show a tendency towards electrostatic ion pairing, but is otherwise neglected. The six empirical parameters are obtained by least squares fitting to osmotic coefficient data sets [12]. Pitzer added to the electrostatic term, a series of ionic strength (and molality) dependent virial coefficients. This in effect allowed constant values for $\beta_{MX}^{(0)}, \beta_{MX}^{(1)}, \beta_{MX}^{(2)}$ within a generous concentration range at any given temperature or pressure while the overall 2nd virial coefficients (the B and Φ terms) vary with solution concentration. The 3rd virial coefficients (the C and ψ terms) are independent of ionic strength.

Pitzer states that mineral solubilities in concentrated electrolyte solutions can be calculated by thermodynamic considerations provided the equilibrium constants are known and the activity coefficients can be obtained [25]. The equilibrium

constant (or solubility product) at a fixed temperature and pressure for the dissolution of a hydrate can be defined as such (using mirabilite as a relevant example):

$$Na_2SO_4.10H_2O = 2Na^+ + SO_4^{2-} + 10H_2O \qquad \textbf{(2.7)}$$

$$\ln K = -(2\mu^0_{Na} + \mu^0_{SO_4} + 10\mu^0_{H_2O})/RT + \mu^0_{Na_2SO_4.10H_2O}/RT \qquad \textbf{(2.8)}$$

Where R is the universal gas constant, T is temperature in K, μ_i^0 is the chemical potential of the solid, water or aqueous ion in a defined standard state. The standard state for the aqueous ions and electrolytes is taken as a one molal solution referenced to infinite dilution at any pressure and temperature. The solid and solvent standard state is taken as the pure phase at the pressure and temperature of interest [25]. This means that the equilibrium constant for the reaction could be calculated providing the chemical potential values are known, however, as good chemical potential data for the solid phase is often scarce [20], the chemical potential is often calculated from solubility data, but as Pitzer notes [20] the "chemical potentials of solids determined in this manner are very useful for mixed electrolyte solutions at saturating molality."

In terms of molalities, the equilibrium constant for the solubility reaction is given by:

$$-\frac{\Delta\mu^0}{RT} = \ln K = 2\ln(m_{Na^+}\gamma_{Na^+}) + \ln(m_{SO_4^{2-}}\gamma_{SO_4^{2-}}) + 10\ln(a_{H_2O}) \qquad \textbf{(2.9)}$$

Where m_i and γ_i represent the molality and activity coefficient of the aqueous ions. Usually a mean activity coefficient is given instead of values for the individual ions.

Using the standard formula $\gamma_\pm = (\gamma_M^y \gamma_X^x)^{\frac{1}{(x+y)}}$ for a salt M_yX_x the equation for the mean activity coefficient becomes:

$$\ln\gamma_\pm = \frac{(2\ln\gamma_{Na^+} + \ln\gamma_{SO_4^{-2}})}{3} \qquad \textbf{(2.10)}$$

Pitzer [20] explains how the use of standard chemical potentials is useful in the case of a ternary system with a common ion using Eq. 2.9. He states that the molality of one of the non common ions is fixed and Eq. 2.9 is solved for the other molality. An iterative method is needed since all three terms on the right hand side depend on both of the molalities.

Harvie, Møller and Weare used the Pitzer equations and parameters to investigate mineral solubility in 5 and 6 components aqueous systems [21, 24] . They make use of the relationship between the standard state chemical potential (μ^0/RT) and the solubility product to obtain the standard state chemical potential for the solid salt from literature solubility data. They set the standard state chemical potential for the ionic species equal to zero, hence the ln$K$ value is the solubility of the solid phase directly [24].

For binary systems, solubility can be calculated for comparison with literature data providing a K_{sp} value and the ion interaction parameters are known [25]. For ternary systems and above, an iterative approach is described by Pabalan [25] to calculate the equilibrium composition, using all the relevant equilibrium constants with a set of non-linear mass action equations and assisting linear charge and mass balance equations. Pabalan compared experimental solubilities with calculated values obtained using the ion interaction equations. The comparison proves that the solubilities in ternary systems (no additional parameters are required for quaternary and more complex systems) are adequately represented by constant θ_{ij} and ψ_{ijk} terms which are either constant with temperature or have a simple dependence with temperature [25]. In short, there was no overall temperature dependence scheme, but a range of simple temperature dependencies for the virial coefficients of various component subsystems. Using Na_2SO_4 as an example:

$$f(T) = Q1 + Q2(T_R - \frac{T_R^2}{T}) + Q3(T^2 + \frac{2T_R^3}{T} - 3T_R^2) + Q4(T + \frac{T_R^2}{T} - 2T_R) +$$
$$Q5[\ln(\frac{T}{T_R}) + \frac{T_R}{T} - 1] + Q6\{\frac{1}{(T-263)} + \frac{(263T - T_R^2)}{[T(T_R - 263)^2]}\} + \qquad \textbf{(2.11)}$$
$$Q7\{\frac{1}{(680-T)} + \frac{T_R^2 - 680T}{[T(680 - T_R)^2]}\}$$

Where T is the temperature of interest and T_R is the reference temperature of 298.15 K. The data in table 2.4 [25] is for use with Eq. 2.11 to predict the new values of $\beta^{(0)}, \beta^{(1)}$ and C^{ϕ}_{MX} with temperature.

	$\beta^{(0)}$	$\beta^{(1)}$	C^{ϕ}_{MX}
Q1	-1.727 E-2	0.7534	1.1745 E-2
Q2	1.7828 E-3	5.61 E-3	-3.3038 E-4
Q3	9.133 E-6	-5.7513 E-4	1.85794 E-5
Q4	0	1.11068	-3.9200 E-2
Q5	-6.552	-378.82	14.2130
Q6	0	0	0
Q7	-96.90	1861.3	-24.950

Table 2.4: The numerical data for Eq. 2.11 to predict the temperature dependence of the second and third virial coefficients.

The mixing parameters (θ_{ij}, ψ_{ijk}) are necessary for calculations pertaining to ternary systems and above. Values for the mixing parameters are obtained experimentally, for example from galvanic cell measurements [12] or activity/osmotic coefficient data or solubility data for common ion mixtures [25]. The θ_{ij} parameters are independent of the oppositely charged ions, therefore to get a value for, say, $\theta_{Na,K}$ all the data for Na^+-K^+, in the form of NaCl - KCl, Na_2SO_4 – K_2SO_4, $NaNO_3$ – KNO_3 etc are considered simultaneously to determine a single value for $\theta_{Na,K}$ and the values of $\psi_{Na,K,Cl}, \psi_{Na,K,SO_4}$ etc. Both θ_{ij} and ψ_{ijk} undoubtedly vary with temperature, but very little, therefore Pabalan and Pitzer [25] hold θ_{ij} at its 25 °C value and assume a very simple temperature dependence for ψ_{ijk}.

The temperature dependence equation shown for Na_2SO_4 is particular to that mineral with similar information given for all binary systems under consideration outlining the temperature dependence of the virial coefficients in a similar manner. In Møller's 1988 paper on the solubility of minerals in the Na-Ca-Cl-SO_4-H_2O system [24] she describes the temperature dependence of the system with one equation, which had been previously specified by Rogers and Pitzer to describe the

temperature dependence of the solution parameters of Na_2SO_4-H_2O. This equation (Eq 2.12) was used with literature data to establish temperature dependant parameters for calculating all the binary interaction parameters, the mixing parameters, A^{ϕ} and the standard state chemical potentials of water and solid salts.

$$Parameter(T) = a_1 + a_2 T + \frac{a_3}{T} + a_4 \ln T + \frac{a_5}{T - 263} + a_6 T^2 + \frac{a_7}{680 - T} + \frac{a_8}{T - 227} \quad \textbf{(2.12)}$$

At high temperatures Spencer et al. [27] felt that the above equation had some problems; mainly that the inverse temperature minus a constant placed constraints on the valid temperature range achievable with this expression. They chose to adapt the equation to the following:

$$P(T) = a_1 + a_2(T) + a_6(T^2) + a_9(T^3) + \frac{a_3}{T} + a_4 \ln T \quad \textbf{(2.13)}$$

They note that the emphasis of the model is on temperatures below 25 °C and because there are fewer terms, the fit at higher temperatures is less accurate than Pabalan and Pitzer [25]. With respect to standard chemical potentials, Spencer et al. [27] note that it would be advantageous to use temperature dependent equations for the standard chemical potentials of the mineral-solution reactions based on heat capacities, enthalpies or entropies. However, they conclude this is not possible for three reasons: heat capacity data for the solid-solution reactions at low temperatures are generally not available; the higher temperature data do not give satisfactory fits to low temperature solubility data if simple extrapolations are made and there are discrepancies in some of the standard chemical potentials based on heat capacity and enthalpy-entropy data even at 25 °C.

They chose to fit solubility data to obtain standard chemical potentials for reactions between solution species and mineral phases. This model was re-evaluated and parameters re-estimated by Marion and Farren [23] for their FREZCHEM program due to an obvious problem with sulphate chemistry in the Spencer et al. [27]

model on which the program is based. Marion and Farren extrapolated published solubility product equations for many sulphate salts (including mirabilite) into the temperature region of interest. The Pitzer equation parameters were estimated from solubility data. Using the temperature dependent equation of Spencer et al. (Eq. 2.13) they minimise the function below:

$$f = \sum[\ln(Ksp) - \ln(IAP)]^2 \qquad \textbf{(2.14)}$$

A description of the iterative process of the program to calculate can be found here [23].

Pitzers expressions for Gibbs free energy, osmotic and activity coefficient as developed from the Guggenheim-Scatchard equations are the basis for many models or solutions which predict mineral equilibria or solubility in concentrated aqueous solutions. The purpose of this section was to give an overview of this important model rather than a full account of the parameters considered and mineral subsystems modelled.

2.4 Polymorphs of sodium sulphate

One of the most interesting aspects of sodium sulphate is the range of polymorphs it exhibits with respect to temperature. These polymorphs, originally reported by Kracek are labelled with Roman numerals I to V. Na_2SO_4 (I) corresponds to the phase which crystallises form the molten salt and Na_2SO_4 (V) to the phase which crystallises from aqueous solution. Kracek and Gibson found that dilatometer measurements on the dry salt were difficult due to the slow attainment of equilibrium in the system and reported hysteresis. They found it almost impossible to obtain a perfectly dry sample of sodium sulphate at temperatures below 200 °C, which is necessary for investigation of phase V, as it remains in phase III after cooling from temperatures above 200 °C [28]. The dry work they did attempt (at a pressure of 50 megabaryes designed to keep water present in the liquid state below 270 °C), yielded some interesting results.

They concluded that although the temperature assignment of the transitions cannot be very accurate, in the region of 514 K, phase III transforms to phase I, although they note some sluggishness over this change and state that the reaction was not complete until 528 – 533 K. On cooling phase I transforms to phase III via phase II. At 509 K, which they state was a reproducible point, phase I transforms to phase II, then a more sluggish transform in the vicinity of 503 – 493 K is labelled as phase II to phase III [28]. They also note that phase III is stable indefinitely at room temperature. They carried out further examination of the dry salt using a pressure dilatometer and a sample which had been dried at a lesser temperature (110 °C) for 2-3 months. Examination of the starting material indicated it was thenardite (phase V) and was subsequently examined over the range 433 – 533 K and at a pressure of 50 megabaryes.

The first phase transition is to phase IV, at a temperature which was hard for Kracek and Gibson to define as the volume of the phase change was small and the rate of reaction slow. They note change of IV – III in the dry sample is also slow and is delayed until at least 493 – 503 K. In contrast, the presence of aqueous solution substantially speeds up the transformations and reduces the hysteresis. The liquid can be seen as providing a medium for re-crystallisation and thus faster attainment of equilibrium. The IV – III and III – I changes are markedly accelerated by the presence of water. They assign the stable phases according to the equation below:

$$Na_2SO_4V \xleftrightarrow{433\text{-}453\,K} Na_2SO_4IV \xleftrightarrow{458\,K} Na_2SO_4III \xleftrightarrow{514\,K} Na_2SO_4I \quad \textbf{(2.15)}$$

They suggested that phase II (which forms at 509 K during cooling of phase I to phase III only) is metastable. The explanation they offer is that in the dry state, phase I shows reluctance to transform into phase III, as the temperature is dropped past the equilibrium temperature of phase III to that of phase II, leads to the temporary appearance of phase II before it converts irreversibly to phase III. As they have stated, water cuts down the hysteresis of the phase transitions and consequently, phase II does not form. They conclude transition of V to IV is sluggish and did not assign a temperature to it, but the IV to III transition was much sharper, occurring at

458 K. The accurate measurement of this temperature was only possible in the aqueous state.

Brodale and Giauque [29] believe that phase IV is stable above 458 K, having been produced by a stable transition from phase V at 458 K and that III is metastable throughout the entire temperature range of the polymorphs. They begin the analysis of the stable phases by constructing a free energy diagram, as shown below in figure 2.4.

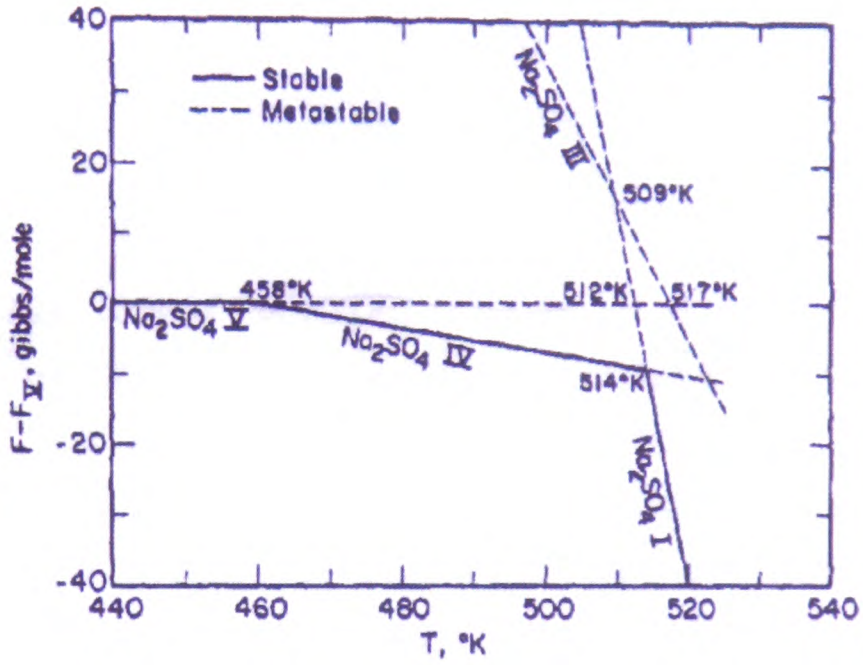

Figure 2.4: Free energy diagram from Brodale and Giauque [29] showing the stable phases (solid lines) and metastable phases (dashed lines).

Heat of solution measurements made by Brodale and Giauque [29] and Pitzer and Coulter [30] provide the equilibrium temperature between metastable phase V and III as 517 K, which they use to anchor the III curve. They state that phase IV must have an enthalpy content and heat capacity similar to phase V due to the overall thermodynamic data and proximity of the phase transitions in the short range above 500 K. They went on to prove experimentally that the state produced by holding Na_2SO_4 at a temperature above the 458 K transition acquired an increased enthalpy of 75 cal/mol, which they assume to be the heat of transition of phase V to phase IV. Extrapolating the thermodynamic data of phase I, they find an intersection between phase I and metastable phase III at 509 K.

A transformation at 509 K was also reported by Kracek and Gibson [28] who discover this transition on cooling the sample and assign it to the equilibrium temperature of the I → II inversion. Brodale and Giauque make no mention of phase II.

In summation, Brodale and Giauque [29] believe (through experimental results and third law treatment of the data) that there are 3 stable phases (I, IV, V) and one permanently metastable phase (III) which can exist indefinitely at room temperature providing it is kept dry.

Further investigations were carried out by Rasmussen et al. [31] using powder diffraction and DSC techniques. Their powder X-ray data shows the existence of the phases 'normally labelled I, II, III and V' but the thermal measurements are less clear. They believe that phase V (their starting material) converts to phase I at 514 K (confirmed by thermal and X-ray methods), which on cooling converts to phase II at 506 K and to phase III at 498 K. They could not find any evidence at all of phase IV using X-ray measurements, but it could not be ruled out on the basis of the DSC measurements.

They go on to analyse the heats of transition and compare it to literature values, although noticeably not the Brodale and Giauque values. They measure the ΔH of V- I transition six times and the ΔH of the III – I and I – III transitions seven times, notably they only report one case in which they find the peaks of the I – II and II – III transitions separated well enough to permit individual determinations of the two transitions.

The sluggishness of the V – I transition is clear as they conclude there is no well defined onset temperature. They note the first small peak begins to appear near 473 K and peak values are found from 518 – 526 K and that with the exception of the V – I transition the temperatures found are within 2 – 4 K of those reported in the literature. With respect to the accuracy of these measurements, Rasmussen et al. note that there is hysteresis associated with the Na_2SO_4 transitions and that temperature measurements depend on the relative positions of the sample and thermocouple and on the method of defining transition temperatures. The phases are confirmed by X-ray diffraction and structures are refined on the basis of published structures for the phases with close agreement.

The phase transitions as described by Rasmussen et al. [31] can be represented as:

$$\begin{aligned} &Na_2SO_4(V) \xrightarrow{513K} Na_2SO_4(I) \\ &Na_2SO_4(III) \xleftarrow{493K} Na_2SO_4(II) \xleftrightarrow{503K} Na_2SO_4(I) \end{aligned} \qquad \textbf{(2.16)}$$

And starting with phase III:

$$Na_2SO_4(III) \xleftrightarrow{515K} Na_2SO_4(I) \qquad \textbf{(2.17)}$$

The transition values are taken from the X-ray analysis (V – I, I – II, II – III) and from both DSC and X-ray (III – I). The DSC values they report for I – II and II – III are 506 K and 498 K respectively.

The results of Wiedemann et al. [32] from DTA and high temperature powder XRD investigations indicate the phase transitions can be viewed as such:

$$\begin{aligned} &Na_2SO_4(V) \xrightarrow{485K} Na_2SO_4(III) \xrightarrow{515-523K} Na_2SO_4(I) \\ &Na_2SO_4(III) \xleftarrow{488-493K} Na_2SO_4(II) \xleftarrow{509K} Na_2SO_4(I) \end{aligned} \qquad \textbf{(2.18)}$$

With phase II occurring on cooling only.

A comparison of the four papers discussed above [28, 29, 31, 32] proves interesting. Table 2.5 lists the transition, temperature of transition and enthalpy of transition for the papers listed.

Data set	Transition	ΔH kJ mol^{-1}	Temperature
[29]	V – IV	0.314	458 K
[31]	V – IV*	0.3	_
[28]	V – IV[a]	_	433 – 453 K
[29]	III – I	6.891 @ 514 K	509 K
[31]	III – I	[7.0, 6.6, 6.6] 5.84	515 K
[28]	III – I[a,b,c]	_	514 K
[32]	III – I	_	515 – 523 K
[29]	IV – I	10.93 @ 514 K	514 K
[28]	IV – III[a]	_	458 K
[29]	V – I	11.22 @ 512 K	512 K
[31]	V – I	[11.7, 10.8, 10.8] 7.42	513 K
[29]	V – III	4.354 @ 514 K	517 K
[31]	V – III	Calc. [4.7, 4.2] 1.58	_
[32]	V – III	_	485 K
[31]	II – III	2.4, 2.3, 1.9	493 K
[28]	II – III[b,c]	_	493 – 503 K
[32]	II – III	_	488 – 493 K
[31]	I – II	[4.6, 4.5] 4.5	503 K
[28]	I – II[b,c]	_	509 K
[32]	I – II	_	509 K

Table 2.5: Comparison of transition temperatures and corresponding ΔH values where applicable, from literature sources listed in the first column. The superscript * represents an estimated heat of transition for the phase change V – IV based on a small uncertainty in the DSC diagram from Rasmussen et al. Superscripts a, b, and c represent whether temperature of transition was found using moist Na_2SO_4 (a) at 50 megabaryes (50 bar), dry Na_2SO_4 at ambient pressure (b) or dry Na_2SO_4 at 50 megabaryes (50 bar) (c). The values in brackets are the literature values quoted by Rasmussen et al. The value outside the bracket is the mean result from their experiments.

Comparison of these four important papers leads to the following conclusions:

1. Phase V is the stable phase at room temperature.

2. Phase III if formed at higher temperatures is stable indefinitely at room temperature providing it is kept dry. If the sample is allowed contact with moisture, phase III converts to phase V under ambient conditions.

3. The presence of water accelerates phase transitions and cuts down the marked hysteresis reported.

4. Kracek et al. and Brodale and Giauque report phase IV, Rasmussen et al. find no evidence of it (X-ray results) although they concur that it cannot be ruled out by an inconsistency in the DSC results. Oddly enough, the ΔH they assign to it (0.3 kJ mol^{-1}) is extremely close to the experimental value of Brodale and Giauque (0.314 kJ mol^{-1}). Both Rasmussen et al. and Brodale and Giauque indicate that the structure of phase IV must be close to that of V. Kracek et al. find the V – IV transition sluggish and difficult to pin a temperature to. The IV – III transition they find more amenable and discover the temperature of transition to be 458 K wet (which Brodale and Giauque assign to the V – IV transition) and 493 – 503 K dry.

5. Phase II is reported by Rasmussen et al. (X-ray and DSC), Wiedemann et al. (X-ray and DTA) and Kracek et al. on cooling phase I in the dry state as a transient phase only. Both report the reversibility of the II $\leftrightarrow$ I transition but the II $\rightarrow$ III transition is irreversible. The measurements made by Kracek et al. under solution at 50 megabaryes show that phase II does not occur, thus it is associated with the hysteresis of cooling phase I. The transition temperature from I $\leftrightarrow$ II is given as 503 K by Rasmussen et al. and 509 K by Kracek et al., and 509 K by Wiedemann et al. It is an interesting comparison that Brodale and Giauque ascribe that same temperature to transition of metastable III to metastable I. Brodale and Giauque do not observe phase II or even mention it. This is possibly because the only dry measurements they make are the heat capacity of phase III measurements carried out over the

range 15 – 300 K, which is possibly below the region at which phase II will be present. Although it should be noted that they use literature values for temperatures above 300 K and still make no mention of phase II.

6. Rasmussen et al. report that dry phase V goes directly, albeit sluggishly, to phase I on heating at 513 K, which is close to the 512 K value noted by Brodale and Giauque. The Brodale value is calculated as the equilibrium between metastable V and metastable I (as can be seen from figure 2.3). Kracek et al. report that on heating phase V transforms to phase IV (sluggish) then IV to III at 458 K (which Brodale and Giauque assign to V→ IV) in the presence of moisture. Kracek et al. report that the IV to III transition is delayed in the dry sample by comparison until 493 – 503 K. In contrast, Wiedemann et al. find phase V transforms to phase I via phase III, with phase III transforming to phase I in the temperature interval 515 – 523 K.

It is clear that there is some ambiguity amongst the literature sources on the phase transitions. All sources agree that phase V is the stable phase at room temperature, that phase III can exist indefinitely at ambient conditions if kept dry and that phase I is the highest temperature phase. The existence of phases II and IV raise some questions, although there is structural evidence of phase II, phase IV could be considered elusive in terms of X-ray evidence. Clearly though, there is some clustering of numbers, therefore it can be assumed that there are definite points at which phase changes occur as shown below:

1. **458 K** is given as the transition temperature (on heating) for V – IV [29] and V – III [32] and IV – III [28]. All of the four papers believe there is an early transition at around **458 K**. Although Rasmussen et al. do not report this in their XRD measurements; they do not rule it out from their DSC measurements.
2. **513 – 515 K** appears to be another transition point. Brodale et al. assign this to IV – I, Kracek et al to III – I, Rasmussen et al. to V – I (when phase V is

the starting material) and III – I (when phase III is the starting material) and Wiedemann et al. to III – I.

3. **509 K** is ascribed to metastable III – metastable I [29] and I – II on cooling [28, 31]. **503 K** is given as the transition temperature of I – II on cooling by Wiedemann et al. [32].

Differential thermal analysis (DTA) at high temperatures and pressures [33] reveals the existence of new Na_2SO_4 phases labelled VI, VII and VIII. The phase diagram does not show phase II (although it is mentioned in conjunction with the work of Kracek et al. [28, 34, 35]). At ambient pressure, the phase diagram seems to suggest (through heating of a dry sample) a phase progression of V → IV → III → I. Although this could possibly be taken from the work of Kracek et al. as there are no experimental points on the diagram until higher pressures. Phase VI was also postulated by Bridgman [36] in his temperature – pressure diagram of the Na_2SO_4 polymorphs, which he describes as not being able to exist at atmospheric pressure. He measured volume change and used the work of Kracek as a guide and aid for phase identification at ambient and low pressures.

2.5 Polymorphs of sodium sulphate and cation substitution

As discussed in the previous section, there are at least five polymorphs of sodium sulphate, with the possibility of another three. Under ambient conditions, only phase V and III exist with V being the stable phase and III being metastable, although III can remain indefinitely at room temperature and pressure without conversion to V providing it is kept dry. Stabilisation of the higher temperature phase I to room temperature has received some interest due the modest amount of ionic conductivity demonstrated by phase I at 250 °C. The use of sodium sulphate as a solid electrolyte is hampered by the temperature requirements of phase I, therefore there has been some interest in stabilising this phase at ambient conditions [37-40]. Cation substitution is a method of doing just that. The Na^+ ions can be replaced to a large extent by K^+, Ag^+, Ni^{2+}, Zn^{2+}, Ca^{2+}, Pb^{2+}, Sr^{2+}, Y^{3+}, La^{3+}, Fe^{3+}, etc. Of particular

interest is the replacement of Na by the aliovalent ions $M^{2+}$and M^{3+} which causes up to 30 % vacancies (□) in the cation sublattice as described by Höfer et al. [39] as:

$$Na_{2-2x}M_x^{2+}\square_xSO_4 \quad \textbf{(2.19)}$$

$$Na_{2-3x}M_x^{3+}\square_{2x}SO_4 \quad \textbf{(2.20)}$$

In these solid solutions the modification of phase I can be stabilised and investigated at room temperature. The samples were prepared by heating relative amounts of the salts (Na_2SO_4 and other metal sulphates such as $ZnSO_4$) to melting point in a platinum crucible and quenching in air. The ionic conductivity results from various solid solutions suggest that the conductivity varies only with the number of vacancies and not with the size or valency of the substituting ion and that Na^+ is the only charge carrier in the Na_2SO_4 (I) solid solutions [39]. This view is contradicted by Singhvi et al. who find that the conductivity peaks when the dopant size is comparable to that of Na^+ (while working with a set vacancy concentration to examine the effect of dopant ion size) [41]. Höfer et al. discuss the effect of the vacancy concentration on ionic conductivity. At low vacancy concentrations, they assume a simple model, where there are no interactions between the mobile Na^+ and the defects (i.e. Y^{3+} and □) which relates to a linear relationship between the conductivity and the vacancy concentration. At high concentrations they describe a more complex situation when interactions between the defects and Na^+ occur, resulting in a decrease in mobility with increasing interaction. As increasing vacancy concentration leads to more migration paths for the sodium ions being created, the decrease in mobility from increasing interaction results in a cancelling out effect. Höfer et al. [39] report that these effects cancel each other out at the conductivity maximum of about 7% □ [42].

Phase III can also be stabilised by cation substitution, this was investigated as a mol % sequence by Freyer et al. and Dharmasena et al. [38, 43]. Both papers mixed the required amounts of various metal sulphate salts with Na_2SO_4, heating the sample to beyond the melting point and quenching to ambient temperature. Dharmasena et al. note that phase III is stabilised by as little as 0.3 mol % $Y_2(SO_4)_3$ and phase I by 3

mol % $Y_2(SO_4)_3$. These results were obtained by powder XRD and Raman Spectroscopy. They carried out some further investigations using calorimetry (DSC) to examine the effect of $Y_2(SO_4)_3$ on the transition temperature of stabilised III to I and concluded that the enthalpy and entropy of phase III approaches that of phase I with increasing substitute cation concentration. They discovered that the entropy of phase I is considerably larger than phase III and the transition temperature of phase III to phase I decreases with increasing mol % $Y_2(SO_4)_3$.

Freyer et al. investigated (using powder XRD and differential thermal analysis) the phase diagram of Na_2SO_4 – $CaSO_4$. Samples were mixed, melted at 1050 °C before quenching to room temperature. The phases were annealed at different temperatures between several weeks and months. They found that 3 mol % $CaSO_4$ produced phase III and that 5.5 mol % $CaSO_4$ and upwards to 20 mol % produced phase I only. After storage at room temperature for 2 years, the sample was re X-rayed and it was found that the 3 mol % $CaSO_4$ sample was phase III, phase I and phase V (thenardite). The higher mol % samples (12.5 mol % to 20 mol % $CaSO_4$) transformed completely to glauberite and thenardite. It is unknown if the samples were kept very dry or not. Freyer et al. list glauberite and thenardite as the equilibrium phases at temperatures below 180 °C and 50 mol % $CaSO_4$, which is the range of interest for this work.

2.5.1 Structural investigations

The stabilisation of high temperature phases to room temperature by the substitution of aliovalent cations is of crystallographic interest also. Shown in table 2.6 is data from Rasmussen et al. [31] giving the cell parameters and space groups of four polymorphs. Much interest has been generated by the stabilisation of phase I and its high ionic conductivity.

Phase	Temp. (K)	a (σ) Å	b (σ) Å	c (σ) Å	Dx Mg m^{-3}	Space group
I	543	5.39357(13)	9.34194(22)	7.24651(22)	2.58	$P6_3/mmc$
II	493	5.30991(22)	9.46928(38)	7.1436(29)	2.63	Pbnm
III	463	5.63041(21)	9.04343(34)	7.03771(24)	2.63	Cmcm
V	293	5.85820(6)	12.29900(13)	9.81380(11)	2.67	Fddd

Table 2.6: Na_2SO_4 polymorph cell parameters. Phase I is hexagonal, but the cell parameters are given in the equivalent orthorhombic setting by Rasmussen et al.

Phase I is the subject of several investigations [31, 37, 40, 44] due to its hard to resolve structure and interesting ionic conductivity. The most interesting fact about phase I, and source of difficulty in resolving the structure is the strong orientational disorder of the SO_4 tetrahedra agreed on by all of the investigations discussed here. Eysel et al. believe this disorder is the reason for the unusual unlimited $SO_4 - CO_3$ substitution. The oscillation of the tetrahedra means that the Na^+ ions can move easily from vacancy to vacancy resulting in dynamic disorder, which is more compatible with the known high ionic conductivity [40]. Structural differences are known to exist between a quickly quenched crystal and a slowly cooled one, the main difference being an enlargement of the unit cell, which is thought to be the result of cation ordering [37] during slow cooling. The main difference between literature sources on the structure of phase I is in the atomic coordinates. A comparison of the unit cell parameters of substituted phase I and pure phase I reveals a smaller cell for the substituted and quenched samples, possibly indicating a higher degree of disorder. There is no corresponding information for substituted phase III.

2.6 References

1. Rodriguez-Navarro, C. and E. Doehne, *Salt weathering: Influence of evaporation rate, supersaturation, and crystallization pattern.* Earth Surface Processes and Landforms, 1999. **24**: p. 191-209.

2. Flatt, R.J., *Salt damage in porous materials: how high supersaturations are generated.* Journal of Crystal Growth, 2002. **242**: p. 435-454.

3. Scherer, G.W., *Crystallization in pores.* Cement and Concrete Research, 1999. **29**: p. 1347 - 1358.

4. Scherer, G.W., *Stress from crystallization of a salt.* Cement and Concrete Research, 2004. **34**: p. 1613 - 1624.

5. Correns, C.W., *Growth and dissolution of crystals under linear pressure.* Discussions of the Faraday Society, 1949. **5**: p. 267-271.

6. Butler, J.N. and D.R. Cogley, *Ionic Equilibrium, Solubility and pH calculations*. 1998, New York: John Wiley and Sons, Inc.

7. Price, C.A. *The use of the sodium sulphate crystallisation test for determining the weathering and resistance of untreated stone*. in *Deterioration and Protection of Stone Monuments*. 1978. Paris: RILEM.

8. Gmelin, L., *Handbuch der Anorganischen Chemie*. Vol. 21. 1966, Berlin: Springer-Verlag.

9. Kracek, F.C., *International Critical Tables of Numerical Data, Physics, Chemistry and Technology (1st Electronic Edition)*, ed. E.W. Washburn. 2003: Knovel. p371.

10. Linke, W.F., *Solubilities of Inorganic and Metal Organic Compounds*. 4th ed. Vol. 2. 1965: American Chemical Society.

11. Plummer, L.N., D.L. Parkhurst, G.W. Fleming, and S.A. Dunkle, *A computer program for incorporating Pitzer's equations for calculation of geochemical reactions in brines*. 1988, US Salinity Laboratory: Reston, Virginia.

12. Pitzer, K.S., *Thermodynamics of electrolytes I: Theoretical basis and general equations.* Journal of Physical Chemistry, 1973. **77**: p. 268-277.

13. Block, J. and O.B. Waters, *The $CaSO_4$-Na_2SO_4-NaCl-H_2O system at 25° to 100°.* Journal of Chemical and Engineering Data, 1968. **13**: p. 336-344.

14. Brönsted, J.N., *International Critical Tables of Numerical Data, Physics, Chemistry and Technology (1st Electronic Edition)*, ed. E.W. Washburn. 2003: Knovel. p216.

15. Hill, A.E. and J.H. Wills, *Ternary systems. XXIV. Calcium sulfate, sodium sulfate and water.* Journal of the American Chemical Society, 1938. **60**: p. 1647-1655.

16. Freyer, D., S. Fischer, K. Köhnke, and W. Voigt, *The formation of double salt hydrates I. Hydration of quenched Na_2SO_4 - $CaSO_4$ phases.* Solid State Ionics, 1997. **96**: p. 29-33.

17. Pabalan, R.T. and K.S. Pitzer, *Thermodynamics of concentrated electrolyte mixtures and the prediction of mineral solubilities to high temperatures for mixtures in the system Na-K-Mg-Cl-SO_4-OH-H_2O.* Geochimica et Cosmochimica Acta, 1987. **51**: p. 2429-2443.

18. Pabalan, R.T. and K.S. Pitzer, *Heat capacity and other thermodynamic properties of $Na_2SO_{4(aq)}$ in hydrothermal solutions and the solubilities of sodium sulfate minerals in the system Na-Cl-SO_4-OH-H_2O to 300 °C.* Geochimica et Cosmochimica Acta, 1988. **52**(10): p. 2393-2404.

19. Pitzer, K.S., *Thermodynamics of Electrolytes. I. Theoretical Basis and General Equations.* Journal of Physical Chemistry, 1973. **77**(2): p. 268-277.

20. Pitzer, K.S., *Thermodynamics*. 3rd ed. 1995: McGraw-Hill.

21. Harvie, C.E., H.P. Eugster, and J.H. Weare, *Mineral equilibria in the six-component seawater system, Na-K-Ca-SO_4-Cl-H_2O at 25 °C. II: Compositions of the saturated solutions.* Geochimica et Cosmochimica Acta, 1982. **46**: p. 1603-1618.

22. Hovey, J.K., K.S. Pitzer, and J.A. Rard, *Thermodynamics of Na_2SO_4(aq) at temperatures T from 273 K to 373 K and of {(1-y)H_2SO_4 + yNa_2SO_4}(aq) at T = 298.15 K.* Journal of Chemical Thermodynamics, 1993. **25**: p. 173-192.

23. Marion, G.M. and R.E. Farren, *Mineral solubilities in the Na-K-Mg-Ca-Cl-SO_4-H_2O system: A re-evaluation of the sulfate chemistry in the Spencer-Møller-Weare model.* Geochimica et Cosmochimica Acta, 1999. **63**: p. 1305-1318.

24. Møller, N., *The prediction of mineral solubilities in natural waters: A chemical equilibrium model for the Na-Ca-Cl-SO_4-H_2O system to high temperature and concentration.* Geochimica et Cosmochimica Acta, 1988. **52**: p. 821-837.

25. Pabalan, R.T. and K.S. Pitzer, *Thermodynamics of concentrated electrolyte mixtures and the prediciton of mineral solubilities to high temperatures for mixtures in the system Na-K-Mg-Cl-SO_4-OH-H_2O.* Geochimica et Cosmochimica Acta, 1987. **51**: p. 2429-2443.

26. Pabalan, R.T. and K.S. Pitzer, *Heat capacity and other thermodynamic properties of Na_2SO_4(aq) in hydrothermal solutions and the solubilities of*

sodium sulfate minerals in the system Na-Cl-SO_4-OH-H_2O to 300 °C. Geochimica et Cosmochimica Acta, 1988. **52**: p. 2393-2404.

27. Spencer, R.J., N. Møller, and J.H. Weare, *The prediciton of mineral solubilities in natural waters: A chemical equilibrium model for the Na-K-Ca-Mg-Cl-SO_4-H_2O system at temperatures below 25 °C.* Geochimica et Cosmochimica Acta, 1990. **54**: p. 575-590.

28. Kracek, F.C. and R.E. Gibson, *The polymorphism of sodium sulfate: III. Dilatometer investigations.* Journal of the American Chemical Society, 1930. **34**: p. 188 - 206.

29. Brodale, G.E. and W.F. Giauque, *The relationship of crystalline I, III, IV and V of anhydrous sodium sulphate as determined by the third law of thermodynamics.* Journal of Physical Chemistry, 1972. **76**(5): p. 737-743.

30. Pitzer, K.S. and L.V. Coulter, *The heat capacities, entropies and heats of solution of anhydrous sodium sulphate and sodium sulphate decahydrate. The application of the third law of thermodynamics to hydrated crystals.* Journal of the American Chemical Society, 1938. **60**: p. 1310-1315.

31. Rasmussen, S.E., J.E. Jørgensen, and B. Lundtoft, *Structures and phase transitions of Na_2SO_4.* Journal of Applied Crystallography, 1996. **29**: p. 42-47.

32. Wiedemann, H.G., W. Smykatz-Kloss, and W. Eysel, *DTA and high temperature x-ray investigations of natural and synthetic thenardites, Na_2SO_4.* Journal of Thermal Analysis, 1980. **2**: p. 347 - 352.

33. Pistorius, C.W.F.T., *Phase diagrams of sodium sulfate and sodium chromate to 45 kbar.* Journal of Chemical Physics, 1965. **43**(8): p. 2895 - 2898.

34. Kracek, F.C., *The polymorphism of sodium sulfate: I. Thermal analysis.* Journal of Physical Chemistry, 1929. **33**(1281-1303).

35. Kracek, F.C. and R.E. Gibson, *The polymorphism of sodium sulphate: II. The densities of anhydrous sodium sulfate at 25 °C.* Journal of the American Chemical Society, 1929. **33**: p. 1304-1308.

36. Bridgman, P.W., *Polymorphic transitions of 35 substances to 50,000 kg/cm^2.* Proceedings of the American Academy of Arts and Sciences, 1937. **72**(2): p. 46 - 121.

37. Armbruster, T., R. Basler, P. Mikhail, and J. Hulliger, *Defect structure of ytterbium(III) doped Na_2SO_4 phase I.* Journal of Solid State Chemistry, 1999. **145**: p. 309 - 316.

38. Dharmasena, G. and R. Frech, *The stabilization of phase III and phase I in sodium sulfate by aliovalent cation substitution.* Journal of Chemical Physics, 1993. **99**(11): p. 8929 - 8935.

39. Höffer, H.H., W. Eysel, and U. von Alpen, *Electrochemistry of Na_2SO_4 (I) solid solutions with aliovalent cation substitution.* Journal of Solid State Chemistry, 1981. **36**: p. 365-370.

40. Eysel, W., H.H. Höfer, K.L. Keester, and T. Hahn, *Crystal chemistry and structure of Na_2SO_4 (I) and its solid solutions.* Acta Crystallographica, 1985. **B41**: p. 5 - 11.

41. Singhvi, A., S. Gomathy, P. Gopalan, and A.R. Kulkarni, *Effect of aliovalent cation doping on the electrical conductivity of Na_2SO_4: Role of charge and size of the dopant.* Journal of Solid State Chemistry, 1998. **138**: p. 183-192.

42. Höfer, H.H., W. Eysel, and U. Von Alpen, *Ionic conductivity of Na_2SO_4-I solid solutions.* Materials Research Bulletin, 1978. **13**: p. 265-270.

43. Freyer, D., W. Voigt, and K. Köhnke, *The phase diagram of the system Na_2SO_4 - $CaSO_4$.* European Journal of Solid State Inorganic Chemistry, 1998. **35**: p. 595-606.

44. Naruse, H., K. Tanaka, H. Morikawa, and F. Marumo, *Structure of Na_2SO_4 (I) at 693 K.* Acta Crystallographica, 1987. **B43**: p. 143-146.

3. Introduction

The purpose of this chapter is to examine the solid mirabilite ($Na_2SO_4 \cdot 10H_2O$) to thenardite (Na_2SO_4) phase transitions with temperature in a sealed system using in-situ temperature controlled powder XRD for phase identification. A thorough understanding of the phase transitions between mirabilite and thenardite is necessary to an understanding of the damage caused by these salts to stone. Stone decay by sodium sulphate still has an air of mystery about it. Partly this stems from an incomplete understanding of this interesting salt. Mirabilite in a closed system (i.e. no evaporation) if heated to above the transition temperature of 32.4 °C forms thenardite crystals in equilibrium with a sodium sulphate solution. When the system is cooled again, at what point does mirabilite precipitate? This question provided the motivation for investigating the phase transitions with temperature. In-situ powder XRD was used as the most applicable, unobtrusive and available method of determining which solid phase forms with temperature in a 'closed' system, the advantages and disadvantages of the instrument and technique are discussed throughout this chapter. The originality of this work lies in investigating this system using a heating/cooling XRD stage.

3.1 $Na_2SO_4 \cdot 10H_2O$ – Na_2SO_4 phase transitions

This experiment was carried out as an in-situ powder XRD study. The diffractometer used was a Bruker D8 using fully monochromated CuKα radiation. A heating-cooling stage fitted with a thermocouple which was located inside the base of the sample holder was used for temperature control. To reach temperatures below 20 °C, liquid nitrogen was pumped through the stage. The starting material was mirabilite ($Na_2SO_4 \cdot 10H_2O$, ACS, reagent grade, 99+ %) which was packed into the sample holder and covered with transparent Kapton film (an adhesive film) to prevent premature sample dehydration. Due to the unstable nature of mirabilite at generally ambient RH conditions, packing of the sample holder had to be done quickly and without prior grinding of the sample. This leads to unavoidable preferred orientation

effects. It should be noted that careful grinding of mirabilite can be carried out if the sample is coated with mineral oil, but this was not considered suitable for investigating in-situ phase change. Mass measurements before and after the experiment (listed at the top of table 3.1) confirmed that moisture loss through the Kapton film was small. The mass loss is given as a percentage of the mass of mirabilite only. Six experiments were carried out to investigate the kinetics of transformation, which are reported here. The first experiment was designed to investigate the effect of prolonged exposure at one temperature on the phase transition; the second and third experiments investigated the effect of refining the temperature interval preceding the thenardite to mirabilite phase transition, while the fourth, fifth and sixth experiments were either to check the reproducibility or examine the effect of prolonging the length of time the sample was held at the lowest temperature for. The starting temperature for each run was 20 °C, with the system given 30 min at each temperature to equilibrate, before a scan was taken (10° 2θ to 45° 2θ) lasting approximately 15 min. The intervals employed, temperature and number of scans per experiment are listed below in table 3.1. The reason behind such small temperature intervals around 32 °C was to examine the data at the accepted transition temperature of 32.4 °C [1].

Diffraction patterns were analysed using DIFFRAC^{plus} evaluation software from Bruker and JCPDS (Joint Committee for Powder Diffraction Studies) cards were used for mineral identification and are detailed with the relevant experiment.

Exp. 1		Exp. 2		Exp. 3		Exp. 4		Exp. 5		Exp. 6	
ML=2.85%		ML=2.65%		ML=2.65%		ML=2.22%		ML=2.05%		ML=2.37%	
Scan	Temp.	Scan	Temp.	Scan	Temp.	Scan	Temp.	Scan	Temp.	Scan	Temp.
1	20 °C	1	20 °C	1	20 °C	1	20 °C	1	20 °C	1	20 °C
2	25 °C	2	25 °C	2	25 °C	2	25 °C	2	25 °C	2	25 °C
3	29 °C	3	29 °C	3	29 °C	3	29 °C	3	29 °C	3	29 °C
4	30 °C	4	30 °C	4	30 °C	4	30 °C	4	30 °C	4	30 °C
5	31 °C	5	31 °C	5	31 °C	5	31 °C	5	31 °C	5	31 °C
6	32 °C	6	32 °C	6	32 °C	6	32 °C	6	32 °C	6	32 °C
7	33 °C	7	33 °C	7	33 °C	7	33 °C	7	33 °C	7	33 °C
8	34 °C	8	34 °C	8	34 °C	8	34 °C	8	34 °C	8	34 °C
9	40 °C	9	40 °C	9	40 °C	9	40 °C	9	40 °C	9	40 °C
10	34 °C	10	34 °C	10	34 °C	10	34 °C	10	34 °C	10	34 °C
11	33 °C	11	33 °C	11	33 °C	11	33 °C	11	33 °C	11	33 °C
12	32 °C	12	32 °C	12	32 °C	12	32 °C	12	32 °C	12	32 °C
13	31 °C	13	31 °C	13	31 °C	13	31 °C	13	31 °C	13	31 °C
14	30 °C	14	30 °C	14	30 °C	14	30 °C	14	30 °C	14	30 °C
15	29 °C	15	29 °C	15	29 °C	15	29 °C	15	29 °C	15	29 °C
16	25 °C	16	25 °C	16	25 °C	16	25 °C	16	25 °C	16	25 °C
17-27	20 °C	17	20 °C	17	20 °C	17	20 °C	17	20 °C	17	20 °C
28	19 °C	18	19 °C	18	15 °C	18	15 °C	18	15 °C	18	19 °C
29	18 °C	19	18 °C	19	10 °C	19	10 °C	19	10 °C	19	18 °C
30	17 °C	20	17 °C			20	5 °C	20	5 °C	20	17 °C
31	16 °C	21	16 °C			21	5 °C	21	7 °C	21	16 °C
32	15 °C	22	15 °C			22	6 °C			22	15 °C
33	10 °C	23	10 °C							23	10 °C
34	5 °C	24	5 °C							24	5 °C

Table 3.1: Experimental details of the six experiments reported to investigate the mirabilite-thenardite phase transitions with temperature. Set temperatures were used to keep results comparable and a scan number is added for convenience. ML is the mass loss of the sample through the Kapton film during the experiments and is measured gravimetrically.

3.1.1 XRD

As can be seen from figures 3.1-3.6, mirabilite loses its water of hydration according to equation 3.1

$$Na_2SO_4 \cdot 10H_2O_{(s)} \leftrightarrow Na_2SO_{4(s)} + 10H_2O_{(l)} \quad \textbf{(3.1)}$$

After the transition temperature, which is 33 °C from these experiments, thenardite exists as small crystals in aqueous suspension which accounts for the high background of the XRD pattern (removed in any figures presented here). It should be noted that although 33 °C marks the dehydration of mirabilite to thenardite, there are some traces of mirabilite at 33 °C in experiments 2 and 5, however the main mirabilite peaks have gone, leaving a trace of mirabilite only.

Thenardite crystallises at temperatures above the mirabilite-thenardite transition temperature as identifiable prismatic single crystals as illustrated by SEM image, figure 3.10. Thenardite formed by mirabilite dehydration results in 'thenardite crystals which pseudomorphically replace the mirabilite with masses of micron sized crystals' [1]. Rodriguez-Navarro et al. note that at RH values > 40 % the evaporation of a sodium sulphate solution resulted in the formation of mirabilite crystals first followed by their dehydration and transformation into microscopic thenardite crystals which were not identifiable by optical microscopy. They present ESEM micrographs of thenardite crystals formed directly from solution and from the dehydration of mirabilite.

Figure 3.11 shows a sodium sulphate crystal grown from aqueous solution at 20 °C and c. 60% RH. The crystal appeared to dehydrate as it took on an opaque powdery appearance. The original crystal formed was not X-rayed, so no identification is possible, but the end product was crushed for XRD and identified as thenardite. At first glance, it would seem likely that the thenardite crystals in figure 3.11 were formed from dehydration of mirabilite, however, the ESEM images presented by Rodriguez-Navarro et al. indicate that the crystal morphology shown in the magnification of figure 3.11 is produced by direct formation of thenardite from solution. Although it is clear that dehydration took place, so it is likely that the

crystal formed originally was a hydrate. Further work would help to determine what the original phase was.

Thenardite is the stable phase for the remainder of the heating sequence (33 °C to 40 °C). The sample is then cooled. During cooling, the most striking feature of the sample is observed: that mirabilite does not re-form at the temperature it dehydrated at. This delayed formation would indicate that the nucleation of mirabilite is difficult, which has been concluded by other researchers [2, 3].

ESEM investigations carried out by Rodriguez-Navarro et al. demonstrated that thenardite does not form mirabilite by progressive water integration into the crystal, but instead via a process of dissolution and precipitation [4]. Mirabilite does not appear to form until 10 °C in the first three experiments but 15°C in experiments 4-6 (figures 3.7-3.9). When it does form, the pattern shows strong preferred orientation effects. Preferred orientation is defined simply as a condition in which the distribution of crystal orientations is non-random[5]. It is often considered a function of grain or crystal size, as large crystals result in line intensities differing markedly from their normal values, assuming all other variables are equal. Variables such as the radiation wavelength used to obtain the data file and the sample pattern and the apparatus used to record the patterns should be kept constant when comparing patterns. The files chosen from the JCPDS database for thenardite and mirabilite are listed as high quality and calculated respectively and in both cases Cu $K\alpha 1$ was used. The preferred orientation effects are indicated by missing peaks and line intensities much different in scale to what would be expected. In this case, crystal size is the most obvious reason behind this effect.

The X-ray patterns for mirabilite re-precipitation are not as good as could be wished for. There is some speculation on the identification as the peak positions are not ideal and the pattern was subject to peak shift through sample height effects anyway, which is corrected in the figures presented. Further work was carried out using parallel beam geometry (Göbel mirror) to avoid peak shift from sample height effects and also to help quantify peak shift by comparison. While this approach avoided peak shift, the peak heights were considerably lower as the scintillation counter had to be used instead of the position sensitive detector (PSD). The result was that the scan achieved in the temperature range of interest (on cooling below 20

°C) was very weak with not enough peaks for identification. The only other hydrate known to exist is $Na_2SO_4 \cdot 7H_2O$, which is listed in the JCPDS database as card no. 40-0727. The 15, °C, 10 °C and 5 °C scans were checked against this card, with no success which leads to the conclusion that although the scan is not a perfect match for mirabilite, it is a much closer fit than the heptahydrate and therefore is more likely to be mirabilite. The possibility of an unknown lower hydrate cannot be ignored.

As can be seen, throughout the 6 experiments there is a strong similarity between the peaks present, as the same peaks often appear in each experiment and the same expected strong peaks are missing.

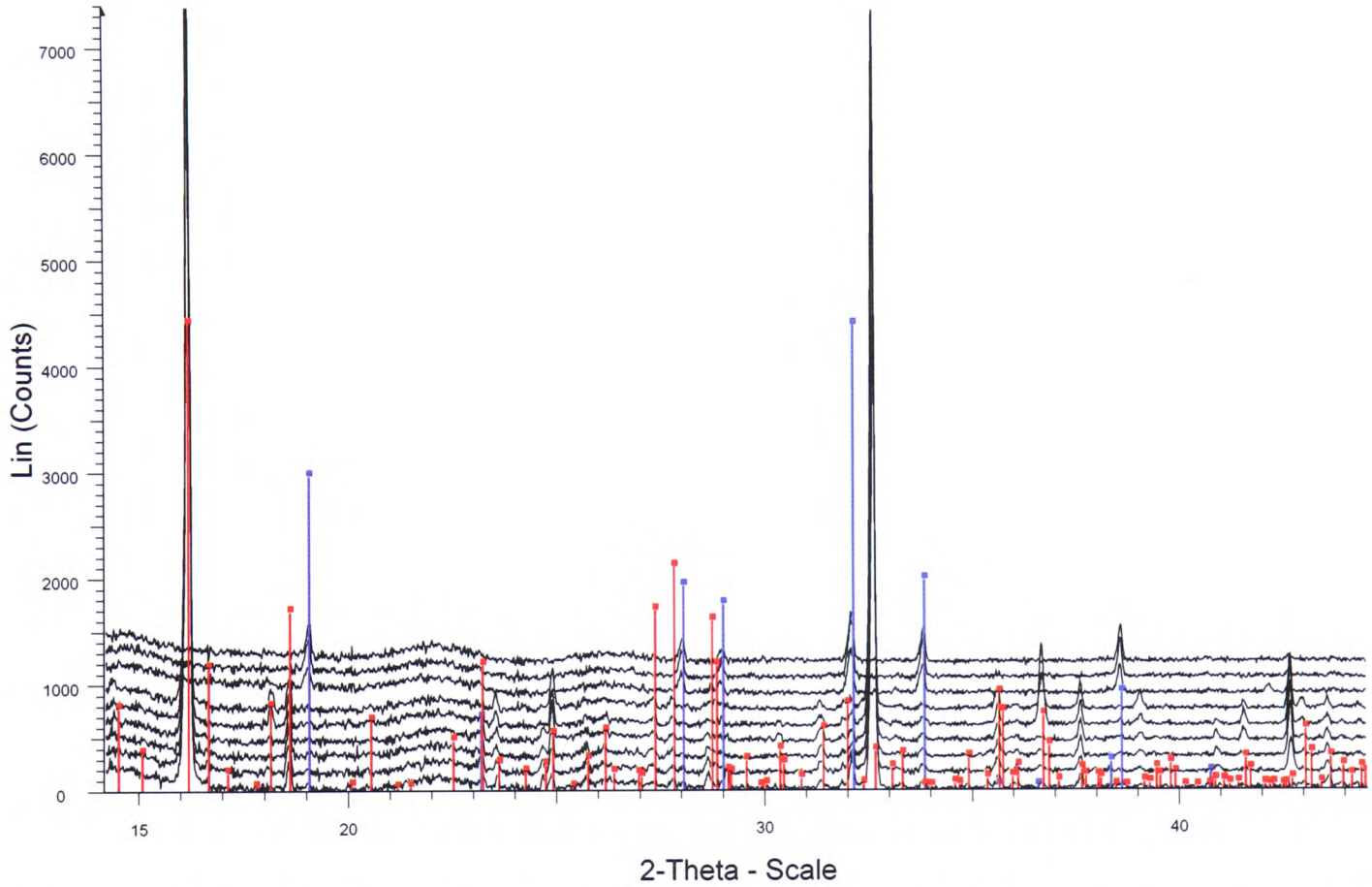

Figure 3.1a: Experiment 1, scans 1-9 as detailed in table 3.1. Thenardite peaks are indicated in blue; mirabilite peaks are indicated in red.

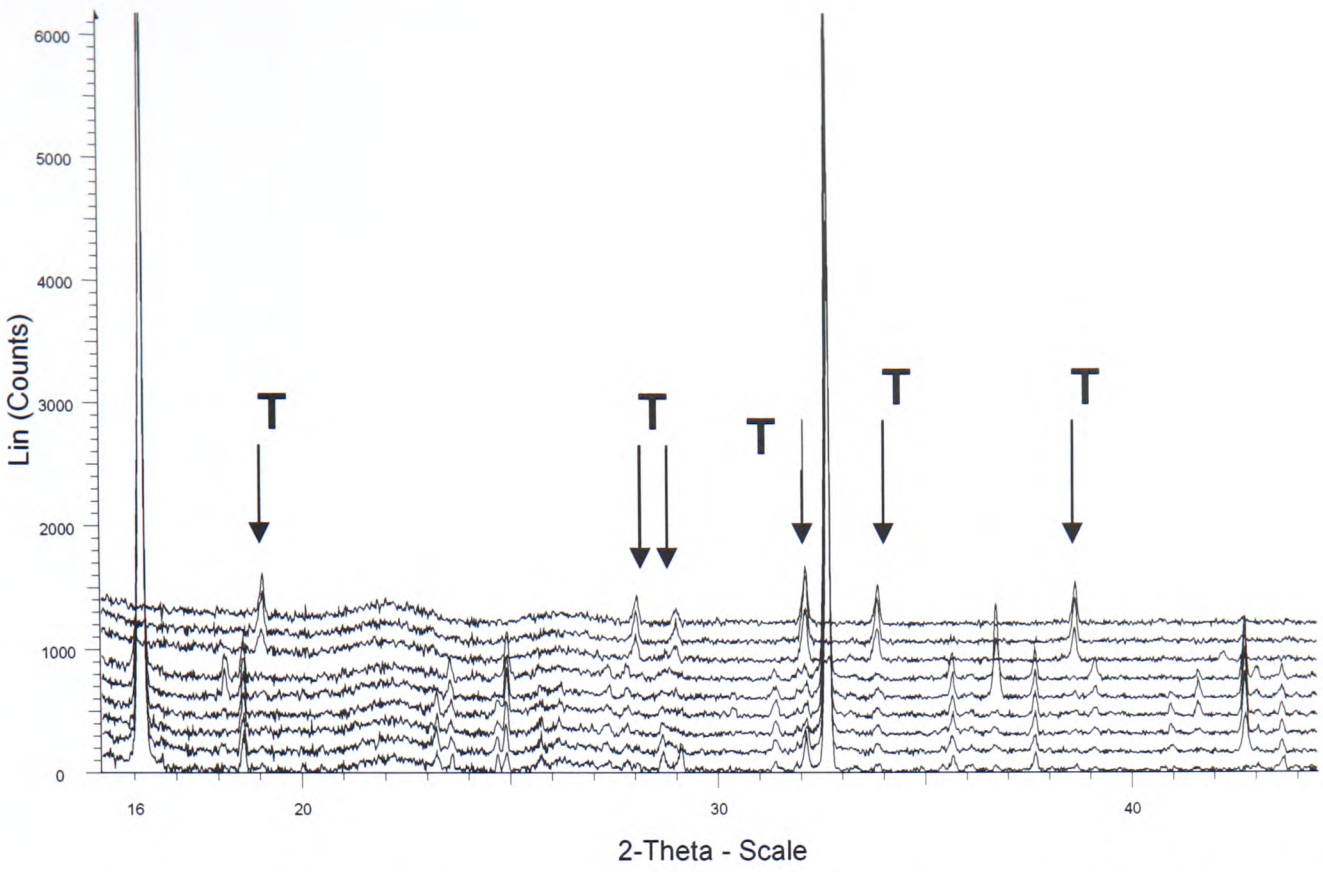

Figure 3.1b: Experiment 1, scans 1-9. For clarity, peaks are shown without JCPDS stick plots. Thenardite peaks are marked T (corresponding to card no. 37-1465) the remaining peaks are mirabilite.

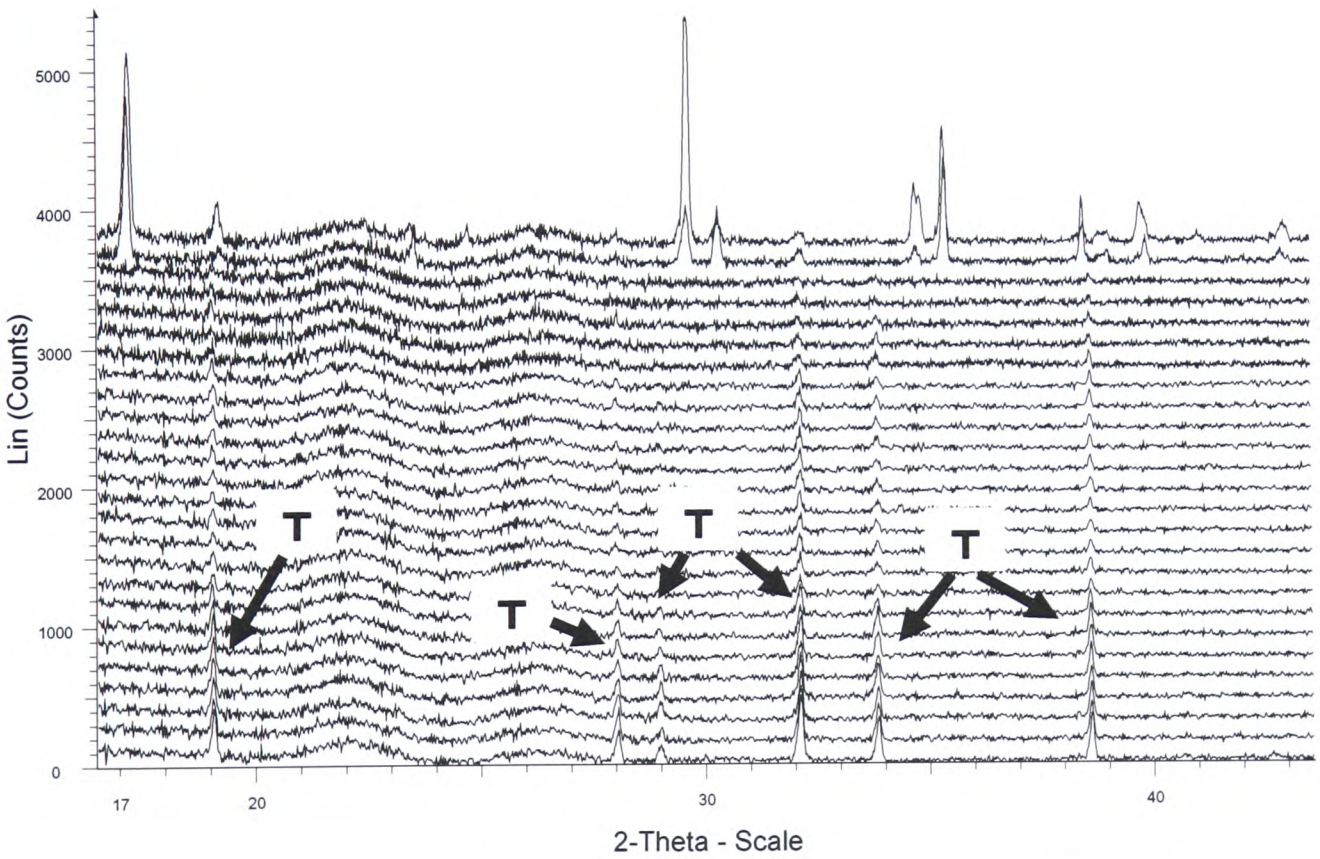

Figure 3.2a: Experiment 1, scans 9-34. Thenardite peaks are marked T, there is a clean transition at 33 °C.

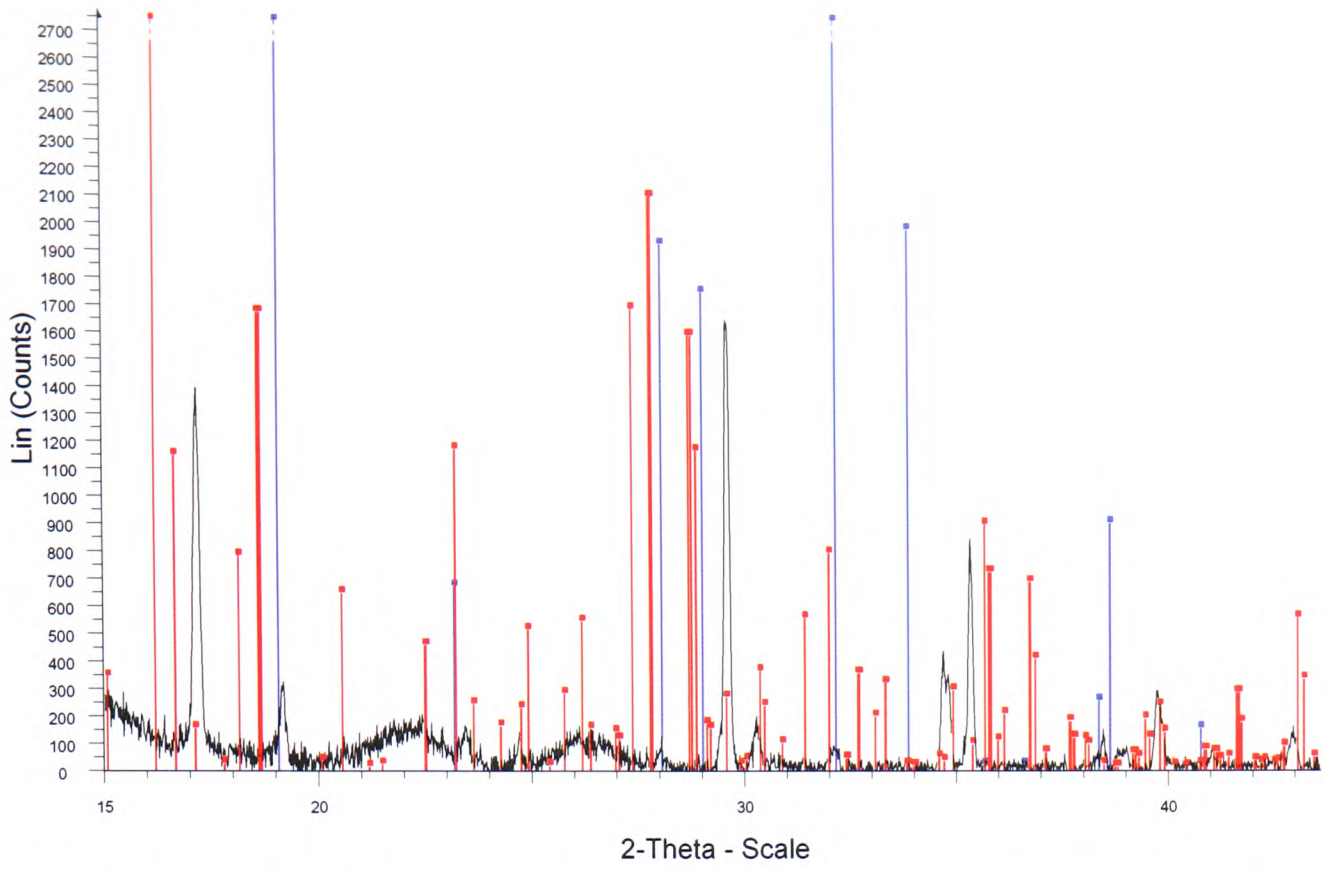

Figure 3.2b. Experiment 1, scan 34. The last scan taken at 5 °C is shown for clarity of fit with mirabilite (red) and thenardite (blue) JCPDS stick plots. Card numbers 75-1077 and 37-1465 respectively.

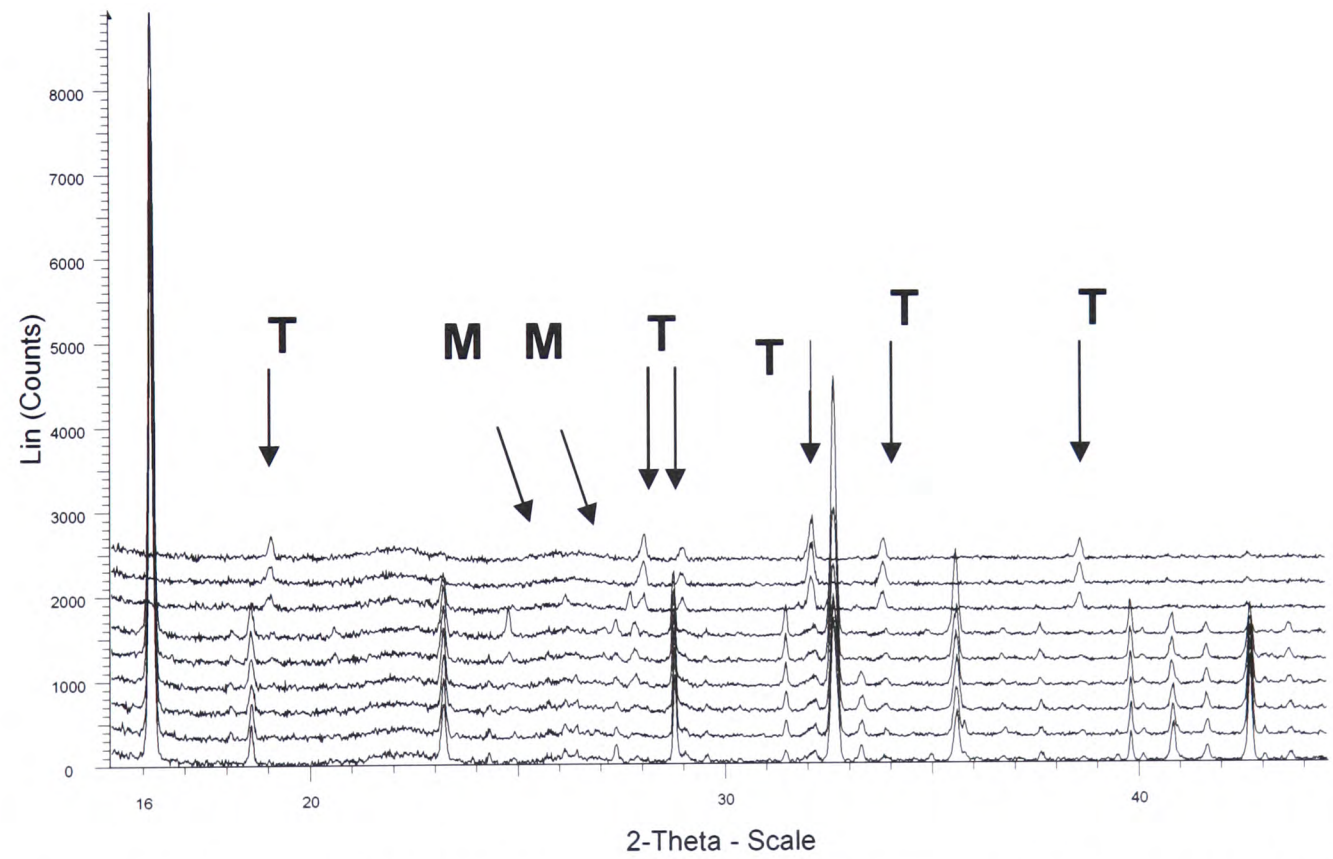

Figure 3.3: Experiment 2, scans 1-9. Thenardite peaks are marked T. A trace of mirabilite is shown at 33 °C (scan 7) is indicated with peaks marked M.

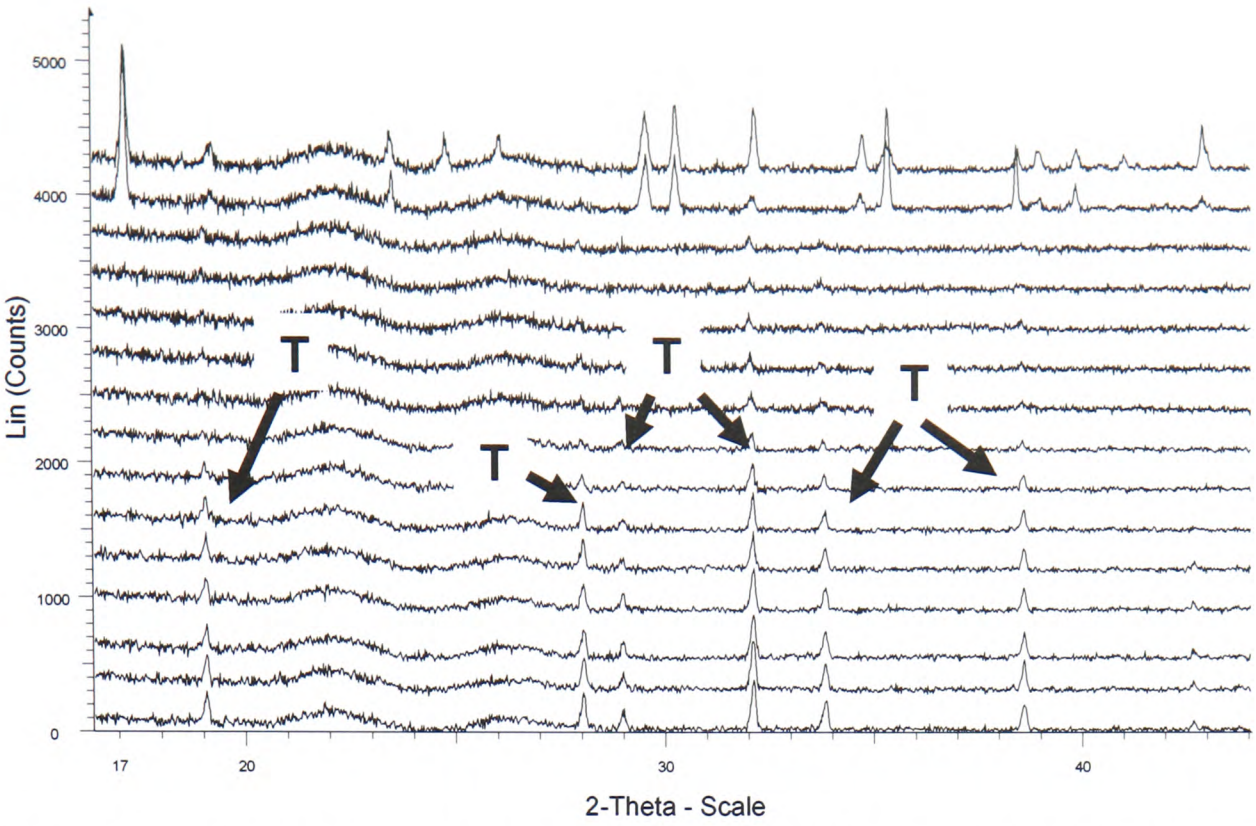

Figure 3.4a: Experiment 2, sample cooling to 5 °C. Scans 10-24. Thenardite peaks are marked T. The unmarked peaks in the last two scans are thought to be mirabilite.

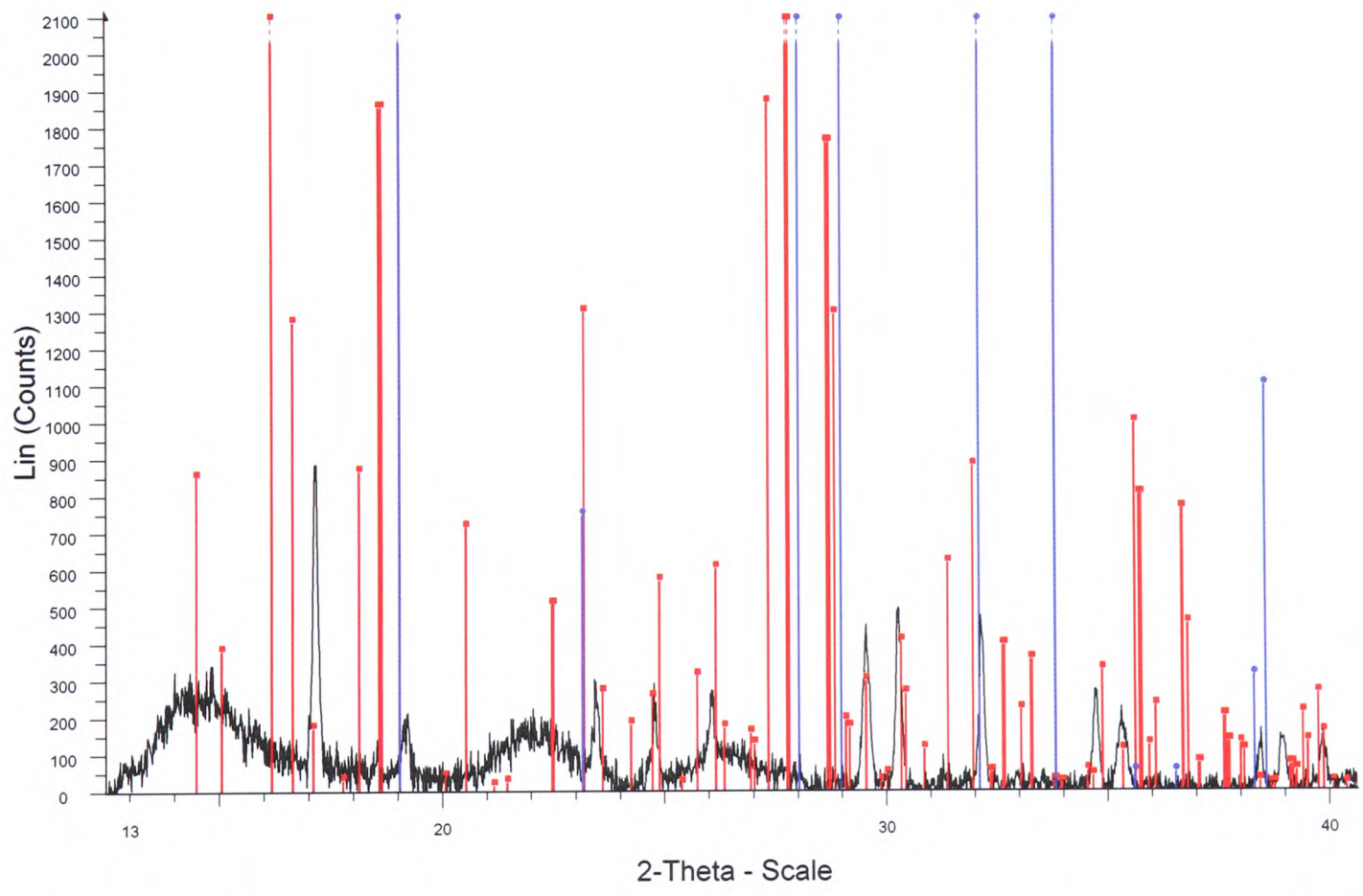

Figure 3.4b: Experiment 2. The last scan taken at 5 °C is shown for clarity of fit with mirabilite (red) and thenardite (blue) JCPDS stick plots. Card numbers 75-1077 and 37-1465 respectively.

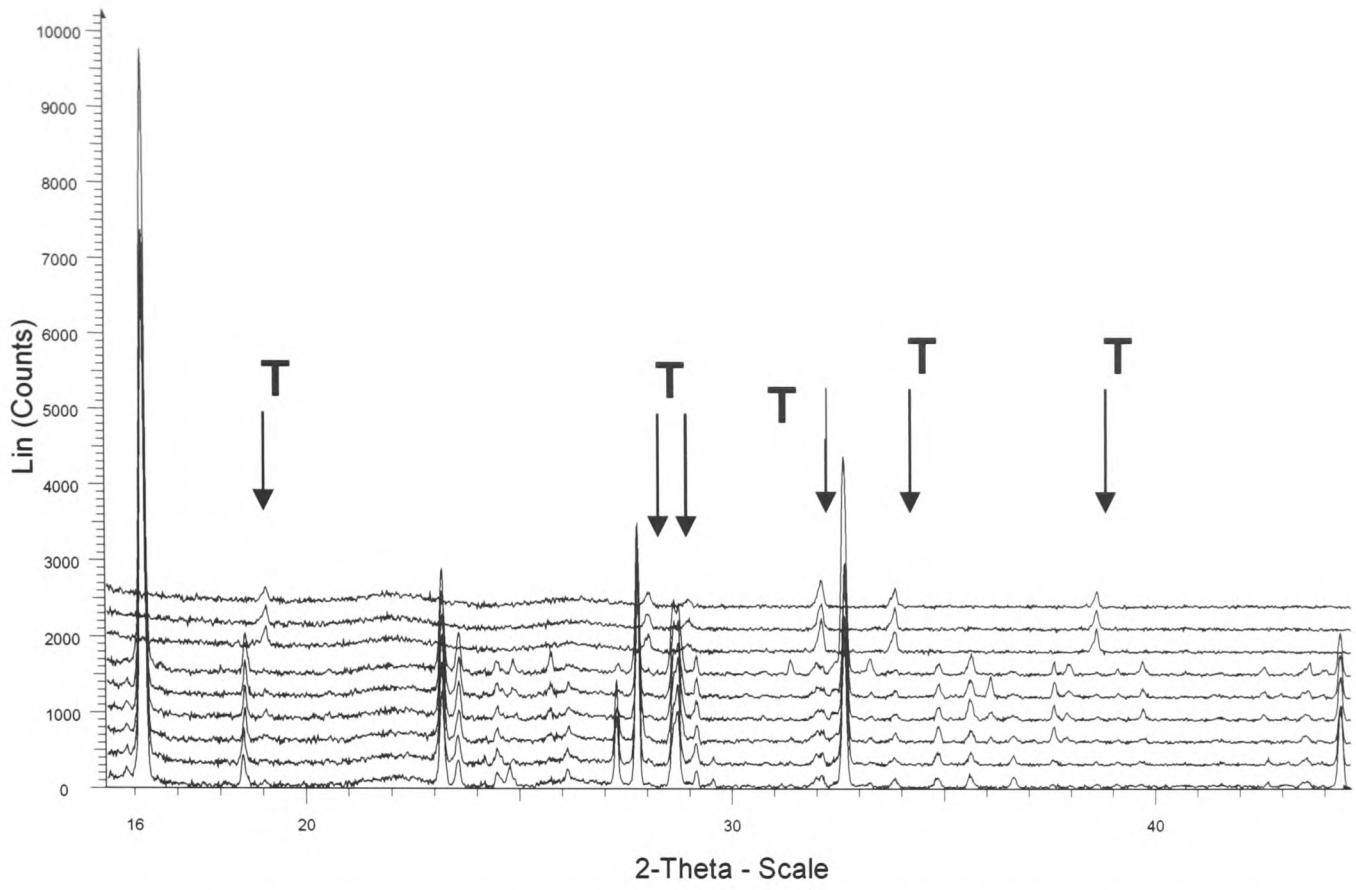

Figure 3.5: Experiment 3, Scans 1-9 are shown. The transition point is shown again to be 33 °C. Thenardite peaks are marked T.

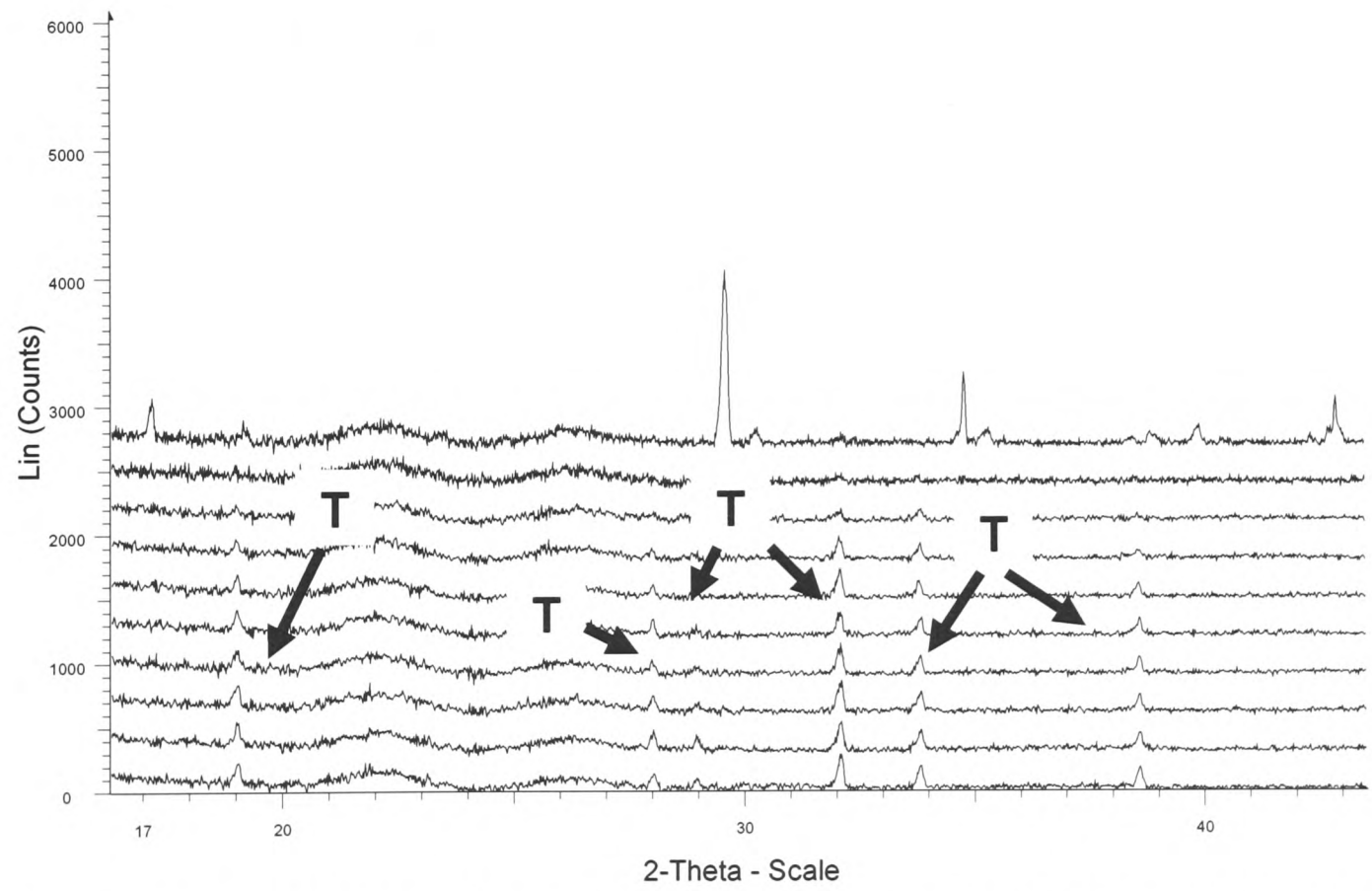

Figure 3.6a: Experiment 3. Scans 10-19. Sample cooling to 10 °C. Thenardite peaks are marked T, the unmarked peak in the last scan is thought to be mirabilite.

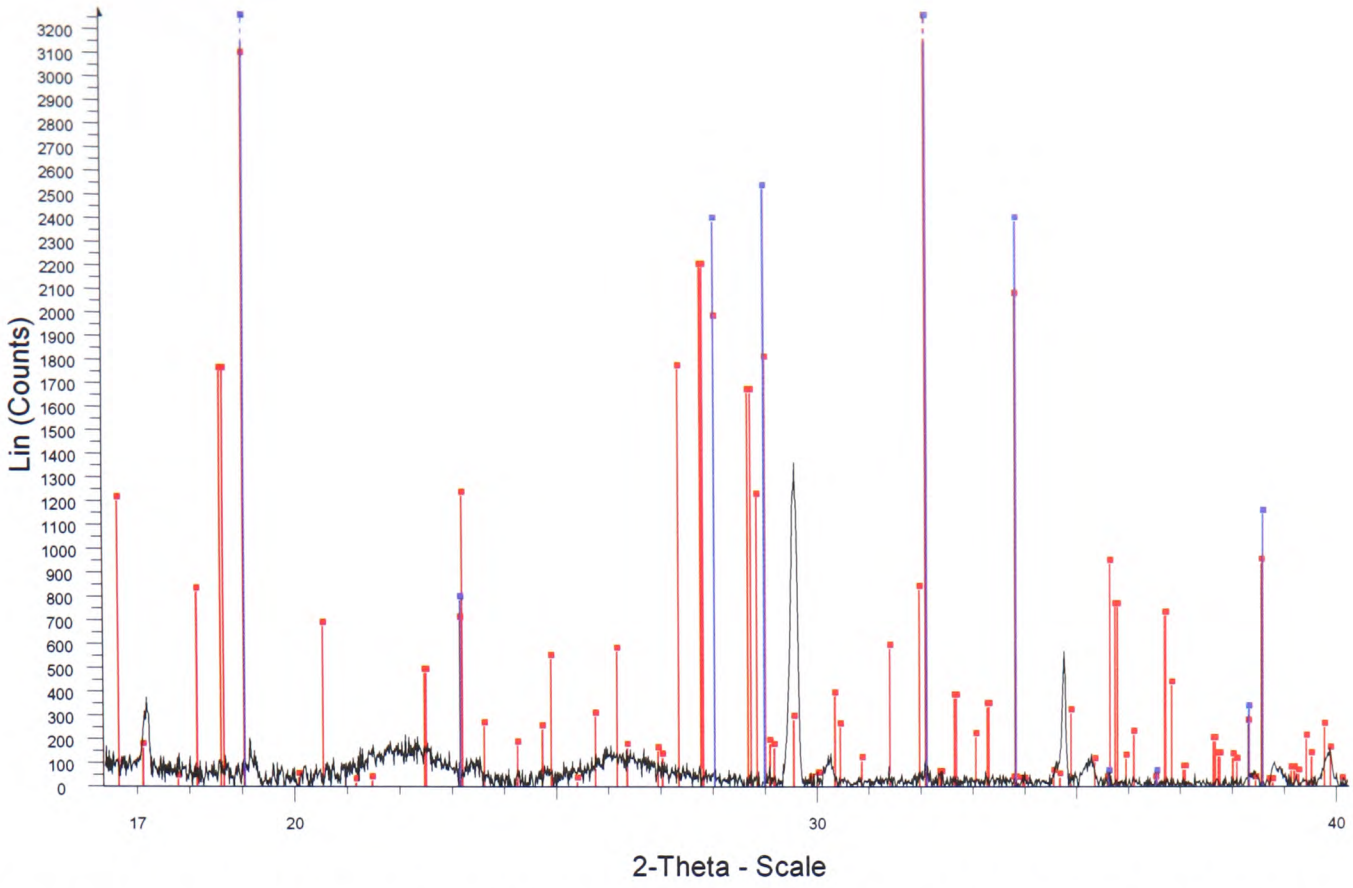

Figure 3.6b: Experiment 3. The last scan taken at 10 °C is shown for clarity of fit with mirabilite (red) JCPDS stick plots. Thenardite peak positions (blue) are indicated for reference. Card numbers 75-1077 (mirabilite) and 37-1465 (thenardite) were used.

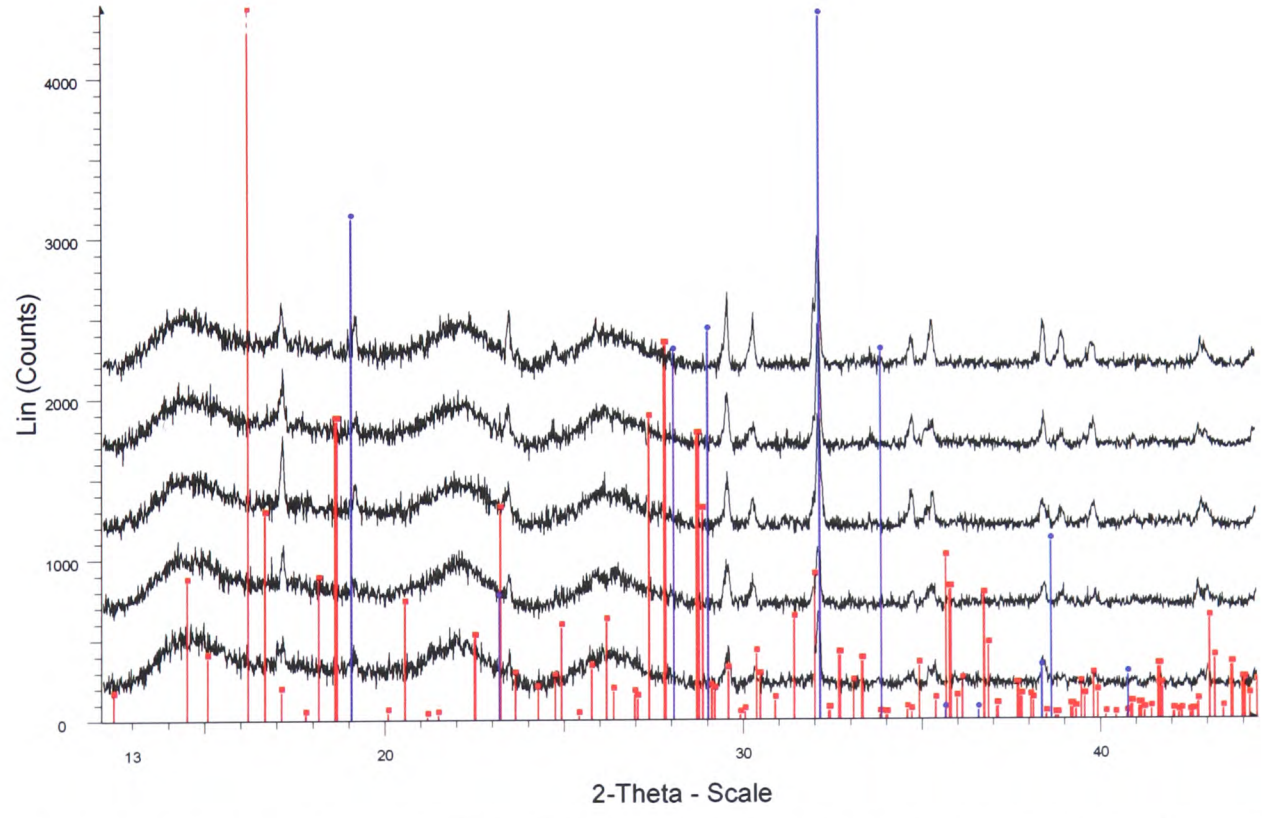

Figure 3.7: Experiment 4. The first scan (nearest the bottom) was taken at 15 °C, with subsequent scans at 10 °C, 5 °C, 5 °C and 6 °C. This shows the early development of mirabilite (red) at 15 °C. Thenardite peak positions (blue) are indicated for reference.

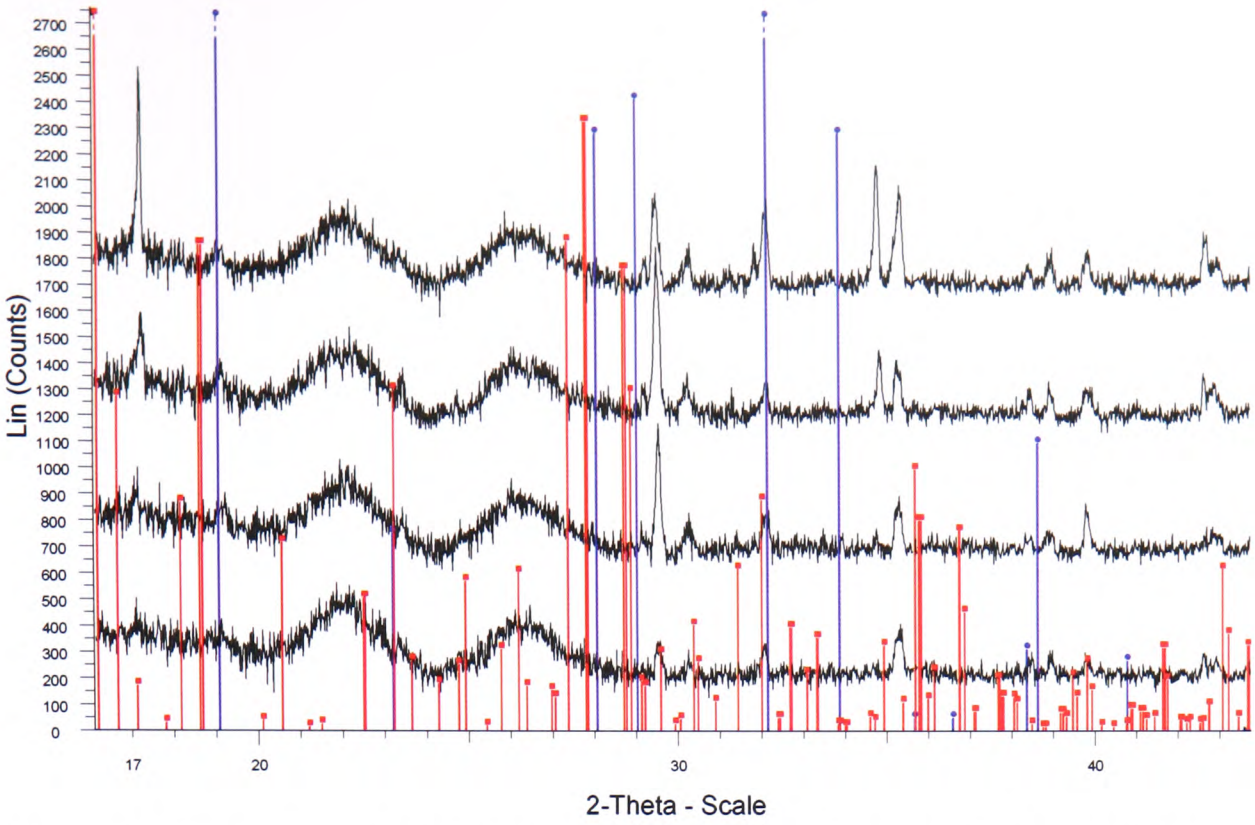

Figure 3.8: Experiment 5. The first scan (nearest the bottom) was taken at 15 °C, with subsequent scans at 10 °C, 5 °C and 7 °C. This shows the early development of mirabilite (red) at 15 °C.

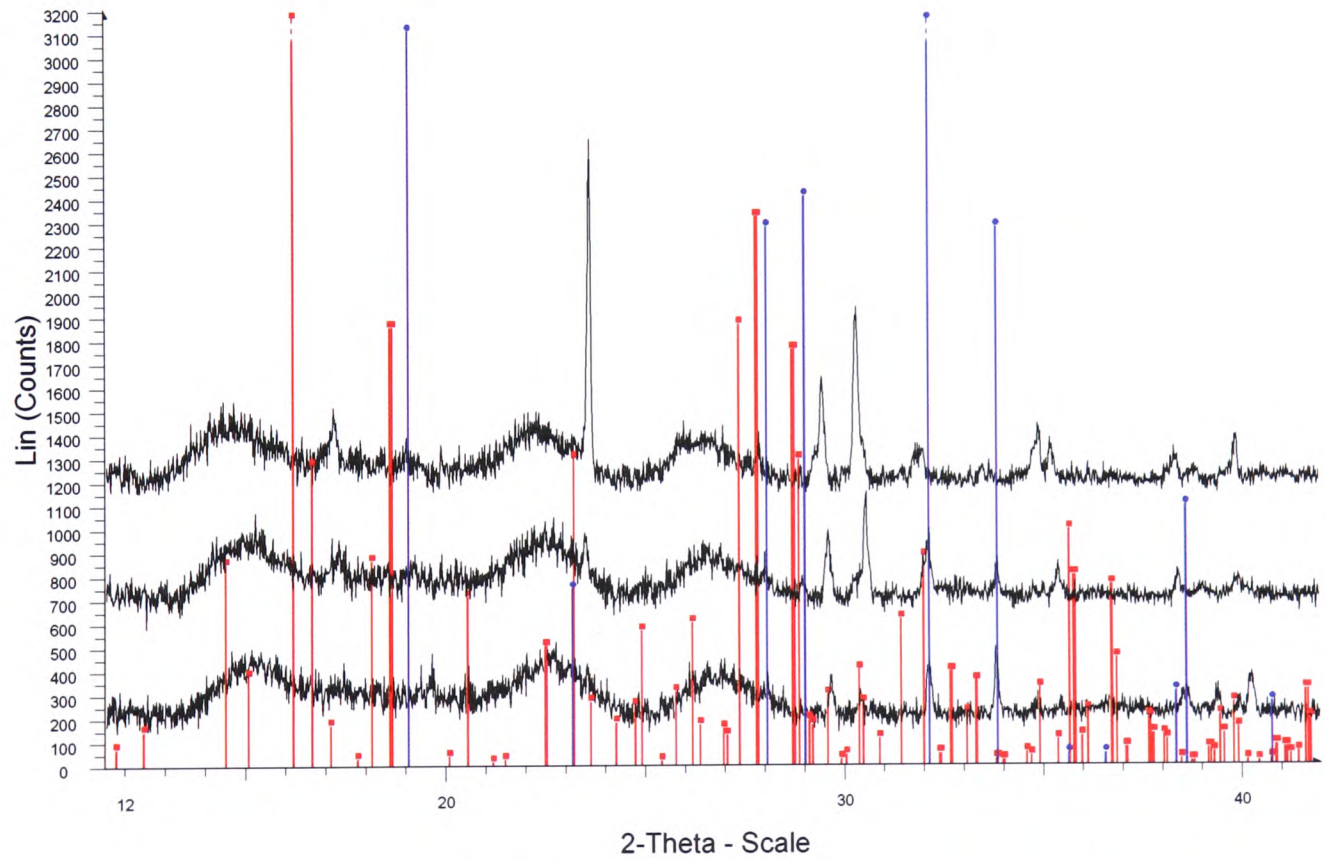

Figure 3.9: Experiment 6. The first scan (nearest the bottom) was taken at 15 °C, with subsequent scans at 10 °C and 5 °C. This shows the early development of mirabilite (red) at 15 °C.

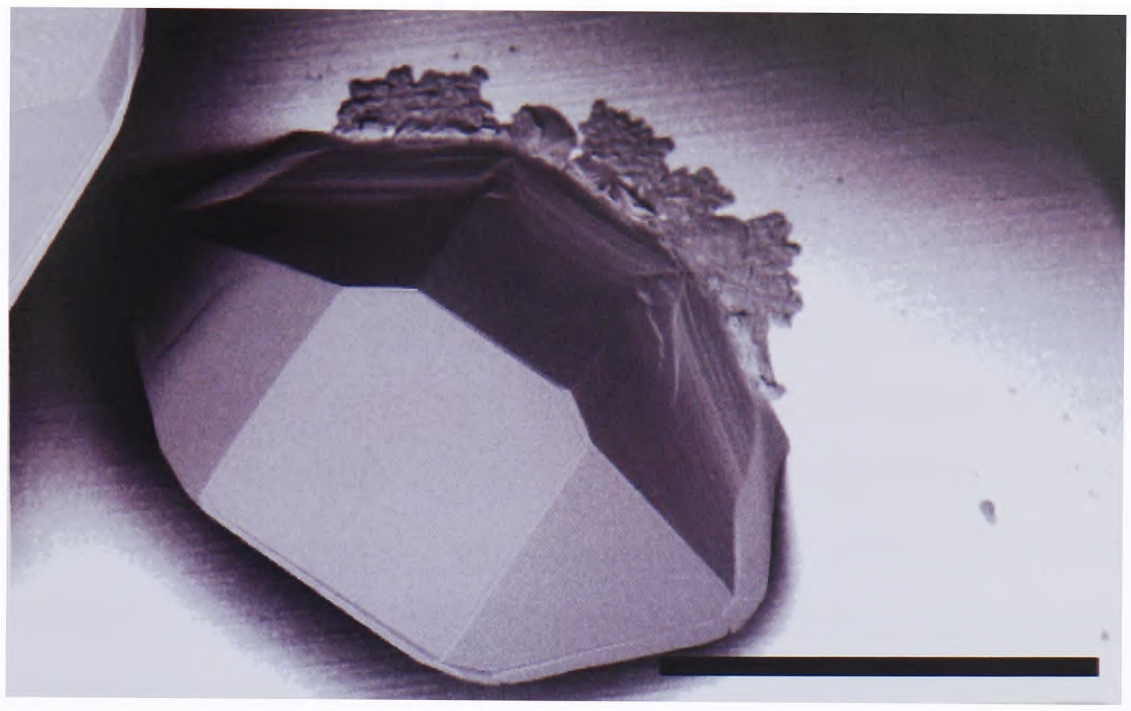

Figure 3.10: An SEM image of a thenardite crystal, grown from solution by evaporation at 45 °C. The identification was verified by powder XRD (some crystals from the same dish were crushed and X-rayed). The scale bar represents 1mm.

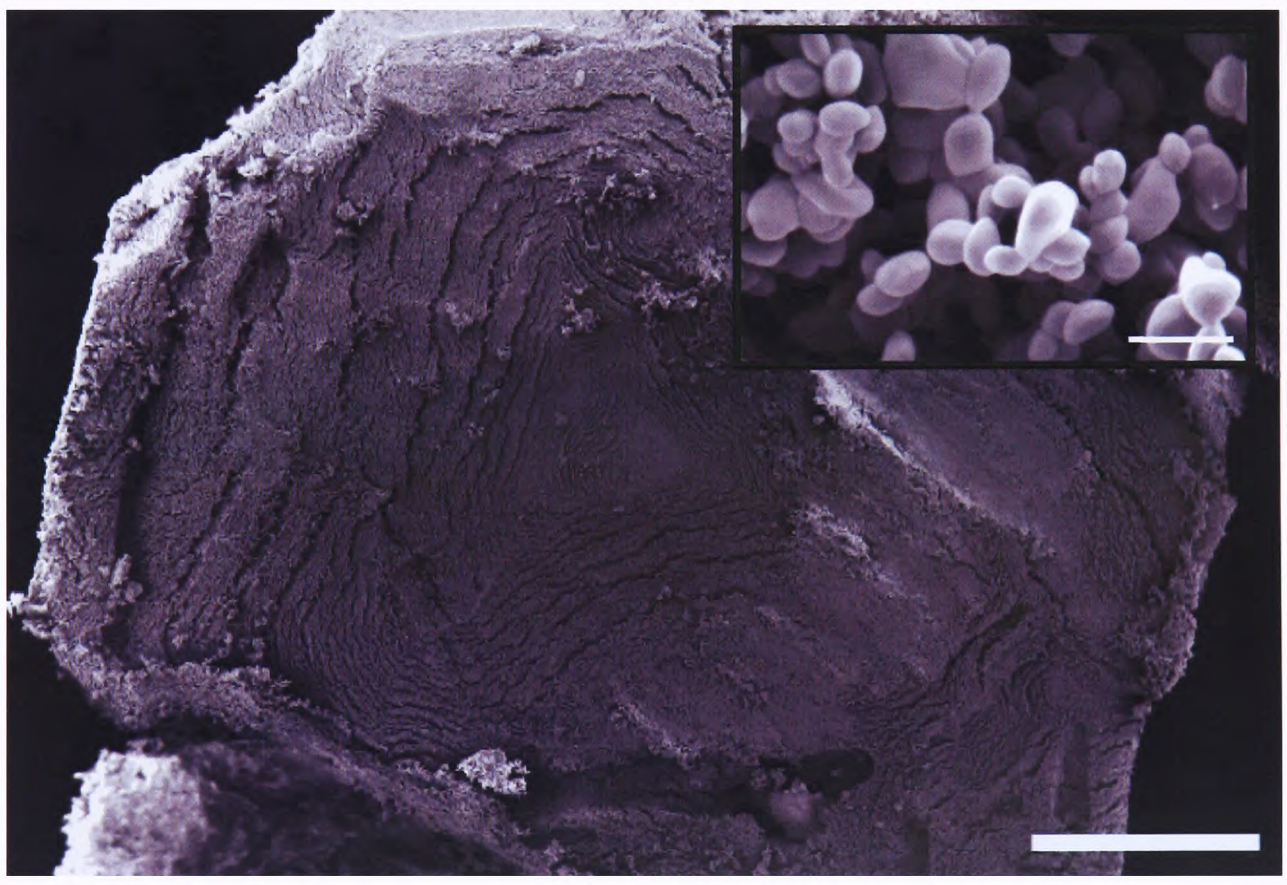

Figure 3.11: An SEM image of a sodium sulphate crystal grown by evaporation at 20 °C and c.60% RH. The final product (thenardite) was verified by XRD (some material from the same crystallisation dish was crushed for powder X-ray analysis). It is suspected that the crystal formed originally was mirabilite (no X-ray confirmation though) which dehydrated to an opaque powder. The scale bar on the main image is 500 μm, the scale bar on the high magnification corner image is 5 μm.

From experiments 1-6, mirabilite dehydrates at very close to the stated literature value of 32.4 °C [6] to form thenardite as predicted. The transition is from a solid to an aqueous suspension. Figures 3.1 – 3.6 have had the background removed for convenience. Due to sample height effects peak shift is inevitable when using Bragg-Brentano geometry, and the patterns shown are corrected for this.

Holding the temperature at 20 °C did not appear to have any effect on what temperature the phase change occurs at as demonstrated by experiment 1 which held the temperature at 20 °C for just over 10.75 h. Although it was noted that thenardite seemed to dissolve a little during the run, mirabilite did not precipitate until 10 °C. Mirabilite precipitation at 20 °C during an indefinite period of time cannot be ruled out though. There does not seem to be any good kinetic reason demonstrated by these experiments to explain why mirabilite precipitates at 10 °C in the first three experiments (carried out consecutively) but 15 °C in the final three experiments (carried out consecutively some months after the first set). Both sets of experiments test whether stepping the temperature down from 20 °C to 15 °C in 1 °C steps or jumping down from 20 °C to 15 °C effects when the precipitation of mirabilite occurs and within the confines of each set, the result is that stepping or jumping the temperature down does not effect the result.

In the second set of experiments, it was tested whether holding the temperature at 5 °C for longer would eventually produce a more conventional powder pattern for mirabilite with less preferred orientation effects. Experiment 4 shows that there is very little difference between the first pattern at 5 °C and the third one, which was technically taken at 6 °C. The precipitation of mirabilite at 15 °C is usually slight, but still noticeable and although the peaks become stronger as the temperature is dropped, a conventional pattern is not achieved. It can be concluded that mirabilite re-precipitates at 10-15 °C under the conditions of these experiments. Although some patterns taken at 15 °C and below show a possible match for thenardite, it is impossible for thenardite to exist in solution during mirabilite precipitation as it would be dissolved. Thenardite peaks are shown in the figures for reference only.

3.1.2 Solubility

Mirabilite begins to precipitate at a lower temperature than might be expected from knowledge of the mirabilite-thenardite transition temperature. It should be noted that the kinetics of this reaction have been examined only in as much detail as the information presented. Therefore the precipitation of mirabilite at slightly higher temperatures under extended time intervals cannot be ruled out. Also the data presented assumes that mirabilite, under the timescales presented, does not precipitate at higher temperatures yet remain undetected due to the limited depth of penetration of conventional laboratory power diffraction equipment. Beam penetration and attenuation is discussed in the next section.

The molar mass of mirabilite corresponds to 78.8 g Na_2SO_4 per 100g H_2O (5.55 m). After the transition point at 32.4 °C thenardite is the stable phase, therefore in order for the thenardite crystals to exist in an aqueous suspension, it must be at least saturated with respect to thenardite at the temperature of the scan. Researchers in the field have long been aware that mirabilite can sustain a high supersaturation before crystallisation occurs. Obviously thenardite can exist, albeit in a metastable condition at temperatures below transition and while there is some experimental solubility data at temperatures below the transition, there is no data at 15 °C and 10 °C [7]. FREZCHEM [8] and PHRQPITZ [9] can be used to predict the solubility of thenardite at 10 °C. FREZCHEM is based on the Spencer-Møller-Weare model which uses the Pitzer [10] equations to calculate the solvent and solute activities.

Chemical thermodynamics of electrolyte systems has been given rigorous attention over the last century resulting in theoretical predictions of electrolyte solubility over various concentration ranges. The simplest theory (Debye-Hückel) is estimated to be correct for ionic strengths of 0.001 – 0.01 m only, making this theory unsuitable for a concentrated sodium sulphate suspension. The Pitzer equations (or derivatives of) are generally thought to be the most suitable for concentrated solutions. A discussion and review of this theory formed part of chapter 2 and as such will not be discussed at length here, except to reiterate that the Pitzer equations are used to predict the osmotic coefficient and the activity coefficient.

As Pitzer notes, the best test of the predicted activity and osmotic coefficient values is in the calculation of the solid solubility in electrolyte solutions, as the calculated solubility can be compared to empirical literature. For binary systems, solubility calculations frequently represent extrapolations of activity and osmotic coefficient data outside the available data range. This can be risky, because as Pitzer points out [11] in some cases the activity coefficient decreases so rapidly that the activity ($m\gamma_{\pm}$) increases only slightly with molality. Then a small error in the estimated $\gamma_{\pm}$ leads to a large error in the calculated solubility. The ion interaction equations could be used to predict the solubility of a solid in aqueous solution providing that the temperature and pressure dependence of the six main empirical parameters ($\beta^{(0)}_{MX}, \beta^{(1)}_{MX}, \beta^{(2)}_{MX}, C^{\phi}_{MX}, \theta_{ij} and \psi_{ijk}$) is known. The equation for the total excess Gibbs energy through appropriate differentiation produces other functions such as heat capacities and excess enthalpies, values which are experimentally obtainable and produce accurate data on the temperature dependence of the ion interaction parameters [12]. Indeed, the data presented in Pabalan et al. [11] indicates that the solubility at high concentration or high temperature can be calculated well using the regression approach they describe.

FREZCHEM uses the Spencer-Møller-Weare model. A description of the model, updated with a further evaluation of sulphate chemistry can be found in Marion et al. [8]. The equation used to define Pitzer equation parameters is:

$$P(T)_j = a_{1j} + a_{2j}T + a_{3j}T^2 + a_{4j}T^3 + a_{5j}/T + a_{6j}\ln(T) \qquad \textbf{(3.2)}$$

Where P is the individual Pitzer parameters, T is the temperature in K of interest and a is a constant defined in table 1 of Marion et al. [8]. J is the *jth* Pitzer equation parameter. The optimisation of the Pitzer parameters is two fold. The a_{ij} parameters are incremented or decremented by Δ_{ij} until an optimum value is found. There are two cycles, one which seeks to improve the a_{ij} parameters for a specific parameter *(j)* and one which seeks to improve a_{ij} for all Pitzer parameters. The program ends when there is a convergence of the a_{ij} values to within Δ_{ij} stated by the program [8]. How actual or practical solubility values are calculated for comparison with literature data is discussed in chapter 2.

Much attention was paid to the Na_2SO_4-H_2O system, as 58 mirabilite solubility values were fed into the program over the temperature range of -1.2 °C to 25 °C and molalities 0.001 m to 2.0 m, which is much more dilute than the system under consideration here. Although there is excellent agreement between the experimental solubility data presented by Linke [13] and the FREZCHEM prediction for the mirabilite solubility up to 25 °C, the prediction of metastable thenardite solubility in the temperature region of the optimization for the program is not accurate as can be seen in figure 3.12:

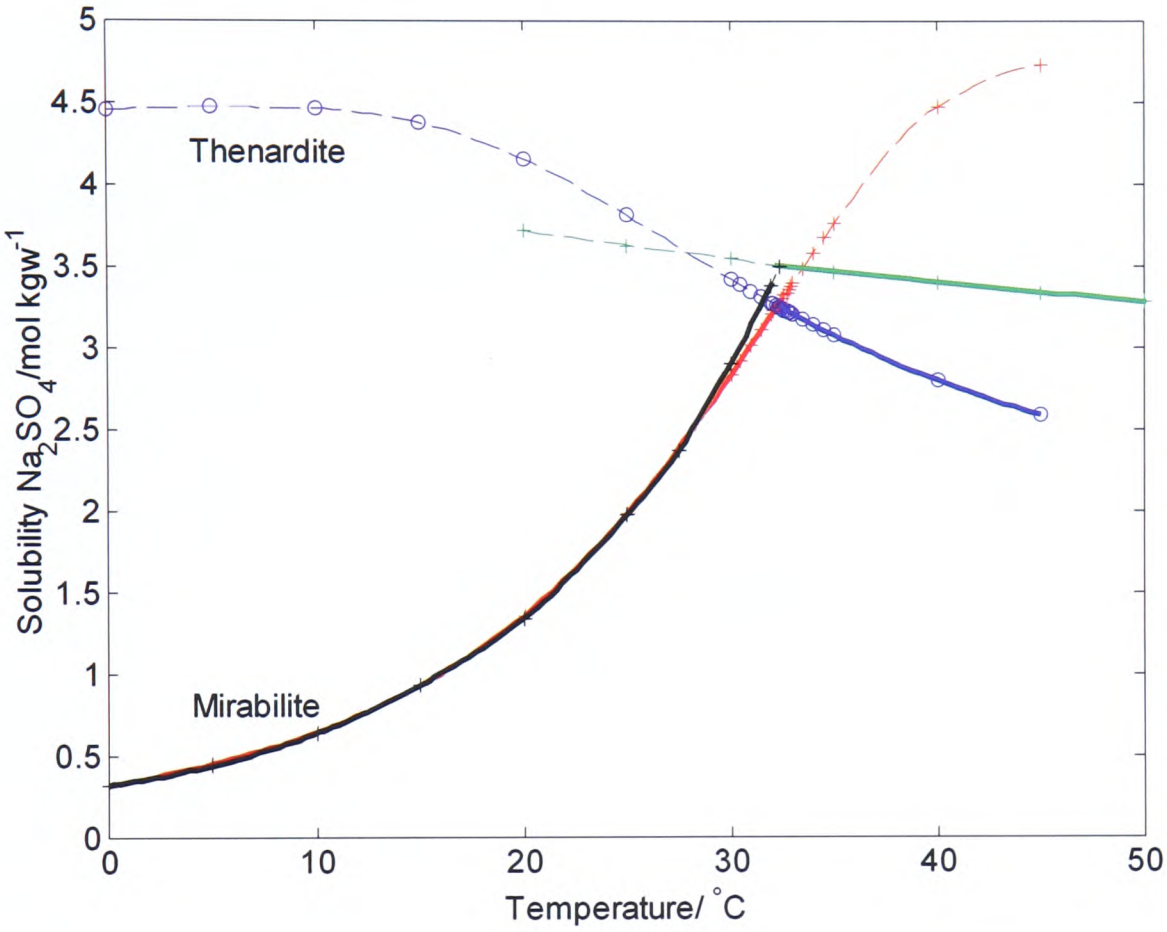

Figure 3.12: The black line is experimental solubility data for mirabilite from [13]. The green is experimental solubility data for thenardite from [7] including three metastable points. The red and blue lines represent the solubility of mirabilite and thenardite respectively as predicted by FREZCHEM. Bold lines indicate the region of stability for each phase. FREZCHEM, C. Hall, unpublished.

As is obvious from figure 3.12, the optimisation of FREZCHEM for mirabilite (below 25 °C) is clearly excellent as the experimental data (black) fits very well to the prediction (red). After 25 °C the fit is clearly less good and starts to deviate from the experimental solubility data. For thenardite, both within (< 25 °C) and outwith the temperature range of optimisation, the fit is clearly inaccurate. Analysis of the

water activity data produced from FREZCHEM provides some further confirmation. An RH-temperature phase diagram of mirabilite-thenardite is produced from the water activity output of the program, which when contrasted with experimental data [7] highlights the deviation between predicted and empirical data. A third data set is added in, calculated according to Eq. (A.11) in [3], which predicts the boundary conditions, when both phases are in equilibrium, which is simply:

$$a_{H_2O} = \sqrt[10]{\frac{K_{mi}}{K_{th}}} \tag{3.3}$$

Figure 3.13 plots the calculated water activity for solutions saturated with respect to thenardite and mirabilite and Flatt's calculated water activity when both phases are in equilibrium. It is clear the predicted data deviates from the experimental data.

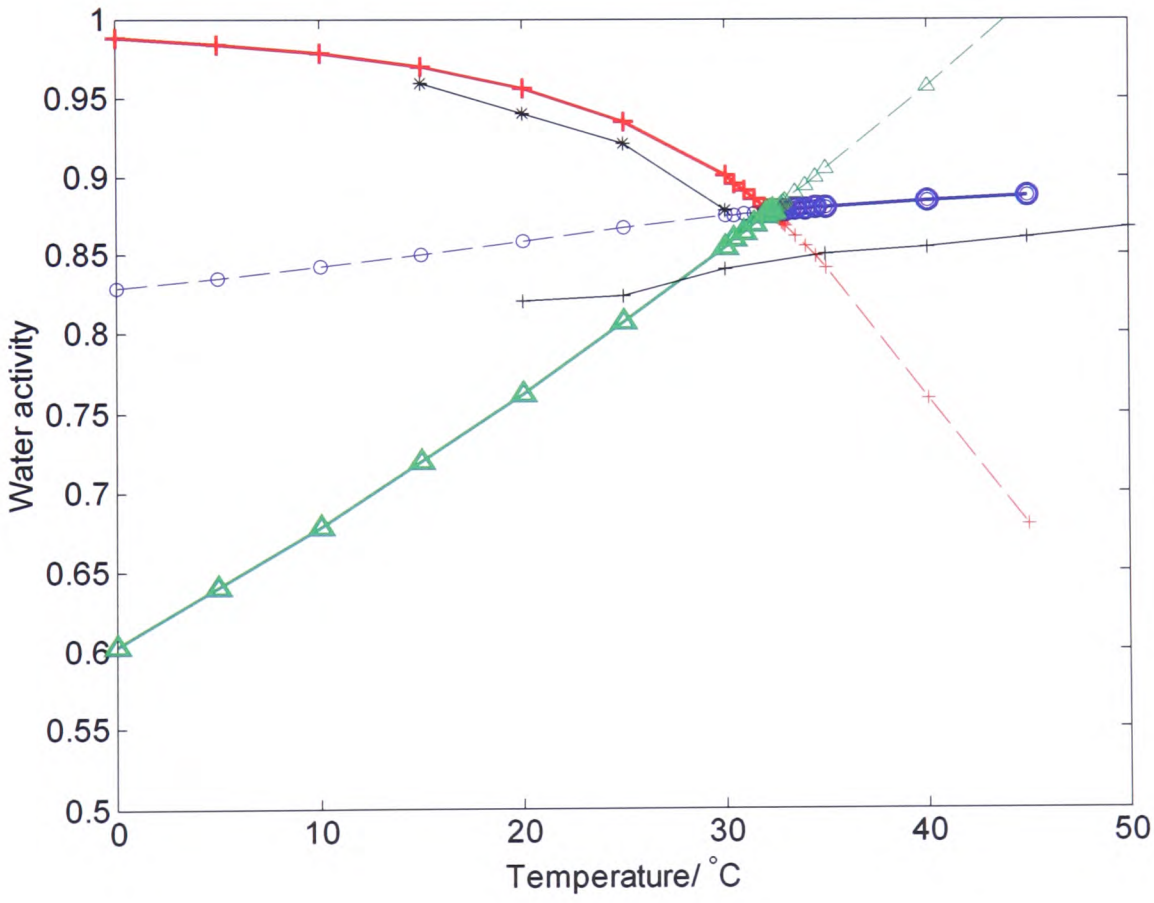

Figure 3.13: The green line represents the mirabilite-thenardite phase transition with respect to RH and temperature. Water activity is taken to be RH/100 and the points are calculated according to Eq. (3.3) using the FREZCHEM output. The red line is the water activity of a solution saturated with respect to mirabilite and the blue line is thenardite. Both data sets are calculated using FREZCHEM. The black asterix points represent experimental mirabilite data; the black crosses represent experimental thenardite data, both data sets from [7]. FREZCHEM, C. Hall, unpublished.

Instead of using FREZCHEM, another approach using PHRQPITZ was tried. The output values of the solubility from PHRQPITZ can be seen in figure 3.14. The solubility values are given in table 3.2. As is clear, the PHRQPITZ prediction is much closer to the experimental data. This was achieved by entering a molality value at saturation (solubility data from literature sources [6, 7]) into PHRQPITZ for thenardite to obtain ion activity values. At saturation K_{sp}= IAP, therefore the K_{sp} was calculated in this way. These K_{sp} values for thenardite over a range of temperatures, including metastable points obtained from Kracek [7], were plotted and fitted with a 3rd order polynomial, which predicts the K_{sp} for temperatures (15 ° - 5 °C) where there is no solubility data. The predicted K_{sp} values for a solution saturated with respect to thenardite at 15 °C to 5 °C were entered back into PHRQPITZ to obtain the molality (solubility) at lower temperatures, which is plotted in figure 3.14.

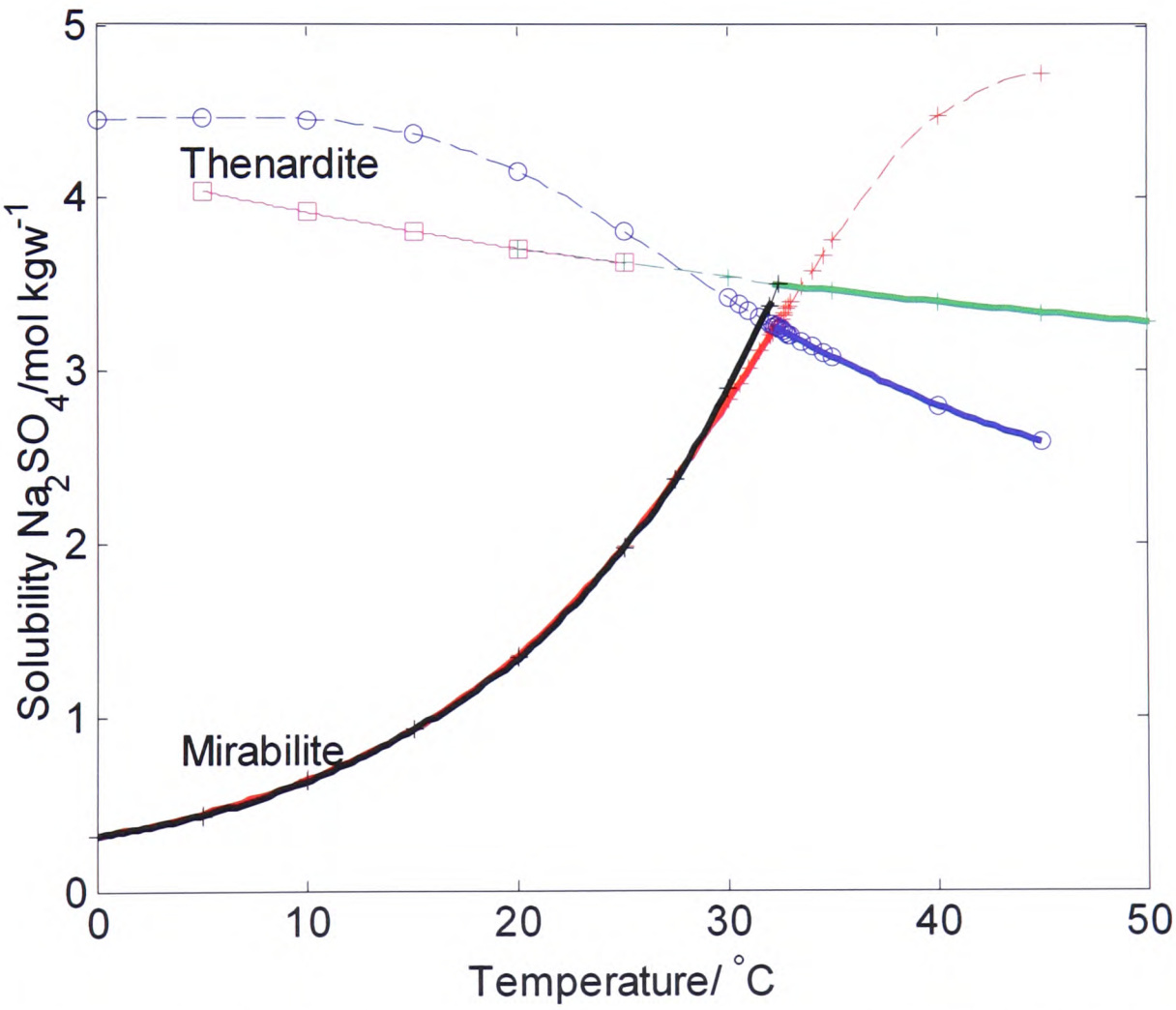

Figure 3.14: An updated version of figure 3.12. The black line is experimental solubility data for mirabilite from [13]. The green is experimental solubility data for thenardite from [7] including three metastable points. The red and blue lines represent the solubility of mirabilite and thenardite respectively as predicted by FREZCHEM. The magenta lines indicate the new thenardite solubility data from PHRQPITZ. Bold lines indicate the region of stability for each phase. PHRQPITZ, C. Hall, unpublished.

Temperature in °C	Solubility in mol Na_2SO_4 per kg water. PHRQPITZ	Solubility in mol Na_2SO_4 per kg water from [7]
25	3.627	3.627
20	3.711	3.713
15	3.811	_
10	3.921	_
5	4.042	_

Table 3.2: Comparison of solubility data for thenardite from PHRQPITZ (column 1) with the literature values from Kracek [7].

3.1.3 X-ray attenuation

At this point it is useful to consider what the effective depth of penetration of the X-ray beam is in a conventional lab instrument. Or put more usefully, to what depth of the specimen does the information in the XRD pattern apply? The beam intensity does not become zero at any one depth, but decreases exponentially with distance below the surface [5]. The attenuation of X-rays is represented as:

$$I = I_0 \exp(-\alpha \rho_b L) \tag{3.4}$$

where I and I_0 are the transmitted and incident intensities, α is the mass attenuation coefficient of the material, ρ_b is the bulk density and L the path length. The stopping distance can be described as:

$$L_e = \frac{1}{\alpha \rho_b} \tag{3.5}$$

where L_e is the stopping distance. This is the thickness of solid material (zero porosity) required to reduce the X-ray intensity to 0.3679 of its incident intensity [14]. For a composite material (mirabilite and Kapton film), this is represented as

$$e^{-1} = \exp[-(\alpha_m \rho_m L_m + \alpha_k \rho_k L_k + \alpha_a \rho_a L_a)] \quad (3.6)$$

The subscripts refer to mirabilite, Kapton and the adhesive backing as appropriate. Values for the mass attenuation coefficient were taken from NIST for Kapton and mirabilite and Cullity [5] for the adhesive. The adhesive is a polysiloxane ($OSi(CH_3)_2$) with a density value of approximately 1200 kg/m^3 [15]. The density in the case of mirabilite is the crystallographic density and for Kapton the value is the density of polyimide also from NIST. All relevant information is presented in table 3.3. Clearly the thickness of material penetrated (which can be calculated from L, the path length) varies with the angle of incidence and diffraction, which is θ in this case. As shallow angles probe less material than high angles. It was observed that e^{-1} which means that 37% of the available X-rays reach the detector resulted in the path length of mirabilite being negative until higher angles, which would indicate that no mirabilite peaks would be seen until 40 2θ°, which is not accurate as the first mirabilite peak is observed at c. 17 2θ°. Therefore the path length of mirabilite penetration was examined as a function of theta and I/I_0, with values ranging from 5% to 95% (under the conditions of 5% to 95% of the beam reaching the reaching the detector). The results are plotted in figures 3.15 and 3.16 which illustrate that in order to see a mirabilite peak at 8.5 θ° then at most 10% of the beam is reaching the detector. The final equation used is a slight modification on Eq. (3.6) as the heating stage has Kapton film windows (which are at right angles to the incident and diffracted beam). The final equation used was:

$$\frac{\ln(I/I_0) + \mu_k l_k + \mu_{kw} l_{kw} + \mu_a l_a}{\mu_m} = l_m \quad (3.7)$$

Material	thickness	μ cm^{-1}	Density (g/cm^3)
Kapton film	0.0025 cm	8.16 cm^{-1}	1.417
Adhesive backing	0.0040 cm	34.22 cm^{-1}	1.2
Mirabilite	N/A	31.20 cm^{-1}	1.47

Table 3.3: Material properties used to calculate beam attenuation. μ is the linear attenuation coefficient. $\alpha=\mu/\rho$

The thickness of mirabilite probed in mm is plotted in figure 3.16. This proves that higher angles probe more of the material and that the bottom of the sample holder is never reached. The sample holder is approximately 0.82 mm deep.

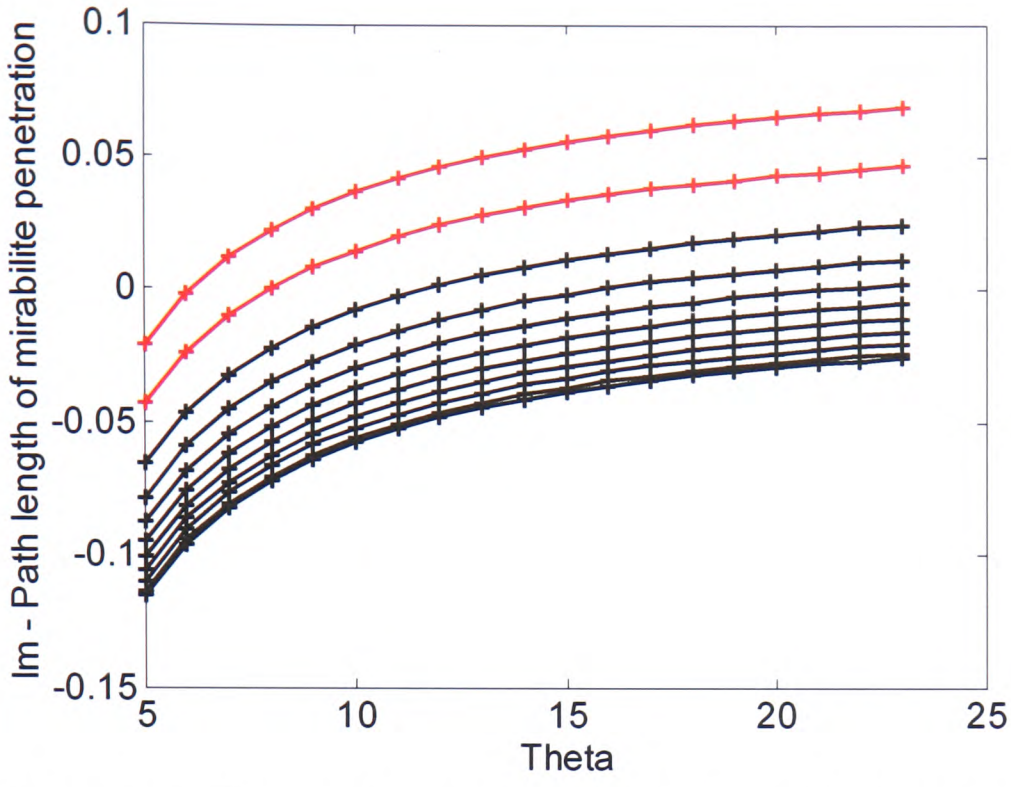

Figure 3.15: The path length of mirabilite penetration (in cm) against the theta angle of the diffractometer. The range used for these experiments was 10 2θ° to 45 2θ°. The top red plots correspond to I/I_0 of 0.05 and 0.10.

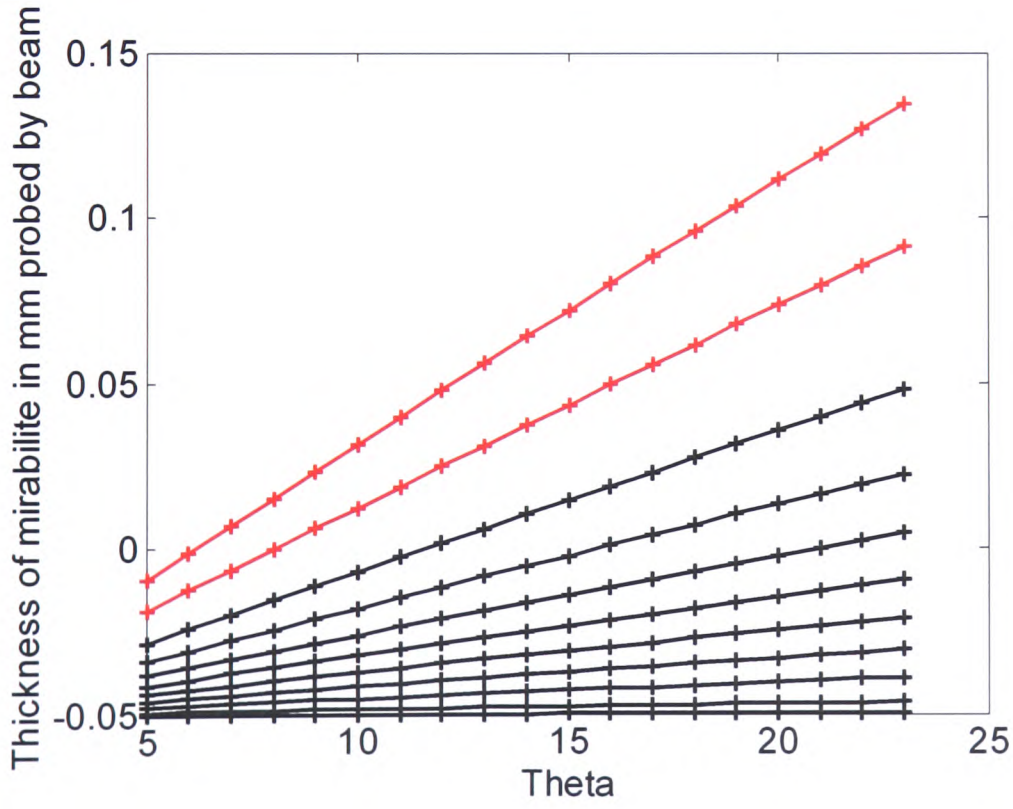

Figure 3.16: The thickness of mirabilite penetration (in mm) against the theta angle of the diffractometer. The range used for these experiments was 10 2θ° to 45 2θ°. The top red plots correspond to I/I_0 of 0.05 and 0.10.

3.1.4 Conclusions

Mirabilite converts to thenardite at 33 °C, which is close to the stated transition temperature of 32.4 °C, and appears to re-precipitate as mirabilite at 10 °C in the first three experiments or 15 °C in the final three experiments. Holding the temperature at 20 °C on the down temperature run did not appear to have any effect on what temperature the phase change occurred at, as demonstrated by experiment 1. It was observed that thenardite did dissolve a little, but the temperature of mirabilite precipitation was the same as experiments 2 and 3. There does not seem to be any good reason why the transition temperature of thenardite to mirabilite was 10 °C for the first 3 experiments and 15 °C for the last 3 experiments. Experiments 1-3 were carried out together, as were 4-6 (some months after 1-3). Both sets of experiments test whether stepping the temperature down from 20 °C to 15 °C in 1 °C steps or jumping the temperature down from 20 °C to 15 °C affects when the precipitation of mirabilite occurs and within the confines of each set, the result is that it does not affect the result. The second set of experiments, tested whether holding the temperature at 5 °C for longer would eventually produce a more conventional powder pattern for mirabilite with less preferred orientation effects. Experiment 4 shows that there is very little difference between the first pattern at 5 °C and the third one (which was technically taken at 6 °C. The precipitation of mirabilite at 15 °C is usually slight, but still noticeable and although the peaks become stronger as the temperature is dropped, a conventional pattern is not achieved. It can be concluded that mirabilite re-precipitates at 10-15 °C under the conditions of these experiments. It should be noted that there is some dubiety over whether the patterns obtained really are mirabilite, but the fit is reasonable and there is a very limited number of possibilities. Examination of the pattern against the JCPDS card (40-0727) for the heptahydrate indicates this phase is not present, which is the only other known sodium sulphate hydrate for which an X-ray pattern exists. An in-situ synchrotron radiation study could help to answer this question.

The beam attenuation was examined to ascertain what depth of sample was being probed by the beam. At best, using the highest angle (22 θ°) and assuming that 95 % of the beam is being attenuated by the sample system, leaving 5 % of the beam

to reach the detector, the thickness of material probed is 0.13 mm. The depth of the holder is 0.82 mm, which proves that the beam does not fully penetrate the sample (i.e. reach the bottom of the sample holder), as expected. This is the penetration depth of solid mirabilite only.

The solubility of thenardite (from PHRQPITZ calculation) at 15 °C is 3.811 mol/kgw, the solubility of mirabilite at 15 °C is 0.929 mol/kgw. Therefore, assuming the solution is saturated with respect to thenardite at 15 °C, mirabilite reaches a 4.1 fold supersaturation before precipitation occurs. At 10 °C, this supersaturation would be 6.19 fold. This is a massive supersaturation to be reached and perhaps sheds some light on why mirabilite is considered to be very damaging to porous materials. Further work would help determine why the transition point from thenardite to mirabilite is different for the two sets of experiments, plus a more thorough understanding of the system could be obtained by the use of synchrotron radiation. Preliminary experiments using synchrotron radiation on the mirabilite – thenardite system indicate that sample rotation (especially in the case of poorly sorted samples) results in a significantly improved powder pattern. The main benefit of synchrotron radiation for this experiment is the ability to scan the sample and achieve full penetration through the sample. The results presented here are by no means definitive, and should be viewed with some caution, but are done to the fullest capacity possible with a laboratory instrument.

3.2 References

1. Rodriguez-Navarro, C., E. Doehne, and E. Sebastian, *How does sodium sulfate crystallize? Implications for the decay and testing of building materials.* Cement and Concrete Research, 2000. **30**: p. 1527-1534.

2. Doehne, E. *In situ dynamics of sodium sulfate hydration and dehydration in stone pores: observations at high magnification using the scanning environmental microscope.* in *3rd International Symposium on the Conservation of Monuments in the Mediterranean Basin.* 1994. Venice.

3. Flatt, R.J., *Salt damage in porous materials: How high supersaturations are generated.* Journal of Crystal Growth, 2002. **242**: p. 435-454.

4. Rodriguez-Navarro, C. and E. Doehne, *Salt weathering: Influence of evaportion rate, supersaturation, and crystallization pattern.* Earth Surface Processes and Landforms, 1999. **24**: p. 191-209.

5. Cullity, B.D., *Elements of X-Ray Diffraction.* 2nd ed. Metallurgy and Metals, ed. M. Cohen. 1978: Addison-Wesley Publishing Company, Inc.

6. Gmelin, L., *Handbuch der Anorganischen Chemie*. Vol. 21. 1966, Berlin: Springer-Verlag.

7. Kracek, F.C., *International Critical Tables of Numerical Data, Physics, Chemistry and Technology (1st Electronic Edition)*, ed. E.W. Washburn. 2003: Knovel. p371.

8. Marion, G.M. and R.E. Farren, *Mineral solubilities in the Na-K-Mg-Ca-Cl-SO_4-H_2O system: A re-evaluation of the sulfate chemistry in the Spencer-Møller-Weare model.* Geochimica et Cosmochimica Acta, 1999. **63**(9): p. 1305-1318.

9. Plummer, L.N., D.L. Parkhurst, G.W. Fleming, and S.A. Dunkle, *A computer program for incorporating Pitzer's equations for calculation of geochemical reactions in brines*. 1988, USGS: Reston, Virginia.

10. Pitzer, K.S., *Thermodynamics*. 3rd ed. 1995: McGraw-Hill.

11. Pabalan, R.T. and K.S. Pitzer, *Heat capacity and other thermodynamic properties of $Na_2SO_{4(aq)}$ in hydrothermal solutions and the solubilities of sodium sulfate minerals in the system Na-Cl-SO_4-OH-H_2O to 300 °C.* Geochimica et Cosmochimica Acta, 1988. **52**(10): p. 2393-2404.

12. Pabalan, R.T. and K.S. Pitzer, *Thermodynamics of concentrated electrolyte mixtures and the prediction of mineral solubilities to high temperatures for*

mixtures in the system Na-K-Mg-Cl-SO_4-OH-H_2O. Geochimica et Cosmochimica Acta, 1987. **51**: p. 2429-2443.

13. Linke, W.F., *Solubilities of Inorganic and Metal Organic Compounds*. 4th ed. Vol. 2. 1965: American Chemical Society.

14. Hall, C. and W.D. Hoff, *Water Transport in Brick, Stone and Concrete*. 2002, London: Spon Press.

15. Ashby, M.F., *Materials Selection in Mechanical Design*. 2nd ed. 1999, Oxford: Butterworth-Heinemann.

4. Introduction

The phase transitions of mirabilite-thenardite were discussed in chapter 3. The purpose of this chapter is mainly to investigate the effect of calcium additions on the crystallisation of sodium sulphate. Rarely do salts precipitate in isolation in nature, therefore the effect of other ions on the crystallisation of sodium sulphate is of interest to understanding more 'realistic' crystallisation. Calcium was chosen because it is commonly occurring, because of the interest surrounding calcium stabilisation of higher temperature polymorphs and because there are known double salts of calcium and sodium sulphate which are also of interest. Two types of experiment are reported, a synchrotron examination of the phase transition of solid mirabilite to thenardite in the presence of gypsum and the formation of sodium sulphate (and a double salt) from an aqueous solution containing calcium at 40 °C, which examines crystallisation by evaporation in the region of thenardite stability. The region of thenardite stability is interesting because of the formation and stabilisation of sodium sulphate phase III, while still being sympathetic to natural temperatures. Synchrotron radiation at station 16.4 was used because of its much greater powers of penetration when compared to the laboratory powder XRD experiments of the previous chapter. Both types of experiment constitute original work as is discussed in the relevant sections.

4.1 $Na_2SO_4 \cdot 10H_2O$ and $CaSO_4.2H_2O$ phase transitions

$CaSO_4.2H_2O$ is another commonly occurring salt mineral, and as salt minerals almost never form singularly, the interaction of mirabilite and gypsum is the subject of this section. This experiment was carried out using energy dispersive synchrotron radiation on station 16.4 (powder diffraction powered by a 6T wiggler) which uses a three element detector system, therefore each complete pattern is comprised of three patterns from the middle, top and bottom detectors. The advantage of synchrotron radiation over the lab instrument is mainly in the increased beam intensity, the depth of penetration of the X-rays and fast collection time which renders this station

excellent for investigating chemical reactions [1]. A glycol cold cell was fitted in the path of the beam (energy dispersive, fixed angle) to heat and cool the sample. Sample temperature was monitored by a thermocouple placed inside the sample. The sample was stationary and not rotated, neither was the sample scanned vertically. All X-ray information is taken from a lozenge shaped volume through the sample. The typical volume of the lozenge is 3 mm^3, therefore this is the volume of sample 'seen' by the beam.

The mirabilite-gypsum sample used had the composition of 90 % mirabilite (by mass), 10 % gypsum (by mass) and was contained in a glass vial with an opening in the lid for the thermocouple to go through, the opening was then sealed with masking tape resulting in very minute mass loss of 0.11 % of the mirabilite measured at the end of the experiment. The composition of 90 % mirabilite and 10 % gypsum was chosen from test samples carried out previously on 16.4, where two samples of composition 90 % mirabilite (10 % gypsum) and 99 % mirabilite (1 % gypsum) were quickly ran. The more interesting sample was the 10 % gypsum one, which produced a double salt known as labile salt, or eugsterite and hence this composition was investigated more fully. Ideally a range of compositions would be investigated.

The temperatures of the set bath (temperature the glycol cold cell was set to), actual bath (the measured temperature of the glycol cold cell) and sample temperature (measured using a thermocouple in the sample) are shown in figure 4.1. The most striking feature during heating is the length of time the sample takes in proportion to the rest of the heating cycle to cross over the mirabilite-thenardite transition point. This possible halt as it is often referred to, is symptomatic of a phase change. The sample temperature cannot rise above the temperature of the phase change (approximately) until the transition has taken place fully; in this case the plateau occurs at c.34 °C, which is just above the mirabilite-thenardite transition point. During cooling there is a possible halt, although it is not quite as marked as the plateau during heating, at c.11 °C. This bears some resemblance to the unsymmetrical thenardite-mirabilite transition observed in the laboratory X-ray experiments detailed in chapter 3.

The chemical reaction which takes place at the mirabilite-thenardite transition point as mirabilite releases its water of hydration results in the formation of

thenardite and labile salt, also known as eugsterite [2] can be loosely represented as Eq. (4.1). If all the gypsum converts to labile salt, the sodium sulphate will exist in solution only, as there would be sufficient water to dissolve all the thenardite produced by the dehydration of mirabilite after the labile salt had taken its share of the sodium sulphate.

$$14Na_2SO_4.10H_2O_{(s)} + 3CaSO_4.2H_2O_{(s)} \leftrightarrow 3Na_4Ca(SO_4)_3.2H_2O_{(s)} + 8Na_2SO_{4(s)} + 140H_2O_{(l)} \quad \textbf{(4.1)}$$

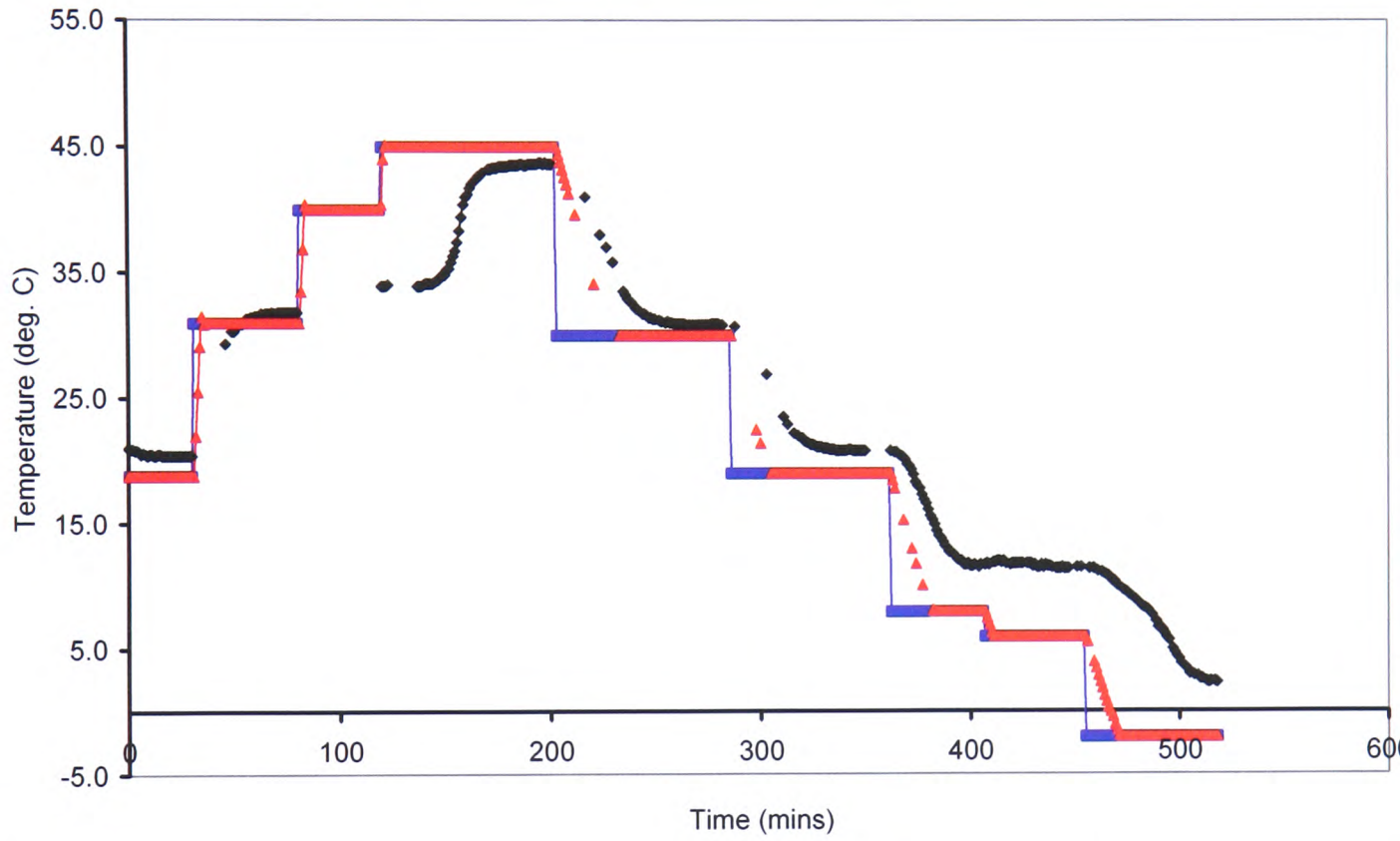

Figure 4.1: Temperature of the bath and sample. The blue points are the set bath temperature, the red points are the actual bath temperature and the black points are the sample temperature.

4.1.1 X-ray data

A 30 min loop scan of 3 min per scan was taken at the first level (indicated by the level actual bath temperature in red) on figure 4.1. This corresponds to a sample temperature of 21.0 °C to 20.4 °C, with scans being taken at one point only without scanning the height of the sample (z axis). Only this first scan of the loop is shown in

figure 4.2 as all subsequent scans show no change. It is clear that the sample composition is mirabilite and gypsum.

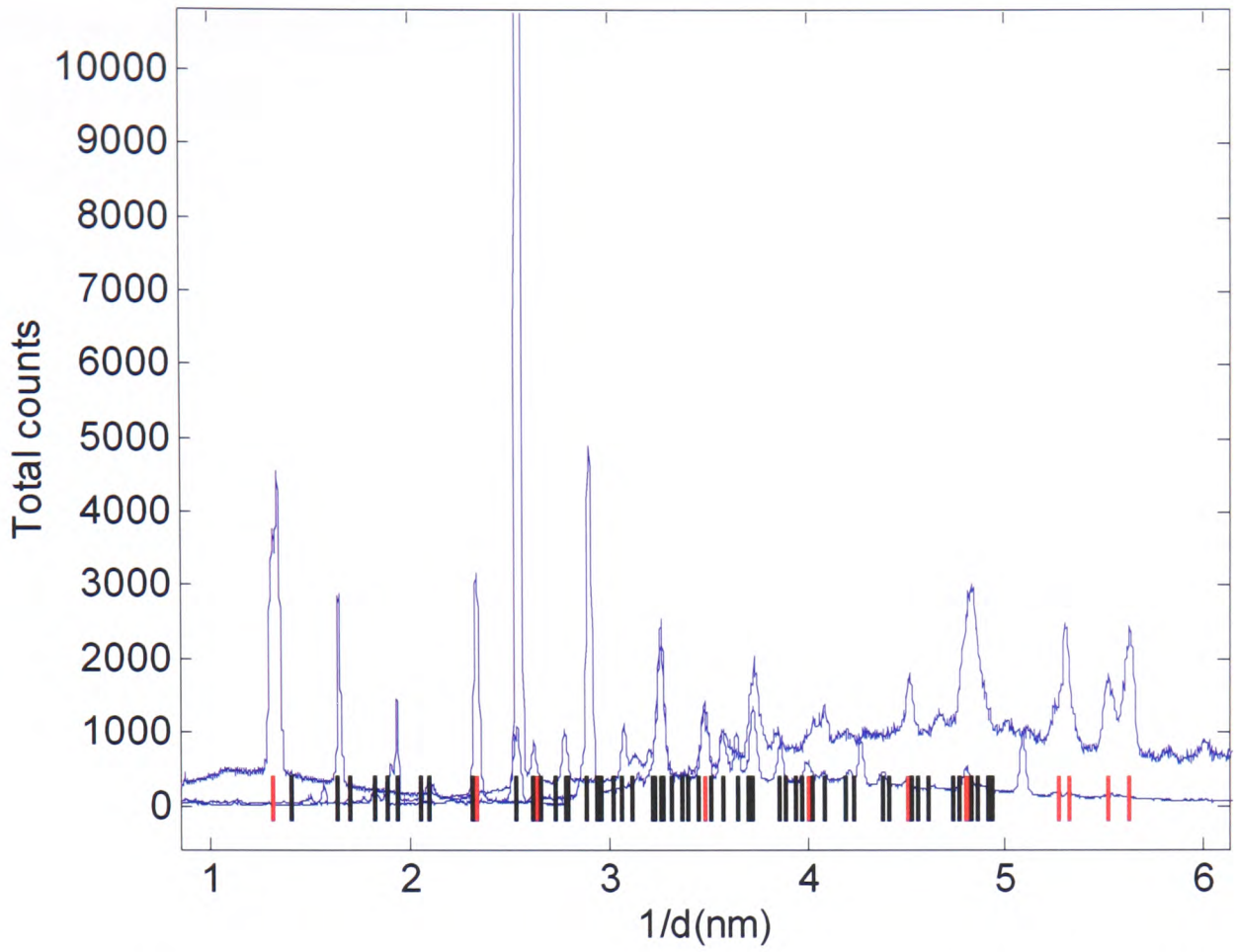

Figure 4.2: First scan at the first temperature level (figure 4.1). Mirabilite (black) and gypsum (red) peak positions are indicated.

The next 30 min set of scans taken were at the second level after heating for 20 min. The temperature range of the scans is 30.3 °C to 31.8 °C. Mirabilite and gypsum still persist, but are clearly diminishing, as can be seen in figure 4.3. The phase transition occurs on the next step up. After heating from the second level for 42 min it appeared that a plateau was occurring. This plateau is indicative of a phase transition as the sample temperature cannot increase until the phase change has completely taken place at this halt point [3].

A three minute scan taken on this plateau after the bath temperature was stepped up to 45 °C and the sample temperature read 33.9 °C, revealed a much larger background and labile salt formation. A large background is indicative of amorphous material, in this case it represents that the sample is now either an aqueous suspension or contains free water. As can be seen from figure 4.4 mirabilite has mostly gone, with one possible peak left, which matches a large peak found in the

previous set of scans and is most likely to be mirabilite, gypsum has visibly decreased but still exists and labile salt has began to form. There is also possibly some evidence of thenardite formation, although it is difficult to be certain as strong peaks are absent and those that are possibly present are difficult to distinguish from gypsum or labile salt. This would indicate 5 phases are present (solution phase, mirabilite, thenardite, gypsum and labile salt). As this is impossible if the system obeys the phase rule (this would be -1 degrees of freedom), perhaps the solution phase is not forming a continuous medium throughout the area seen by the beam, which is picking up isolated pieces of un-reacted material. This is concurrent with the visual appearance of the sample, for unlike the pure sodium sulphate system of the previous chapter, the system with gypsum added does not visually liquefy, but instead has a moist feel to it, as tests on a separate vial of sample have shown. Further testing could provide clearer answers on this subject.

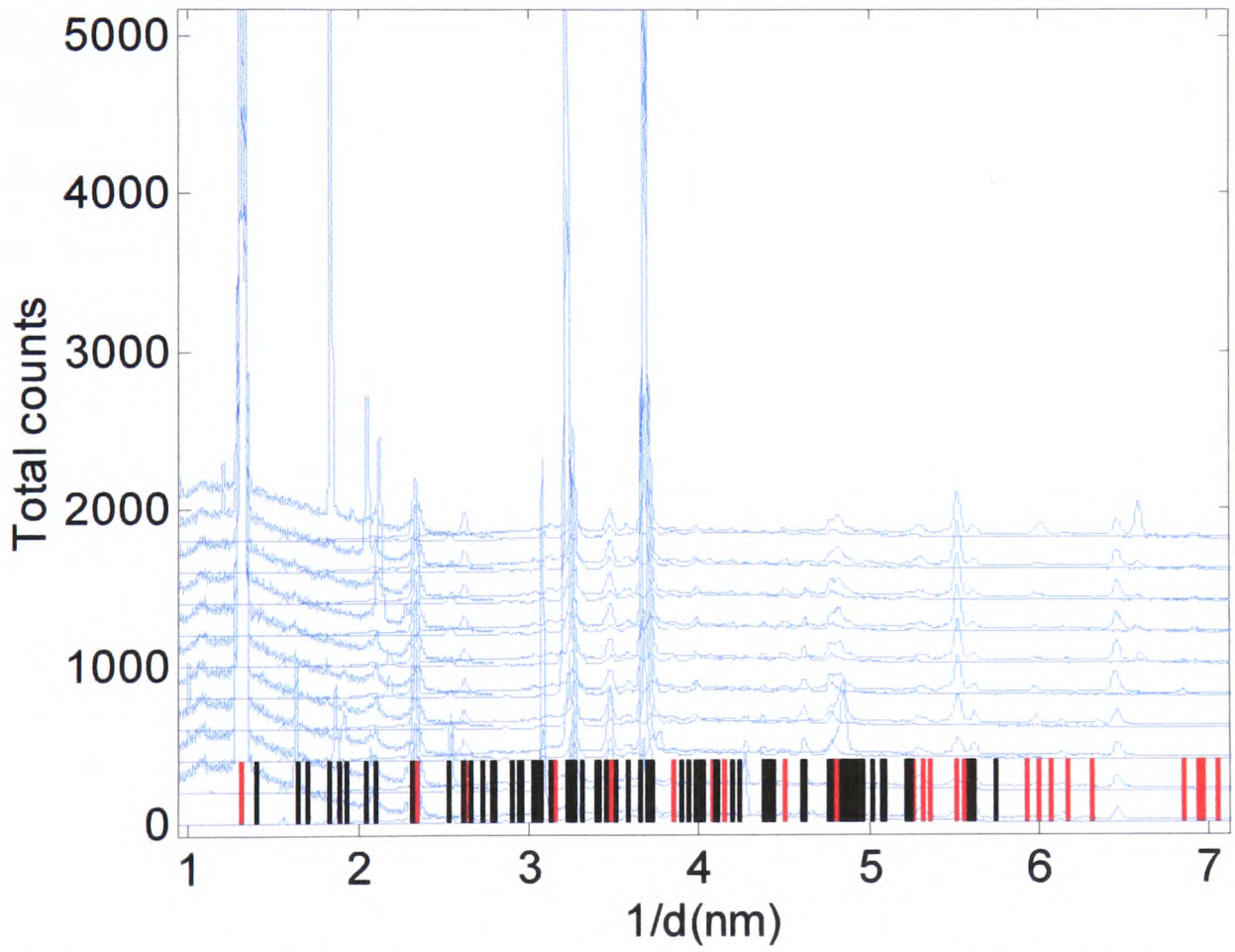

Figure 4.3: 10 x 3 min scan at the second level (ascending) in figure 4.1. Mirabilite (black) and gypsum (red) peak positions are indicated. First scan (bottom scan) was taken at a sample temperature of 30.3 °C and last scan (top scan) was taken at a sample temperature of 31.8 °C. Scans from the top and bottom detector are plotted.

Further changes take place in a 10 x 3 min scan taken during the heating section (from the sample temperature plateau at 34 °C up to a sample temperature of 42.9 °C). Gypsum decreases further to a trace amount and labile salt increases. The first and last scans are plotted to indicate the changes taking place during this loop scan. The highlighted mirabilite peaks in figure 4.4b have gone, indicating mirabilite has fully converted to thenardite as can be seen in figure 4.5. Although the temperature interval between scan one and scan ten is 8.9 °C, the gypsum level drops rapidly in the first few scans, leaving a trace amount by scan five. The sample temperature at the beginning of scan five is 34.8 °C and the temperature at the end is 35.3 °C, which indicates the sample is moving away from a halt point.

It is predicted by the phase rule that the sample temperature cannot rise if there are four phases present (assuming three components and holding the pressure constant [4]). Therefore it would seem that the mirabilite-thenardite conversion must be complete and that either gypsum or thenardite must dissolve before the sample temperature will rise, leaving at most two solid phases and the solution phase (P=3). This of course applies to a solution in contact with the minerals concerned and a system at equilibrium, whereas in this case, there could be isolated crystals detected by the beam as the sample temperature is rising but gypsum is definitely present and thenardite possibly is. Oddly enough, the most obvious thenardite peaks are on the last scan only as indicated by arrows in figure 4.5, for which there is no obvious explanation because as more gypsum converts to labile salt, more solid thenardite will dissolve. Clearly there is some gypsum, albeit a small amount and a tenuous indication of thenardite after the halt point, which would contradict the phase rule (assuming equilibrium conditions, which is not necessarily the case) unless we assume that the thenardite peaks present after the halt point are particles isolated from the solution phase. The thenardite peaks highlighted in figure 4.5 are not present in the next heating scan (sample temperature 43.2°C to 43.6°C). It would appear though that the mirabilite-thenardite conversion is complete before the sample temperature rises, as predicted by the phase rule.

Sample cooling reveals no changes at all to the sample until a sample temperature of 11.7 °C is reached. After 28 min at 11.8/7 °C there is a noticeable decrease in the background, which usually indicates the reformation of crystalline

material, although there are no obvious phase changes occurring. It takes 43 minutes from the sample temperature reaching 11.7 °C for real compositional changes to occur. The background lowers during the 30 minutes in total of this scan (corresponding to the downward step of 11.4 °C - 7.7 °C in figure 4.1). It is obvious (especially in the bottom detector patterns) that labile salt diminishes while gypsum increases as illustrated in figure 4.6.

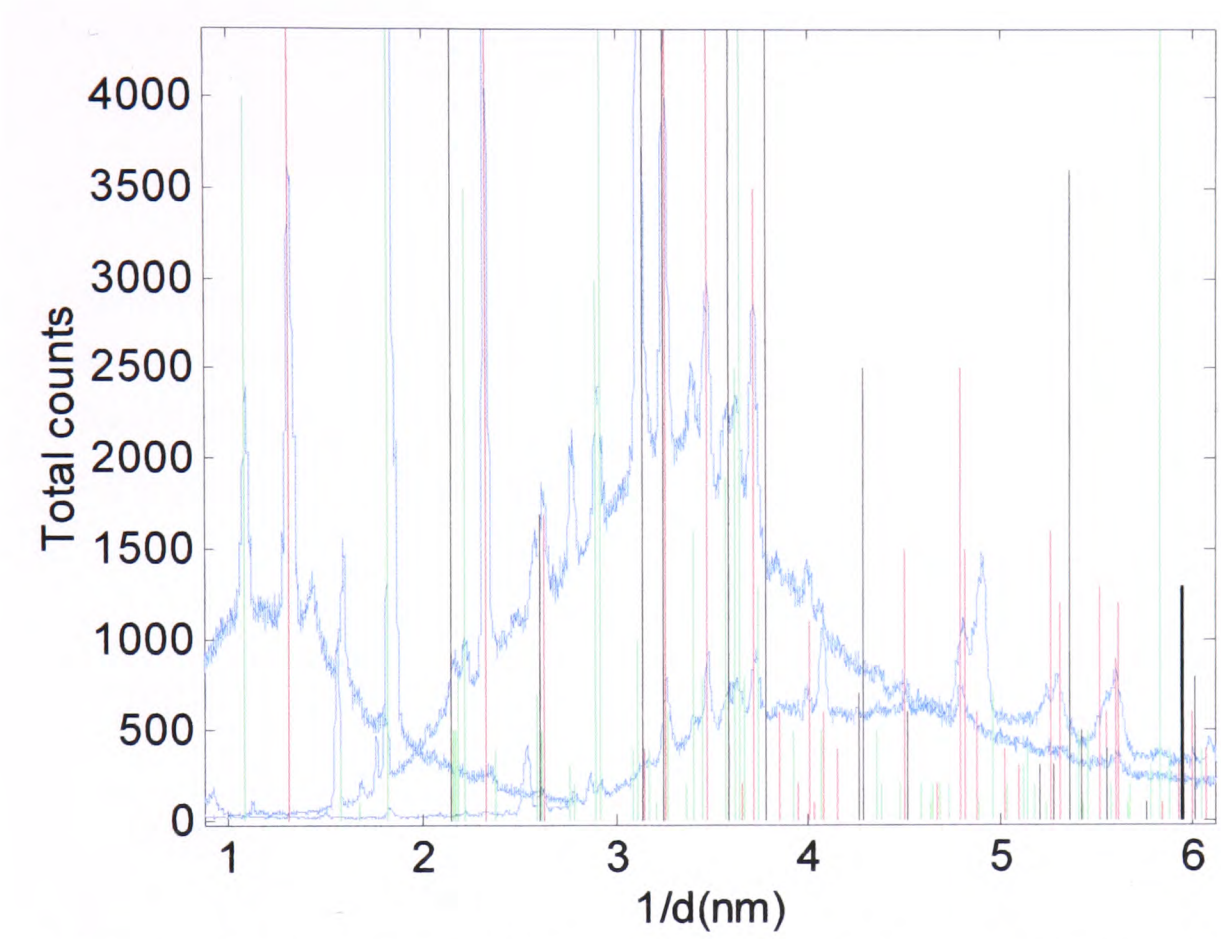

Figure 4.4a: A (one scan only) 3 min scan taken after 45 minutes of heating to 45 °C. Sample temperature read 33.9 °C. The raised background is indicative of the increased water content of the system. Gypsum (red), labile salt (green) and thenardite (black) peak positions are indicated. Bottom, middle and top detector patterns are plotted.

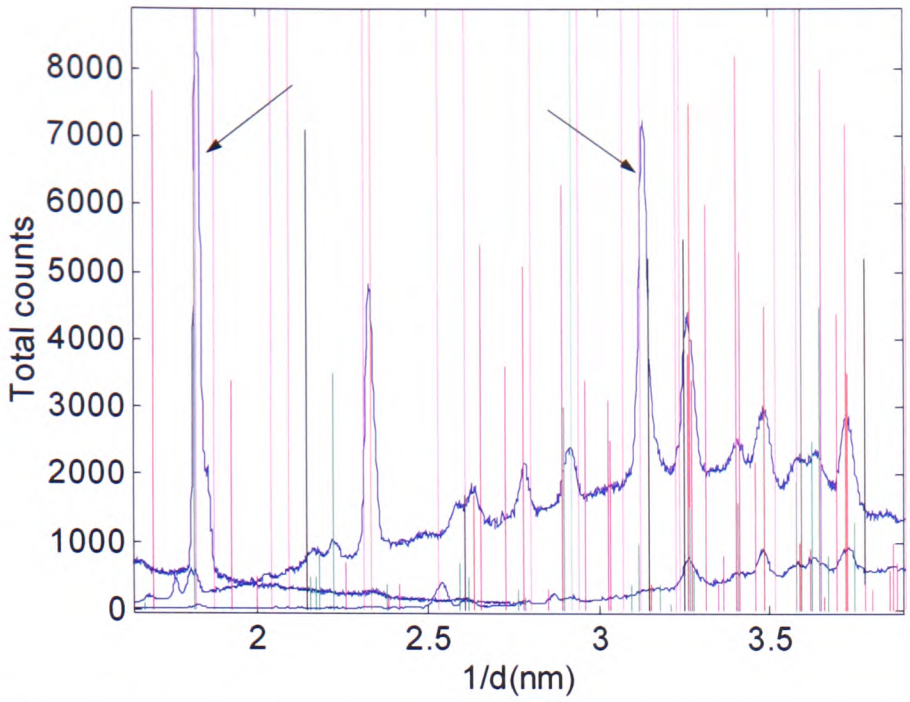

Figure 4.4b: A close up of part of figure 4.4a. The same mineral peak positions are plotted with the addition of mirabilite (magenta). The arrows point to two probable mirabilite peaks. The left hand peak matches a peak from the previous scan, taken at 31.8 °C. The right hand one is not present in the remainder of the heating scans and is a reasonable fit for mirabilite.

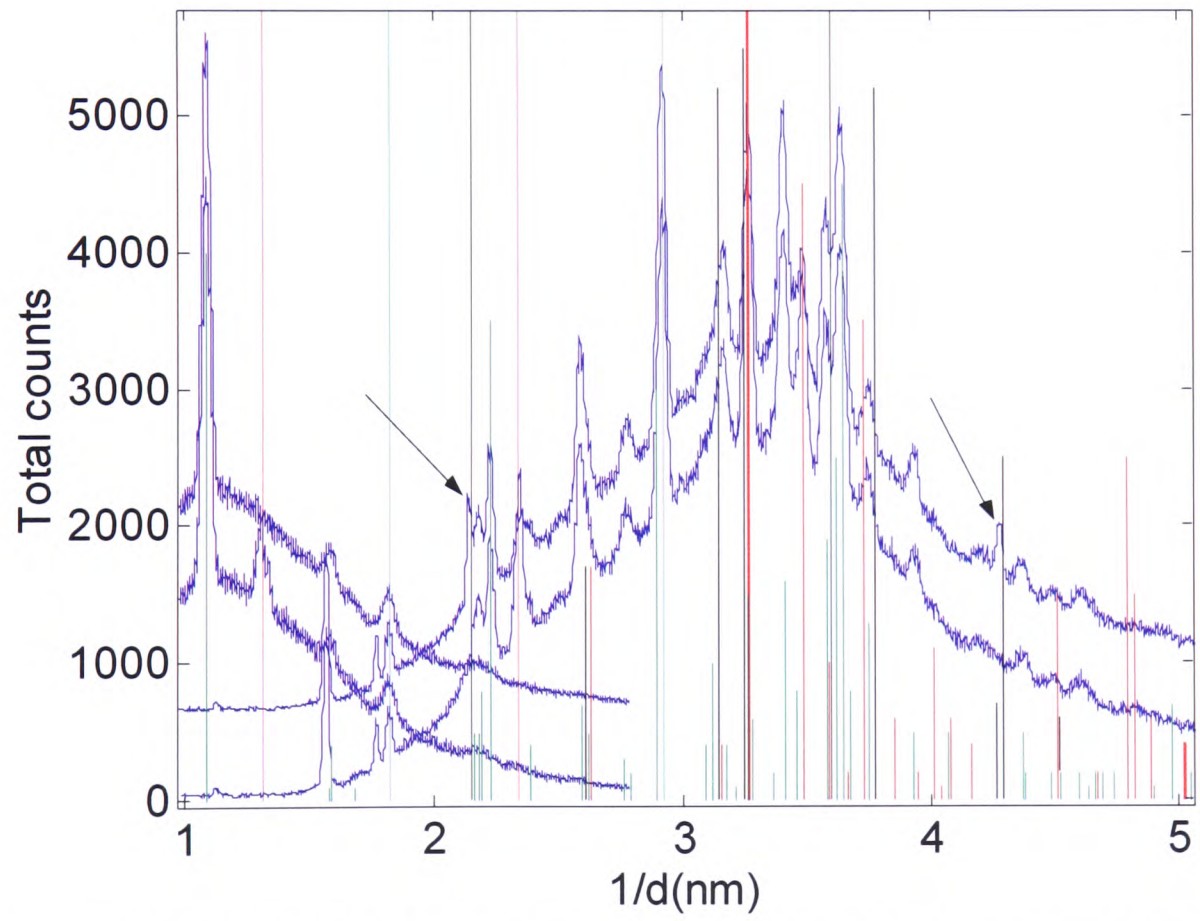

Figure 4.5: The first (bottom) and last (top) scan of the 10 x 3 min scans taken on the heating curve of the sample temperature from 33.9 °C to 42.9 °C in figure 4.1. Gypsum (red), labile salt (green) and thenardite (black) peak positions are indicated. Sample temperature during the first scan was 33.9 to 34.0 ºC and sample temperature of the last scan was 42.4 ºC to 42.7 ºC. Bottom and middle detector patterns are plotted. The arrows point to two possible thenardite peaks.

There are no further compositional changes in the sample after figure 4.6. Although the sample temperature is taken down to 2.3 °C, the pattern remains mostly gypsum with some labile salt and one extra peak, which could as easily be heptahydrate as mirabilite. One peak is not enough for identification. The sample was then left in a refrigerator overnight at -5 °C for 15.5 hours before being scanned again. The change is quite dramatic. Mirabilite is fully formed and gypsum is present. There is no trace of labile salt.

Figure 4.7 plots the fourth scan (a set of scans, one taken every 2 mm of the sample vertically. This is the only z scan that was carried out for this sample) after removal from the refrigerator along with the first scan from the last set of cooling scans (sample temperature of 2.8-2.9 °C with no scanning the sample vertically) taken the previous day. As can be seen, labile salt has disappeared, mirabilite and gypsum are fully formed.

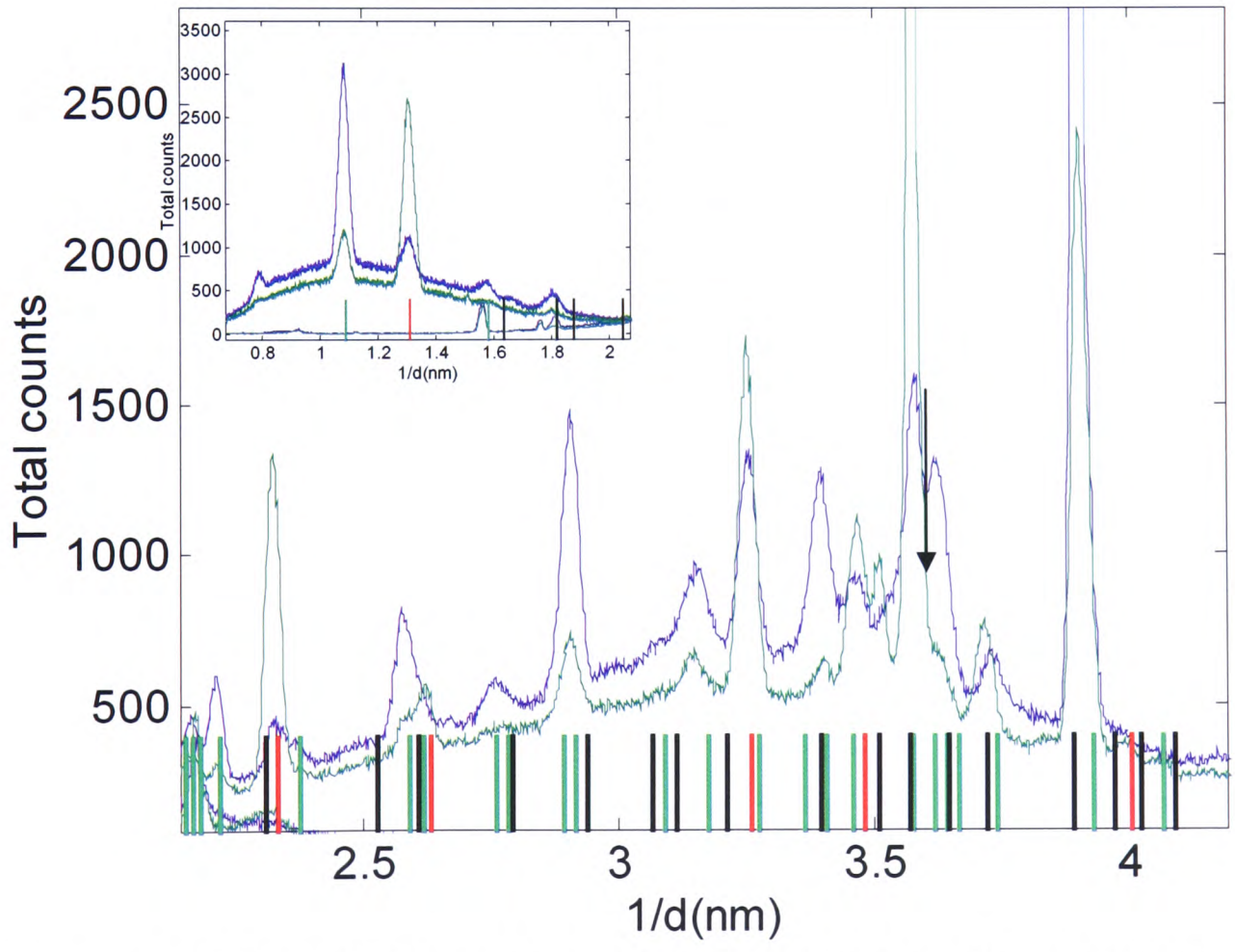

Figure 4.6a: The main figure shows the middle detector pattern of the sample cooling (sample temperature) from 11.4 °C to 7.7 °C. The green pattern is the end pattern (7.7 °C) which shows a lesser amount of labile salt (bright green), and increased gypsum (red) plus one possible mirabilite peak (black) highlighted by the arrow. This one peak could also be heptahydrate as shown in figure 4.6b.The inset image is the bottom detector and depicts beautifully the decrease in labile salt occurring simultaneously with the increase in gypsum.

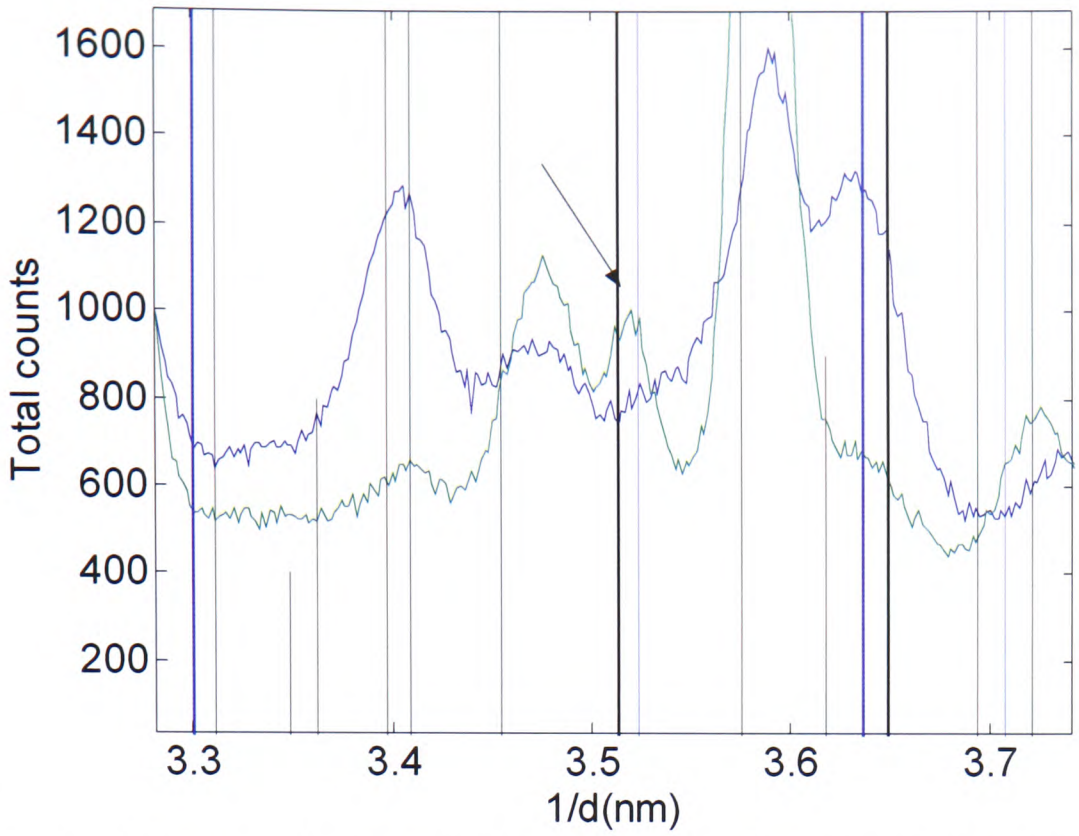

Figure 4.6b: An enlargement of part of figure 4.6a. Heptahydrate (blue) and mirabilite (black) peal positions are indicated. The peak which could be either mirabilite or heptahydrate is marked with an arrow. One peak is not sufficient for phase identification.

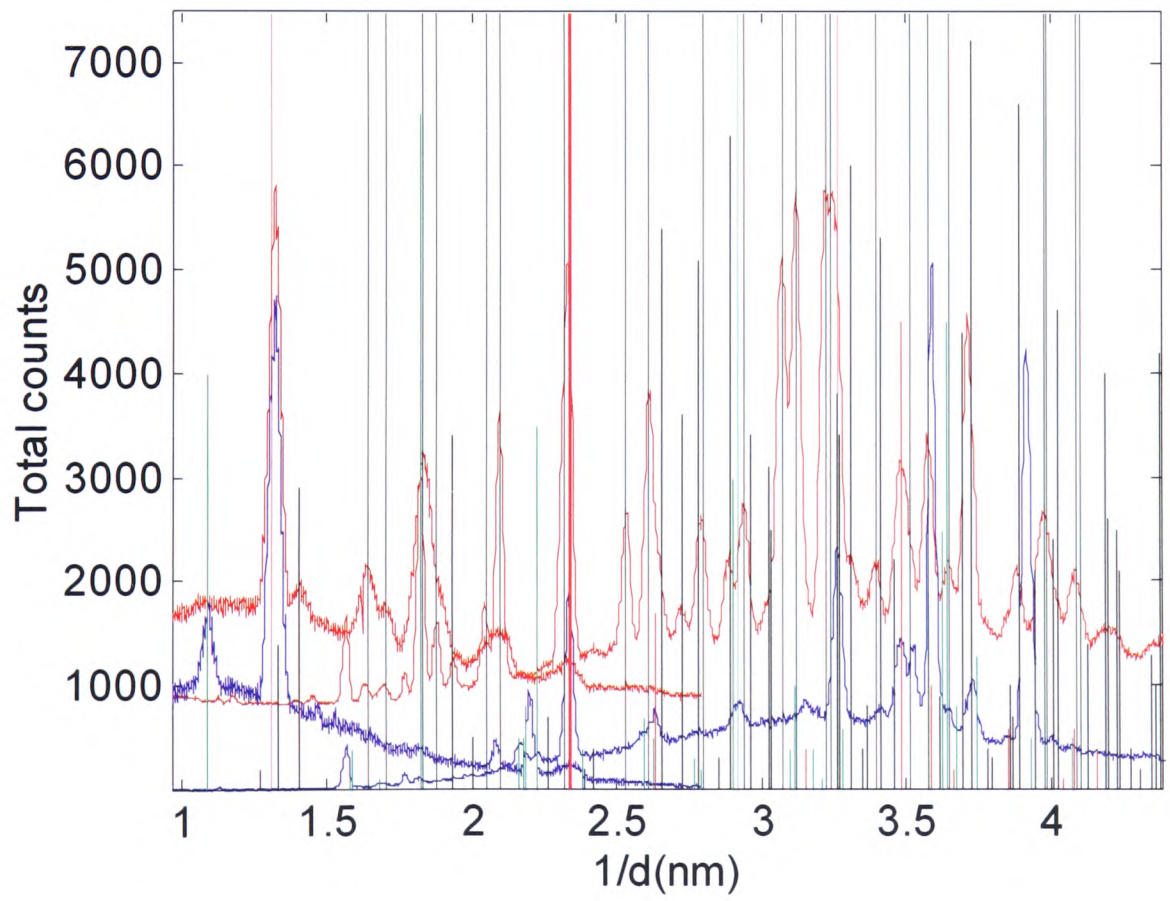

Figure 4.7: The red scan is after overnight refrigeration and the blue scan was taken at 2.9 – 2.8 °C. Mirabilite (black), gypsum (red) and labile salt (green) peak positions are indicated. The precipitation of mirabilite and dissolution of labile salt is marked. Scans from the bottom and middle detectors are shown.

It is possible to calculate the amount of labile salt produced from the original known amounts of mirabilite and gypsum at 35 °C, if the system is viewed in an idealised manner. Making the original assumption that all the gypsum is transformed to labile salt (although there is some left over, it is a trace amount and is over looked for the purposes of this calculation) and that labile salt is insoluble, this gives a first approximation of the solution composition. From that solution composition (purely aqueous sodium sulphate), a corresponding calcium sulphate concentration in solution (from the slight dissolution of labile salt) is obtained by curve fitting the 35 °C data of Hill and Wills [5] from which the sodium sulphate concentration is recalculated, taking into account the extra sodium sulphate produced by the dissolution of labile salt. This iterative process is repeated until convergence, which gives a final amount (wt %) of sodium sulphate, calcium sulphate and water, constituting the solution phase. The results are shown in table 4.1 and displayed in figure 4.9.

Mineral/water	Result - Wt %	Result – g/kgw	Result - molal
$CaSO_4$	0.0818	1.197	0.0088
Na_2SO_4	31.5997	462.534	3.2563
H_2O	68.3185		

Table 4.1: The results (and solubility comparison) of the predicted composition of the solution phase after the formation of labile salt based on the 35 °C solubility data of Hill and Wills [5].

It can be seen from table 4.1 that using the labile salt solubility data of Hill and Wills for the solution phase of this system results in only one solid phase present, which is labile salt. Of course, the Hill and Wills data refers to equilibrium conditions, whereas the system described here may not be at equilibrium, which makes any assessment of the solution composition an approximation only. The solubility of labile salt in a sodium sulphate solution at 33 °C can also be calculated using PHRQPITZ [6] as shown in figure 4.8. This is perhaps less accurate than the experimental data of Hill and Wills (at 35 °C) as it was calculated using a K_{sp} value

for the system at 25 °C, the only K_{sp} value in the software databank, and hence the calculation of the solution composition presented here uses the Hill and Wills data.

As the sample temperature is cooled, the X-ray results show an increase in the amount of gypsum present, a decrease in the amount of labile salt present and a possible indication of mirabilite (or heptahydrate) at 7.7 °C. The sodium sulphate in solution begins to be supersaturated with respect to mirabilite quite quickly. Assuming negligible composition changes due to the alteration in the solubility of labile salt, the sodium sulphate solution has reached supersaturation with respect to mirabilite by 31 °C, although, crystallisation of mirabilite is not detected until approximately 7.7 °C, which, even then, is not certain. Theoretically, as mirabilite crystallises, labile salt goes back into solution, liberating calcium sulphate which reforms as gypsum. Why mirabilite is not more strongly evident from the X-ray results during cooling, in tandem with gypsum is unknown. After overnight refrigeration, the result is reformation of the original components of the system, as seen from the pattern taken the next day.

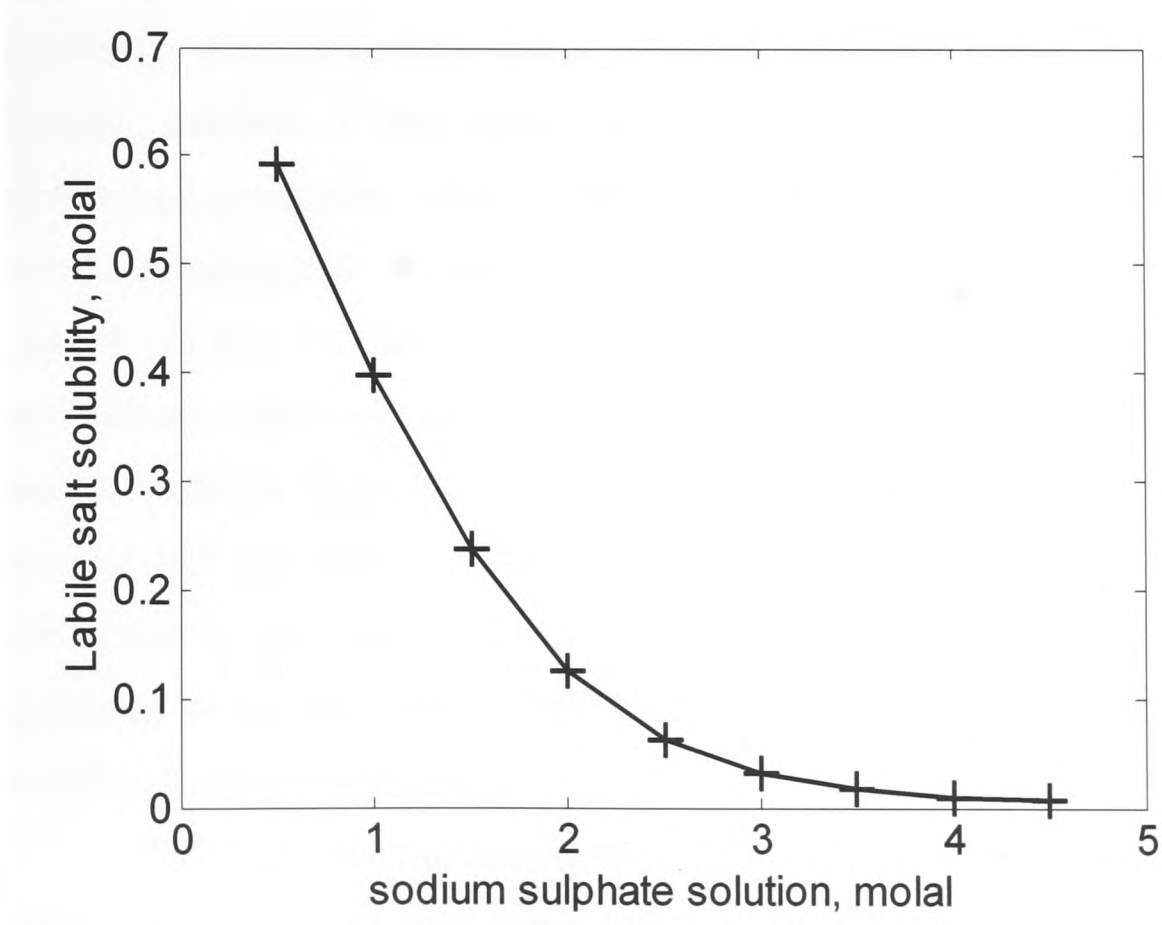

Figure 4.8: The calculated (PHRQPITZ) labile salt solubility in a sodium sulphate solution of set concentration (as given by the x-axis) at 33 °C. PHRQPITZ simulation, C. Hall, unpublished.

4.1.2 Conclusion

Mirabilite and gypsum interact through the mirabilite-thenardite conversion. Aqueous solution is required to dissolve the gypsum to produce labile salt. As can be seen, labile salt forms at approximately 33.9 °C which is very close to the mirabilite-thenardite transition point of 33 °C (32.4 °C literature value) based on the experiments in the previous chapter.

When mirabilite releases its water of hydration in a closed system, it must reasonably produce a solution saturated with respect to the thenardite crystals produced from the dehydration. As the water is produced forming a thenardite saturated solution, gypsum must dissolve to form labile salt. The possible halt on heating indicates an invariant point. The sample temperature cannot rise until the phase change (mirabilite to thenardite) has completely taken place. Mirabilite must fully convert to thenardite and then one solid phase must dissolve, assuming the solution phase is in continuous contact with the sample, which may not be the case as previously discussed. This leaves at most two solid phases in contact with the aqueous solution, if the phase rule is applicable under these potentially non-equilibrium conditions. What is observed experimentally is that one solid phase is strongly evident after or during the mirabilite-thenardite conversion (labile salt) with gypsum existing as a trace amount after the halt point, which is possibly un-reacted material and some indication of thenardite after the halt point, which again could be material isolated from the solution phase. The calculation presented based on the work of Hill and Wills is idealised and assumes that all gypsum converts to labile salt, which is not necessarily the case, but indicates that with the given starting quantities of gypsum and mirabilite, the only solid phase present in contact with solution should be labile salt.

Hill and Wills [5] indicate that labile salt will not form when mirabilite is the stable phase and will only form rapidly in the presence of solid thenardite. This would suggest that thenardite forms first and is subsequently dissolved by further formation of labile salt, if all of the thenardite produced is in contact with the solution phase. Labile salt is metastable with respect to glauberite in the temperature region 25 – 75 °C, however Hill and Wills note that it can remain in contact with its

conversion to glauberite taking place. The 35 °C isotherm of Hill and Wills is particularly relevant to this experiment. They present data which shows that labile salt can be formed directly from gypsum and aqueous sodium sulphate. The results are given in wt % of the final solution composition at equilibrium, with labile salt as the solid phase. The final solution composition of this experiment is plotted against the Hill and Wills data in figure 4.9. Naturally the fit is good, as this data was used to calculate the solubility of labile salt for this experiment.

Wt % Na_2SO_4	Wt % $CaSO_4$	Solid phase	reference
29.31	0.084	Glauberite	[5]
28.34	0.099	Glauberite	[5]
25.17	0.146	Glauberite	[5]
23.06	0.199	Glauberite	[5]
22.65	0.206	Glauberite and gypsum	[5]
32.85	0.065	Thenardite and labile salt	[5]
31.66	0.078	Labile salt	[5]
31.18	0.088	Labile salt	[5]
30.48	0.102	Labile salt	[5]
27.25	0.176	Labile salt	[5]
26.70	0.200	Labile salt and gypsum	[5]
31.5997	0.0818	Labile salt	This work

Table 4.2: The final solution composition data from Hill and Wills at equilibrium, listing the solid phase with data from this work for comparison.

On cooling the sample, labile salt seems to exchange for gypsum in the temperature range 11.4 – 7.7 °C, and there is a slight attempt at sodium sulphate reformation. Clearly the re-precipitation of mirabilite and gypsum takes place much more slowly than the dehydration stage; this is evident from the lack of a definite halt point during the course of the experiment. It is assumed though that a sample temperature plateau would eventually happen as mirabilite begins to properly form.

The complete reformation of mirabilite and gypsum is obvious from the final XRD pattern taken after the sample sat overnight in the refrigerator. Further investigation on the cooling halt point would provide a more complete answer.

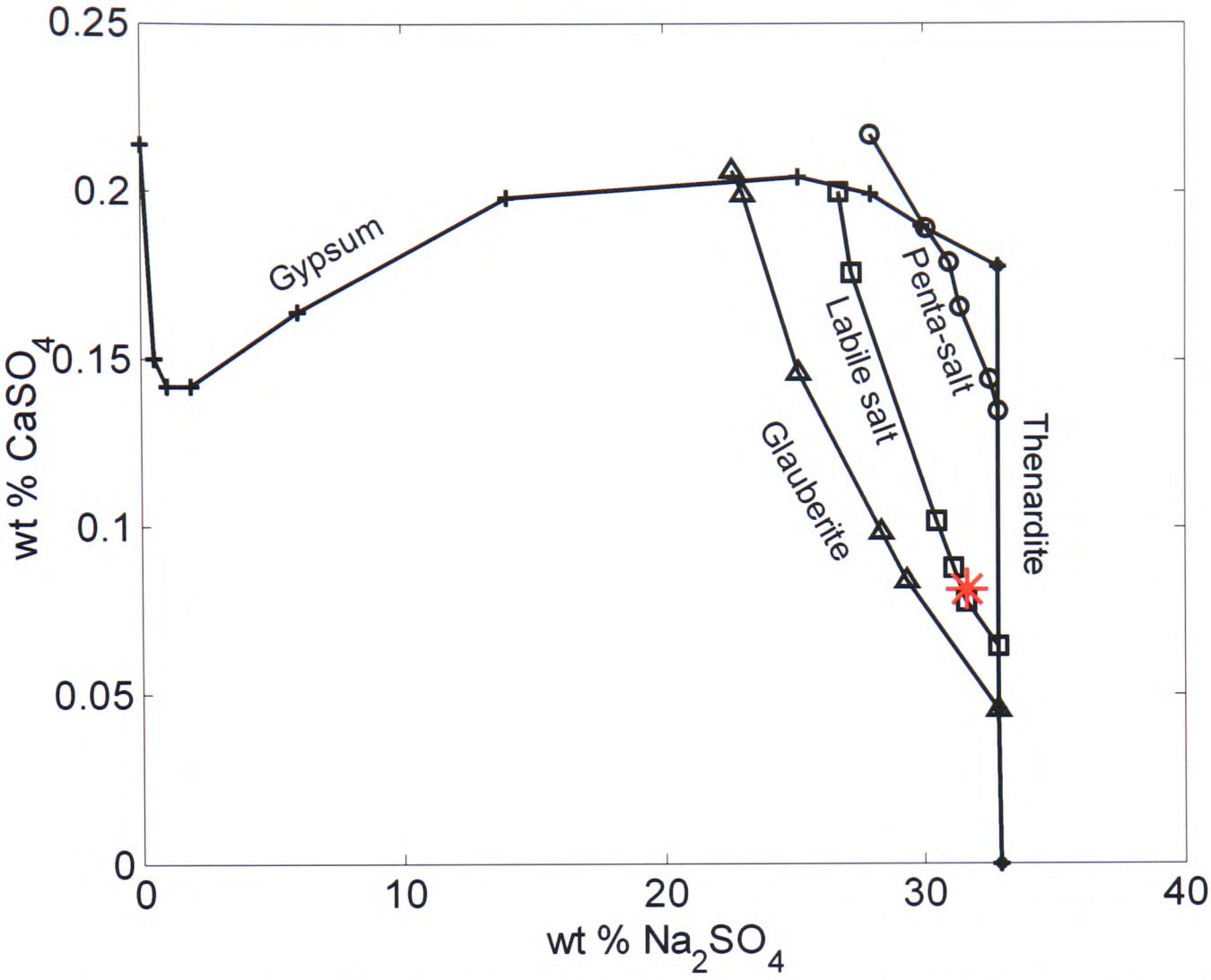

Figure 4.9: Saturated solution composition, 35°C isotherm from Hill and Wills [5] in black with the data point (possible composition of the solution phase) from this work plotted as a red asterix.

4.2 Crystallisation from solution

The purpose of this section was to examine the crystallisation of sodium sulphate doped with calcium in the region of thenardite stability. 40 °C was chosen as being above the mirabilite-thenardite transition point while still being sympathetic to real world conditions.

The stabilisation of Na_2SO_4 III and I by cation substitution is known [7-10], but through quenching a melt formed at high temperatures (~950 – 1100 °C) rather than growth by solution evaporation. Sodium sulphate is well known to have five polymorphs [7, 8, 10-13] stable over a wide range of temperatures. Na_2SO_4 (V) also

known as thenardite is the stable phase at room temperature. The other polymorph this chapter is primarily concerned with is Na_2SO_4 (III), which is noted to be stable in dry air indefinitely [14], although there is evidence that water has a catalytic effect on the Na_2SO_4 transitions in favour of phase V [11]. Many cations are known to stabilise phase III and I, for example, Y, Dy, Ce, Ca, La, Yb and Eu [7] but more commonly occurring cations (Ca, Cu, Al, K and Mg) were examined for this work, with the emphasis on calcium.

4.2.1 Experimental methods

A Na_2SO_4 solution was prepared using two methods: saturation by excess at 20 °C (the solution was stored in an environmental cabinet with excellent temperature control) or more commonly by dissolving a set amount (c.19.2544 g) of anhydrous Na_2SO_4 in 100 g of water [15]. Analytical reagent grade anhydrous sodium sulphate (Fisher, +99%) was used in either case. The solution was filtered using vacuum filtration methods with Sartorius cellulose nitrate filters (0.45 μm pore diameter). Other aqueous solutions prepared were $CaSO_4.2H_2O$ (Riedel de Haën, +99% purity), $CuSO_4.5H_2O$ (Fisher, +99%), $Al_2(SO_4)_3.18H_2O$ (Riedel de Haën, extra pure, 100-110%), K_2SO_4(Fisher, +99%), $MgSO_4.7H_2O$ (Fisher, +99%) which were also filtered using the same method. 3 ml (or 4 ml for some experiments) of Na_2SO_4 and a second cation solution from the list above, was pipetted (using an eppendorf electronic *Multipipette Pro* pipette) into a glass Petri dish and subsequently crystallised by evaporation in an air oven at 40 °C for a set length of time. In some cases prior mixing of the solutions took place in disposable Bibby Sterilin universal tubes using a magnetic stir bar before being pipetted into the Petri dish. In these cases, the solution was twice filtered, once using the vacuum method and secondly using a syringe filter (PES, Nalgene, sterile, 0.2 μm pore size) as the mixed solution was pipetted into the Petri dish.

The resulting crystals were powdered for analysis by powder XRD (Bruker D8 using fully monochromated CuKα radiation), identified using EVA (Bruker evaluation software) and quantified using TOPAS (Bruker, AXS software) for semi-

quantification of phases present. A more detailed description of the experimental procedure will be given as each experiment is discussed.

4.2.2 Na_2SO_4 and Ca

A series of experiments was undertaken to examine the amount of Na_2SO_4 III that could be produced with variations in calcium concentration. To do this, a known volume of aqueous sodium sulphate solution (1.355 molal) was mixed with the same known volume of a Ca containing solution ($CaCO_3$ or $CaSO_4.2H_2O$) of set concentration and evaporated in an air oven at 40 °C. The concentration of the Ca solution was measured using ICP-OES before crystallisation and occasionally the resulting crystals were dissolved (after XRD analysis) and the Ca concentration was measured again using ICP-OES. Tables 4.3-4.7 present the experimental variables and the results:

Sample no.	Molality Na_2SO_4	Molality Ca solution	Volume Na_2SO_4	Volume Ca solution	Mass Na_2SO_4	Mass Ca solution
1	1.355	0.00012	3 ml	3 ml	3.666	3.214
2	1.353	0.00012	3 ml	3 ml	3.701	3.220
3	1.353	0.00012	3 ml	3 ml	3.593	3.231
4	1.355	0.00012	3 ml	3 ml	3.696	3.229
5	1.355	0.00012	5 ml	5 ml	5.689	4.988
6	1.355	0.00012	5 ml	5 ml	5.684	4.996
7	1.355	0.00024	3 ml	3 ml	3.504	3.214
8	1.356	0.00024	4 ml	4 ml	4.537	3.988
9	1.355	0.00026	5 ml	5 ml	5.704	4.993
10	1.355	0.00049	5 ml	5 ml	5.683	4.997
11	1.355	0.00059	3 ml	3 ml	3.698	3.191
12	1.355	0.00059	3 ml	3 ml	3.628	3.231
13	1.355	0.00062	3 ml	3 ml	3.710	3.224
14	1.356	0.00059	4 ml	4 ml	4.542	3.986
15	1.355	0.00060	5 ml	5 ml	5.719	5.000
16	1.355	0.00120	3 ml	3 ml	3.493	3.234
17	1.355	0.00121	3 ml	3 ml	3.640	3.201
18	1.355	0.00121	3 ml	3 ml	3.699	3.216
19	1.355	0.00121	3 ml	3 ml	3.744	3.220
20	1.356	0.00118	4 ml	4 ml	4.539	3.993
21	1.355	0.00119	15 ml	15 ml	17.068	14.964

22	1.355	0.00119	15 ml	15 ml	17.057	14.980
23	1.355	0.00119	4 ml	4 ml	4.550	3.994
24	1.355	0.00119	4 ml	4 ml	4.535	3.982
25	1.355	0.00152	3 ml	3 ml	3.695	3.239
26	1.355	0.00154	3 ml	3 ml	3.682	3.254
27	1.355	0.00154	3 ml	3 ml	3.699	3.190
28	1.355	0.00153	3 ml	3 ml	3.714	3.222
29	1.356	0.00154	4 ml	4 ml	4.548	3.990
30	1.355	0.00242	3 ml	3 ml	3.715	3.232
31	1.356	0.00240	4 ml	4 ml	4.564	4.003
32	1.355	0.00290	5 ml	5 ml	5.692	4.987
33	1.355	0.00479	3 ml	3 ml	3.563	3.190
34	1.356	0.00480	4 ml	4 ml	4.569	3.995
35	1.355	0.00480	15 ml	15 ml	17.056	14.992
36	1.355	0.00480	15 ml	15 ml	17.064	14.996
37	1.355	0.00480	4 ml	4 ml	4.551	3.990
38	1.355	0.00480	4 ml	4 ml	4.550	3.996
39	1.355	0.00767	3 ml	3 ml	3.659	3.195
40	1.355	0.00766	3 ml	3 ml	3.715	3.218
41	1.355	0.00766	3 ml	3 ml	3.725	3.213
42	1.355	0.00765	3 ml	3 ml	3.735	3.211
43	1.356	0.00766	4 ml	4 ml	4.558	4.015
44	1.355	0.0153	3 ml	3 ml	3.671	3.210
45	1.353	0.0153	3 ml	3 ml	3.682	3.200
46	1.353	0.0153	3 ml	3 ml	3.728	3.241
47	1.355	0.0153	3 ml	3 ml	3.606	3.220

Table 4.3: Column 1 is the sample number, column 2 is the concentration of the Na_2SO_4 solution used, column 3 is the concentration of the $CaSO_4.2H_2O$ or $CaCO_3$ (samples 1-6 only) solution used, expressed in moles of $CaSO_4.2H_2O$ or $CaCO_3$ per kg water. For samples 1-6 and 44-47, the $CaCO_3$ and $CaSO_4.2H_2O$ solutions were prepared by excess, the concentration given is therefore the solubility of the reagent. The measured concentration, using ICP-OES, is discussed in table 4.4. Columns 4 and 5 give the volume of each solution pipetted into the crystallisation dish. For accuracy, the volume of solution used was weighed; this is given in columns 6 and 7. Samples 5-6, 9-10, 15, 21-22, 32, 35, 37 were pre-mixed before a set mass (given in table 4.10) was pipetted into the Petri dish.

Sample no.	Ca conc. predicted ppm	Ca conc. measured ppm	XRD results		
			Na_2SO_4 III	Na_2SO_4 V	Labile salt?
1	4.73	5.54	0 %	100 %	No
2	4.77	5.37	0 %	100 %	No
3	4.77	5.37	0 %	100 %	No
4	4.77	5.54	0 %	100 %	No
5	4.77	26.5	6.40 %	93.60 %	No
6	4.77	4.94	0 %	100 %	No
7	9.78	10.13	5.72 %	94.28 %	No
8	9.78	8.29	0 %	100 %	No
9	10.47	8.14	0 %	100 %	No
10	19.78	21.44	19.46 %	80.54 %	No
11	23.74	26.96	19.84 %	80.16 %	No
12	23.74	26.96	28.20 %	71.80 %	No
13	24.67	26.86	19.62 %	80.38 %	No
14	23.74	24.43	20.17 %	79.83 %	No
15	24.44	23.21	14.08 %	85.92 %	No
16	47.94	48.1	40.20 %	59.80 %	No
17	48.41	49.27	39.76 %	60.24 %	No
18	48.41	49.27	31.95 %	68.05 %	No
19	48.41	52.75	27.74 %	72.26 %	No
20	47.48	47.56	35.92 %	64.08 %	No
21	47.71	52.97	35.61 %	64.39 %	No
22	47.71	52.97	34.60 %	65.40 %	No
23	47.71	52.97	32.93 %	76.07 %	No
24	47.71	52.97	14.51 %	85.49 %	No
25	60.97	61.51	41.63 %	58.37 %	No
26	61.9	62.02	46.31 %	53.69 %	No
27	61.9	62.02	44.71 %	55.29 %	No
28	61.2	67.21	52.72 %	47.28 %	No
29	61.9	66.81	48.63 %	51.37 %	No
30	96.8	105.14	49.23 %	50.77 %	No
31	96.33	98.86	57.32 %	42.68 %	No
32	95.87	105.3	46.52 %	53.48 %	No
33	191.88	203.68	70.68 %	39.56 %	No

34	192.12	205.93	63.76 %	36.24 %	No
35	192.12	205.93	64.37 %	35.63 %	No
36	192.12	209.22	56.39 %	43.61 %	No
37	192.12	209.22	54.94 %	45.06 %	No
38	192.12	209.22	60.29 %	39.71 %	No
39	306.86	326.18	59.12 %	40.88 %	Trace
40	306.86	335.16	49.84 %	50.16 %	Trace
41	306.86	335.16	62.65 %	37.35 %	Trace
42	306.4	334.63	44.07 %	55.93 %	Trace
43	306.4	319.72	41.01 %	58.99 %	Trace
44	612.22	630.28	21.01 %	78.99 %	Yes
45	612.22	670.44	13.96 %	86.04 %	Yes
46	612.22	670.44	23.50 %	76.50 %	Yes
47	612.22	660.61	3.97 %	96.03 %	Yes

Table 4.4: Column two shows the predicted calcium concentration of the Ca solution used, taken from the known concentration of the solution. Column three is the measured calcium concentration of the solution, using ICP-OES. Columns four and five are the relative percentages of phase III and V in the end product. The last column indicates whether labile salt precipitated or not.

Experiments 39-47 show varying amounts of labile salt. For 39-43 this is a trace amount only, but for 44-47, the amount is more substantial, estimated at 2-4 %. As such, the quantitative XRD values are inaccurate for 44-47, as TOPAS calculates the percentage relatively rather than absolutely. No structural information is available for labile salt, which means the % composition of the samples containing labile salt cannot be accurately determined as the amount of labile salt present cannot be quantified using TOPAS. The accuracy of TOPAS is discussed in chapter 5.

The experimental method was examined and in two distinct ways. Experiments 21-24 and 35 to 38 examined the effect of using a plastic or glass Petri dish and the effect of stirring the solution. The variation in results between seemingly alike experiments was investigated by crystallising the solution in pairs i.e. crystallising two samples of the same solutions at the same time. These details are outlined in table 4.5

Sample no.	Dish used	Pre-mixed	XRD results		
			Na_2SO_4 III	Na_2SO_4 V	Labile salt?
1	Glass	No	0 %	100 %	No
2	**Glass**	**No**	**0 %**	**100 %**	**No**
3	**Glass**	**No**	**0 %**	**100 %**	**No**
4	Glass	No	0 %	100 %	No
5	***Glass***	***Yes***	***6.40 %***	***93.60 %***	***No***
6	***Glass***	***Yes***	***0 %***	***100 %***	***No***
7	Glass	No	5.72 %	94.28 %	No
8	Glass	No	0 %	100 %	No
9	Glass	Yes	0 %	100 %	No
10	Glass	Yes	19.46 %	80.54 %	No
11	**Glass**	**No**	**19.84 %**	**80.16 %**	**No**
12	**Glass**	**No**	**28.20 %**	**71.80 %**	**No**
13	Glass	No	19.62 %	80.38 %	No
14	Glass	No	20.17 %	79.83 %	No
15	Glass	Yes	14.08 %	85.92 %	No
16	Glass	No	40.20 %	59.80 %	No
17	**Glass**	**No**	**39.76 %**	**60.24 %**	**No**
18	**Glass**	**No**	**31.95 %**	**68.05 %**	**No**
19	Glass	No	27.74 %	72.26 %	No
20	Glass	No	35.92 %	64.08 %	No
21	Glass	Yes	35.61 %	64.39 %	No
22	Plastic	Yes	34.60 %	65.40 %	No
23	Glass	No	32.93 %	76.07 %	No
24	Plastic	No	14.51 %	85.49 %	No
25	Glass	No	41.63 %	58.37 %	No
26	**Glass**	**No**	**46.31 %**	**53.69 %**	**No**
27	**Glass**	**No**	**44.71 %**	**55.29 %**	**No**
28	Glass	No	52.72 %	47.28 %	No
29	Glass	No	48.63 %	51.37 %	No
30	Glass	No	49.23 %	50.77 %	No
31	Glass	No	57.32 %	42.68 %	No
32	Glass	Yes	46.52 %	53.48 %	No
33	Glass	No	70.56 %	29.44 %	No

34	Glass	No	63.76 %	36.24 %	No
35	Plastic	Yes	64.37 %	35.63 %	No
36	Glass	Yes	56.39 %	43.61 %	No
37	Plastic	No	54.94 %	45.06 %	No
38	Glass	No	60.29 %	39.71 %	No
39	Glass	No	59.12 %	40.88 %	Trace
40	**Glass**	**No**	**49.84 %**	**50.16 %**	**Trace**
41	**Glass**	**No**	**62.65 %**	**37.35 %**	**Trace**
42	Glass	No	44.07 %	55.93 %	Trace
43	Glass	No	41.01 %	58.99 %	Trace
44	Glass	No	21.01 %	78.99 %	Yes
45	**Glass**	**No**	**13.96 %**	**86.04 %**	**Yes**
46	**Glass**	**No**	**23.50 %**	**76.50 %**	**Yes**
47	Glass	No	3.97 %	96.03 %	Yes

Table 4.5: Column 2 shows the type of Petri dish used. Column 3 indicates if the solutions were pre-mixed before being pipetted into the Petri dish. Columns 4-6 are the TOPAS results as seen in table 4.6. The samples in bold were crystallised in pairs to examine the consistency of the results from two samples produced under exactly the same conditions from the same solutions. The two samples (5 and 6) in italics were crystallised at the same time, but using two different $CaCO_3$ solutions, both prepared by excess. The first solution (sample 5) was allowed to sit for over 1 month, the second solution was allowed to sit for c. 20 hours. Neither were stirred.

The final two tables of data for this series of experiments give the mole fraction (table 4.6) of $CaSO_4$ in the evaporated end product calculated to compare the results with Freyer et al. [9]. This is assuming that there is no water left in the system. Table 4.7 gives any small remaining water content of the system as a % error. This is potentially important as many authors have noted that moisture speeds up the conversion of phase III to V [16, 17] but the experimental difficulty of removing water from sodium sulphate should be noted [11, 17]. Kracek [17] writes that "it was found impossible to prepare from solution crystals of Na_2SO_4 which were entirely free from microscopic cavities, including solution. All attempts to remove the water from these cavities below 150 °C were abortive." This implies that at the temperature of this experiment (40 °C), it is almost guaranteed that there will be fluid inclusions in the crystals.

Sample no.	Mole fraction $CaSO_4$ or $CaCO_3$ (samples 1-6)	Mol % $CaSO_4$ $CaCO_3$ (samples 1-6)
1	0.000	0.010
2	0.000	0.010
3	0.000	0.010
4	0.000	0.010
5	0.001	0.051
6	0.000	0.010
7	0.000	0.019
8	0.000	0.016
9	0.000	0.016
10	0.000	0.041
11	0.000	0.048
12	0.000	0.049
13	0.000	0.048
14	0.000	0.047
15	0.000	0.045
16	0.001	0.091
17	0.001	0.089
18	0.001	0.088
19	0.001	0.093
20	0.001	0.092
21	0.001	0.102
22	0.001	0.102
23	0.001	0.102
24	0.001	0.102
25	0.001	0.110
26	0.001	0.111
27	0.001	0.110
28	0.001	0.119
29	0.001	0.129
30	0.002	0.186
31	0.002	0.190
32	0.002	0.203
33	0.004	0.375
34	0.004	0.394

35	0.004	0.402
36	0.004	0.402
37	0.004	0.402
38	0.004	0.403
39	0.006	0.584
40	0.006	0.591
41	0.006	0.589
42	0.006	0.587
43	0.006	0.612
44	0.011	1.118
45	0.012	1.185
46	0.012	1.171
47	0.012	1.192

Table 4.6: The experiment number and corresponding mole fraction and mol % of $CaSO_4$ (or $CaCO_3$ for samples 1-6) in the sample (evaporated to dryness) at the end of the experiment as calculated from the ICP-OES measurement of the Ca content of the solution used for the experiment.

Sample no.	Length of time in the oven in days	Calculated mass	Actual mass	% error
1	6	0.5919	0.5917	-0.03
2	4	0.5975	0.5979	0.07
3	4	0.5801	0.5808	0.12
4	5	0.5966	0.5971	0.08
5	15	0.7789	0.7740	-0.66
6	15	0.7786	0.7676	-1.42
7	5	0.5658	0.5671	0.24
8	7	0.7326	0.7381	0.75
9	5	0.7789	0.7815	0.33
10	5	0.7791	0.7828	0.47
11	2	0.5971	0.5974	0.05
12	2	0.5859	0.5857	-0.02
13	5	0.5992	0.6000	0.13
14	7	0.7337	0.7347	0.13
15	5	0.7811	0.7834	0.30
16	4	0.5645	0.5662	0.30
17	2	0.5880	0.5885	0.09
18	2	0.5976	0.5988	0.20
19	5	0.6048	0.6050	0.02
20	7	0.7337	0.7280	-0.77
21	7	1.2931	1.2912	-0.15
22	7	0.6893	0.6902	0.14
23	7	0.7345	0.7371	0.35
24	7	0.7329	0.7345	0.22
25	5	0.5971	0.5987	0.27
26	1	0.5951	0.5963	0.33
27	1	0.5980	0.5998	0.31
28	5	0.6002	0.6017	0.25
29	7	0.7352	0.7317	-0.48
30	5	0.6007	0.6022	0.24
31	7	0.7382	0.7439	0.78
32	5	0.7813	0.7847	0.44
33	5	0.5772	0.5787	0.26
34	7	0.7405	0.7412	0.09

35	7	0.6911	0.6919	0.12
36	7	1.2944	1.2914	-0.23
37	7	0.7375	0.7394	0.26
38	7	0.7363	0.7390	0.36
39	4	0.5932	0.5963	0.52
40	1	0.6030	0.6054	0.40
41	1	0.6047	0.6064	0.28
42	5	0.6063	0.6082	0.31
43	7	0.7403	0.7479	0.91
44	6	0.5990	0.6026	0.59
45	4	0.6012	0.6043	0.52
46	4	0.6086	0.6116	0.49
47	5	0.5888	0.5916	0.48

Table 4.7: The length of time the sample was in the oven (40 °C) is given in days in column one. Columns two and three are what the mass at dryness is expected to be and what the mass of the sample on leaving the oven is respectively. The percent error is the discrepancy between the expected and actual mass. A negative error means the measured mass is less than the predicted mass. The solution concentration used for calculation of mass at dryness was the ICP-OES measured concentration.

The general trend is that increased calcium concentration leads to a greater % of phase III formation. This is best demonstrated graphically as shown in figure 4.10 against the mol % of $CaSO_4$ in the dried end product.

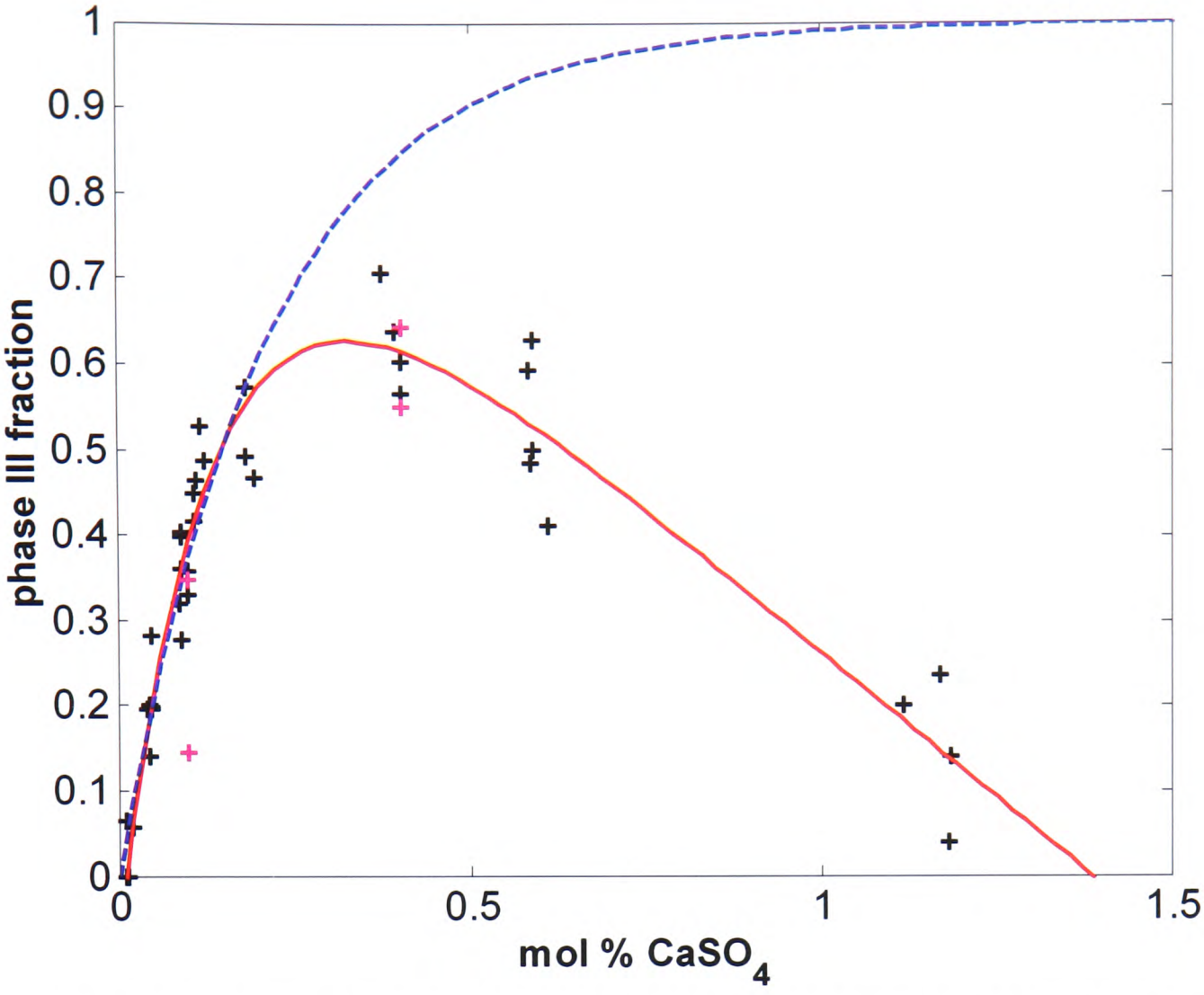

Figure 4.10: The mol % of $CaSO_4$, using the measured Ca concentration of the solution, against the fraction of phase III in the end product. The crosses represent experimental data points, the solid line and dashed line are functions fitted to the data. Black crosses indicate a glass Petri dish was used, magenta crosses indicate a plastic Petri dish was used. Eqs. 4.2 and 4.3 represent the two functions shown. The values for α_1, α_2, α_3 and α_4 are 4.6564, 7.2763, 0.6784 and -0.0590 respectively.

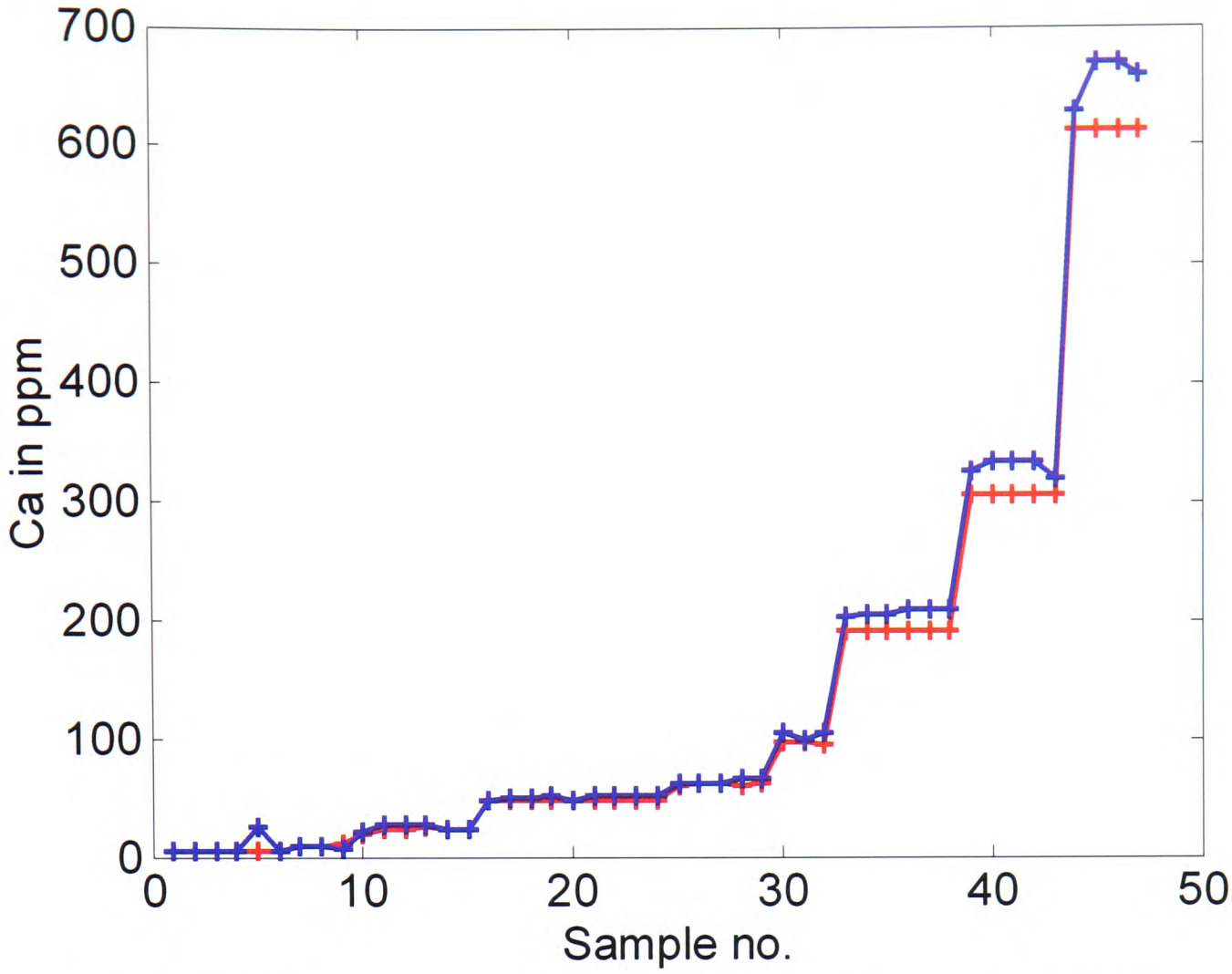

Figure 4.11: ICP-OES measurement of the Ca solution used for samples 1-47. The red plot is the expected Ca concentration (in ppm) of the solution used for crystallisation; the blue plot is the measured Ca concentration of the solution.

It is clear from figure 4.10 that although there is some scatter, the fraction of the sample precipitating as phase III increases according to the function:

$$y = 1 - \exp(-\alpha_1 x) \tag{4.2}$$

Although the data is more generally represented (increasing and decreasing) by:

$$y = 1 - \exp(-\alpha_2 x) - \alpha_3 x + \alpha_4 \tag{4.3}$$

The point of highest % of phase III precipitating corresponds to the highest Ca or $CaSO_4$ concentration used before labile salt precipitation. The downward slope after that represents increasing Ca concentration, but also increasing labile salt precipitation.

Examination of the factors that affect the % of phase III formed begins with the Petri dish as this is the crystallisation substrate and therefore its surface energy characteristics must have some bearing on the result. Samples 21-24 and 35-38, as shown in table 4.4 examine the effect of a plastic dish, with a premixed solution, a glass dish with a premixed solution and one of each dish type with no prior mixing of the solution. There is no obvious difference from pre-mixing the solution, but the plastic substrate can markedly reduce the % of phase III formed if the solution does not completely cover the surface. When the surface is completely covered, the % of phase III produced is comparable with the glass substrate, this is clear from figure 4.10. The black crosses represent experimental data using a glass substrate; the magenta crosses represent the plastic substrate. It is clear that the plastic dish can give similar results to the glass dish providing the surface is fully covered. On the occasions when the surface was not fully covered (i.e. when a larger dish was used) the % of phase III formed is distinctly lower. Under this condition, it is possible that crystals were forced to nucleate on other crystals, which perhaps favoured phase V through the early formation and subsequent growth of V, although this explanation is purely conjecture.

The Ca solution for experiments 1-6 was prepared using $CaCO_3$ by excess. The Ca concentration, assumed from the solubility of calcite at 20 °C, is 4.77 ppm, with this in mind, experiments 5 and 6 were set up to test if the length of time a $CaCO_3$ solution was allowed to sit before filtering off the excess solid affected the resulting Ca concentration of the solution. The ICP-OES results indicate that the Ca concentration is significantly higher for sample 5, which was allowed to equilibrate for 1 month. In contrast the Ca concentration of the sample 6, which was allowed to equilibrate for about 20 hours, is within 0.17 ppm of what would be expected for a saturated solution. The difference in these Ca concentrations is reflected in the results as no phase III is evident in sample 6.

Pairs of samples crystallised together from the same solutions (samples 2-3, 11-12, 17-18, 26-27, 40-41, 45-46) indicate that the scatter in the results is likely to be related to the kinetics of crystallisation rather than any small discrepancies in solution concentration as there is a noticeable difference in the % of phase III formed from pairs of seemingly identical samples.

Freyer [9] notes that in the range $0 < xCaSO_4 \leq 20$ mol % Na_2SO_4 III is produced by the lower amounts of $CaSO_4$ (x = 3 mol %) while Na_2SO_4 I is produced by higher amounts of substitution (x = 5.5 – 20 mol %). Melting the solid salts can result in a sample that is pure phase III or phase I. These metastable phases, although stabilised by cation substitution are subject to changing to more conventionally recognised stable forms. Freyer discovers that over the course of 2 years the sample of phase III produced by x = 3 mol % $CaSO_4$ had altered to contain phase III, I and V (thenardite), whereas samples with a higher mol % of $CaSO_4$ (12.5 – 20 %) altered to thenardite and glauberite completely. Thenardite and glauberite are the stable phases in Freyer's phase diagram for the temperature and mol % range used in these experiments.

In aqueous experiments (this work), comparatively little Ca can be substituted before labile salt precipitates out, effectively capping the amount of Na_2SO_4 III that can form. It is known that labile salt only forms rapidly in the presence of solid thenardite [5] therefore it is hypothesised that Na_2SO_4 (possibly V or III) forms first followed by rapid precipitation of labile salt in the samples with higher Ca concentration.

4.2.3 Cation substitution

Dharmasena et al. [7] find that 0.3 mol % $Y_2(SO_4)_3$ is required to fully form phase III and 3 mol % $Y_2(SO_4)_3$ is required to fully form phase I. The valency of the potentially substituting cation was not considered to be important as a range of cation valencies were chosen from Ca^{2+} to Ce^{4+} all of which substituted, resulting in phase III or I. The ionic radii, according to Dharmasena et al. might be significant as all the metal sulphate salts chosen had a cation radius very close to the value for sodium.

To examine this theory, solutions of the following salts were crystallised with sodium sulphate using the same method as described for Ca solutions: $Al_2(SO_4)_3.18H_2O$, $CuSO_4.5H_2O$, $MgSO_4.7H_2O$, K_2SO_4. Table 4.9 gives the mol % of the salt in the final dried sample. Much less work was done on these other salts as the main focus of the project was on calcium. The little data obtained is presented here as a point of interest rather than a definitive guide. Further work could certainly be

undertaken in this area. Table 4.8 lists the ionic radius value of cations used in this work. As can be seen, cations with a radius incomparable to that of sodium can substitute. This is also known from several literature sources [10, 18, 19].

cation	Ionic radius in Å	Na_2SO_4 III
Na^+	1.02	n/a
Ca^{2+}	0.99	Yes
Al^{3+}	0.535	Yes
Cu^{2+}	0.73	Yes
Mg^{2+}	0.72	No
K^+	1.38	No

Table 4.8: The ionic radius of the metals used in the cation substitution experiments. Column two data from Shriver and Atkins [20]. Column three indicates whether or not phase III was formed from the experiments carried out in this work.

Salt used	Mol % anhydrous salt	cation conc. predicted in ppm	cation conc. actual in ppm	Phase III
$MgSO_4.7H_2O$	0.204	_	_	No
K_2SO_4	0.060	_	_	No
$CuSO_4.5H_2O$	0.065, 0.274	48.35, 192.28	53.7, 203.7	Yes
$Al_2(SO_4)_3.18H_2O$	0.074, 0.299	47.90, 191.78	52.0, 209.5	Yes

Table 4.9: The mol% of $MgSO_4$, K_2SO_4, $CuSO_4$ and $Al_2(SO_4)_3$ in the evaporated end product. The predicted ion concentration (Al and Cu) of the solution used is given in ppm. The actual ion concentration of the solution used is measured using ICP-OES.

The only salts which produced Na_2SO_4 (III) in addition to calcium were $Al_2(SO_4)_3.18H_2O$ and $CuSO_4.5H_2O$, therefore it could be expected that the ionic radius of Al and Cu is comparable to Na, but as is obvious from table 4.8, this is not the case. A paper on the phase equilibria of Na_2SO_4-K_2SO_4 by Eysel [21] indicates that K^+ can substitute into the sodium sulphate lattice to form phase III and I, however this is formation from cooling the melt rather than aqueous solution. Ba^{2+}

and Mg^{2+} can also substitute for Na^+ ions to form Na_2SO_4 (I) [8, 22] although there is no indication whether or not these ions also substitute to form phase III. Dharmasena observed that phase I was never formed without the primary formation of phase III at a lower mol % of the substituting cation [7]. The aqueous experiments reported in this work indicate that K^+ and Mg^{2+} do not substitute for Na^+ to produce phase III under the conditions of these experiments, however the formation of phase III by the substitution of Ba^{2+}, K^+ and Mg^{2+} for Na^+ in aqueous solution cannot be ruled out completely as few experiments were carried out and further work would be useful.

Atomistic computer simulation work (unpublished) was carried out by T. G. Cooper and N. H. de Leeuw, University College London, with the aim of investigating the hydrous and anhydrous stabilities and morphologies of the two stable forms of Na_2SO_4 (V and III) at ambient temperatures. A mixture of computer codes was used to derive a theoretical and potential model, modelling through energy minimisation, the bulk, surfaces and hydrated surfaces of Na_2SO_4 III and V. A general description of atomistic modeling techniques can be found in [23], with a description of the code (METADISE) [24] and general method used to model the surfaces. A general description of the modelling procedure for hydrated surfaces using DL_POLY 2.9 [25] computer code can be found in [26] and general procedure for modelling the bulk using PARAPOCS [27] and GULP [28] code from [29]. Defect ions, K^+, Mg^{2+} and Ca^{2+} were substituted into the bulk and onto the surfaces of the two phases to determine which phase was present under different conditions. They discovered that the substitution of surface Na^+ with Ca^{2+} in aqueous solution is more favourable overall for phase III than V and therefore concluded that Ca^{2+} defects are more likely in phase III than V. Substitution of Mg^{2+} on the surface was found to be unfavourable for either phase, due to the small size of the ion not fitting well in the cation sites on the surfaces. The significantly larger K^+ ion was found to be energetically favourable for both phases, but more likely to occupy the larger cation channels of phase III than V. It was found, through estimation of the segregation energies that absorption of defects at the surface are generally likely to stay at the surface (with the exception of a few crystal faces) and not segregate into the bulk of the crystal. Comparing the theoretical simulation with the experimental work presented here, there is a close match for Ca^{2+}, which does stabilise phase III, a

reasonable match for Mg^{2+}, which does not stabilise phase III and a mismatch for K^+ which also did not stabilise phase III. It should be noted though, that the calculated percentage of cation defects in the modeling work of Cooper and de Leeuw is 25 %, which is much higher than the amounts of defect cations used experimentally. It is also true that further experimental work could be done to examine if any defect cations are present in phase V, since it is assumed that the defect cations sit in phase III when present.

The conductivity of Na_2SO_4 (I) solid solutions is well documented and strongly correlated with the vacancy concentrations, which are introduced when aliovalent cations substitute for Na^+ in Na_2SO_4 [22]. The formula can be represented as:

$$2Na^+ = 1M^{2+} + 1\square \qquad \textbf{(4.4)}$$
$$3Na^+ = 1M^{3+} + 2\square$$

Where M is an aliovalent cation and □ is a vacancy. The corresponding formula of the solid solution is [22]:

$$Na_{2-2x}M_x^{2+}\square_xSO_4 \qquad \textbf{(4.5)}$$
$$Na_{2-3x}M_x^{3+}\square_{2x}SO_4$$

Eysel et al. noted that with increasing amounts of M^{2+} and M^{3+} ions, the peaks of the powder diffraction pattern became broader, showing greater structural disorder [8]. The experiments here have comparatively little cation substitution, and as is obvious from figures 4.12 and 4.13, the peaks are relatively sharp and match the JCPDS card peak positions well, with no obvious peak broadening.

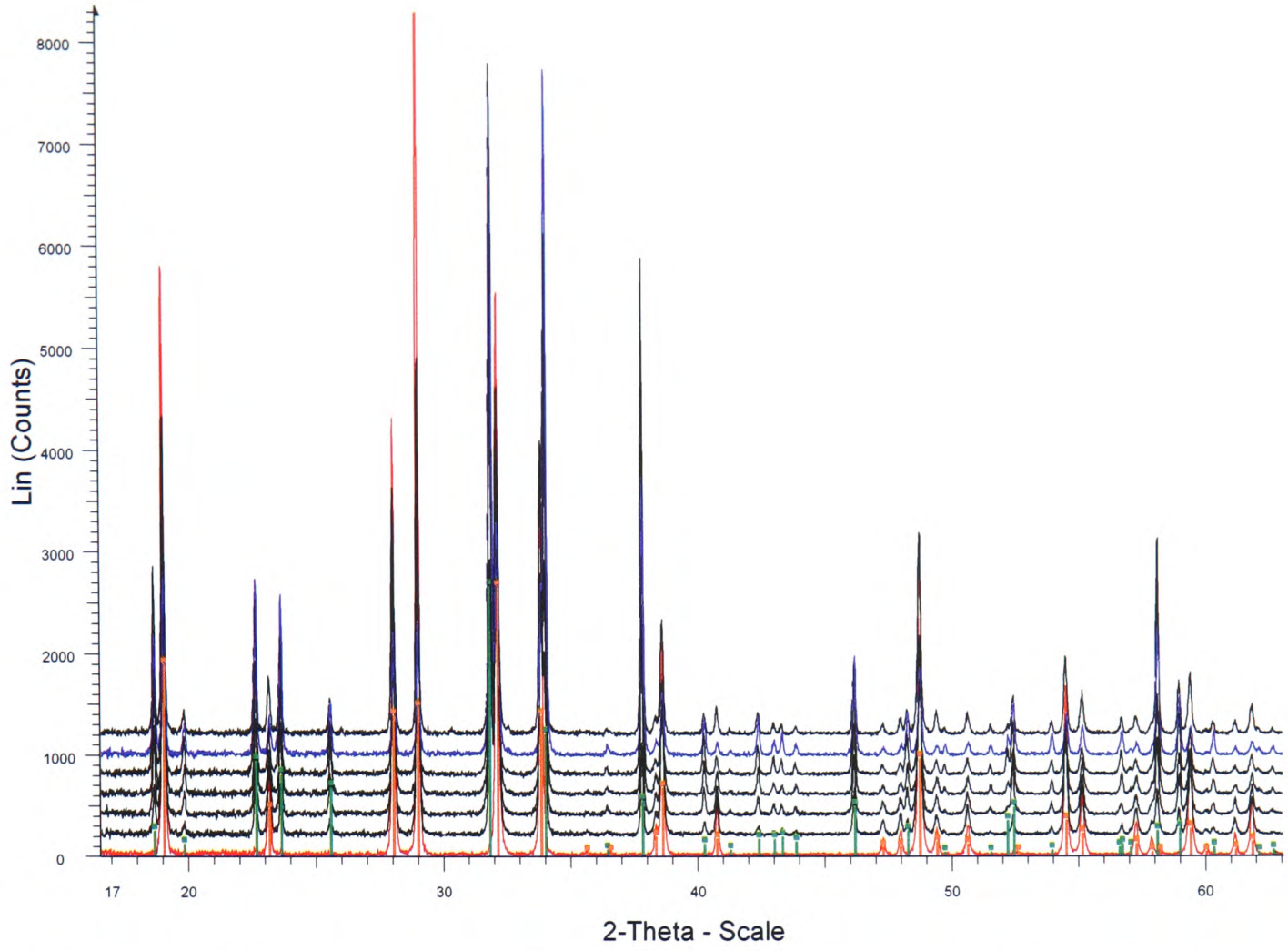

Figure 4.12: Samples 8, 14, 20, 29, 31, 34 and 43 in order of increasing $CaSO_4$ mol %. There is some change in the width of the peaks; however the marked difference between the first scan of lowest Ca concentration (red) and the scan of second highest Ca concentration (blue) is the increase in the % of phase III and the decrease in the % of phase V. Phase V (thenardite) peaks are indicated in orange (card no. 037-1465) and phase III peaks are indicated in green (card no. 024-1132).

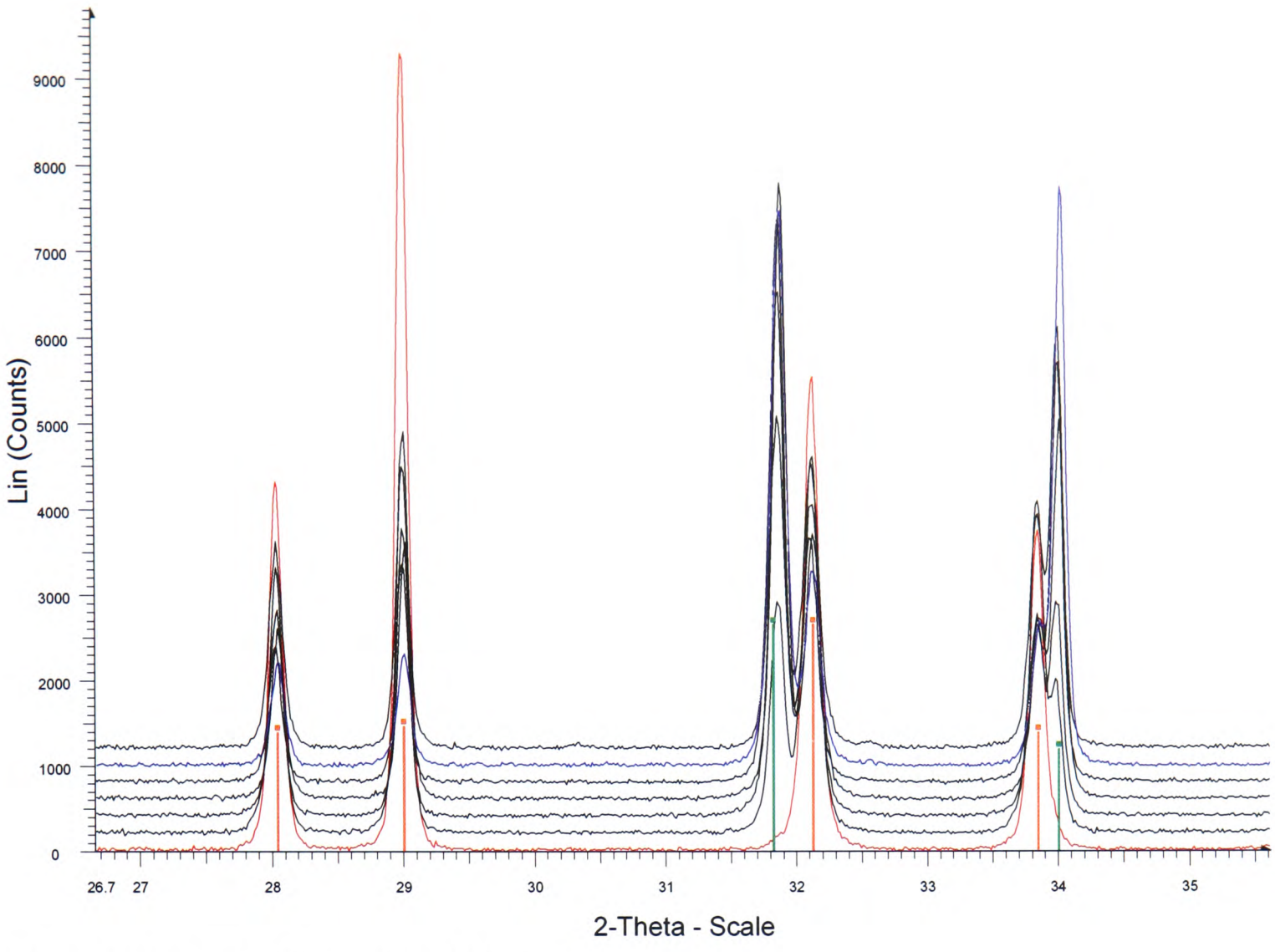

Figure 4.13: a magnified section of figure 4.12.

As can be seen from figure 4.12, the peak height for phase V is much stronger in the first scan (red) of lowest $CaSO_4$ mol %, whereas phase V (orange lines, card no. 037-1465) is weaker and III (green lines, card no. 024-1132) is stronger in the blue plot of second highest $CaSO_4$ mol % before the onset of labile salt precipitation. There is possibly some slight broadening of the peaks of phase III, but nothing very obvious.

4.2.4 Conclusions

Many literature sources highlight the substitution of various metal cations into the sodium sulphate lattice thus stabilising the higher temperature phases down to room temperature [7-10, 21, 22]. Stabilised phase I is the phase of most interest to many due to the higher ionic conductivity introduced by vacancies in the lattice as a result of cation substitution [22]. The purpose of these experiments was to examine phase III, which although metastable at room temperature [11], has been known to form at

temperatures slightly above room temperature (313-343 K) and remain stable indefinitely in dry air [14] without cation substitution. In contrast, phase I cannot be quenched to room temperature as it transforms on cooling to the more ordered phase II and III, without cation substitution [10].

Phase III, can also be stabilised effectively to room temperature by a lesser amount of cation substitution than is required to transform a sample completely into phase I [7, 9]. Almost all of the literature data is on samples formed from quenching the melt, whereas the data reported here is produced from samples formed by evaporation of an aqueous solution at 40 °C. Only relatively small amounts of calcium can be substituted to form phase III before the formation of a double salt (labile salt) takes place. It was also impossible to form a sample completely in phase III without precipitating phase V also.

Other cations were also investigated; aluminium and copper II produced a comparable result, while potassium and magnesium did not appear to substitute. Eysel et al. and Höfer et al. [8, 22] note that magnesium and potassium both substitute into the phase I lattice. However there is no guarantee that a cation which stabilises the disordered phase I from a melt, will stabilise the more highly ordered phase III from aqueous solution. Theoretical simulations by Cooper and de Leeuw on the substitution of cation defects onto the surface of Na_2SO_4 indicates that Ca^{2+} is likely to substitute onto the surface of phase III (in preference to V), that Mg^{2+} substitution is not favourable for either phase and that K^+ can substitute into the surface of either, with a preference for phase III.

Dharmasena et al. [7] point out the ionic radii of the substituting cations used in their investigation are very close to the ionic radius of sodium. However, the results presented here and elsewhere [8, 9, 21, 22] show that many ions, exhibiting a wide range of ionic radius values, substitute. While the size of the ion has some relevance, whether an ion can substitute requires computation of the energetics of the process to ascertain whether or not it is energetically favourable for an ion to substitute. Similar calculations on the incorporation of Al^{3+} and Cu^{2+} defects would be very interesting as Cu^{2+} and Mg^{2+} have very similar ionic radius values, yet one encourages the formation of phase III (experimentally) while the other does not and Al^{3+} has a significantly smaller ionic radius than Cu^{2+} or Mg^{2+}.

4.3 References

1. Barnes, P., S.L. Colston, A.C. Jupe, S.D.M. Jacques, M. Attfield, R. Pisula, S. Morgan, C. Hall, P. Livesey, and S. Lunt, *Structure and Performance of Cements*, ed. J. Bensted and P. Barnes. 2002, London and New York: Spon Press.

2. Vergouwen, L., *Eugsterite - a new salt mineral.* American Mineralogist, 1981. **66**: p. 632-636.

3. Whittaker, A.G., A.R. Mount, and M.R. Heal, *Physical Chemistry*. Instant notes, ed. B.D. Hames. 2000, Oxford: BIOS Scientific Publishers, Ltd.

4. Findley, A., *The phase rule and its applications*. 1951, New York: Dover Publications.

5. Hill, A.E. and J.H. Wills, *Ternary systems. XXIV. Calcium sulfate, sodium sulfate and water.* Journal of the American Chemical Society, 1938. **60**: p. 1647-1655.

6. Plummer, L.N., D.L. Parkhurst, G.W. Fleming, and S.A. Dunkle, *A computer program for incorporating Pitzer's equations for calculation of geochemical reactions in brines*. 1988, USGS: Reston, Virginia.

7. Dharmasena, G. and R. Frech, *The stabilization of phase III and phase I in sodium sulfate by aliovalent cation substitution.* Journal of Chemical Physics, 1993. **99**(11): p. 8929-8935.

8. Eysel, W., H.H. Hofer, K.L. Keester, and T. Hahn, *Crystal chemistry and structure of Na_2SO_4 (I) and its solid solutions.* Acta Crystallographica, 1985. **B41**: p. 5-11.

9. Freyer, D., W. Voigt, and K. Kohnke, *The phase diagram of the system Na_2SO_4-$CaSO_4$.* European Journal of Solid State Inorganic Chemistry, 1998. **35**(10-11): p. 595-606.

10. Armbruster, T., R. Basler, P. Mikhail, and J. Hulliger, *Defect structure of ytterbium(III) doped Na_2SO_4 phase I.* Journal of Solid State Chemistry, 1999. **145**: p. 309-316.

11. Brodale, G.E. and W.F. Giauque, *The relationship of crystalline forms I, III, IV and V of anhydrous sodium sulfate as determined by the third law of thermodynamics.* Journal of Physical Chemistry, 1972. **76**(5): p. 737-743.

12. Naruse, H., K. Tanaka, H. Morikawa, F. Marumo, and B.N. Mehrotra, *Structure of Na_2SO_4 (I) at 693 K.* Acta Crystallographica, 1987. **B43**: p. 143-146.

13. Rasmussen, S.E., J.E. Jorgensen, and B. Lundtoft, *Structures and phase transitions of Na_2SO_4.* Journal of Applied Crystallography, 1996. **29**: p. 42-47.

14. Amirthalingam, V., M.D. Karkhanavala, and U.R.K. Rao, *Topotaxic phase change in Na_2SO_4.* Acta Crystallographica, 1977. **A33**: p. 522.

15. Linke, W.F., *Solubilities of Inorganic and Metal Organic Compounds*. 4th ed. Vol. 2. 1965: American Chemical Society.

16. Freyer, D., W. Voigt, and K. Köhnke, *The phase diagram of the system Na_2SO_4-$CaSO_4$.* European Journal of Solid State Inorganic Chemistry, 1998. **35**(10-11): p. 595-606.

17. Kracek, F.C. and R.E. Gibson, *The polymorphism of sodium sulfate: III. Dilatometer investigations.* Journal of the American Chemical Society, 1930. **34**: p. 188 - 206.

18. Eysel, W., H.H. Höfer, K.L. Keester, and T. Hahn, *Crystal chemistry and structure of Na_2SO_4 (I) and its solid solutions.* Acta Crystallographica, 1985. **B41**: p. 5-11.

19. Singhvi, A., S. Gomathy, P. Gopalan, and A.R. Kulkarni, *Effect of aliovalent cation doping on the electrical conductivity of Na_2SO_4: Role of charge and size of the dopant.* Journal of Solid State Chemistry, 1998. **138**: p. 183-192.

20. Shriver, D.F. and P.W. Atkins, *Inorganic Chemistry*. 3rd ed. 1999, Oxford: Oxford University Press.

21. Eysel, W., *Crystal chemistry of the system Na_2SO_4-K_2SO_4-K_2CrO_4-Na_2CrO_4 and of the glaserite phase.* American Mineralogist, 1973. **58**: p. 736-747.

22. Hofer, H.H. and W. Eysel, *Electrochemistry of Na_2SO_4 (I) solid solutions with aliovalent cation substitution.* Journal of Solid State Chemistry, 1981. **36**: p. 365-370.

23. Titiloye, J.O., N.H. de Leeuw, and S.C. Parker, *Atmostic simulation of the differences between calcite and dolomite.* Geochimica et Cosmochimica Acta, 1998. **62**(15): p. 2637-3641.

24. Watson, G.W., K.E. Toby, N.H. de Leeuw, D.J. Harris, and S.C. Parker, *Atomistic simulation of dislocations, surfaces and interfaces in MgO.* Journal of the Chemical Society Faraday Transactions, 1996. **92**(3): p. 433-438.

25. Forester, T.R. and W. Smith, *DL_POLY user manual*, in *CCLRC, Daresbury Laboratory, UK*. 1995: CCLRC, Daresbury Laboratory, Warrington, UK.

26. de Leeuw, N.H., *Molecular dynamics simulations of the growth inhibiting effect of Fe^{2+}, Mg^{2+}, Cd^{2+} and Sr^{2+} on calcite crystal growth.* Journal of Physical Chemistry B, 2002. **106**: p. 5241-5249.

27. Parker, S.C. and G.D. Price, *Computer modelling of phase transitions in minerals.* Advances in Solid State Chemistry, 1989. **1**: p. 295-327.

28. Gale, J.D., *GULP: a computer program for the symmetry-adapted simulation of solids.* Journal of the Chemical Society Faraday Transactions, 1997. **93**(4): p. 629-637.

29. Rabone, J.A.L. and N.H. de Leeuw, *Interatomic potential models for natural apatite crystals: Incorporating Strontium and the Lanthanides.* Journal of Computational Chemistry, 2006. **27**(2): p. 253-266.

5. Introduction

The purpose of this chapter is to examine a case of real world stone decay for evidence of salt damage. Skara Brae is a Neolithic settlement located on the western shore of the Island of Orkney, off the Northern tip of Scotland. It is a collection of huts, connected by a series of low alleyways as shown in figure 5.1. Originally unearthed by a storm in 1850, it has been subject to excavation until final excavations took place in the early 1930's. One of the 'Houses' in particular, House 7 (figure 5.2), is showing signs of severe stone decay. After excavation, it was found to be in poor condition as reports from 1929 state that the original stone fittings were uncovered from 'saturated sand merging into the red clay of the floor', a 'shiny mass having much the same consistency of a blanc mange'. The same author remarks in 1930 'I feel strongly that in the interests of posterity a hideous roof ought to be erected over hut 7', 'so many important stones are of this terribly friable rock that prolonged exposure will certainly undermine the structure.' [1]

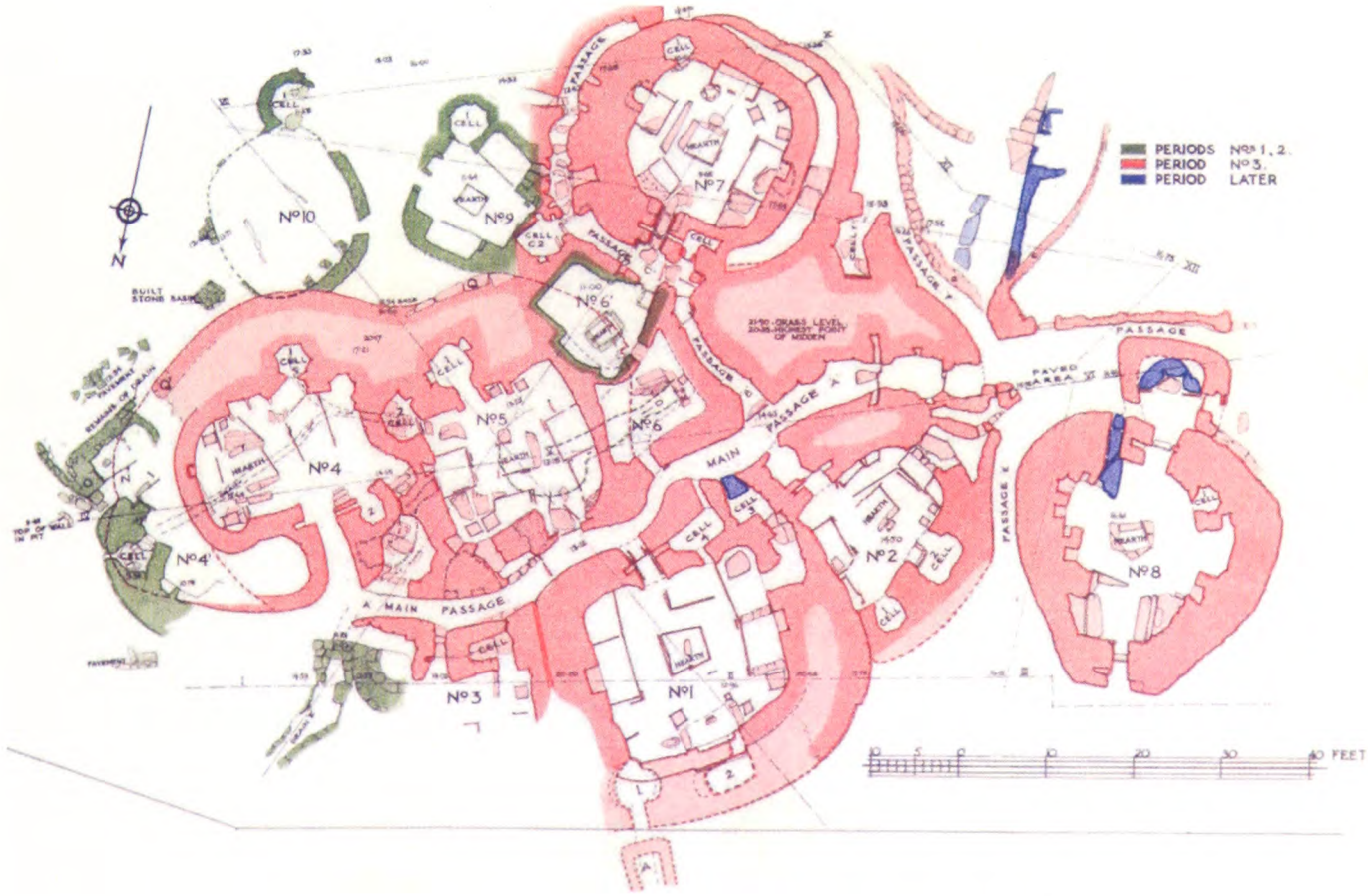

Figure 5.1: Map of the Skara Brae settlement from 1930 [2]. Provided by Historic Scotland, private communication from L. Fleming.

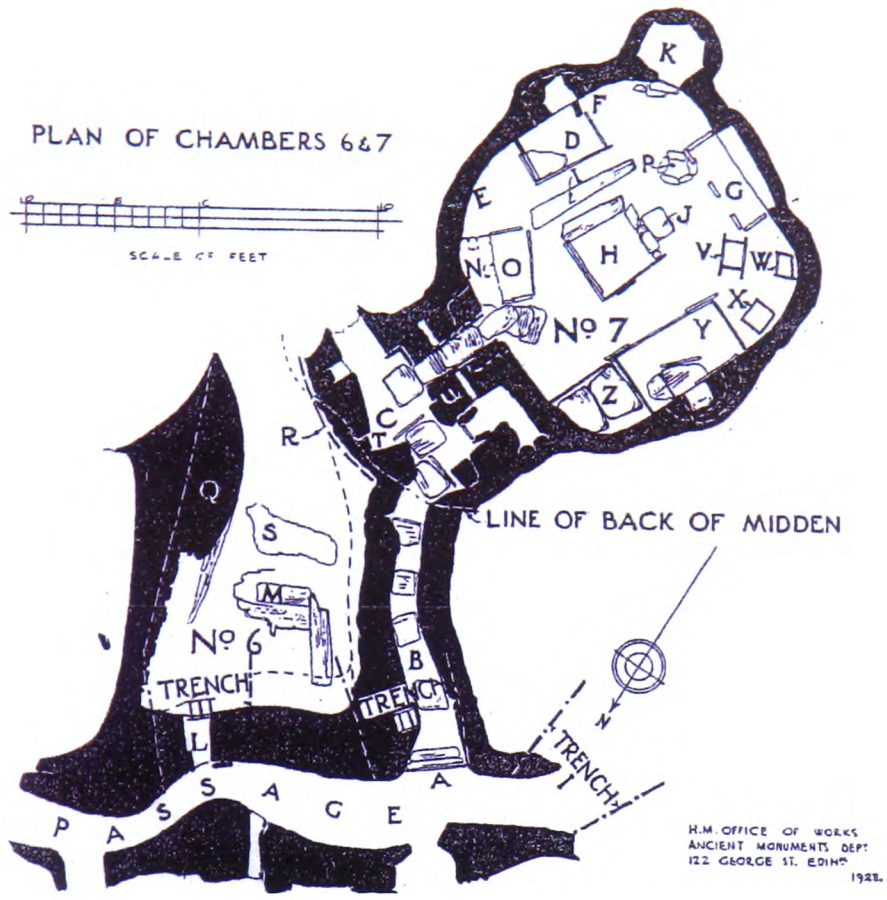

Plan of Chambers Nos. 6 and 7 at Skara Brae.

Figure 5.2: Plan of house 6 and 7 from 1928 provided by Historic Scotland.

Figure 5.3: A photograph of the roof over house 7, taken in August 2004.

House 7 exhibits the most dramatic levels of decay. This study originated to examine House 7 for signs of salt decay as bands of efflorescence had been reported during routine site visits by Historic Scotland and surface scaling is extreme in places.

The purpose of this study therefore was to shed some light on the possible mechanisms of this decay, concentrating on salt analysis. In order to do this, two main routes were taken: Analysis of samples from inside the House with analysis and further testing of background rock samples chosen by Ewan K. Hyslop [3]. The methodology used can be described in stages:

1. Collection of samples from the site itself: These are fallen fragments from inside the house, salt and surface brushings (from stones which had a powdery residue on the surface – brushed from the surface to test for salts), sand from the thin layer (placed there by Historic Scotland) covering the 'floor' of the House, soil samples from directly beneath the sand layer and water collection samples from the damp area of the house (as described in figure 5.7)
2. Collection of background samples. These are large rock samples, similar to the stone types found in House 7 for further testing requiring large samples.
3. Powder X-ray analysis and thin section analysis to identify the stone types present. ICP-OES and IC analysis to examine and quantify the soluble salts present.
4. Water transport testing, including novel use of modelling package HYDRUS 2D to examine the water transport characteristics of the monuments and to estimate (quantitively) the soluble salts potentially deposited by the water flux through the stone types.
5. Swelling/contraction analysis, carried out by G. W. Scherer's research group at Princeton University, USA to estimate if this mechanism is a potential source of damage.

Two excursions were made to House 7 to collect samples and examine the site, one in the spring (March 2004) and the second in the late summer

(August/September 2004). Figure 5.4 shown below is a schematic diagram of House 7 (not to scale).

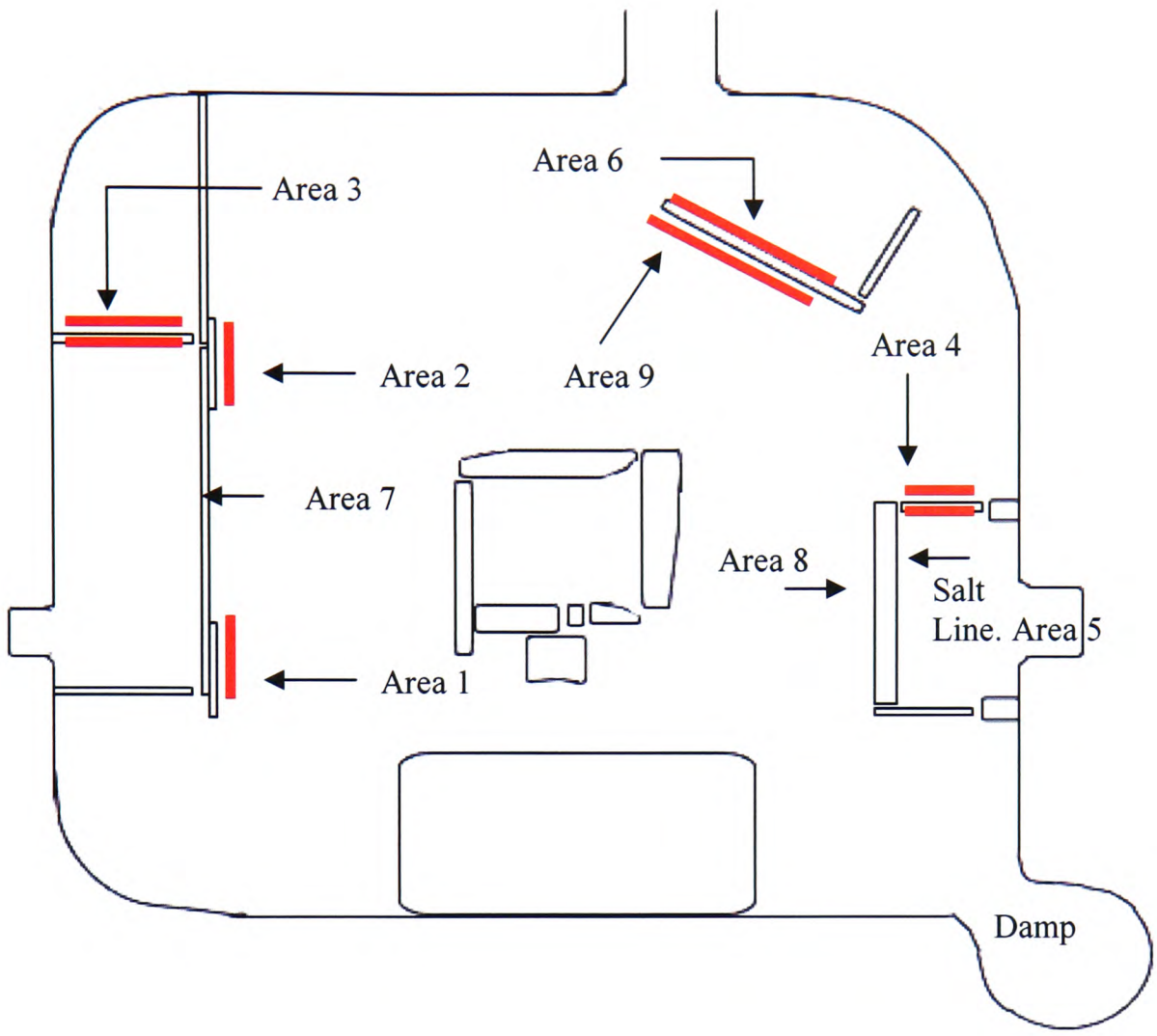

Figure 5.4: Sketch diagram of House 7 (not to scale). The red lines indicate the more dramatic areas of decay. The small "cave" on the southeast corner appears to be very damp with water visibly dripping down the walls. The approximate dimensions of House 7 are 17 feet (left to right) by 16.5 feet (top to bottom).

Figure 5.5: One of the worst areas of decay, showing the top of the slabs weathered to a thin sharp point. Photograph taken during the March (2004) visit. This is also the area where the data logger for the house is located. Stone slab in centre of image is approximately 71 cm tall, 24 cm wide and 2.5 cm thick tapering off towards the top. Area 3.

Figure 5.6: Another area showing dramatic decay. Photograph taken during the March (2004) visit. Stone slab is approximately 57 cm high, 52 cm wide and 3.5 cm thick. Area 4.

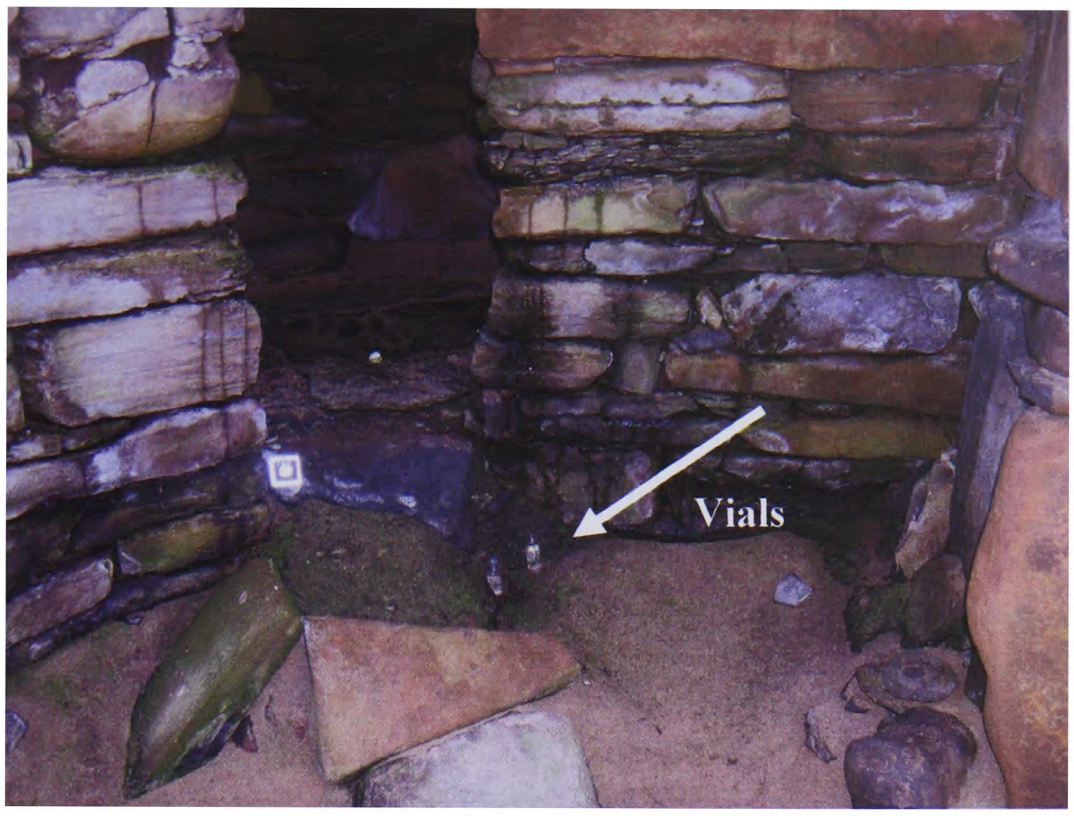

Figure 5.7: The damp area of House 7. Collection vials were set up overnight to collect a sample of the water filtering through the walls. Photograph taken in March 2004.

Figure 5.8: Salt lines on the same stone as figure 5.6, but taken in Aug/Sept 2004. Small corner image is a higher magnification view of the salt. Scale indicated in caption for figure 5.6.

5.1 X-ray powder diffraction analysis

The samples analysed using XRD are fallen stone flakes only. These were ground and packed for powder diffraction analysis. Semi-quantitative analysis was achieved using TOPAS, a commercially available X-ray analysis package from Bruker. The

main constituents are quartz, feldspar, carbonate (dolomite/ankerite and calcite), mica (muscovite) and in a few samples, halite. The average amounts of these minerals (averaged over all samples taken) is:

Sample	Quartz	Feldspar	Mica	Carbonate	Halite	Gypsum
Area 1	38	41	17	2	2	
Area 2	18	26	26	30		
Area 3	24	28	23	25		
Area 4	22	26	21	31		
Area 5	13					87
Area 6	29	30	17	24		
Area 7	32	33	15	20		
Area 9	31	35	21	11	2	
Average	26	31	21	21	1	
Stdev.	8	5	4	11	1	
Range	24	16	12	31	3	

Table 5.1: The average amount (weight %) of minerals present in stone flake samples collected during March 2004 visit calculated from X-ray data. TOPAS was used to give a semi-quantitative representation of the relative amounts of each mineral constituent in the sample. These values are approximate only and are not absolute values. The average for halite is taken over all samples rather than purely the 4 samples (out of 16) which were identified as containing halite. The sample from area 5 is a salt brushing rather than a stone flake. The value for gypsum is not averaged as it was only found in one sample. Grey boxes indicate the mineral was not detected. Carbonate comprises calcite and dolomite/ankerite.

Area	Quartz	Feldspar	Mica	Carbonate	Halite	Gypsum	Chlorite	Sample type
1	34	41	19	4	2			spall
3	14	32	21	32	1			spall
3	28	36	17	19				spall and residue
3	10	18		16		56		salt brushing
4	10	11	7	6		66		salt brushing
4	22	27	17	33	1			spall
4	21	28	15	35	1			powder residue
4	24	30	17	28	1			powder residue
4	24	30	14	31	1			spall and residue
5	15	15				70		salt brushing
5	16	12	8		2	62		salt brushing
7	27	33	12	15	1		12	spall
9	18	20		3	6	53		salt brushing
9	10	15		7	3	65		salt brushing

Table 5.2: Average mineral content (weight %) for samples from August/September 2004 visit calculated from x-ray data. TOPAS was used for semi-quantitative analysis and should be viewed as approximate only. A mixture of spall, salt brushings and surface residue brushings were taken. No averages are given due to the variation in sample type, causing an average value to be less meaningful. It should be noted that the presence of halite in small quantities is difficult to be certain of, therefore values under 2 % should be viewed with some caution.

The consistently high feldspar content could be considered odd, however, there is a potential source of feldspar in the form of granite (foliated granite of the Moine supergroup) 4 km away from the Bay of Skaill. This could account for the high level of feldspar found in these samples and is discussed further in the 'background rocks' section. Mainly though, these spall fragments are weathered and as such their composition cannot be taken as being the same as the source rock, as grains could be shed in the weathering process.

The largest deviation is clearly in the carbonate. It was noted that some samples had very little carbonate (1-3 %) whereas others had 20-30 % carbonate. Further testing (thin section, ICP-OES) was used to investigate this. Some samples taken contained halite. This is not surprising, given the coastal location of the site, but the only visible salt efflorescence line found in March (as indicated on figure 5.4) was identified through XRD as gypsum. Many more salt lines were found during the summer visit, which also analysed as gypsum. Environmental conditions (temperature and RH) are important in understanding salt crystallisation and which phases are able to crystallise.

Tables 5.3, 5.4 and 5.5 contain the temperature and RH data from Houses 1 and 7. The average, maximum, minimum and range are calculated from the raw data, which was sampled every 40 minutes. RH, air temperature and surface temperature are shown and it is clear that the range of values in House 1 (in all three tables) is almost always higher than House 7, especially during the summer months. It can be concluded (based on the data available) that the roof keeps the air temperature and relative humidity at more constant levels than uncovered House 1 with the damp corner and roof in House 7 keeping the RH high, which is reflected in the minimum RH value (House 7) as this is often significantly higher than House 1, especially during the summer months. The maximum temperature value (air) for House 1 is noticeably higher than the maximum air temperature of House 7 during the summer months (May – August), which would appear to not be the case for the minimum air temperature, as House 7 is on average 2.8 °C higher than House 1, with no obvious seasonal dependence. The average air temperature values are similar for Houses 1 and 7, with 7 being on average a little (~2 °C) warmer in the summer. Interestingly the range of values for the surface temperature in House 7 seems to match House 1

more closely than for air temperature or RH. Also, on average, the surface temperature in House 7 is a little higher than House 1. The general conclusions to be drawn from this analysis is that the air temperature and surface temperature are on average, a little higher in House 7 than House 1 (by ~ 1-2 °C), that the roof seems to keep the range of values (air temperature and RH) lower for House 7 than House 1 and that the damp corner (and water ingress) is probably responsible for the higher minimum RH of House 7. The average RH of House 1 is higher than House 7 for many of the months sampled (April 2003 to November 2003) but the minimum RH for House 7 is significantly higher during the summer, which is important in terms of keeping salts in solution. Analysis of this data set is based on the information presented (monthly averages, maximum, minimum and range), further information in the form of the raw data (data points sampled every 40 minutes) would allow standard deviations to be calculated which would enable better analysis on the effect the roof has on the RH and temperature inside the Houses. While the range indicates the maximum and minimum values, it does not indicate how frequent the upper or lower values are.

The minimum RH value of House 7 is noticeably high and would probably keep halite in solution during the winter as the ERH (equilibrium relative humidity) of NaCl is 75 %. Of course this is the ERH of a single salt, whereas mixed salts are known to behave differently. Price [4] discusses experimental RHXRD measurements as part of his report on the theoretical prediction of ERH for mixed salts notes that the successive crystallisation of salt minerals that would be expected from equilibrium thermodynamics was not observed. Instead the minerals crystallised at very low RH values and mostly together. It should be noted that the experimental results in the report are for the system Na-K-Mg-NO_3-SO_4-H_2O which does not contain Cl or Ca but it is reasonable to assume that halite is unlikely to precipitate on the surface as efflorescence at RH values greater than 75 % [4], this is what is largely observed. Testing with RUNSALT [5] is discussed in the next section. The noted efflorescing material is gypsum. During the summer visit there were obvious salt lines on many of the stones a few centimetres from the ground as shown in figure 5.5. Again, these were gypsum with minor halite and were brushed from areas 5, 8, 9 and 3. Often the stone surface has a powdery residue. Some of this

was brushed off and analysed as having a similar composition to that of the rock with a small amount of halite, typically 1-2 wt % (note that small amounts are unlikely to be very accurately estimated by TOPAS).

Month	House 1 avg	House 1 min.	House 1 max.	House 1 range	House 7 avg.	House 7 min.	House 7 max.	House 7 range
Nov-02	91.6	73.0	97.5	24.5	94.1	84.0	97.5	13.5
Dec-02	91.0	74.0	97.0	23.0	93.6	85.0	97.0	12.0
Jan-03	89.1	68.0	97.5	29.5	94.8	84.0	98.0	14.0
Feb-03	89.2	73.5	96.5	23.0	93.4	87.5	97.5	10.0
Mar-03	87.8	63.5	96.5	33.0	88.0	69.0	96.0	27.0
Apr-03	82.8	49.5	96.0	46.5	78.4	61.0	88.5	27.5
May-03	82.9	31.5	96.5	65.0	76.0	55.5	91.0	35.5
Jun-03	82.9	28.5	96.0	67.5	76.1	58.5	87.0	28.5
Jul-03	82.4	23.5	95.0	71.5	76.4	54.0	88.5	34.5
Aug-03	82.5	37.0	96.0	59.0	76.5	58.5	88.0	32.5
Sep-03	84.9	63.0	95.5	32.5	77.9	56.5	91.0	34.5
Oct-03	84.4	62.5	95.5	33.0	82.5	65.0	92.0	27.0
Nov-03	93.4	62.0	97.5	35.5	90.5	76.5	95.5	19.0
Dec-03	89.1	66.5	97.5	31.0	92.4	79.5	96.5	17.0
Jan-04	91.4	72.0	97.5	25.5	95.1	86.0	97.5	11.5
Feb-04	88.2	69.5	97.5	28.0	92.8	80.0	97.5	17.5
Mar-04	89.0	74.0	96.0	22.0	89.3	80.0	95.0	15.0

Table 5.3: RH maximum, minimum, average and range from House 7 and House 1

Month	House 1 avg.	House 1 min.	House 1 max.	House 1 range	House 7 avg.	House 7 min.	House 7 max.	House 7 range
Nov-02	7.0	0.2	10.6	10.4	7.3	3.3	9.7	6.4
Dec-02	5.1	-0.2	8.8	9.0	5.9	2.7	8.1	5.4
Jan-03	4.7	-3.0	10.0	12.9	4.5	0.2	7.4	7.2
Feb-03	4.4	-0.5	8.0	8.6	4.7	2.3	7.7	5.4
Mar-03	6.5	1.1	11.3	10.3	7.7	3.8	12.5	8.7
Apr-03	9.4	3.5	19.8	16.3	11.3	6.6	16.9	10.3
May-03	10.2	3.7	25.4	21.7	12.5	6.6	18.9	12.3
Jun-03	14.2	10.0	31.1	21.1	16.4	13.2	23.9	10.7
Jul-03	16.1	11.0	35.6	24.7	18.1	13.3	26.2	12.9
Aug-03	15.6	10.9	32.3	21.4	18.0	13.7	24.7	10.9
Sep-03	12.6	7.1	18.3	11.2	14.9	10.2	20.1	10.1
Oct-03	8.0	1.5	13.0	11.5	9.5	4.7	14.6	9.9
Nov-03	6.6	0.0	11.5	11.4	7.6	3.3	10.2	6.8
Dec-03	5.3	-3.3	10.2	13.5	5.3	-0.4	8.1	8.5
Jan-04	4.4	-0.4	8.2	8.6	4.4	1.1	6.3	5.2
Feb-04	5.0	-0.2	10.0	10.2	4.9	1.8	7.3	5.5
Mar-04	5.3	1.6	10.2	8.6	6.1	4.0	10.1	6.1

Table 5.4: Air temperature data for Houses 1 and 7, in °C. All RH and temperature data was provided by Historic Scotland from dataloggers set up on site.

Month	House 1 avg.	House 1 min.	House 1 max.	House 1 range	House 7 avg.	House 7 min.	House 7 max.	House 7 range
Nov-02	6.7	-1.4	10.8	12.2	7.3	3.1	11.1	8.0
Dec-02	4.8	-0.2	8.8	9.0	5.8	2.3	8.5	6.2
Jan-03	4.4	-3.0	10.0	13.0	4.6	-0.1	8.4	8.5
Feb-03	4.2	-0.5	8.0	8.5	5.0	2.3	12.2	9.9
Mar-03	7.0	1.1	22.6	21.5	9.2	4.8	26.1	21.3
Apr-03	10.4	2.2	25.7	23.5	11.3	6.6	31.0	24.4
May-03	11.5	2.9	33.0	30.1	14.8	6.8	36.0	29.2
Jun-03	15.3	8.8	35.8	27.0	18.8	13.9	40.7	26.8
Jul-03	17.4	9.8	40.1	30.3	20.3	14.0	42.5	28.5
Aug-03	16.6	9.8	36.5	26.7	20.0	14.0	39.6	25.6
Sep-03	13.5	6.2	31.3	25.1	16.4	10.1	33.9	23.8
Oct-03	8.0	-0.3	14.6	14.9	10.1	4.9	24.6	19.7
Nov-03	6.7	0.0	11.5	11.5	7.8	3.5	11.3	7.8
Dec-03	4.9	-5.4	10.2	15.6	5.4	0.1	8.7	8.6
Jan-04	4.1	-1.0	8.4	9.4	4.5	0.8	7.0	6.2
Feb-04	5.0	-0.5	10.5	11.0	5.3	1.6	9.4	7.8
Mar-04	5.3	0.7	14.9	14.2	7.3	4.2	23.6	19.4

Table 5.5: surface temperature maximum, minimum, average and range from House 7 and House 1. The datalogger was located in area 3.

5.2 Soluble salt analysis

Samples were leached in de-ionised water as they were found or in some cases for comparison they were dried to constant mass first in an air oven before being leached in deionised water. The resulting aqueous phase was analysed using ICP-OES (Induction Coupled Plasma Optical Emission Spectroscopy) and IC (Ion Chromatography) much of the ICP-OES and IC work was carried out by Dr Peter Anderson, School of Chemistry, with some samples analysed by the author.

In addition to the spall fragments; soil, sand and water samples were analysed. These soil and sand samples were dried and then leached in a similar manner to the spall fragments. On both visits water was collected from the damp area labelled in figure 5.4. Vials were set up as shown in figure 5.7 to catch the run off. Salt brushings were identified using XRD and therefore secondary analysis was unnecessary. The ICP-OES and IC data sets were analysed in three distinct ways to produce the results shown below:

- The percentage of salt in each sample. This can be taken as a guide to the salt content of the area the sample came from. Note that as only a limited number of samples were taken and analysed, this cannot be treated as absolute. This was determined using the total ion count from the aqueous analysis rather than traditional analysis of total dissolved solids, which involves evaporating the aqueous solution to constant mass. For the sake of greatest accuracy, a gravimetric analysis of total dissolved solids would be beneficial for confirmation.

- The percentage of each ion making up the total ionic composition of each water sample analysed. The ICP-OES and IC results are given in ppm (mg/l) for each ion, these values were summed and the value for every ion analysed as being present was divided by the total sum (total ion count), this is then expressed as a percentage. The result was matched against seawater to investigate if seawater was the dominant source of the species in solution or not. It should be noted though that the absolute concentration of ions in solution in ppm is considerably lower than pure seawater (3.5 % salinity)

- A correlation matrix was used to correlate the ions in solution from each sample to investigate the relationship between the species in solution.

Area	No. of aqueous solutions analysed	Wt % salt in samples (average)	Stdev
1	6	**1.70**	**0.203**
Soil, area 1	1	**6.16**	-
2	6	**1.22**	**0.308**
3	10	**1.07**	**0.752**
Soil, area 3	2	**0.28**	**0.170**
4	6	**1.29**	**0.602**
Soil, area 5	1	**0.20**	-
Sand, area 5	2	**0.47**	**0.085**
6	5	**1.12**	**0.222**
7	4	**1.25**	**0.292**
Soil, area 7	2	**2.33**	**0.283**
Sand, area 8	1	**1.47**	-
9	3	**0.69**	**0.121**

Table 5.6: The average % (by mass) of salt in the number of samples listed which correspond to separate leachate samples. Soil and sand samples are not included in the average.

The soil from Area 1/7 seems particularly high in salt, of course, this is purely based on the samples taken, and a more thorough statistical analysis of the salt content of the soil could only be undertaken with further sampling. The salt content of the sand layer seems generally very low (with the exception of area 8, which is an area showing efflorescence) indicating that the sand layer is unlikely to be a source of salt contamination. The salt content of the samples is often over 1%. A private communication with Professor Clifford Price, University College London, yielded information that a salt content of 1% and above warrants concern. Of course, the salt content could be artificially high as wind blown particles are a possibility in the summer months when the glass roof is opened. As there are few real standards in determining what is or is not a salt weathering problem it is difficult to say with any certainty whether this mechanism is a major risk for the site or not.

Seawater data was taken from Aquatic Chemistry [6] and compared with the ICP-OES and IC data for the samples. A chart of each area shows the composition of the samples. Navy blue is used for seawater and red for other spall and brushing samples. Water collection and soil samples are treated separately.

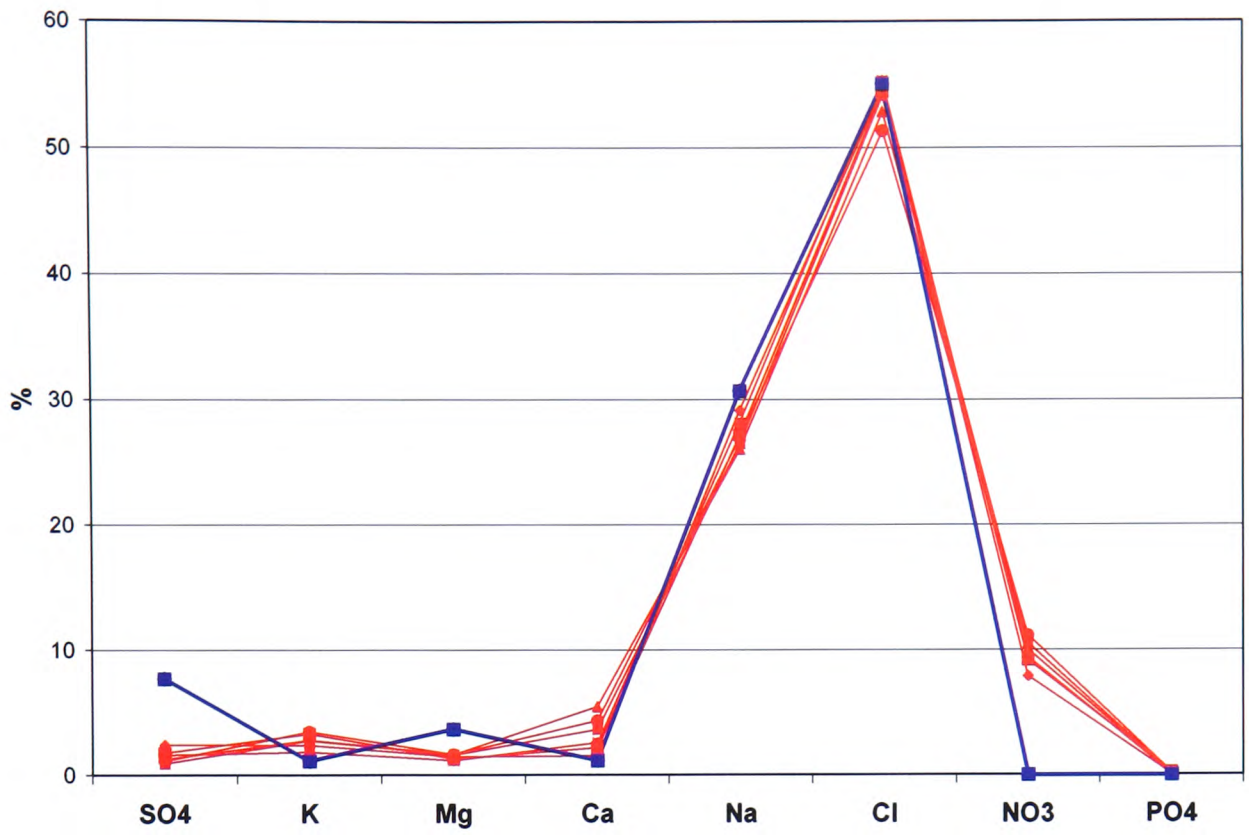

Figure 5.9: Area 1, showing the amount of each ion present (units of ppm) as a percentage of the total composition of the aqueous filtrate (y-axis) against the ion (x-axis). Seawater (dark blue) is shown for comparison.

The samples appear to correspond very well with seawater, with the addition of nitrates (possibly from the soil, as the area was effectively buried for a long period of time), a slightly greater amount of calcium, but lesser amount of magnesium and sulphate. Sodium chloride from the sea is the obvious source of the salt contamination of these particular samples.

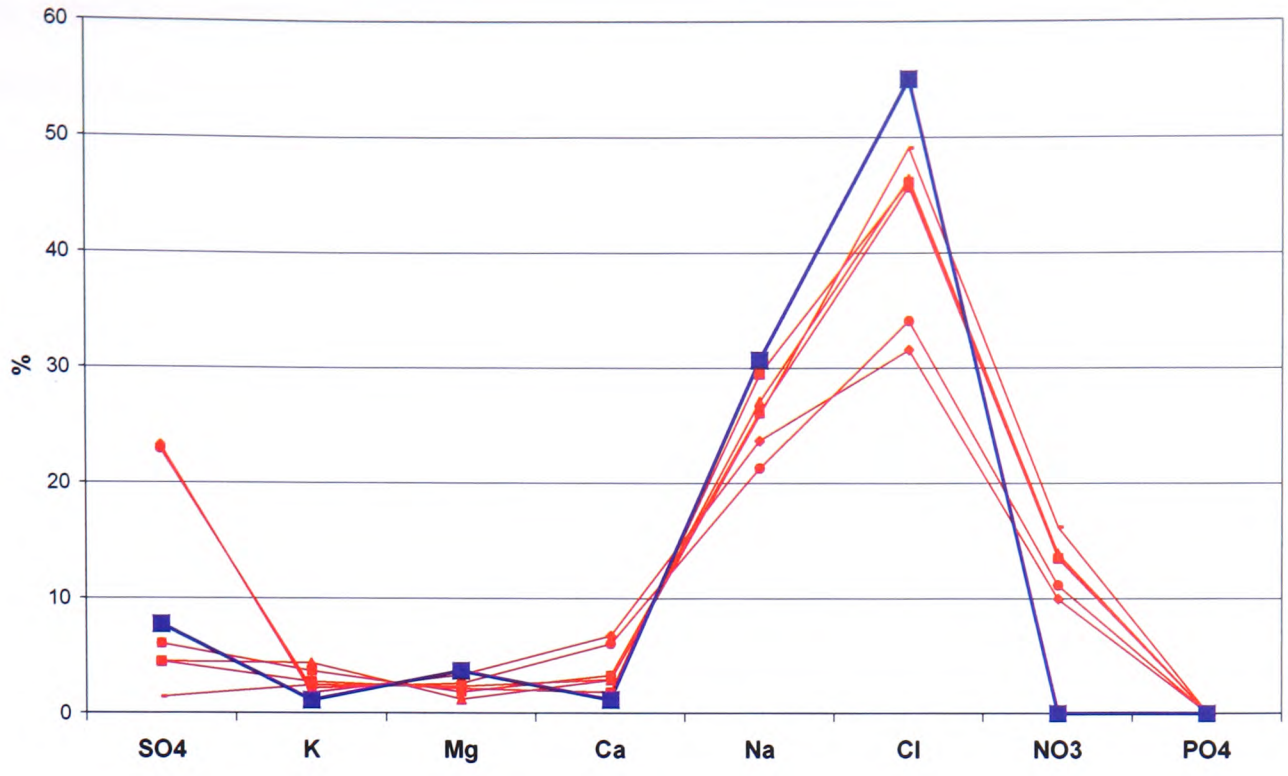

Figure 5.10: Area 2, showing the amount of each ion present (units of ppm) as a percentage of the total composition of the aqueous filtrate (y-axis) against the ion (x-axis). Seawater (dark blue) is shown for comparison.

In area 2 there is some obvious deviation from the seawater signature; two samples in particular which have a higher % of sulphate than would be expected from seawater correspondingly have a higher % of calcium, providing some indication of gypsum formation.

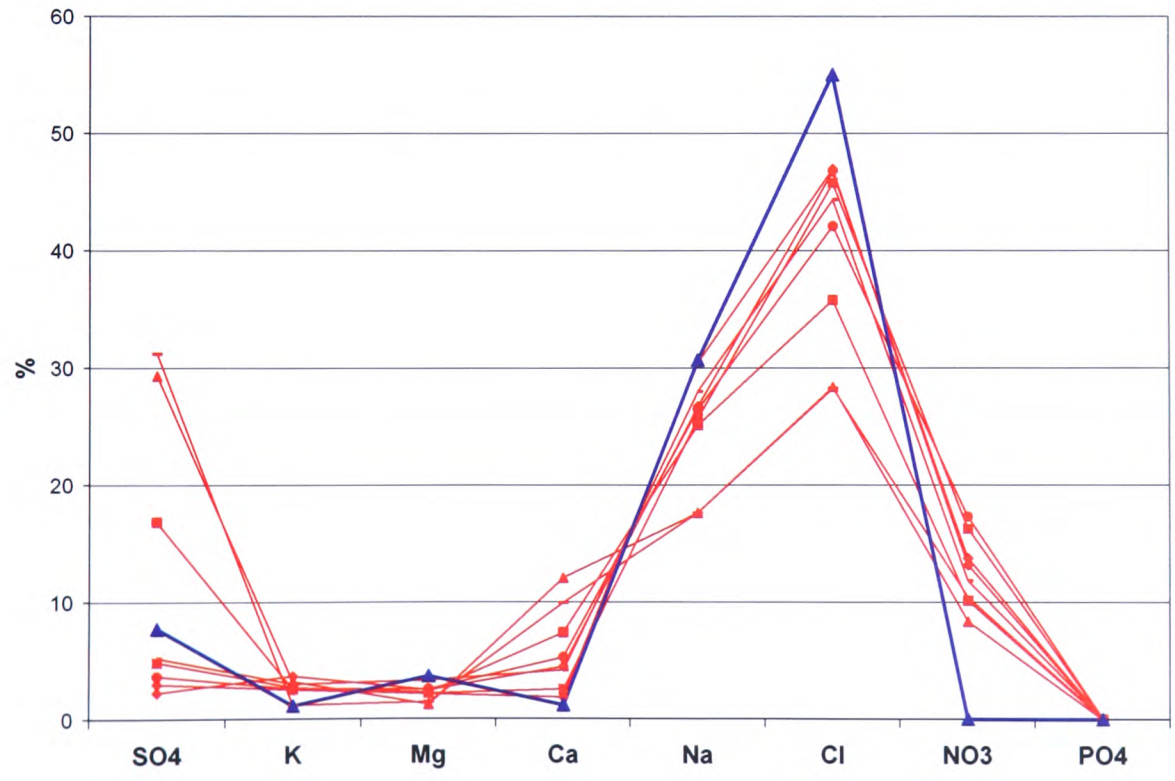

Figure 5.11: Area 3, showing the amount of each ion present (units of ppm) as a percentage of the total composition of the aqueous filtrate (y-axis) against the ion (x-axis). Seawater (dark blue) is shown for comparison.

In area 3, deviation from seawater is shown more strongly. The samples high in sulphate (from the first and second visits) also show heightened levels of calcium, further indicating the presence of gypsum.

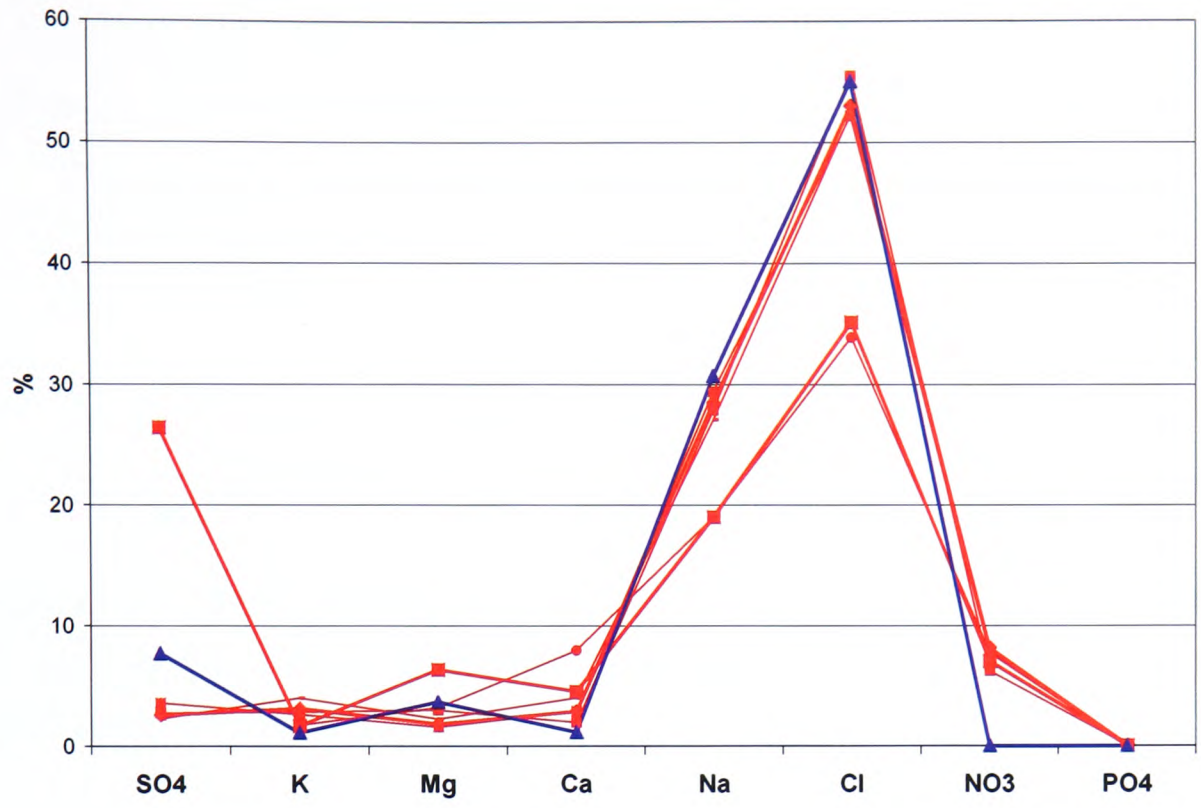

Figure 5.12: Area 4, showing the amount of each ion present (units of ppm) as a percentage of the total composition of the aqueous filtrate (y-axis) against the ion (x-axis). Seawater (dark blue) is shown for comparison.

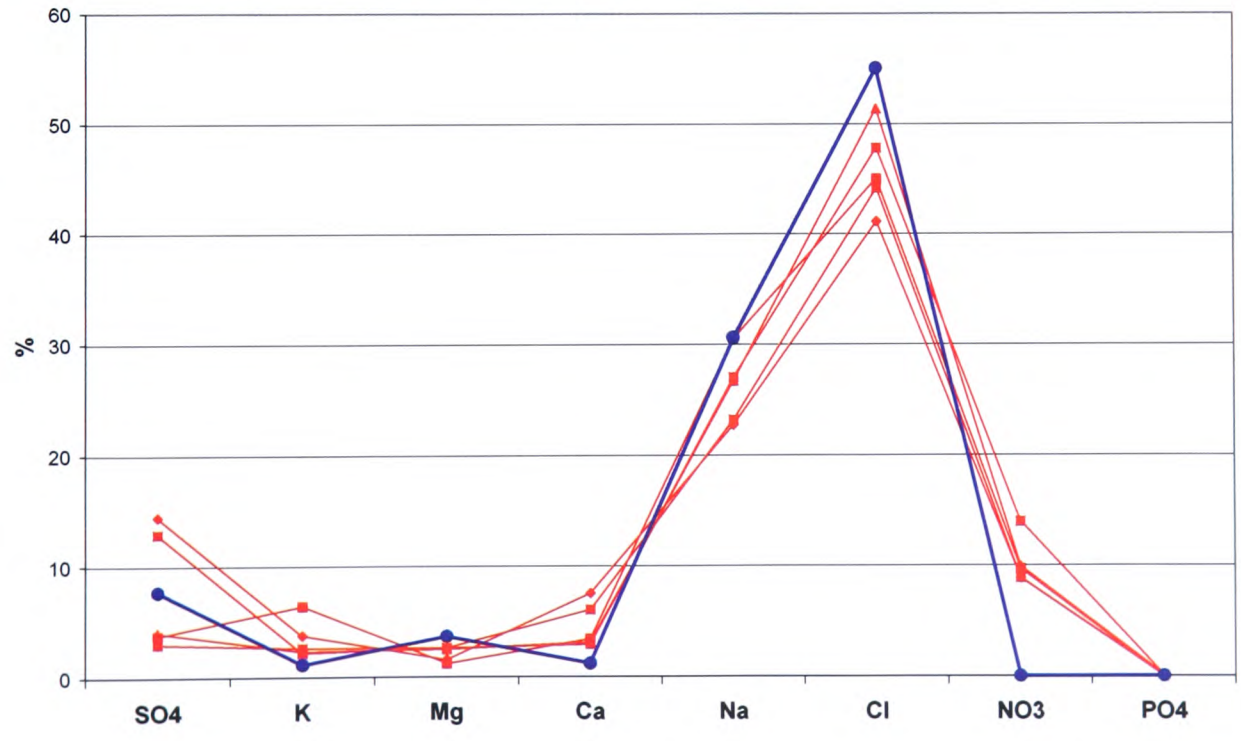

Figure 5.13: Area 6, showing the amount of each ion present (units of ppm) as a percentage of the total composition of the aqueous filtrate (y-axis) against the ion (x-axis). Seawater (dark blue) is shown for comparison.

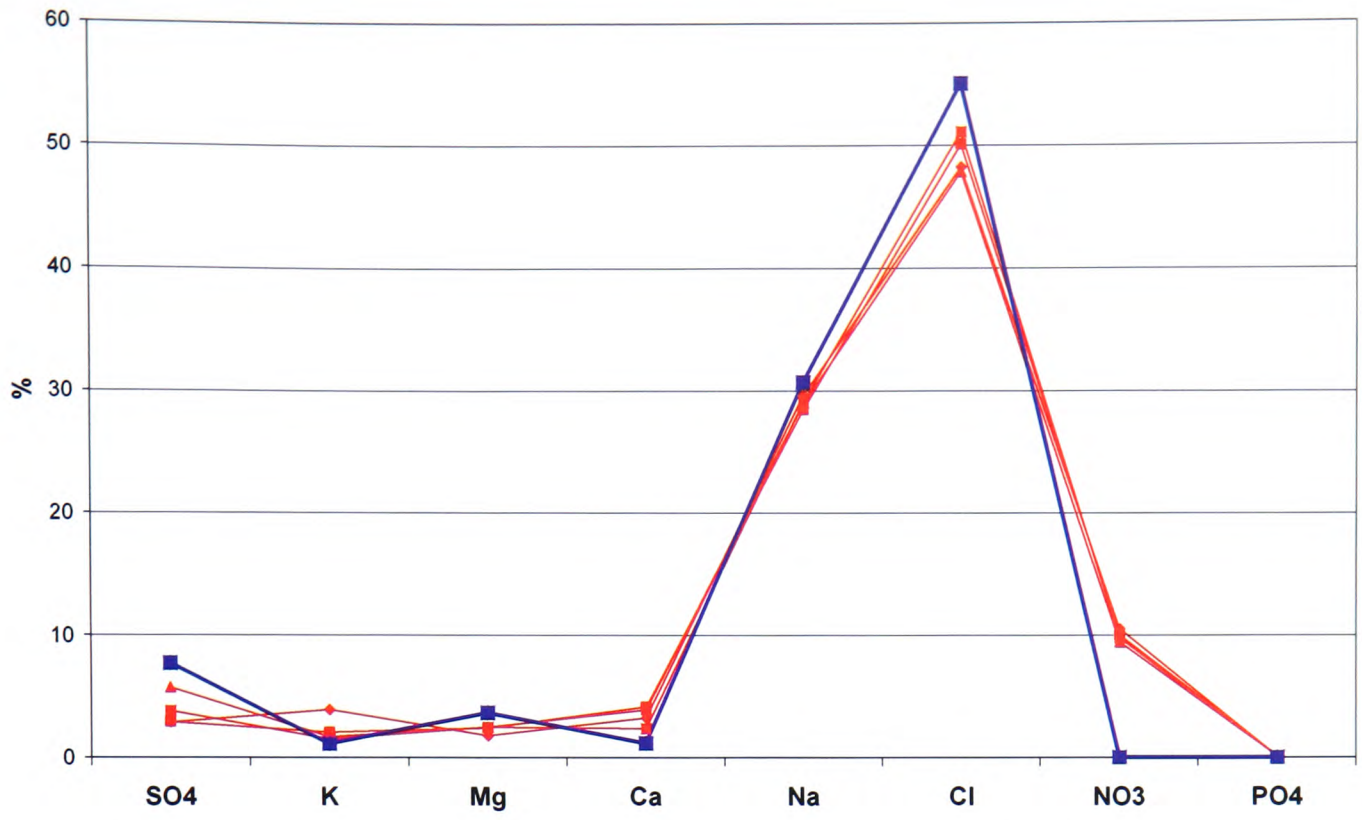

Figure 5.14: Area 7, showing the amount of each ion present (units of ppm) as a percentage of the total composition of the aqueous filtrate (y-axis) against the ion (x-axis). Seawater (dark blue) is shown for comparison.

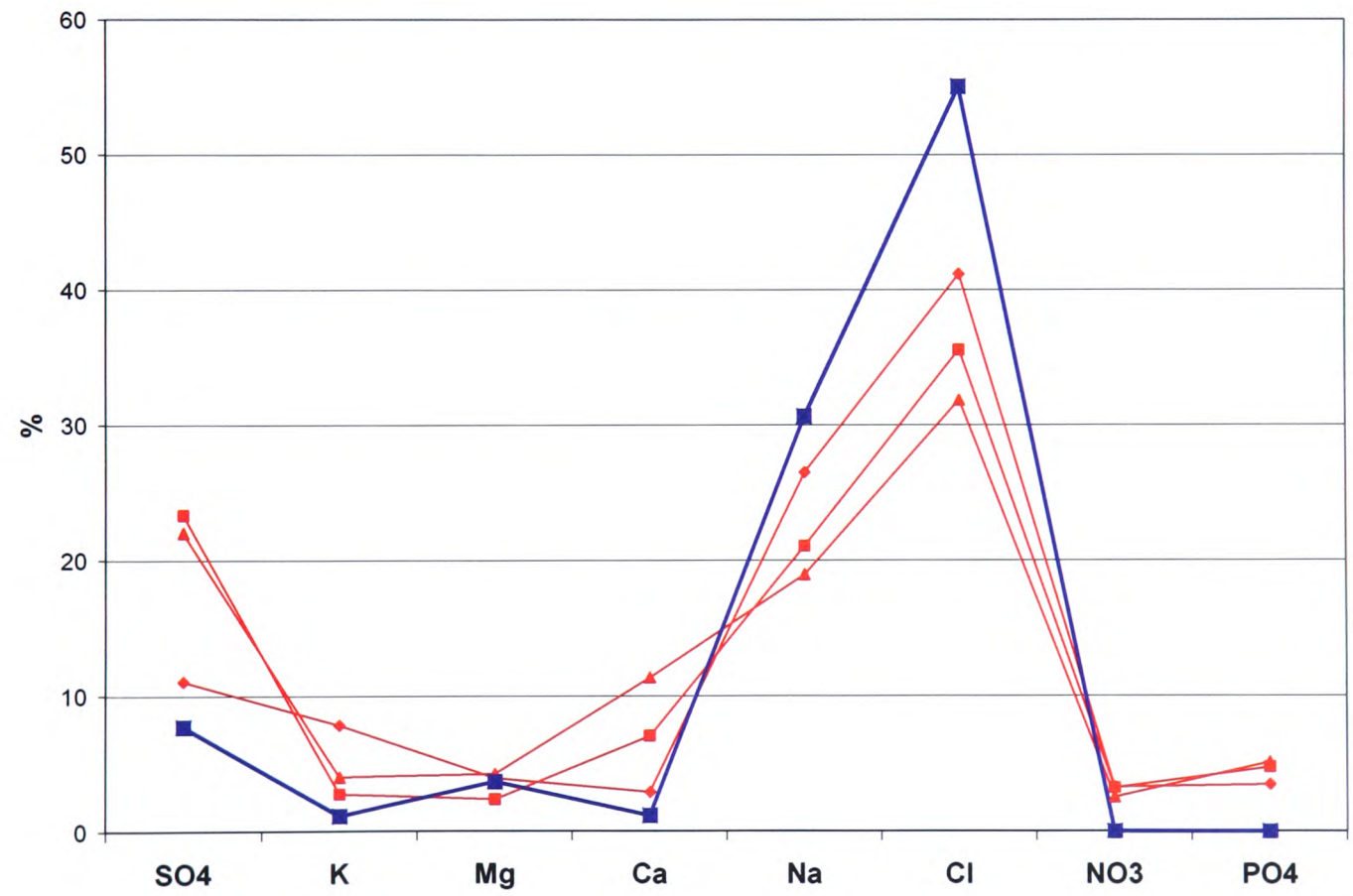

Figure 5.15: Area 9, showing the amount of each ion present (units of ppm) as a percentage of the total composition of the aqueous filtrate (y-axis) against the ion (x-axis). Seawater (dark blue) is shown for comparison.

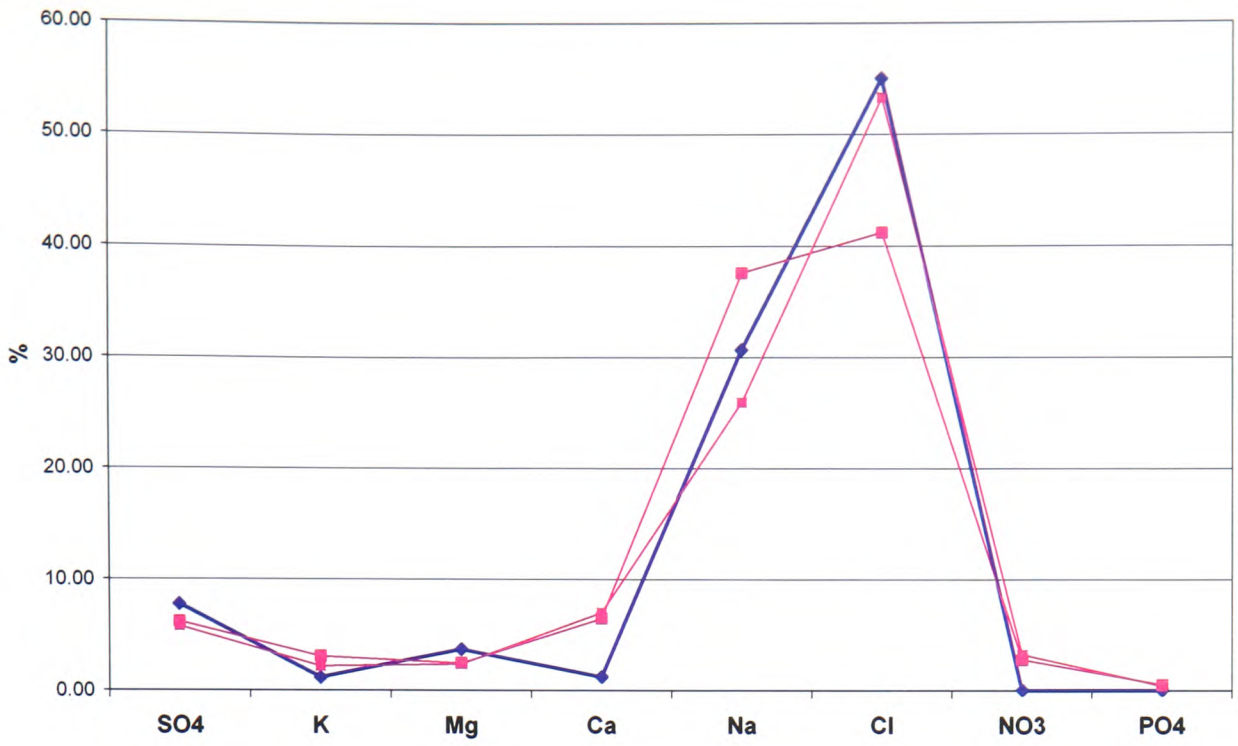

Figure 5.16: Water collection samples from the second visit, showing the amount of each ion present (units of ppm) as a percentage of the total composition of the aqueous filtrate (y-axis) against the ion (x-axis). Seawater (dark blue) is shown for comparison.

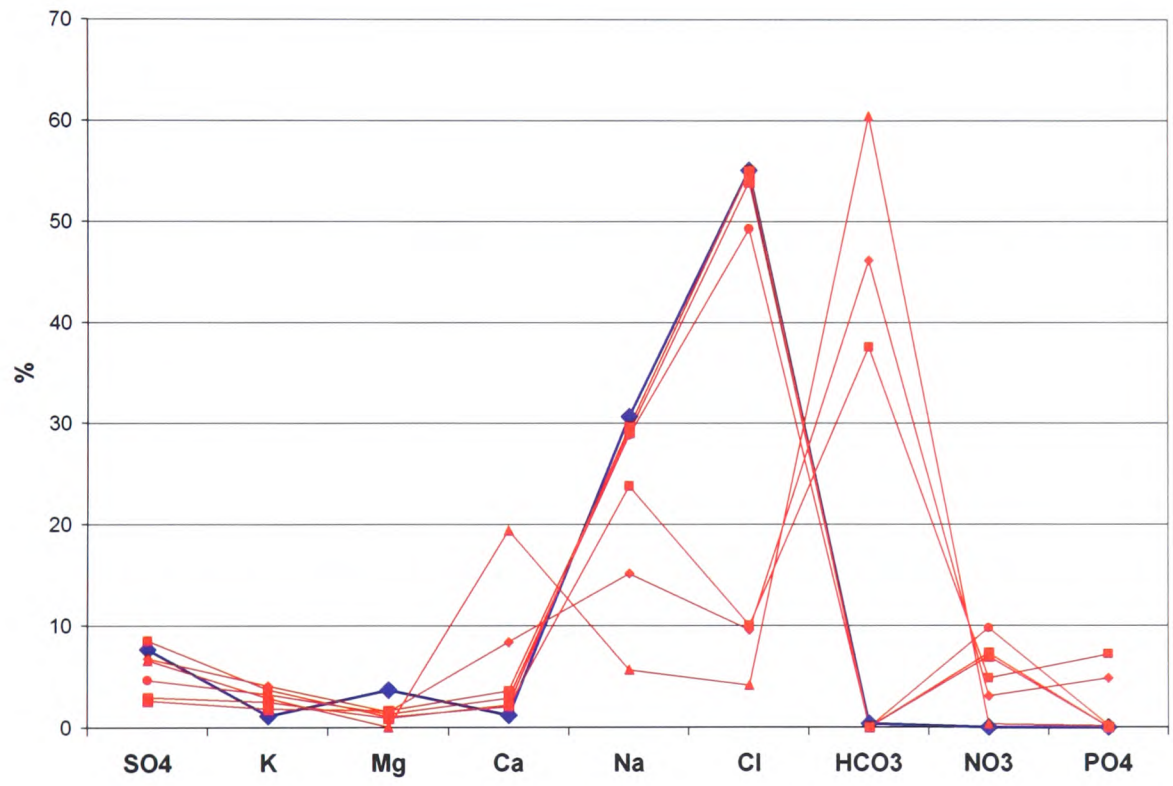

Figure 5.17: Soil samples, showing the amount of each ion present (units of ppm) as a percentage of the total composition of the aqueous filtrate (y-axis) against the ion (x-axis). Seawater (dark blue) is shown for comparison. The soil samples from areas 1 and 7 correspond well to seawater whereas the soil samples from areas 3 and 5, which have a very low salt content as discussed, contain bicarbonate species as calculated from the analytical results using PHREEQC. **NOTE** that a zero value for bicarbonate indicates the ion was not actively predicted based on the charge balance error, not that the ion is not present. For greatest accuracy a total alkalinity determination should be carried out.

The main point to note is that most of the samples have a seawater signature, but some samples show excess levels of sulphate, bicarbonate and calcium. It is possible that the source of these ions is not just seawater, with the weathering of the stone slabs in House 7 providing an extra source. Brushing samples and freshly fallen flakes from higher up the stone can show heightened levels of sulphate, whereas gypsum precipitation from seawater ingress, due to its lower solubility would be expected along the bottom of the stones (as is found to be the case), which possibly points to weathering of the stone for heightened sulphate levels found higher up the slab. However, fragments from the ground more often show high sulphate content and their history is unknown, which means they could be from the gypsum rich lower region of the stone. Looking at the calcium %, this is more often higher than seawater, which points to weathering of the stones carbonate cement.

Usually atmospheric pollution contributes to the sulphate content of monuments, which cannot be ruled out but is considered unlikely due to the remote location of the site and because it is covered most of the year.

The water collection vials from both visits were analysed, and general seawater dominance was also noted, which could provide a possible source of seawater to the house over time. Carbonate and bicarbonate content was calculated using PHREEQC [7] and was not determined analytically. Only samples which indicated a substantial deficit of anions after the charge balance error (CBE) was calculated (a positive CBE of greater than 10% was considered substantial) were examined numerically with PHREEQC to ascertain if any other species were possibly present. The pH of the filtrate was measured using an electronic pH meter and compared with the predicted pH from the PHREEQC output. If the two pH values were more than 5% of the measured value apart, the data set was not used, if they were within 5%, the bicarbonate, carbonate and hydroxide results were added to the analytical results. The soil samples, with the exception of areas 1 and 7, show low levels of all ions (<13 ppm Cl for) which can make accurate analysis of these very dilute solutions challenging. It is possible therefore that the CBE error is analytical error rather than the presence of an unidentified anion (carbonate, bicarbonate), but this is considered unlikely. However, for greatest accuracy, total alkalinity should be measured.

Although seawater is mainly responsible for the salt content of the sample, the calcium, sulphate and bicarbonate levels indicate that another mechanism is also present. Thin section and XRD analysis of some of the flakes and the background rocks indicate that pyrite is present or was present in many of the samples. A good general description of pyrite oxidation can be found in Stumm and Morgan [6] which highlights how pyrite oxidation results in the weathering of calcite cement:

Pyrite oxidation is complex, with many side reactions occurring simultaneously [8-10]. The initial pyrite oxidation reaction is:

$$FeS_{2(s)} + \frac{7}{2}O_2 + H_2O = Fe^{2+} + 2SO_4^{2-} + 2H^+ \quad \textbf{(5.1)}$$

$$Fe^{2+} + \frac{1}{4}O_2 + H^+ = Fe^{3+} + \frac{1}{2}H_2O \quad \textbf{(5.2)}$$

$$Fe^{3+} + 3H_2O = Fe(OH)_{3(s)} + 3H^+ \quad \textbf{(5.3)}$$

$$FeS_{2(s)} + 14Fe^{3+} + 8H_2O = 15Fe^{2+} + 2SO_4^{2-} + 16H^+ \quad \textbf{(5.4)}$$

Equation 5.1 releases dissolved ferrous iron and acidity into the water. Subsequently the dissolved ferrous iron undergoes oxygenation to the ferric iron (equation 5.2) which then hydrolyses to form the insoluble "ferric hydroxide" (equation 5.3), releasing more acidity and coating the surroundings. Ferric iron can also be reduced by pyrite itself (equation 5.4), where the FeS_2 is again oxidised and acidity is released along with the additional ferrous irons which re-enters the cycle at equation 5.2.

Sulphuric acid is known to attack calcite which can raise the pH of the pore water/solution, neutralising the acid produced:

$$CaCO_3 + 2H^+ = Ca^{2+} + CO_2 + H_2O \quad \textbf{(5.5)}$$

Bicarbonate can form from the additional dissolution of calcite from carbon dioxide according to:

$$CaCO_3 + CO_2 + H_2O = Ca^{2+} + 2HCO_3^- \quad (5.6)$$

Micro-organisms also play a part in controlling the oxidation rate of pyrite and affect the dissolution of calcite indirectly by the production of CO_2 from respiration or degradation of organic matter [11].

Gypsum is a common solid phase resulting from the breakdown of a calcite matrix from pyrite oxidation [12]. According to:

$$Ca^{2+} + SO_4^{2-} + 2H_2O = CaSO_4.2H_2O \quad (5.7)$$

The ease with which pyrite oxidises is important. A study by Hercod et al. found that pyrite contributed a disproportionate amount to the total weathering flux through secondary dissolution of $CaCO_3$ by H_2SO_4. They conclude that this process accounts for nearly half of the carbonate dissolution within the basin even though pyrite is a trace constituent [11]. This indicates that even small amounts of pyrite are potentially damaging.

A study on the effects of RH on pyrite oxidation [13] yields some useful information on the reactivity of pyrite in moist air. The study was carried out on pyrite crystals rather than pyrite containing sediment, but found that humid environments with RH less than 95 % can promote the disintegration of museum pyrite samples as ferrous sulphate phases precipitate. At moderate RH (~70 %) the solution that develops on oxidising pyrite surfaces can become very acidic [13].

This naturally leads to a discussion of the oxidation product. Iron oxides, ferric hydroxide and ferrous sulphates are all reported as being pyrite oxidation products in literature sources and this is discussed further on in conjunction with thin section analysis. In general, pyrite oxidation could possibly explain the heightened levels of calcium and sulphate found in solution and the predicted bicarbonate levels. However, it is possible that gypsum rich parts of the monument were brushed (in the case of surface brushings). Although gypsum crystallisation might not be expected further up than the efflorescence lines at the bottom from capillary rise alone, the site was buried until 1850 and therefore possibly saturated with sea water during this time.

The final set of analysis carried out on the ICP-OES/IC data was a correlation matrix. This produces a set of results that examine how well ions are correlated with each other, if at all. Data was analysed in sets from the 1st and 2nd visit.

	Cl	NO_3	PO_4	SO_4	K	Mg	Ca	Na
Cl	1.00	0.78	-0.34	-0.34	0.62	0.42	0.19	0.98
NO_3	0.78	1.00	-0.54	-0.21	0.40	0.49	0.14	0.83
PO_4	-0.34	-0.54	1.00	0.23	-0.06	0.11	0.15	-0.41
SO_4	-0.34	-0.21	0.23	1.00	-0.24	0.32	0.68	-0.30
K	0.62	0.40	-0.06	-0.24	1.00	0.08	0.20	0.60
Mg	0.42	0.49	0.11	-0.32	0.08	1.00	0.48	0.46
Ca	0.19	0.14	0.15	0.68	0.20	0.48	1.00	0.18
Na	0.98	0.83	-0.41	-0.30	0.60	0.46	0.18	1.00

Table 5.7: Correlation matrix for samples (stone flake only) taken during the 1st visit.

Samples from the second visit were analysed in the same manner. Only spall and surface brushing samples are included in either correlation matrix, soil, sand and water collection samples are not included. No salt line brushings are included as these were not leached for aqueous analysis.

The closer the value to unity, the stronger the correlation of the ions in solution and the more closely 'linked' they are, which is a good method of investigating which ions 'mirror' each other or not. The most relevant correlations are between sodium and chloride, and calcium and sulphate. Sodium and chloride is unsurprisingly the highest correlation listed for both data sets, with calcium and sulphate being the second highest for the second visit results. This is as expected considering the known seawater signature of the sample and the evidence of solid gypsum found on site, most notably from samples taken during the second visit. A point to note is the correlation between chloride/sodium and nitrates. Nitrates, often found in soils have several different sources, mainly human and animal waste and fertilisers. As the site is laid on and backed up in midden [2] (source of waste) and the site was buried for an extended period of time, it is possible that the salt contamination and nitrates are from the same source of seawater rich soil/midden.

However, water samples from the damp area also contain nitrate and this would provide a fresh source of salts to the site through time. Other, perhaps unexpectedly high, correlations are: potassium and chloride (1st and 2nd visit samples) and calcium and nitrate, nitrate and sulphate from the 2nd visit samples. RUNSALT [5] was used to ascertain which salts were likely to precipitate under the environmental conditions of the site. Temperature and RH data collected from the site during 2003/2004, supplied by Historic Scotland, was used in RUNSALT as described in the next section.

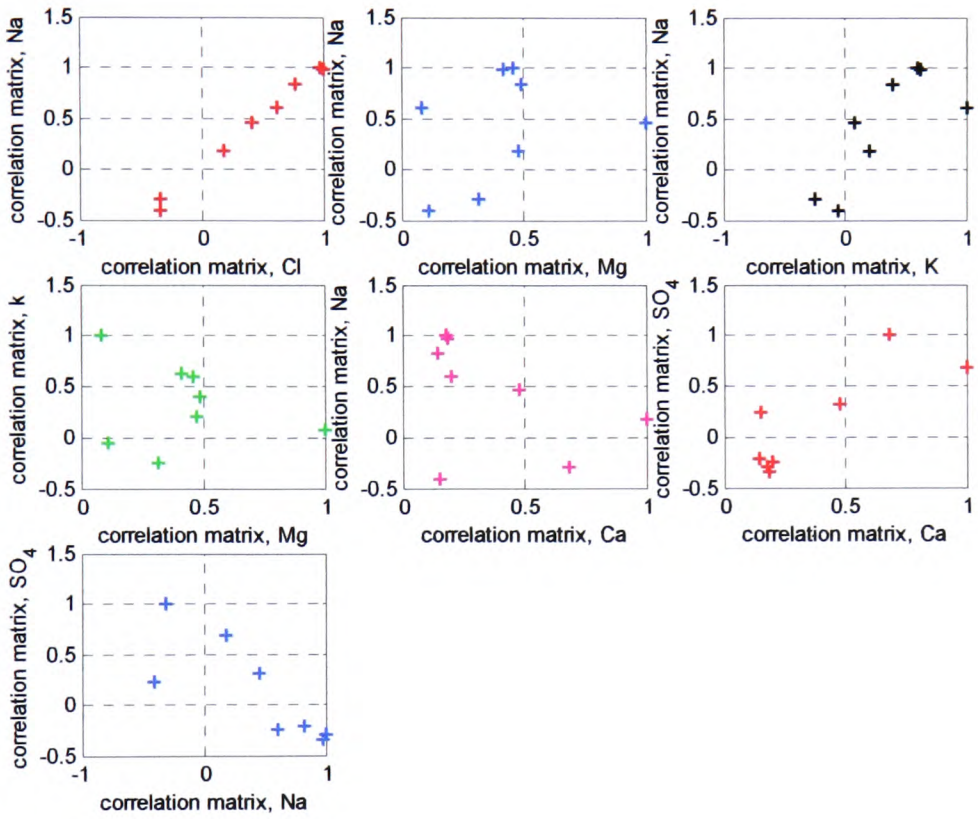

Figure 5.18: Correlation matrix plot of the spall samples from the 1st visit

	Cl	NO_3	PO_4	SO_4	K	Mg	Ca	Na
Cl	1.00	0.62	0.27	0.44	0.71	0.33	0.46	0.98
NO_3	0.62	1.00	0.59	0.81	0.56	0.22	0.91	0.74
PO_4	0.27	0.59	1.00	0.30	-0.01	-0.16	0.47	0.43
SO_4	0.44	0.81	0.30	1.00	0.66	0.58	0.95	0.52
K	0.71	0.56	-0.01	0.66	1.00	0.51	0.31	0.69
Mg	0.33	0.22	-0.16	0.58	0.51	1.00	0.61	0.28
Ca	0.46	0.91	0.47	0.95	0.61	0.31	1.00	0.58
Na	0.98	0.74	0.43	0.52	0.69	0.28	0.58	1.00

Table 5.8: Correlation matrix of spall and brushing samples from the 2nd visit.

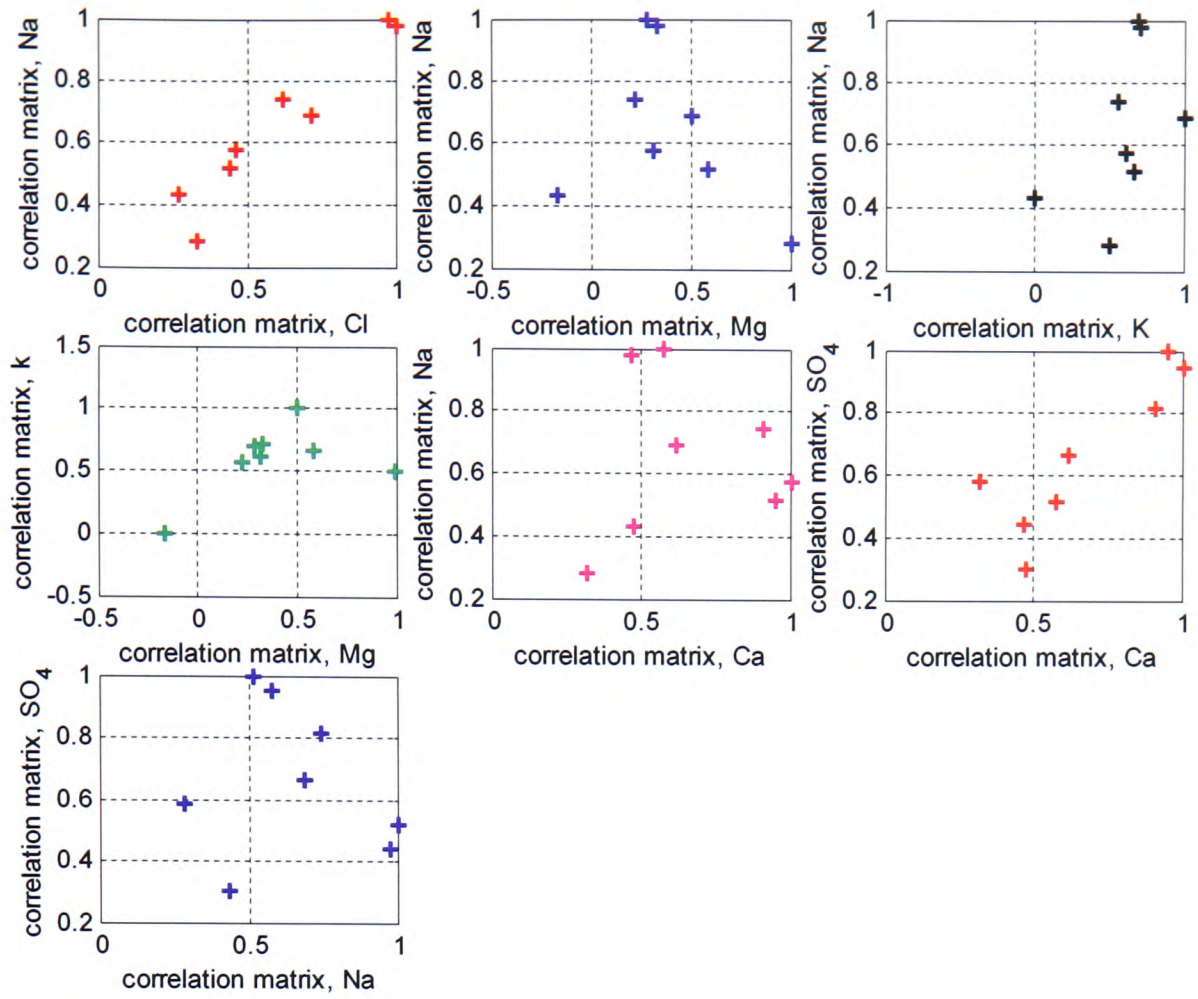

Figure 5.19: Correlation matrix plot of the spall and brushing (stone surface only, not pure salt brushings) samples from the 2nd visit.

5.2.1 Precipitation prediction analysis

The purpose of this section was to ascertain whether salts other than halite and gypsum are present to explain the correlations mentioned in the previous section. ICP-OES data was used to predict which phases would crystallise under the environmental conditions of the house, given in tables 5.3 and 5.4. The program used was RUNSALT [5], which is based on ECOS [4] and the environmental conditions used for the simulation were taken from the average of the values corresponding to the month of the visit. For samples collected during March (2004) the data used was 7.7 °C and 69-96 % RH (although this is the data for March 2003, the RH range for March 2004 was 80 – 96 %, therefore the March 2003 data was used as it represents the worst case scenario in terms of salt crystallisation potential). For August (2004) the data used was 18 °C and 59-88 % RH, which is the data from August 2003 as

that was the only data available for August. For every sample, gypsum and halite precipitation was predicted. Gypsum, with an ERH (equilibrium relative humidity) of >99 % [4] is almost guaranteed; halite was predicted to crystallise when the RH dropped below ~ 73%. In a few cases, other salts were predicted as indicated in table 5.8.

Sample	Na	Ca	Mg	K	SO_4	PO_4	NO_3	Cl	Salts predicted
137004 surface brushing	203.0	48.3	67.8	17.8	281.8	0.04	75.4	375.0	Bloedite Hexahydrite Starkeyite
152003 spall	138.1	77.9	11.5	9.5	245	0.39	81.5	222.0	Nitratine Bloedite Starkeyite
152004 surface brushing	92.5	38.7	15.6	8.5	129.0	0.04	38.0	165.0	Bloedite Hexahydrite Stakeyite

Table 5.9: ICP-OES/IC data for samples for which RUNSALT predicts salts other than halite and gypsum will crystallise. Salts produced include halite and gypsum for every sample listed. All samples are from the second visit. First visit samples (under the relevant environmental conditions) are predicted to produce only gypsum and halite. Values are given in ppm. Surface brushing indicates removal of some powdery residue from the stone surface, and is not a salt line brushing.

Figures 5.20 – 5.22 are outputs from RUNSALT which indicate the salts precipitated and the quantity. RUNSALT does not have an input parameter for total alkalinity or carbonate/bicarbonate species and automatically charge balances the input data. Also it is a requirement of the system that gypsum is removed before calculation of the precipitating species. This means that the input data is modified automatically to remove calcium and sulphate species that would result in gypsum precipitation.

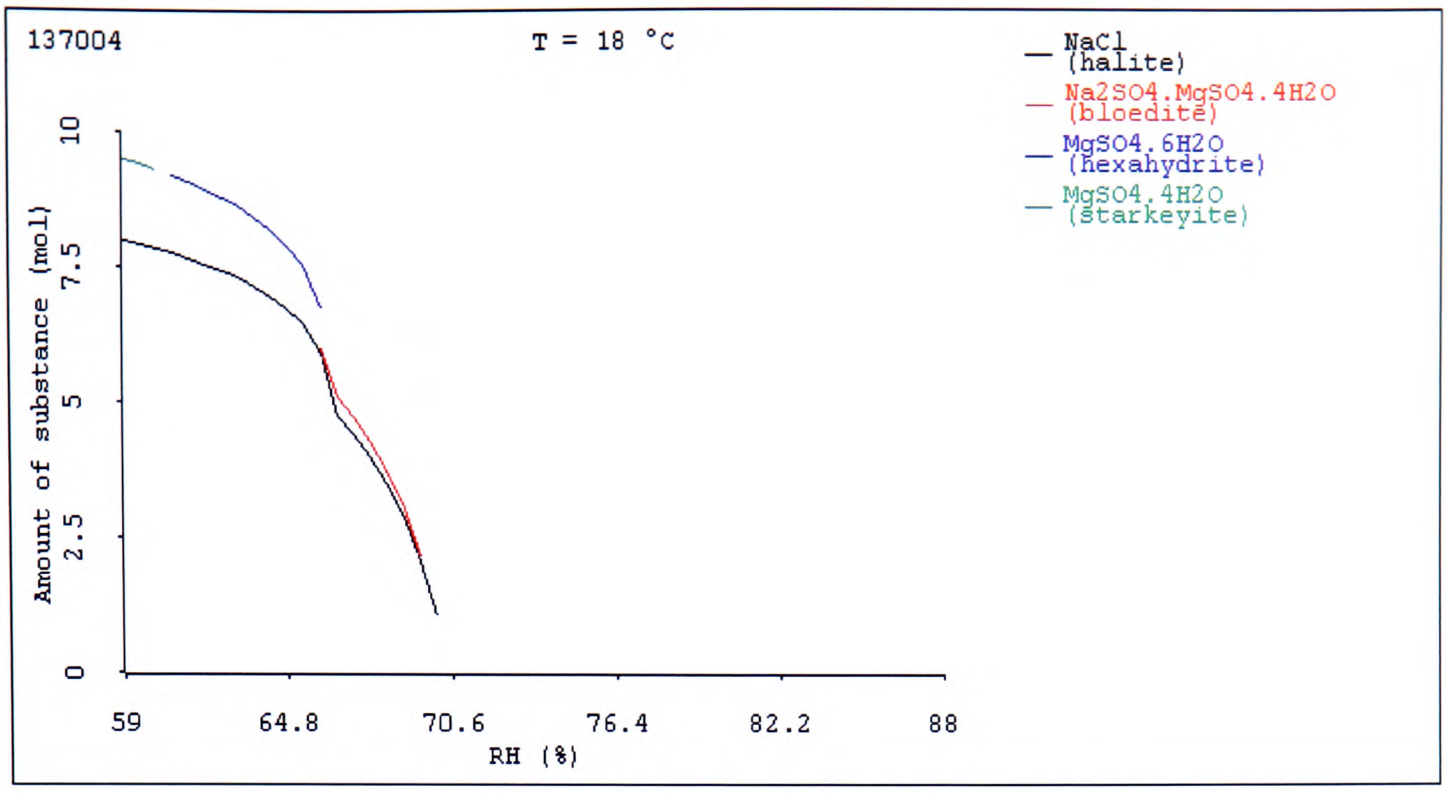

Figure 5.20: Output from RUNSALT for sample 137004, indicating at what RH value the salt is precipitating from solution. Gypsum was removed from the system.

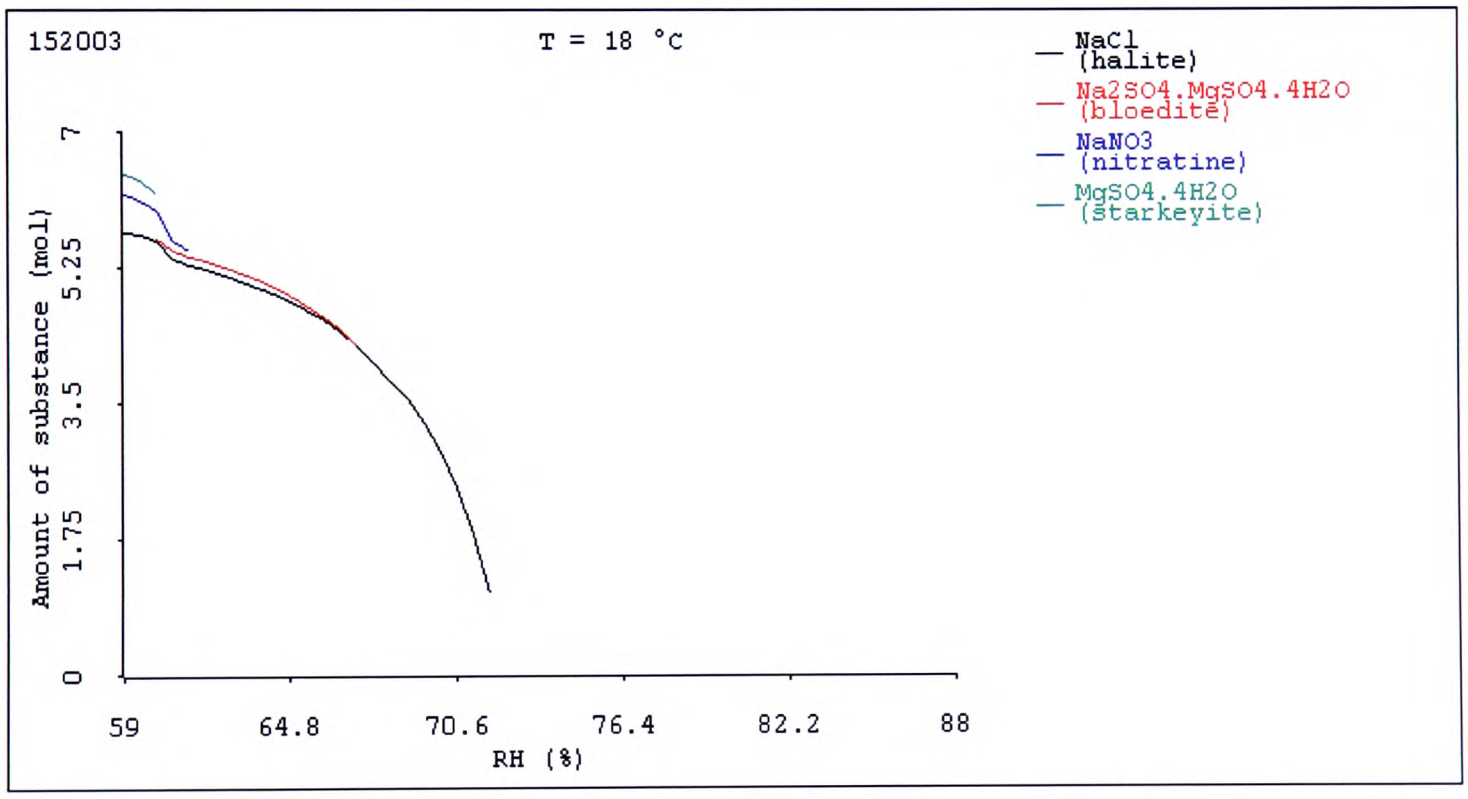

Figure 5.21: Output from RUNSALT for sample 152003, indicating at what RH value the salt is precipitating from solution. Gypsum was removed from the system.

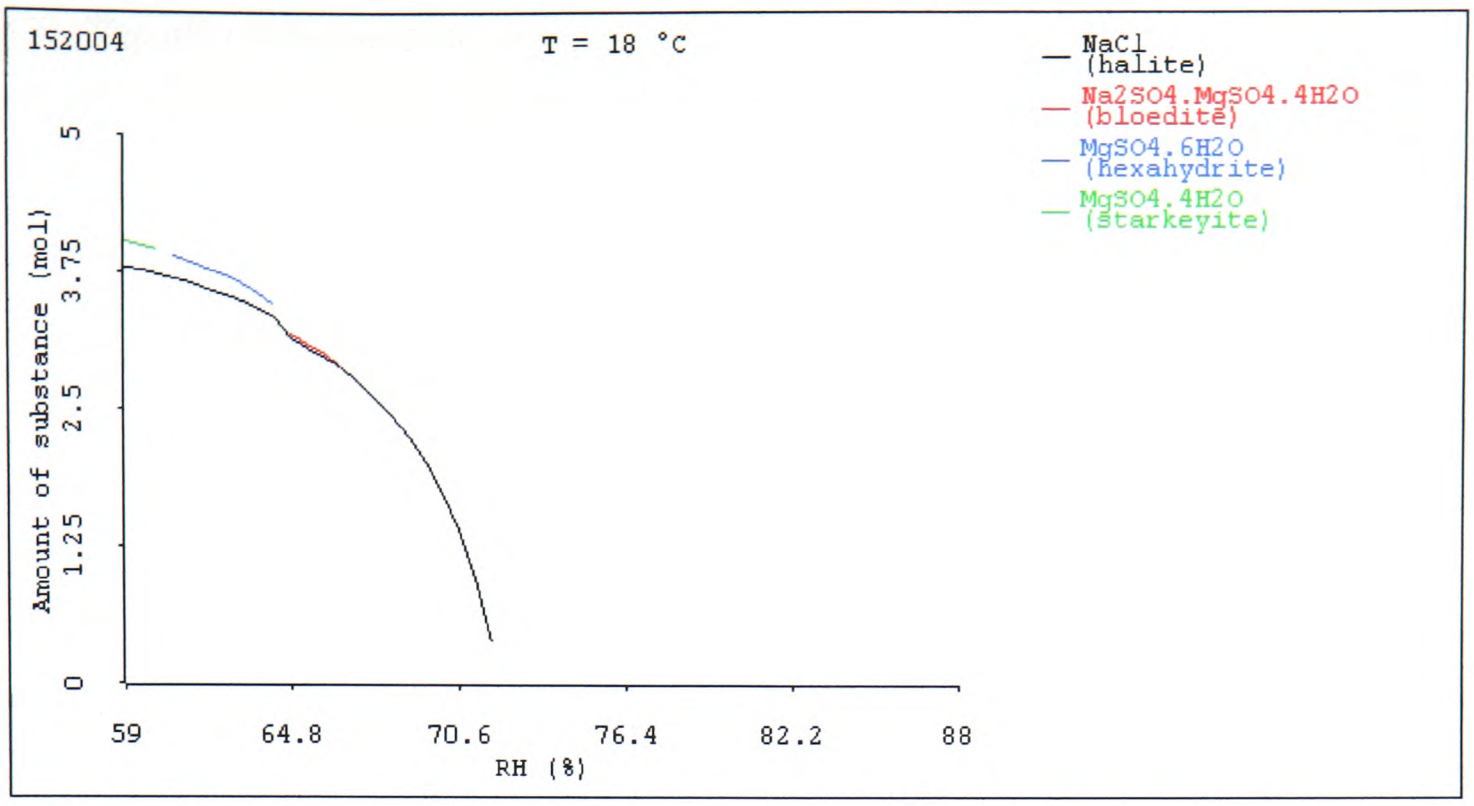

Figure 5.22: Output from RUNSALT for sample 152004, indicating at what RH value the salt is precipitating from solution. Gypsum was removed from the system.

As can be seen, the other phases are fairly minor and have not been found during the X-ray analysis (in contrast to gypsum and halite), therefore it is reasonable to assume these phases are of limited importance. These minor phases are sulphates and a nitrate, with no indication of potassium chloride, therefore the high correlation observed between potassium and chloride, calcium and nitrate, nitrate and sulphate is not clearly understood.

5.2.2 PHREEQC and charge balance errors

Charge balance errors were estimated using the following relationship from [14]:

$$\%CBE = \frac{\sum(z_{c_i} \cdot M_{c_i}) - \sum(z_{a_i} \cdot M_{a_i})}{\sum(z_{c_i} \cdot M_{c_i}) + \sum(z_{a_i} \cdot M_{a_i})} \cdot 100 \qquad \textbf{(5.8)}$$

Where M_c and M_a are the cation and anion molarities respectively, z_c and z_a are the absolute values of the cation and anion charges respectively. 51 water samples in total were analysed for Na^+, Ca^{2+}, K^+, Mg^{2+}, Cl^-, SO_4^{2-}, PO_4^{3-} and NO_3^-. Carbonate and bicarbonate were not determined analytically but calculated using PHREEQC

[7]. The pH of the leachate solution was measured and compared to the predicted pH of the PHREEQC output. PHREEQC was only used for samples if the following two conditions were met: There was a noticeable positive charge balance error (in excess of 5%, a 5% error is considered reasonable [14]) and the predicted pH is within 5% of the measured pH (error on the pH measurement does not exceed 5% of the average value). For these samples, PHREEQC is used to charge balance the data which effectively raises the pH with the addition of CO_3^{2-}, HCO_3^- and OH^-. Samples exhibiting a negative charge balance error were found to be unsuitable for this treatment with PHREEQC, as the predicted pH is much more acidic than the measured pH due to the fact that PHREEQC balances the charge with the addition of H^+ ions.

Ammonium was measured for 4 samples and found to be at most 5 ppm (0.57% of the total ion count of the sample). In these cases it is taken into consideration when calculating the % CBE, but was found to make very little difference. Samples were included (51 samples in total) with a CBE of <10 % leaving the total average CBE of 3.37 % and a standard deviation of 2.47. This average value falls within acceptable limits of <5 %.

5.3 Thin Section analysis

Spall fragments from the site were thin sectioned for petrographic analysis. Samples were cut using a continuous rim diamond saw blade and a 50:50 mix of ethylene glycol and methylated spirit as the coolant/lubricant, impregnated with "Epo-thin" epoxy and covered with a glass coverslip. All thin sections presented here were made by Mr Michael Hall, School of Geosciences. Dr Ewan Hyslop, British Geological Survey, kindly assisted with the analysis of these samples.

The most obvious point to note is the rust-coloured coating obscuring the grains. Analysis of some sections under incident light show highly altered crystals of sulphide, often with a rust coloured iron halo, evidence of the oxidation process. Grain size is very fine, ranging from mudstone to siltstone to fine sandstone, as grain size rarely exceeds 0.125 mm. A publication on the iron staining of a pyrite containing marble indicates that the ferruginous staining observed is often the result

of minute particles of iron III oxides transported by water flow through the material [15]. Matero et al. believe that hydrated ferric hydroxides and ferric sulphates are responsible for the iron discolouration of the marble in question [15]. In this case it is not clear whether iron oxides, hydroxides, sulphates or a combination of all three are responsible for the discolouration of the stone, also the weathering of iron rich carbonate species, such as ankerite can cause rusty orange staining. Further analytical investigation would be required to determine which iron minerals are present.

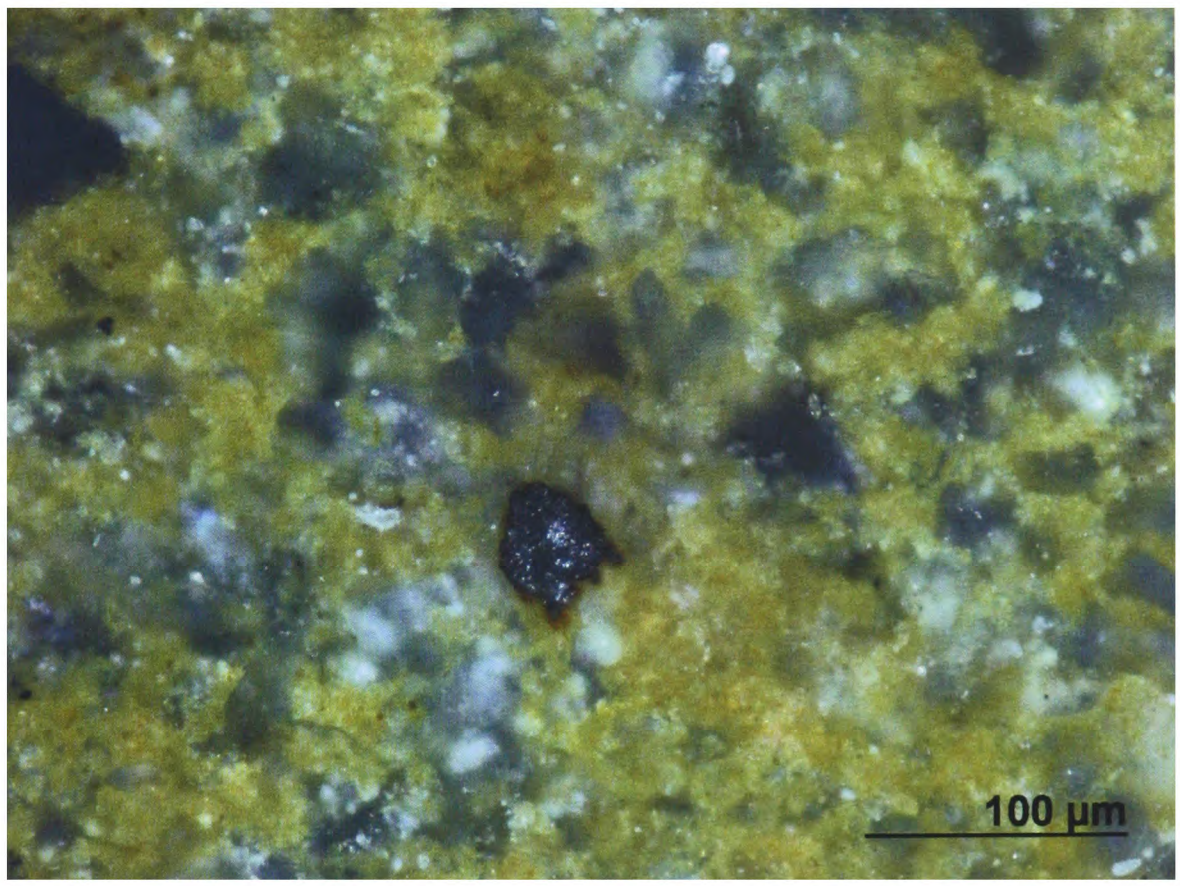

Figure 5.23: thin section micrograph, taken under plane polarised light in incident mode. Scale bar is shown at the bottom right. A weathered sulphide inclusion is shown in the centre with characteristic red/brown halo.

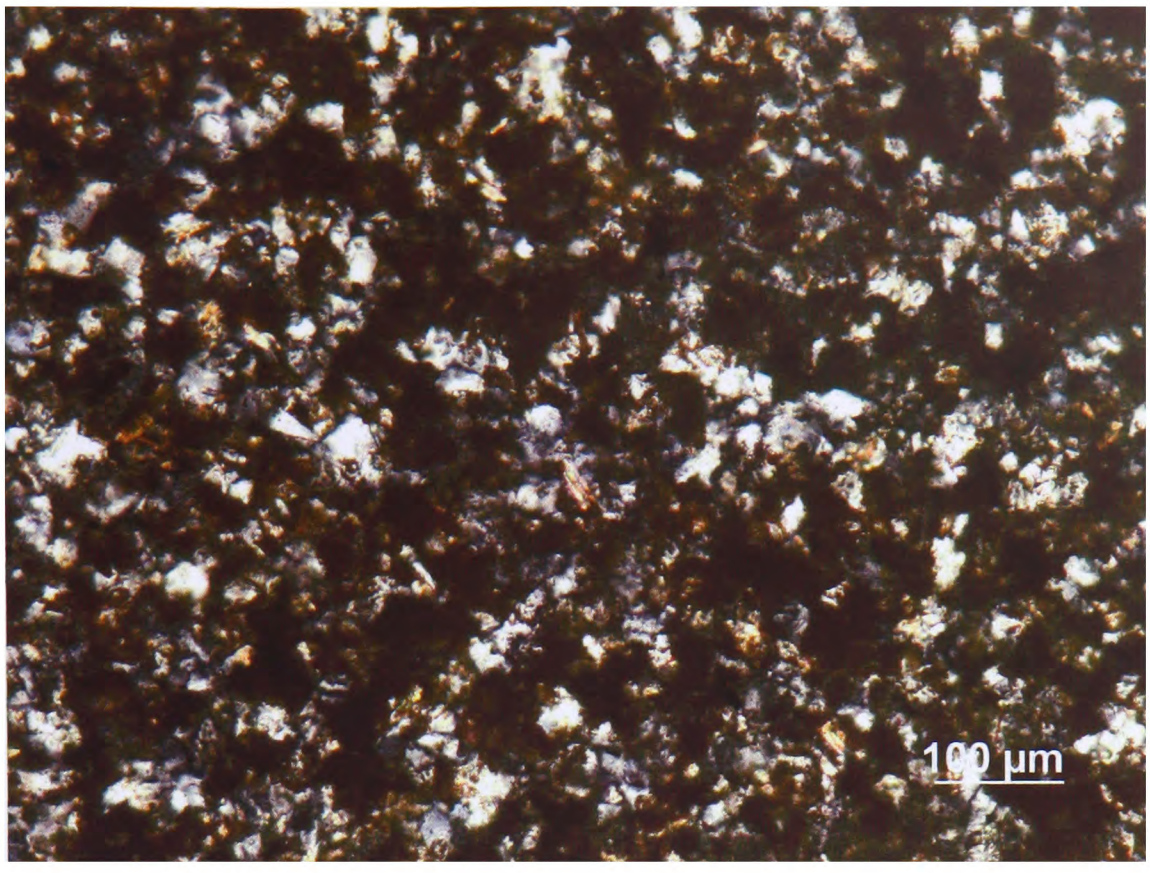

Figure 5.24: Thin section micrograph taken under crossed polars in transmitted light. General nature of the material (heavy iron staining) is shown.

Due to the weathered nature of the material, very little else can be deduced from section analysis. The background rocks collected from the 2nd visit, were used for this purpose.

5.4 Background rocks

Background rocks were collected for further analysis and testing [3] from the foreshore in front of Skara Brae (SK1 – SK5) and from in situ outcrops (HY225190) on the south side of the Bay of Skaill (SK9 – SK12). As it was not possible to sample significant amounts of stone from House 7 this material was collected for further analysis and testing in order to determine the composition of the stone types and further identify the likely mechanisms of stone decay. The main rock types are presented with a brief description of the hand specimen by E. K. Hyslop followed by X-ray results of the sample and thin section analysis.

SK 1

A weathered flagstone with a laminated appearance (bedded on mm scale). Very fine grained and relatively soft, with a friable texture, weathered to pale brown-orange colour.

XRD: quartz, calcite, dolomite/ankerite, muscovite, plagioclase feldspar, chlorite, kaolinite, K-feldspar. Ratio of quartz to feldspar is 1:1.94, as calculated using TOPAS.

Thin section: Very fine grained laminated material of siltstone/mudstone, with some bands of larger grained quartz and feldspars. A little iron staining is visible through the section and no obvious pyrite. Secondary calcite veins are apparent which are often opened. This could be a sampling artefact or dissolution, but bears a closer resemblance to a sampling artefact. The coarser grained bands contain chlorite. Overall, a very fine, friable material that splits easily along the bedding.

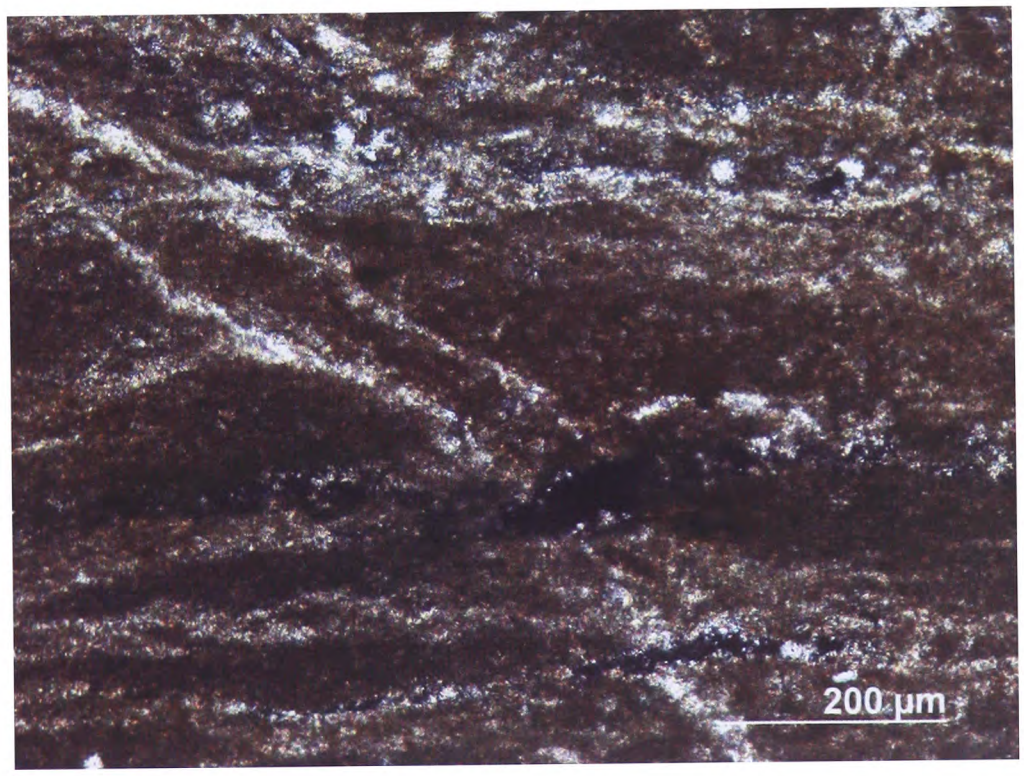

Figure 5.25: Thin section micrograph of SK 1 under crossed polars in transmitted light. General stratigraphy and veining is shown.

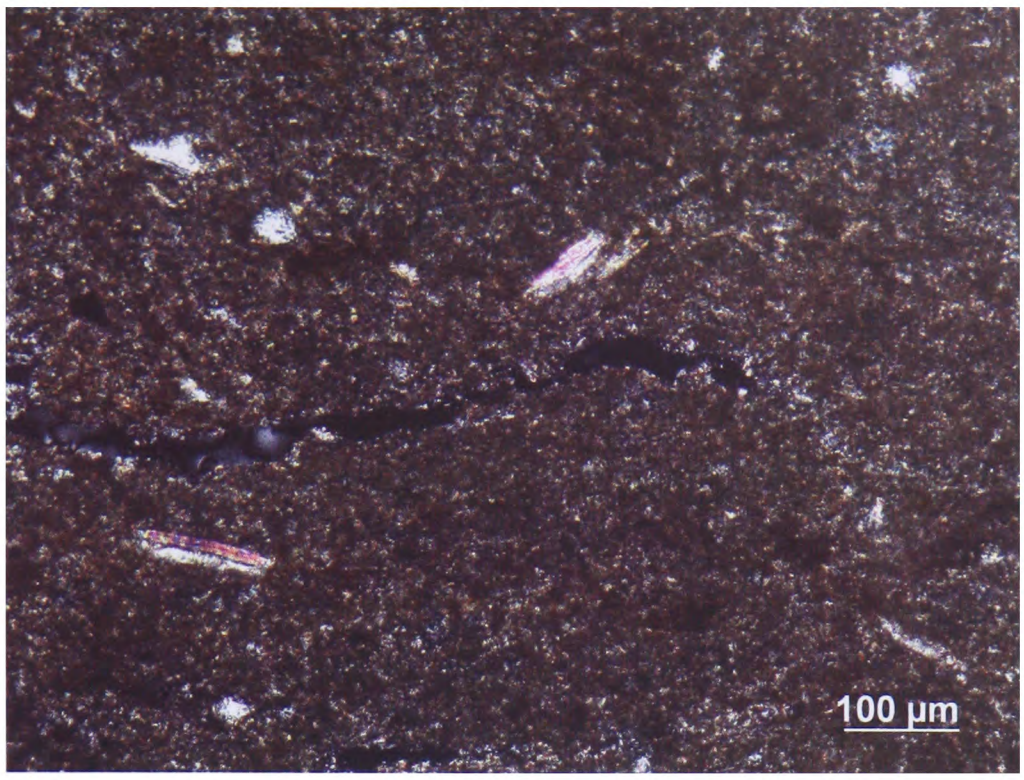

Figure 5.26: Thin section micrograph of SK 1 under crossed polars in transmitted light. An open vein and some muscovite flakes are shown. Some fragments of calcite along the edge of the vein indicate it was originally a calcite deposit.

SK 2

A mid grey-blue flagstone with uniform texture and a bed thickness of 40-50 mm. Grey-blue colour represents the unaltered material, but a weathered outer skin (5-10 mm thick), which is orange-brown colour is also apparent. This is a competent material when unaltered, but weathered surfaces are distinctly less competent. Outer surfaces (in the hand specimen) display syneresis cracks and sulphide inclusions are obvious on the boundary between weathered and unweathered sample.

XRD results: quartz, calcite, plagioclase feldspar, chlorite, kaolinite, muscovite, dolomite/ankerite, K-feldspar and pyrite. In the weathered section, carbonate is only a few % indicating it has been leached out of the stone. Ratio of quartz to feldspar is 1:1.23, averaged over two samples.

Thin section: Fine grained (<0.125 mm) sandstone with carbonate cement and very large areas of sulphide (mm scale) which form a border between the iron stained weathered section and the unweathered section. The sulphide masses are of messy and irregular shape mostly with some indication of cubed edges also there are other

grains present in the large sulphide masses (mica etc). Overall, a competent stone with a strongly weathered section adjacent to the layer of large pyrite (identified by XRD) inclusions. The weathered section appears to contain less cementing material. Grains are often poorly sorted and angular.

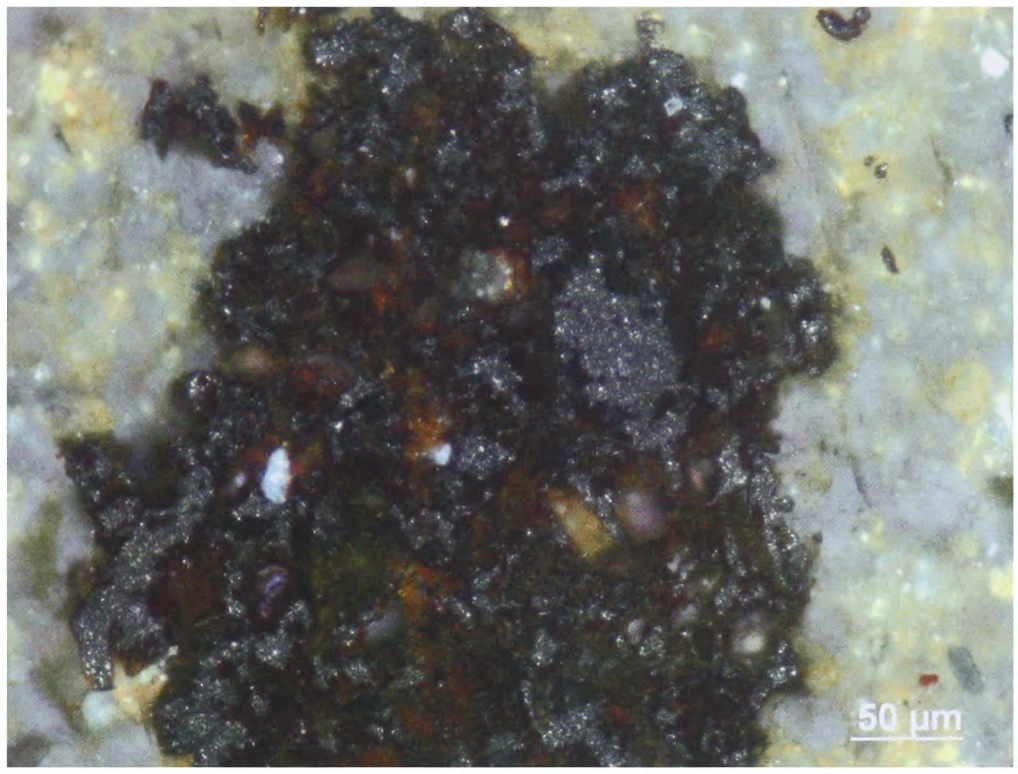

Figure 5.27: Thin section micrograph of SK 2 under plane polarised light in incident mode. A large pyrite crystal and iron stained surroundings are shown.

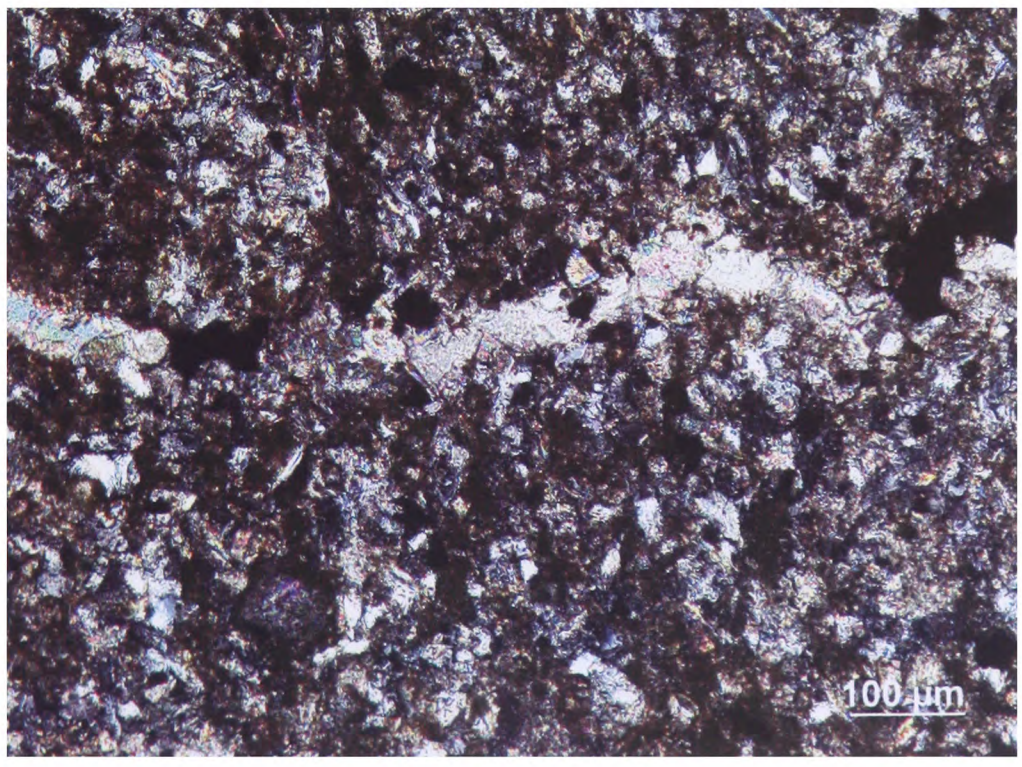

Figure 5.28: Thin section micrograph of SK 2 under crossed polars in transmitted light. Calcite vein and iron staining is shown.

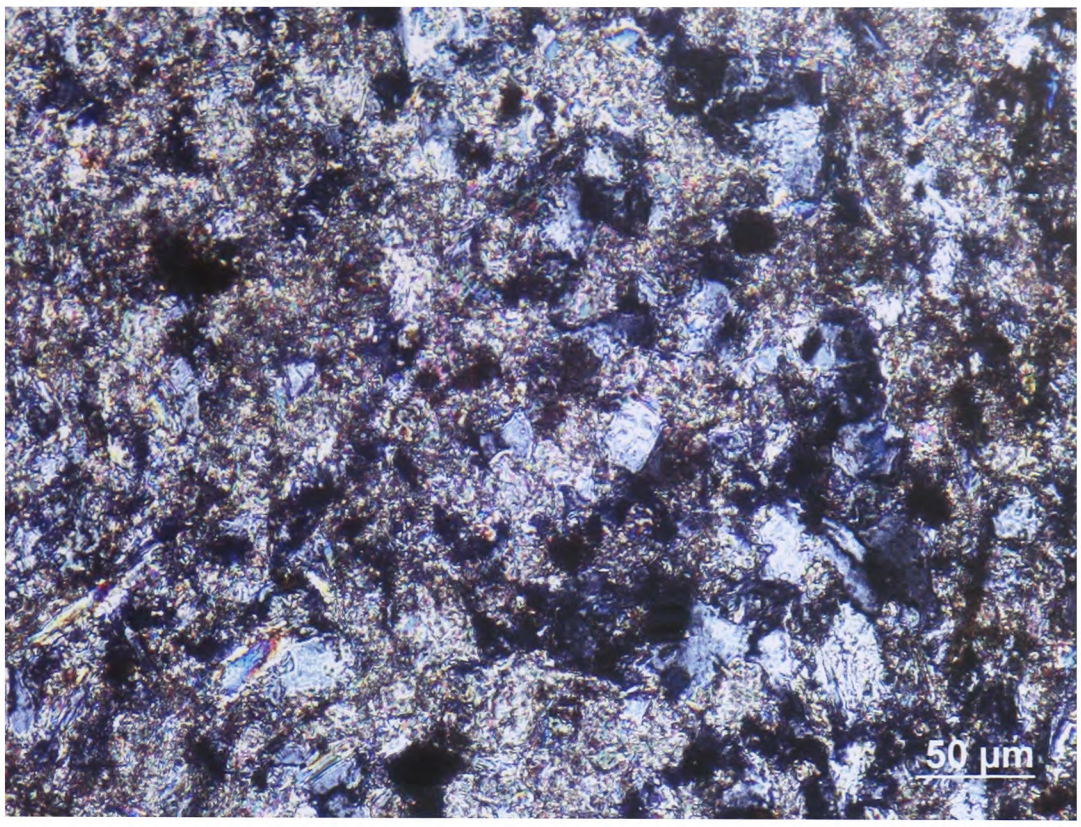

Figure 5.29: Thin section micrograph of SK 2 under crossed polars in transmitted light. This is the unweathered section, showing abundant calcite cement and fine grains.

SK 3

A light blueish grey flagstone comprising thick beds (several cms) but containing thinner laminated layers a few mm thick. There is an outer skin weathered to paler orange brown and syneresis cracks are evident in the hand specimen.

XRD results: quartz, calcite, dolomite, plagioclase feldspar, muscovite, K-feldspar, kaolinite and chlorite in the unweathered area. The weathered section was too thin to sample effectively. The ratio of quartz to feldspar is: 1:1.26. Overall, very similar to SK2, but without the obvious large sulphide inclusions.

SK 4

A dark grey flagstone showing no weathering with small muscovite flakes and possible black fossil fragments.

XRD results: quartz, calcite, ankerite/dolomite, muscovite, plagioclase feldspar, K-feldspar, kaolinite and chlorite. Ratio of quartz to feldspar is: 1:1.67.

Thin section: Laminar siltstone/fine grained sandstone (grain size <0.125 mm), with bands of organic rich mud and larger grained quartz and feldspar. Long black fragments of presumably fossilised material as they do not reflect in incident light. Overall, the most competent and unweathered of the background rocks. Grains appear to have a bituminous mud coating. This rock type can be seen in House 7 as some of the pieces in excellent condition. There appears to be little sulphide in this section and no weathering at all.

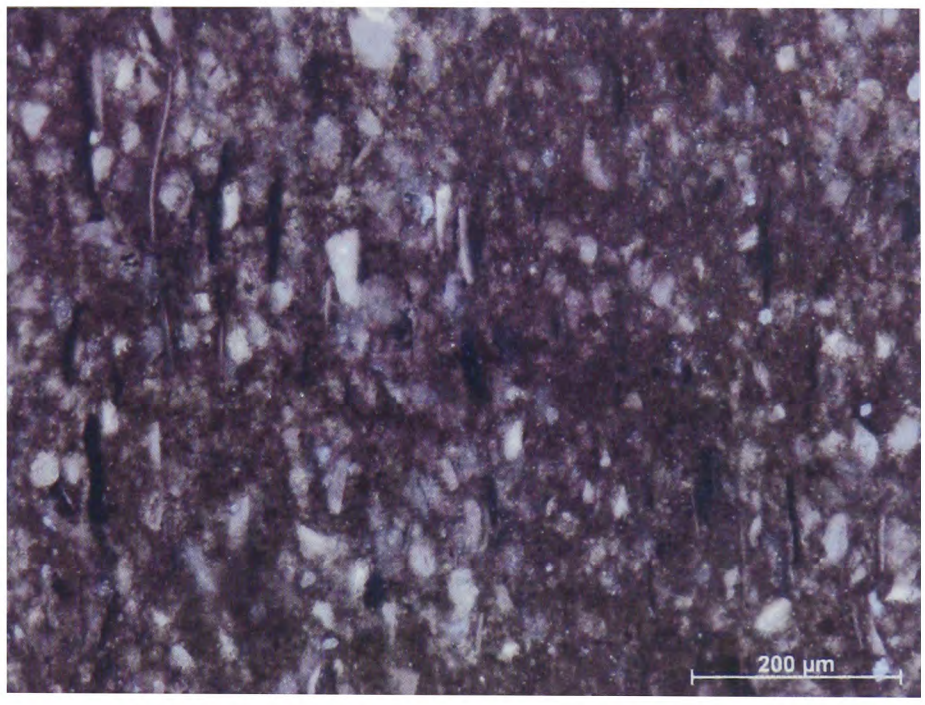

Figure 5.30: Thin section micrograph of SK 4, taken in plane polarised light in incident mode. The long black flecks are shown (presumably organic material).

SK 5

Pale blueish-grey flagstone with syneresis cracks on the outer surface. A weathered orange skin <10 mm thick is present. Very similar to SK 3.

XRD results: quartz, plagioclase feldspar, calcite, dolomite/ankerite, muscovite, K-feldspar and chlorite. Ratio of quartz to feldspar is 1:1.52 (averaged over two samples). These are the results for the unweathered section only.

SK 9

Laminated flagstone showing some deterioration with development of orange-brown weathered surfaces and delamination along the bedding planes with micaceous

surfaces. Bedding thickness is variable, and the colour of the beds varies (light brownish-grey to mid grey where fresh). A mixed lithology of 'muddy carbonate' beds containing syneresis types mixed with thinner bedded dark muddy shale layers.

XRD results: quartz, plagioclase feldspar, muscovite, K-feldspar and dolomite. These are the results for the unweathered section only as the weathered section was too thin to sample effectively. Ratio of quartz to feldspar is 1:1.42.

Thin section: a very laminar stone with varying grain size from siltstone to sandstone. Fractures look like calcite veins that have been picked out or dissolved out and are surrounded by iron staining. Some large (cm) syneresis features along the bedding. Iron staining (orange-brown in transmitted light and brighter orange in incident light) and some black staining is concentrated along the open fractures. There are also open pathways without iron staining, which could be sampling artefacts. Whether the black staining (remains opaque under incident light) is iron oxide or organic material is unknown. Altered sulphides are found throughout the section.

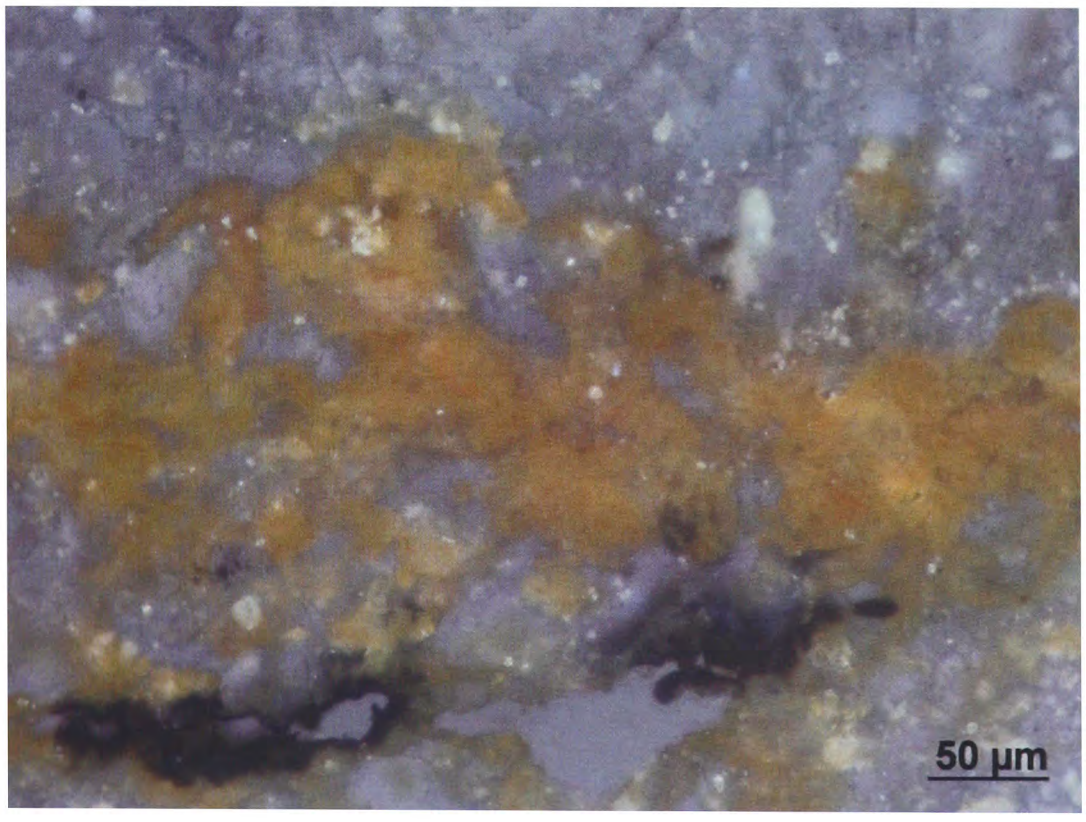

Figure 5.31: Thin section micrograph of SK 9, taken under plane polarised light in incident mode. Heavy iron staining around a weathered vein is shown.

SK 10

Thin irregular bedded pale grey-brown siltstone, weathered to orange-brown outer skin.

XRD results: quartz, plagioclase feldspar, dolomite, calcite, K-feldspar and muscovite. This is the constituent minerals of the unweathered section. Ratio of quartz to feldspar is: 1:1.29.

Thin section: Siltstone/fine grained sandstone. The outer crust is heavily stained with iron which obscures any cementing material present. It would appear the calcite cement is being leached out of the rock in places. Altered sulphides common throughout the section.

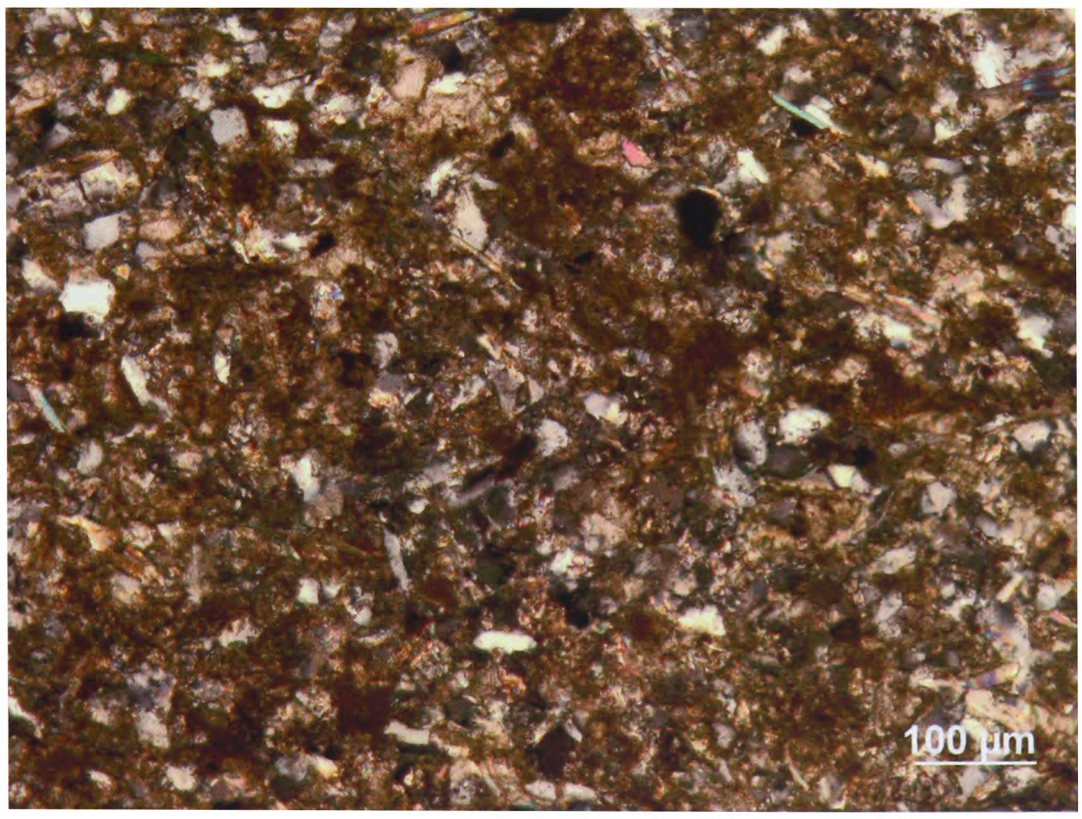

Figure 5.32: Thin section micrograph of SK 10 taken under crossed polars in transmitted light. General weathered appearance of the stone is shown and the angular nature of the poorly sorted grain structure.

SK 11

Thickly bedded (50-60 mm) carbonate (muddy limestone) with mid-grey blueish colour. A uniform internal texture weathering to a bright orange-brown outer skin (concentric weathering). One outer bedding surface shows syneresis cracks.

XRD results: Both the weathered skin and the very competent core material were sampled. The unweathered section contains ~ 26% carbonate, whereas the soft and friable weathered section contains no carbonate as detected by XRD. Mineral constituents are: Quartz, plagioclase feldspar, K-feldspar, calcite and dolomite/ankerite (carbonate in the unweathered section only) and muscovite. Ratio of quartz to feldspar is: 1 to 0.73 (unweathered, average of two samples) and 1 to 0.65 (weathered, average of two samples).

Thin section: Weathered siltstone/fine grained sandstone (grain size <0.125 mm) with distinct boundary between weathered and unweathered section. Weathered section is obscured by a heavy iron staining. Overall, fairly uniform, but showing distinct weathering. Altered sulphides common throughout section.

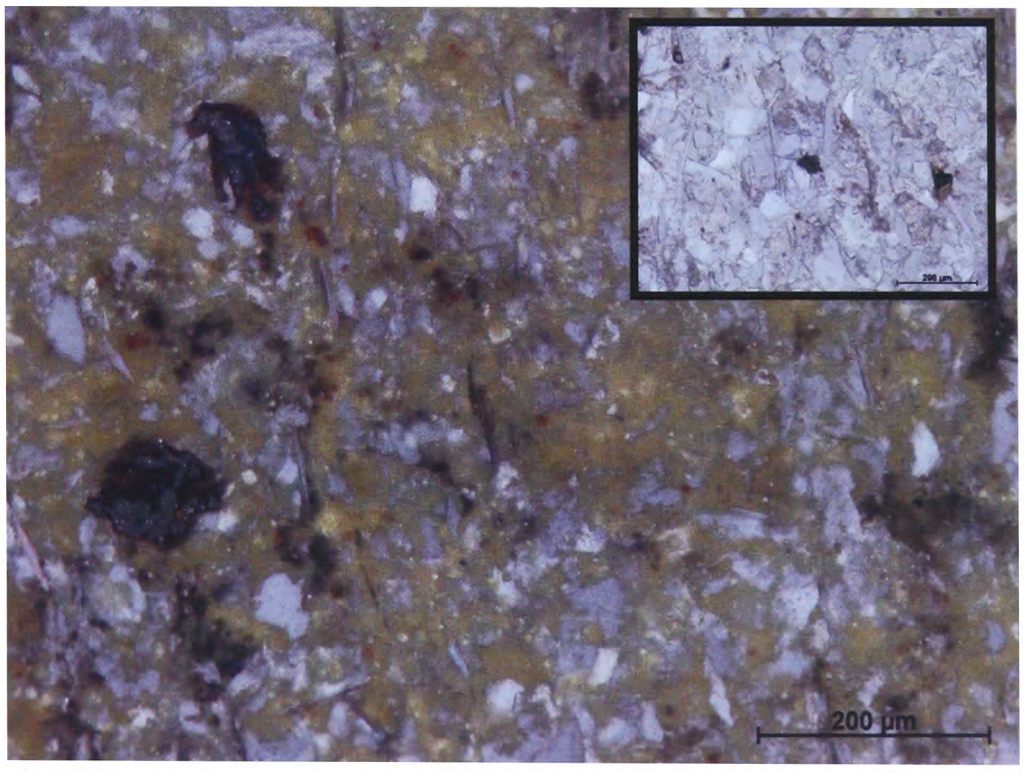

Figure 5.33: Thin section micrograph of SK 11 taken under plane polarised light in incident mode. General iron staining of the stone is shown and the angular nature of the grain structure. The top right hand corner image is of the unweathered area shown for contrast.

SK 12

Completely altered flagstone with strong orange-brown colour throughout. Very soft and permeable to water.

XRD results: No carbonate at all. Minerals present are quartz, plagioclase feldspar, K-feldspar and muscovite. The ratio of quartz to feldspar is 1 to 0.73 (average of two samples).

Thin section: Completely weathered sandstone/siltstone. The whole section has strong iron staining and exhibits secondary porosity. An open vein running through the section is strongly iron stained, indicating fluid transport and deposition of an iron mineral.

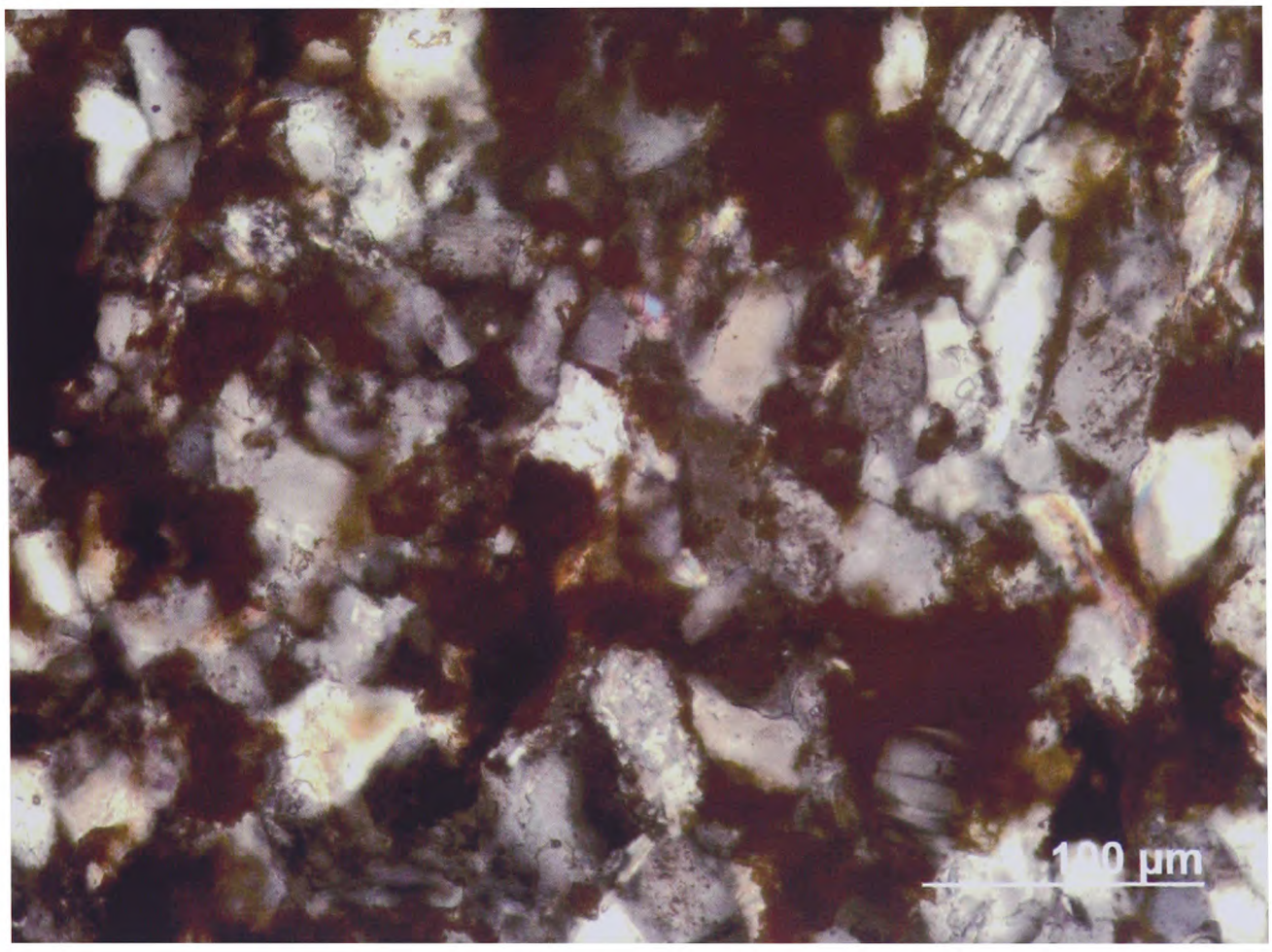

Figure 5.34: Thin section micrograph of SK 12 taken under crossed polars in transmitted light. General weathered appearance of the stone is shown and feldspar content is indicated by twinning (plagioclase) and possible untwined weathered grains of feldspar (dusty appearance). The angular nature of the grains is also emphasised. Scale bar reads 100 µm.

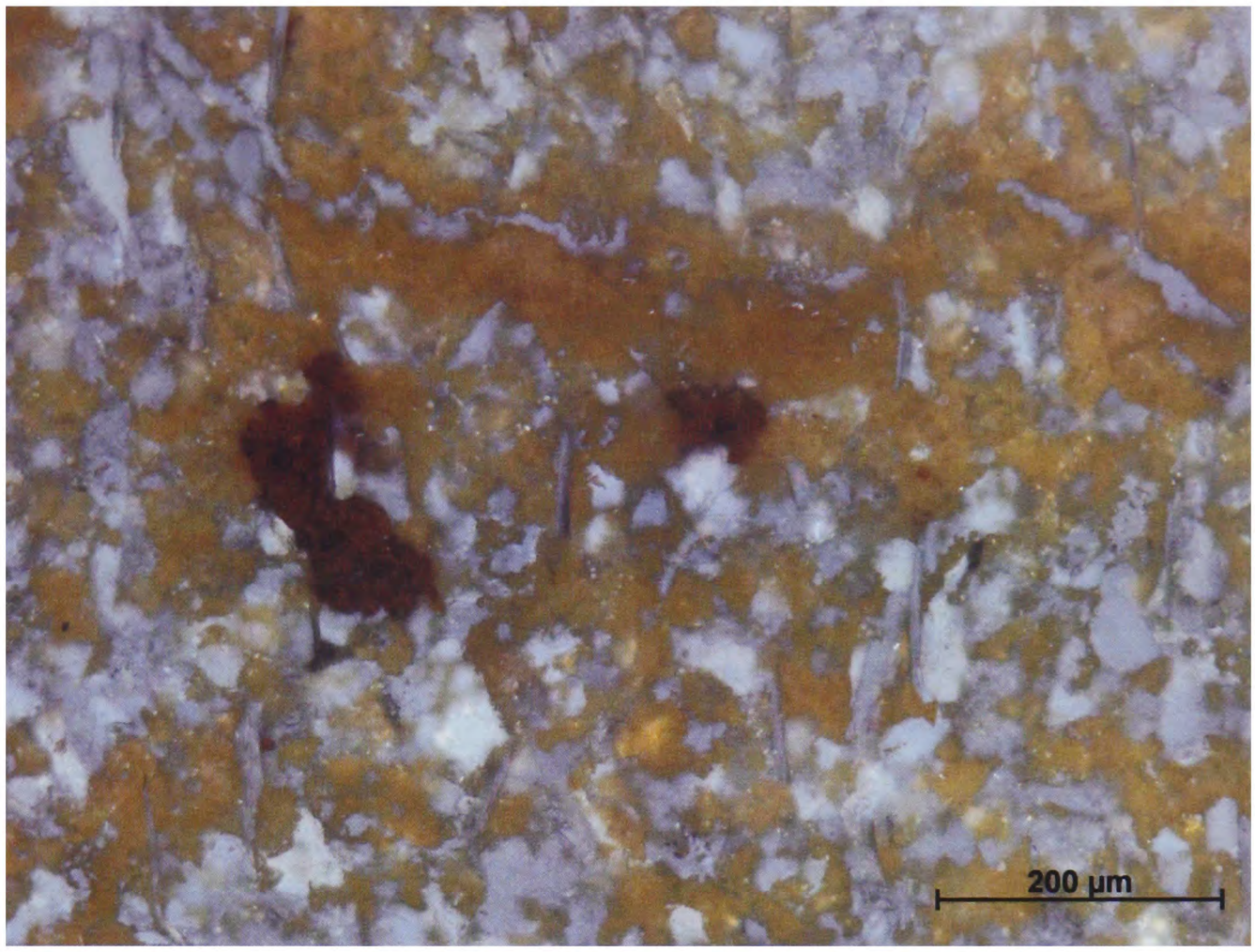

Figure 5.35: Thin section micrograph of SK 12 taken under plane polarised light in incident mode. Yellowish iron staining is shown with a darker red patch.

In many of the sections, staining can be bright orange in incident light (orange/brown in transmitted light) with patches of strong red. The strong red usually, although not always surrounds altered pyrite grains and is possibly another iron mineral although there is no analytical data available. The red colour is not as apparent in transmitted light as it is in incident light. Further analytical work could be undertaken to ascertain which iron minerals are present. The cementing material is calcite and dolomite, although ankerite cannot be ruled out from the XRD data. It is possible then that the rusty orange colour is in part due to the weathering of any ankerite present.

The poorly sorted and angular nature of the grains in the rock samples indicates that these sedimentary rocks were deposited close to the source of the grains. The percentage of feldspar in these samples is high, indicating that the source rock was feldspar rich. A granite outcrop, listed as a foliated granite of the Moine Supergroup (still in existence) is located 4 km away, which could provide the feldspar content and would also account for the chlorite found in some of the SK

rocks. Chlorite is a common product of the hydrothermal alteration of biotite, pyroxenes and amphiboles in igneous rocks [16] suggesting the incorporation of material from the nearby foliated granite. However, the consistently high percentage of feldspar in comparison to quartz in all the samples is considered unusual as the samples collected are unlikely to be from the same facies of the Stromness Flagstones (the nearest formation to the Bay of Skaill, as discussed p150) as indicated by their varying lithology. TOPAS calculates the mineral percentage from profile matching using a non-linear least squares method on a wt % basis and is known to be accurate. In order to confirm the accuracy of the TOPAS calculation 7 samples of known wt % composition made up of pure phases (quartz, calcite, albite, kaolinite, muscovite and pyrite) were analysed by Jiemen Lu, Geology, University of Edinburgh. The highest absolute error on albite analysis for these samples was no greater than 3.2 wt %, corresponding to a relative error of 12.9 %. The average absolute error was 1.17 % for albite, indicating that TOPAS is indeed accurate. However, why the feldspar content is so high in comparison to quartz, remains something of a mystery.

Figure 5.36: Syneresis cracks on an article in House 7. Syneresis cracks are a few cm long (c. 3 cm).

Syneresis cracks are evidence of a period of subaqueous exposure during the deposition of the sediment. This exposure may have resulted in saline conditions. Framboidal pyrite can form [17] at a redox front from oxygen bearing (possibly shallow) to hydrogen sulphide bearing waters, forming quickly from bacterial sulphate reduction in the presence of iron. Therefore it is possible that pyrite formed from bacterial sulphate reduction and during this subaqueous episode, which would account for the layer of pyrite found a few cm below the syneresis marked surface of SK 2.

A map of the geology of western Orkney [18] shows that the nearest flagstone formation to the Bay of Skaill is the Stromness Flagstones, which would seem the most likely material for the furniture of House 7. Fannin [18] describes the rock facies present in the Orcadian basin and their interrelationship. He describes generally fine, silty, calcareous sandstones which can, depending on the lamina being sampled, contain pyrite. He also mentions "iron-rich dolomite beds. They are obvious in the field because of their distinctive rusty orange weathering." Mention is also made of the bituminous matter present, which is observed in thin section (potentially SK 4) and general fine grain size. Syneresis cracks are evident on many of the articles in House 7, which indicates that some of the strata were laid down under evaporation conditions. However, despite the strong evidence of desiccation, no evaporite minerals have been found, and Fannin states that "evaporites are unknown in the Orcadian Basin" although Parnell [19] describes pseudomorphs after gypsum in the Old Red Sandstone Orcadian Basin, indicating some dubiety on the presence of evaporite minerals. It is fairly clear that the stone furniture in House 7 is constructed from Stromness Flagstone. The difference in the samples is accounted for by the varying composition of the facies.

5.5 Water transport testing and modelling

Water transport testing on the background rocks was undertaken to shed light on how susceptible to the transport of salt solutions the articles in House 7 are likely to be.

Sorptivity and vacuum saturation testing were the techniques used for this section. The porosity and sorptivity results are given in table 5.9.

Sample	Sorptivity mm $min^{-1/2}$	Porosity (1st set) %	Porosity (2^{nd} set) %	Porosity (3^{rd} set) %
SK 12	0.4743	30.91	28.35	
SK 4 Perp.	0.0004	1.52	1.82	
SK 1 Perp.	0.0708	15.34	15.23	16.23
SK 11 perp.	0.0610	11.30	11.46	11.92
SK 11 parallel	0.0017	0.70	1.07	0.92
SK 2 Perp.	0.0143	5.21	4.96	5.52
SK 2 Parallel		1.05		
SK 9 Perp.	0.0007	2.43	2.32	2.40
SK 9 Parallel		1.93	2.30	2.17
SK 5 Perp.	0.0109	2.91		3.31
SK 5 Parallel	0.0143	2.91		3.31
SK 9 Perp.	0.0101	2.12		2.53
SK 9 Parallel	0.0267	2.12		2.53
Cleris limestone	**1.49**	**29.0**		
Sander sandstone	**0.16**	**1.7**		
Léine limestone	**0.99**	**24.5**		
Engineering clay brick	**0.09**	**6.5**		
Savonnières limestone parallel	**0.66**	**38.0**		

Table 5.10: Comparison of all the sorptivity and porosity values for SK samples and some values for other typical building materials for comparison [20]. Sorptivity results are obtained by least squares fitting in MATLAB. Perp indicates that the sorptivity is measured perpendicular to the bedding planes, parallel indicates that the sorptivity is measured parallel to the bedding planes. The SK11 perp sample was mostly weathered crust, whereas the SK11 parallel sample had almost no weathered crust.

The sorptivity and porosity of the background rocks was determined gravimetrically and via vacuum saturation, in the case of the porosity measurement, and in accordance with experimental procedure laid out in Hall and Hoff [20]. The samples

(1^{st} set) were kept under vacuum for 1 hour before the pump was switched off and deionised water was allowed to flow in through a separate inlet in the chamber. The samples were consequently immersed in water (still under vacuum) for 3 hours before the chamber was vented and the samples were stored under water at atmospheric pressure overnight (c. 24 hours). For the second set, the samples were given 2 hours in air under vacuum and 6 hours immersion in water (still under vacuum) before the chamber was vented and the samples were stored under water at ambient pressure for about 48 hours. For the third set, the samples were under vacuum in air for 3 hours before immersion in water (still under vacuum) for a further 1 hour finishing with immersion in water at atmospheric pressure for 5 days. The samples are kept under vacuum to remove trapped air before being saturated with water so as to achieve a more accurate figure for the porosity. The first and second set of results was obtained by H. J. M. Fleck and the third set by the author.

The open (accessible) porosity is defined as a ratio of densities:

$$f = \frac{\rho_s - \rho_b}{\rho_s} \tag{5.9}$$

Where ρ_b is the bulk density and ρ_s is the solid density. Using liquid saturation methods, the porosity is defined as:

$$f = \frac{W_s - W_d}{V\rho_w} \tag{5.10}$$

Where W_s and W_d are the saturated and dry masses respectively of the specimen, ρ_w is the density of water and V is the bulk volume of the specimen. To calculate the bulk volume, the Archimedes principle was used:

$$V = (W_s - W_a)/\rho_w \tag{5.11}$$

Where W_s and W_a are the saturated weights in air and immersed in the saturating liquid (water) of density ρ_w, respectively.

The sorptivity, defined as the cumulative absorption per unit of inflow surface area A, is:

$$i = \frac{\Delta W}{\rho A} = St^{1/2} \qquad \textbf{(5.12)}$$

Where S is the sorptivity. This holds true only when the material is sufficiently fine pored that the effects of gravity can be neglected. A plot of i against $t^{1/2}$ gives the sorptivity value, which is defined as the gradient of the slope, providing the data can be represented as a straight line fit. The positive y intercept at $t^{1/2} = 0$ is due to surface and edge effects. Therefore unsealed samples (such as these) are prone to rapid filling of surface pores on the sides of the specimen [20]. Figures 5.37 and 5.38 are i against $t^{1/2}$ plots for the SK cores and larger samples respectively.

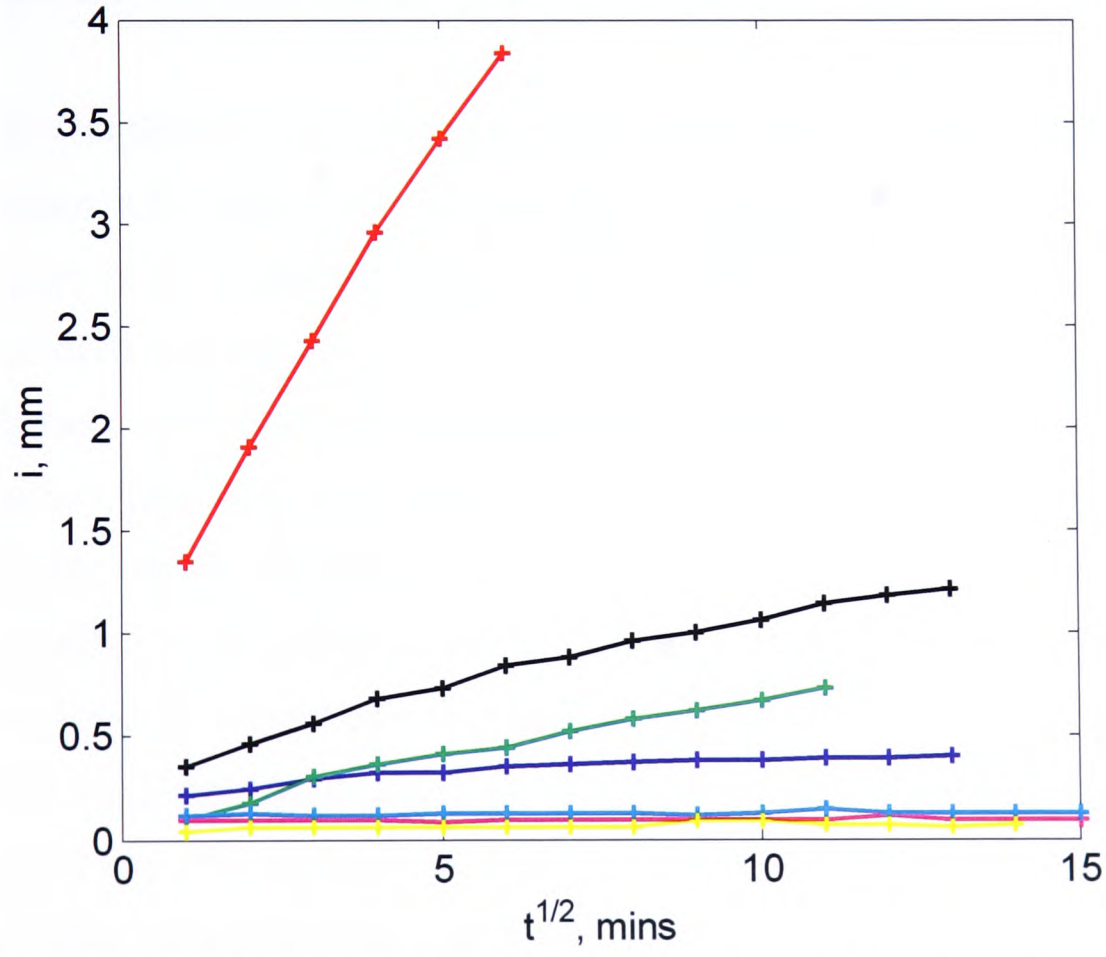

Figure 5.37: Sorptivity plots for SK 12 (red), SK 1 perpendicular (black), SK 11 perpendicular (green), SK 2 perpendicular (blue), SK 4 perpendicular (magenta), SK 9 perpendicular (cyan) and SK 11 parallel (yellow).

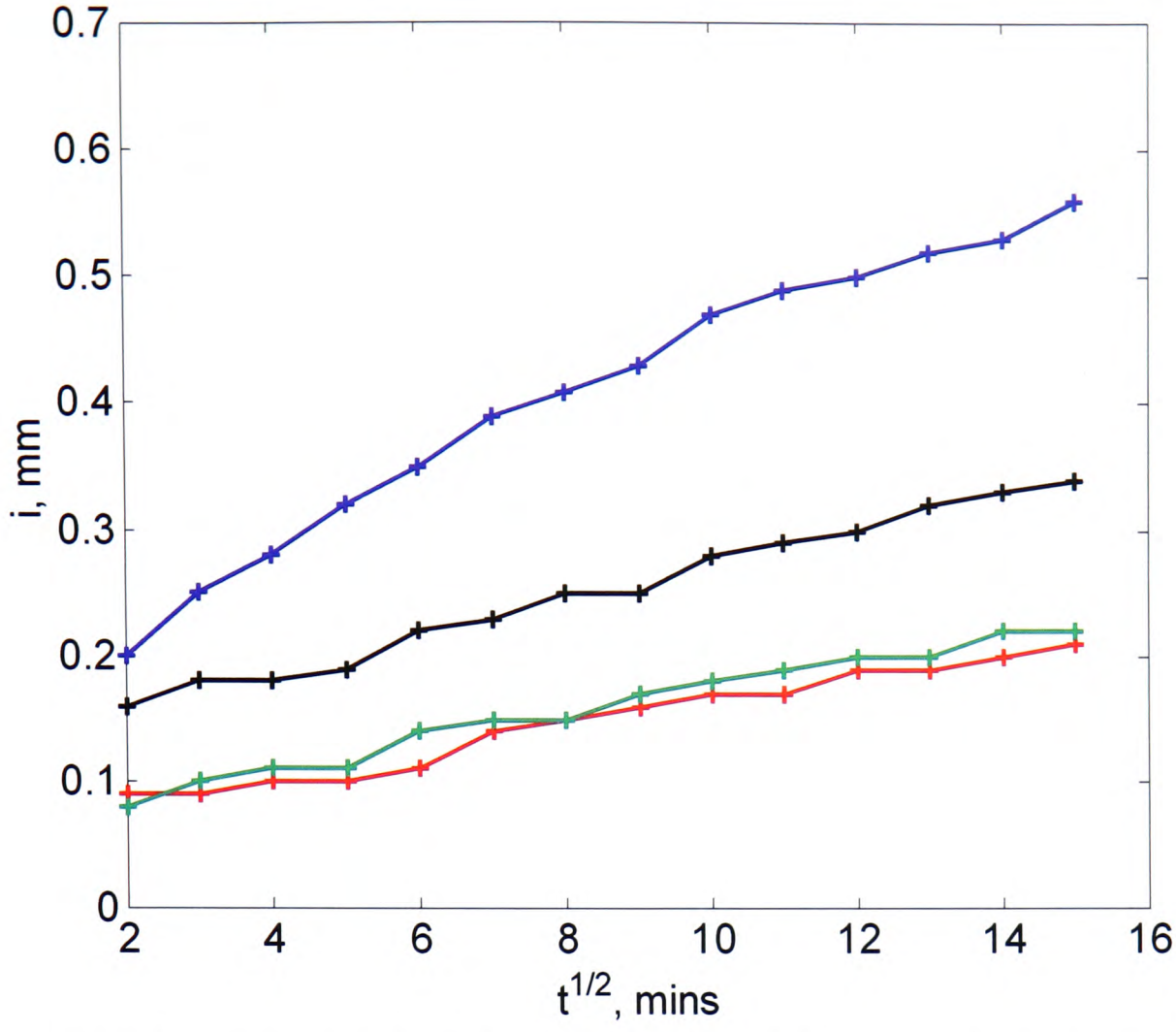

Figure 5.38: Sorptivity plots for SK 9 parallel (blue), SK 9 perpendicular (red), SK 5 parallel (black) and SK 5 perpendicular (green). These are new, larger samples.

The most striking aspect of these stones is the very low sorptivity and porosity. The 3 samples with higher porosity are SK 11 (perpendicular), SK 12 and SK 1. SK 1 appears to be a naturally friable material with little competence, SK 12 is the fully weathered specimen and SK 11 (perpendicular) is the weathered crust of SK 11 (parallel). The suspected high secondary porosity is confirmed directly by these two samples, indicating that water transport (including salts in solution) through these samples, unless weathered, is a very slow process. The sorptivity in different orientations with respect to the bedding was tested (larger SK 5 and 9 samples) and it was shown that water transport is slightly higher through the bedding layers (parallel to the bedding) than it is against the bedding, but the porosity and sorptivity values are still low. For comparison, some typical stone values are given and it is clear that the value for engineering clay brick (designed to have a low porosity) is closest in value to the unweathered specimens. The weathered samples behave more like conventional limestones (especially savonnières). The outcome is that the water

transport through these stones is very slow, with the possibility of a good deal of unconnected, closed pores. Parnell notes that these stones only exhibit significant porosity where the calcite is weathered out [21] which fits well with the results observed here.

5.5.1 MIP investigation

Due to the very low porosity of some of the samples, as indicated by vacuum saturation testing, two very different samples were sent for mercury intrusion porosimetry (MIP) to MCA services, Cambridge, UK for analysis. SK12 and SK4 were chosen as SK12 has a more regular porosity and SK4 is an example of the very low porosity stones present. MIP was used to check that the vacuum saturation results are accurate and to provide extra information on the pore size distribution of the sample. The results are shown below in figures 5.39 and 5.40.

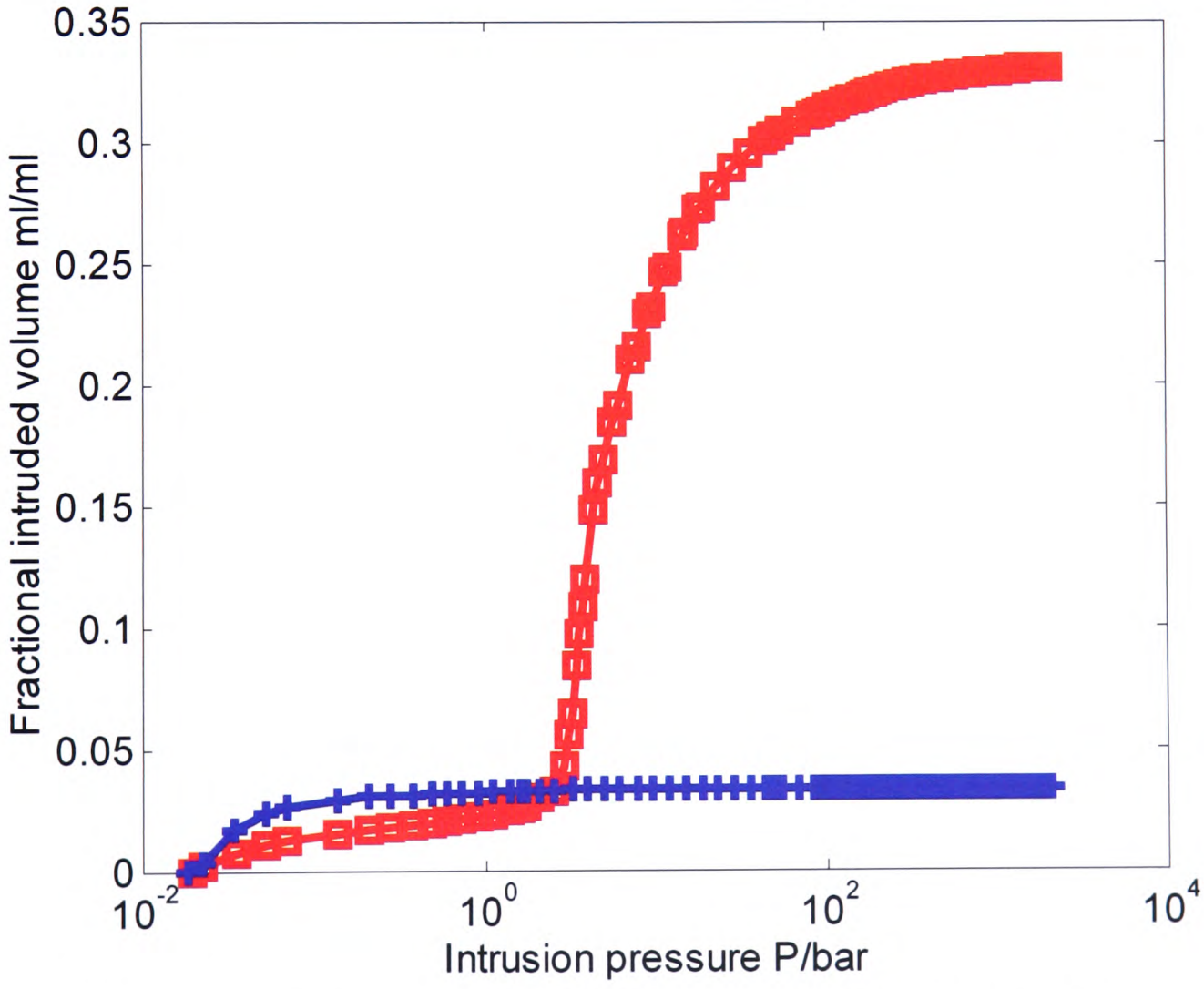

Figure 5.39: Mercury intrusion porosimetry profiles for SK12 (red) and SK4 (blue).

The open porosity of SK12 from the MIP plot is 34.3 %, which fits reasonably well with the vacuum saturation range of 28.5 % – 31.0 %. The point of inflection marks the point at which the mercury penetrates past the surface layer of the sample [20]. For SK 12 a pressure of 3.70 bar corresponds to this inflection point, which relates to an equivalent pore diameter of 4.012 μm, as can be seen in figure 5.40. It should be pointed out that this pore diameter cannot be taken too literally, and corresponds more to the largest diameter of a sphere of mercury that can percolate through the material [20].

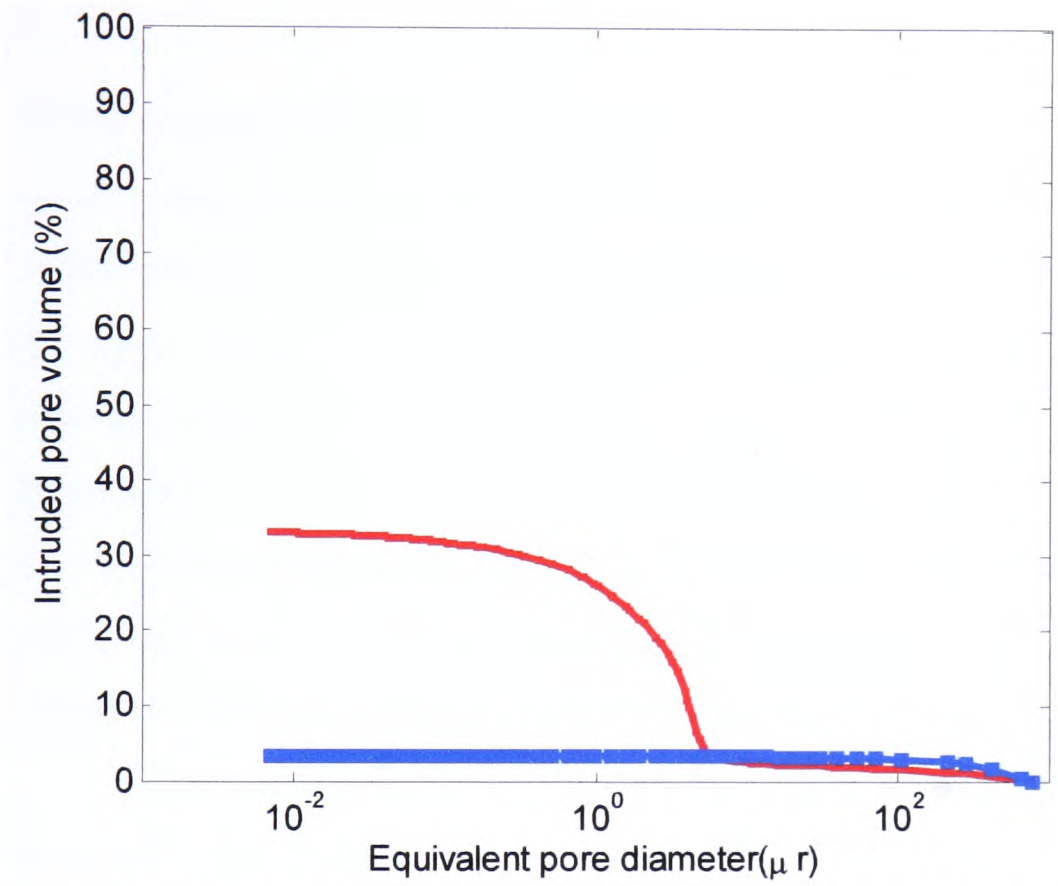

Figure 5.40: Equivalent pore diameter plotted against intruded pore volume. The red plot is SK 12, the blue is SK 4. The equivalent pore diameter is better thought of as the largest size of sphere of mercury that can percolate the pore system.

The plot for SK 12 is a fairly standard MIP plot for a porous building stone. The plot for SK 4 is more unusual. The porosity value for SK 4 is given as 3.34 % by MIP, which again fits reasonably well with the vacuum saturation values of 1.52 % and 1.83 % and confirms this to be a very low porosity material. Most notable is the lack of an inflection point. The pore sizes that can be probed by MIP vary from 100 μm at the lowest pressure to 2.5 nm at the highest [20]. Mercury probes the accessible pores, which would indicate that there are comparatively few open pores. It is also possible from the lack of inflection point that any undetected open porosity is too

fine to be seen by either technique used (MIP or vacuum saturation). This relates to the thin section and X-ray analysis in that the suspected secondary porosity of the highly weathered SK 12 is confirmed, in contrast to the low porosity of the unweathered SK 4. MIP gives an approximate value for the diameter of the largest sphere that can percolate through SK 12 (4.012 μm) but indicates, in the case of SK 4, that the vast majority of pores are either closed or too fine to be probed by this technique.

5.5.2 HYDRUS 2D modelling

Water transport (with or without solutes present) through the stones can be modelled in 2D using HYDRUS 2D [22]. This can provide information on the total mass of water, and hence soluble salts, that have been transported through the stone. A more thorough definition of water transport processes is given in the next chapter, but detailed here are the basic equations used by HYDRUS 2D to model the flow and discuss the parameters used. HYDRUS 2D numerically solves the Richards equation for saturated-unsaturated water flow and the convection-dispersion equation for heat and solute transport. The theoretical description given here is taken from [22], where a more detailed description of the package can be found.

The modified Richards equation assumes that the sample is a variably saturated, rigid, porous material exposed to a two dimensional, isothermal, Darcian flow of water and that transport in the vapour phase is insignificant. Darcy's law states that the volumetric flow of liquid through a porous medium obeys the simple relation: $Q = kA\Delta p/L$. Where Q is the volumetric flow rate, A is the cross sectional area, L is the length of the specimen, k is a constant and Δp is the hydrostatic pressure difference across the sample [20]. This applies to saturated flow only, for unsaturated flow, the permeability (k) becomes the capillary/hydraulic conductivity, K. The modified Richards equation uses K rather than k:

$$\frac{\partial \theta}{\partial t} = \frac{\partial}{\partial x_i}[K(K_{ij}^A \frac{\partial h}{\partial x_j} + K_{iz}^A)] - S \qquad \textbf{(5.13)}$$

Where θ is the volumetric water content, K is the unsaturated hydraulic conductivity function, h is the pressure head, S is a sink term, x_i are the spatial coordinates (i = 1,2, etc), t is time and K_{ij}^{A} are components of a dimensionless anisotropy tensor, which is used to account for an anisotropic sample. The sink term relates the volume of water removed per unit time from a unit volume of soil due to plant water uptake [22]. The main unsaturated parameters (saturated flow is a rarity under real conditions, therefore unsaturated flow is investigated here) are *K(h)* and *θ(h)* and are in general, highly non-linear functions of the pressure head. K is considered to be strongly dependant on θ. The water retention, *θ(h)* and conductivity *K(h)* functions are given by:

$$S_e = |\alpha h|^{-n} \qquad \text{When } h < -1/\alpha \qquad \textbf{(5.14)}$$

$$S_e = 1 \qquad \text{When } h \geq -1/\alpha$$

$$K = K_s S_e^{2/n+l+2} \qquad \textbf{(5.15)}$$

Where S_e is the effective water content and is defined as:

$$S_e = \frac{\theta - \theta_r}{\theta_s - \theta_r} \qquad \textbf{(5.16)}$$

In which θ_r and θ_s are the residual and saturated water content respectively [22]. α is the inverse of the air entry value or a bubbling pressure, n is a pore size distribution index and l is a pore connectivity parameter, K_s is the saturated hydraulic conductivity. n, l and α are empirical coefficients affecting the shape of the hydraulic functions [22].

Unsaturated hydraulic conductivity is expressed using the soil hydraulic function of Van Genuchten and the statistical pore size distribution of Mualem. The expressions of Van Genuchten are given as:

$$\theta(h) = \theta_r + \frac{\theta_s - \theta_r}{[1+|\alpha h|^n]^m} \qquad \text{when } h<0$$

$$\theta(h) = \theta_s \qquad \text{when } h \geq 0 \qquad \textbf{(5.17)}$$

$$K(h) = K_s S_e^l [1-(1-S_e^{1/m})^m]^2 \qquad \textbf{(5.18)}$$

where

$$m = 1-1/n \quad \text{when } n>1 \qquad \textbf{(5.19)}$$

The five independent parameters (θ_r, θ_s, α, n and K_s) make up in part the water inflow parameters, input into HYDRUS 2D by the user to define the flow problem. A third set of equations implemented in HYDRUS 2D are modified Van Genuchten equations to add flexibility to the description of the hydraulic properties near saturation.

$$\theta(h) = \theta_a + \frac{\theta_m - \theta_a}{(1+|\alpha h|^n)^m} \qquad \text{when } h<h_s \qquad \textbf{(5.20)}$$

$$\theta(h) = \theta_s \qquad \text{when } h \geq h_s$$

and

$$K(h) = K_s K_r(h) \qquad \text{when } h \leq h_k$$

$$K(h) = K_k + \frac{(h-h_k)(K_s-K_k)}{h_s-h_k} \qquad \text{when } h_k<h<h_s \qquad \textbf{(5.21)}$$

$$K(h) = K_s \qquad \text{when } h \geq h_s$$

Respectively, where

$$K_r = \frac{K_k}{K_s}\left[\frac{S_e}{S_{ek}}\right]^l \left[\frac{F(\theta_r)-F(\theta)}{F(\theta_r)-F(\theta_k)}\right]^2 \qquad \textbf{(5.22)}$$

$$F(\theta) = \left[1 - \left[\frac{\theta - \theta_a}{\theta_m - \theta_a} \right]^{1/m} \right]^m \quad \textbf{(5.23)}$$

$$S_{ek} = \frac{\theta_k - \theta_r}{\theta_s - \theta_r} \quad \textbf{(5.24)}$$

These equations allow for a non-zero minimum capillary height, h_s, by replacing the parameter θ_s in Van Genuchten's retention function by a fictitious (extrapolated) parameter θ_m slightly larger than θ_s. The change from θ_s to θ_m effects the value of the hydraulic conductivity function when n is small (e.g., $1.0<n<1.3$). For increased flexibility the parameter θ_r in the retention function was replaced by the fictious parameter $\theta_a \leq \theta_r$ [22].

This leaves 9 unknown parameters which comprise the full set of water flow input values, defined by the user in HYDRUS 2D. The simplest case is when $\theta_a = \theta_r$, $\theta_m = \theta_k = \theta_s$ and $K_k = K_s$ which uses Eqs. 5.17-5.19 and ignores the extra inputs for the near saturation case [22]. These parameters, being more applicable to soils than to rigid porous solids can be scaled to suit a solid for which some water transport parameters are known. The measured parameters available are the sorptivity and the porosity. The porosity is equal to the saturated water content which gives three parameters $(\theta_k, \theta_s, \theta_m)$ out of nine. The other parameters are scaled to produce a cumulative flow output that matches the measured sorptivity. The following relation is used for the scaling procedure:

$$S = (2 f_e K_e |\psi_f|)^{1/2} \quad \textbf{(5.25)}$$

Where K_e is the effective permeability or hydraulic conductivity of the material, f_e is the effective porosity and ψ_f is the effective capillary potential. There is experimental evidence that f_e is quite close to the saturation water content in many cases [20] therefore it is assumed to be so in this case. The capillary potential is related to α by the following law:

$$\alpha = \psi_c^{-1} \tag{5.26}$$

Therefore it can be assumed, and is confirmed in practice, that S varies as the square root of f_e and K_e, and varies as the reciprocal of the square root in the case of α. The residual water content is given a negligible, low value, such as 0.01 [23] and n is given a value between 1 and 2 depending on how coarse the pores are thought to be. For SK 12 a value of 1.7 was used, for SK 9 and 1, a value of 1.3 was used to reflect the comparatively finer pore structure. K_k, K_s and α were scaled (assuming K_s=K_k which is given by K_e) to produce an output sorptivity as close as possible to the measured sorptivity of the samples. The slab from area 4 (showing extensive damage) was modelled for this set of experiments. Boundary conditions were set to constant zero pressure for the inflow face and atmospheric for the other 3 faces. An initial pressure head was calculated from the capillary potential using the relation:

$$\ln\frac{p}{p_0} = -\frac{\psi_c M_L g}{RT} \tag{5.27}$$

Where P/P_0 is the RH, M_L is the molar mass of water, g is gravitational acceleration, R is the universal gas constant, T is the temperature in Kelvin and ψ_c is the capillary potential. An average RH and temperature, recorded in house 7 over the period November 2002 to March 2004 of 86.34 % and 10.23 °C respectively were used. The resulting capillary potential (in cm) was taken as the initial condition pressure head.

For the evaporation rate, sufficient data to calculate an accurate value was unavailable; therefore a value of 0.01 mm/hour was used. This is slightly lower than the value of 0.06 mm/hour which is given as the average evaporation rate under standard conditions of exposure in the UK [20], however the consistently high RH in House 7 is likely to lead to a reduced evaporation rate. This value is fairly arbitrary; a much more accurate value could be produced from setting up an evaporimeter on site.

The results listed in table 5.11 represent the preliminary stage only as they assume the stone is sitting in a pool of aqueous solution, which is not the case. A more realistic scenario would be water transport from the water table through the soil

to the monument, which is given in table 5.12. It should be noted that these results require further substantiation.

The results shown below in table 5.11 assume idealised hydraulic contact and uses the ICP-OES/IC results for the water collection sample (taken from the damp corner of the site – total ion count is 556 ppm) as an approximation of the dissolved salt content of the water being wicked up into the stone. The results given in table 5.12 are a re-run of the simulation but assume the solution is transported through one meter of soil before reaching the stone. In short, the results are based on the assumption that the water table is one meter below the site. Obviously this and the soil type (sandy clay) are purely an assumption that would require further field work for substantiation. For illustrative purposes, figure 5.41 a and b show the HYDRUS 2D material selection and output.

Sample	**Water flux through the sample per year**	**Maximum amount of solid salt deposited**
SK 1 (situated with water flow perpendicular to the bedding).	6.53 litres	3.63 g
SK 12	27.23 litres	15.14 g
SK 9 (situated with water flow perpendicular to the bedding).	5.15 litres	2.87 g

Table 5.11: The steady state water flux through each sample, using the geometry of the area 4 slab. The maximum amount of solid salt that could be deposited per year is also estimated.

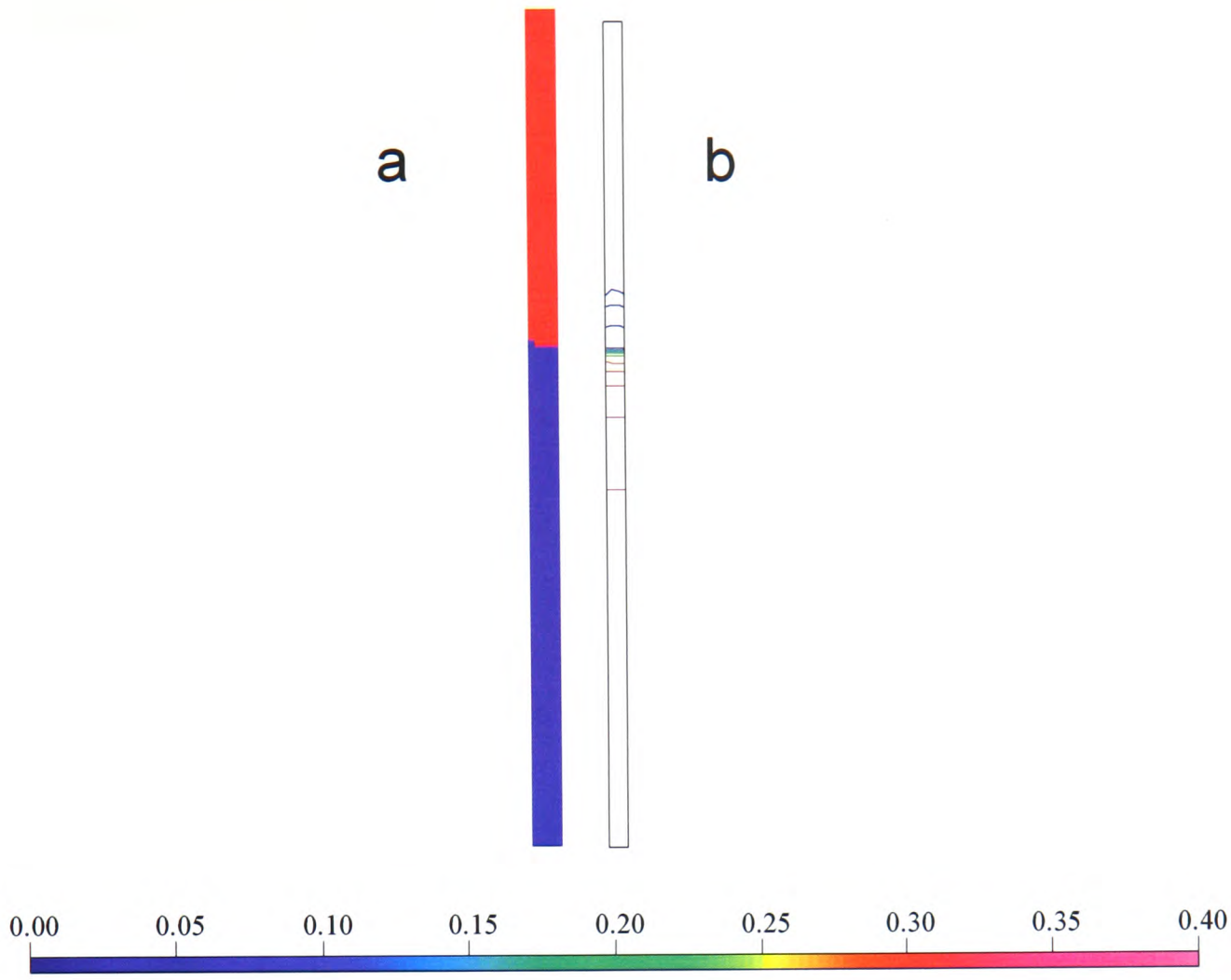

Figure 5.41: a is the material selection; red is the stone (SK12) section being modelled (57cm high by 3.5cm wide) and blue is the soil type (sandy clay, 1m high by 3.5 cm wide). b is the output (HYDRUS 2D) of the water transport after 1,000,000 minutes through SK12. The colour spectrum along the bottom indicates the water content which demonstrates how little water is being transported through the stone, even the porous ones. The stone slab dimensions are 57cm x 52cm x 3.5cm (area 4 on sketch diagram).

Sample	Water flux through the sample per year (steady state)	Maximum amount of solid salt deposited in g	Maximum amount of solid salt deposited over 5000 years
SK 1 (situated with water flow perpendicular to the bedding).	2.64 litres	1.47 g (0.00601% of the monument)	7350 g (23.12% of the monument)
SK 12	6.58 litres	3.65 g (0.01976% of the monument)	18250 g (49.70% of the monument)
SK 9 (situated with water flow perpendicular to the bedding).	1.64 litres	0.91 g (0.00320% of the monument)	4550 g (13.78% of the monument)

Table 5.12: The predicted amount of salt deposited per year and over 5000 years if the stone were dried out, based on the assumption that the aqueous solution has to travel through one meter of soil before reaching the stone.

The following assumptions were made to obtain the simulation results given in tables 5.10 and 5.11:

1. The stone monument dimensions are: 52 x 57 x 3.5 cm, which are measurements taken from a slab in area 4, showing severe decay.
2. The water table is located one meter below the site (table 5.11).
3. The soil type is sandy clay for the results in table 5.11. No flux boundary conditions are assumed for the soil transport (table 5.11).
4. The density values for the stone were taken from vacuum saturation results.
5. The aqueous solution is distributed evenly throughout the stone (in the case of columns 3 and 4 from table 5.11).
6. The water transport through the stone is constant once steady state is reached (this is unlikely as there will be distinct variations in the water table position and supply of water to the stone over 5000 years)

7. That there is no variation in the atmospheric boundary conditions, which is unlikely to be the real world case.

Obviously the amount of salt stated in table 5.10 is unlikely to be deposited at any one point in time. As the solution passes through the stone, the aqueous phase evaporates slowly at the atmospheric boundary potentially leaving small amounts of salt behind which are continually re-dissolved by solution moving through the material until supersaturation is reached with respect to a particular phase. Obviously gypsum crystallises readily as it has a low solubility of 1.9305 g $CaSO_4$ per kg of water at 10 °C [24], which corresponds to 1.9268 g $CaSO_4$ per kg of solution. From the ICP-OES/IC results the water collection solution contains 56.817 mg of $CaSO_4$ per litre of solution. Therefore, to reach the solubility of gypsum, roughly more than 33.9 litres (which corresponds to 5.2 years for SK 1 from table 5.10 data or 12.8 years from the more realistic values given in table 5.11) of solution would have to have deposited all ionic material (through drying presumably) in the transport path of the solution before this deposited material would stop going back into solution at the highest point of capillary rise. This is purely a rough approximation only and does not take into account the common ion effect or accurate solution modelling.

However, the figures give an idea of the time scales involved for the build up of salts to occur and indicate that this occurs over an extended period of time. The values given for the % of salt comprising the stone slab cannot be taken too literally, as they assume that the salt is distributed evenly throughout the stone. Also, a measure of the total dissolved solids from ICP-OES results was used, which does not guarantee that all of the salt exists in solid form unless the monument is dried completely, which is an unlikely scenario. The water transport simulation indicates that steady state is reached fairly early on, therefore the water or aqueous solution is not going to reach the top of the slab during the course of this simulation (694.4 days). It does give some indication of the potential (albeit higher than is likely) salt levels and more definite information on the water flux through the stone. These results represent preliminary investigations of this nature and as such require further substantiation.

5.6 Elastic modulus and swelling/drying stress

Samples of SK 1, 2, 4, 9, 11 and 12 were investigated for damage due to the hydration of clays by G. W. Scherer's research group at Princeton University, USA. From the XRD results, SK 1, 2 and 4 contain chlorite, kaolinite and muscovite, SK 9, 11 and 12 contains muscovite. Illite, although not obviously present, possibly exists as a trace amount in all of the SK samples.

It is understood that wetting and drying cycles can lead to the swelling and contracting of clay bearing stones [25-28] resulting in damage due to the stresses produced from each cycle. When a perfectly dry stone is wetted by rain, the surface tends to expand relative to the dry interior, resulting in compressive stresses in the wet region and tension in the dry region. As the depth of the wetted region increases, the volume of swelling stone increases, while the volume of dry stone resisting its expansion decreases. When the water has nearly reached the centre of the block, the small remaining volume of dry stone cannot resist the force exerted on it by the much larger volume of wet stone so the dry region is stretched by an amount equal to the swelling strain, ε_s. The tensile stress in the dry region at that point is given by Eq. 5.28

$$\sigma_d = \frac{E_{dry}\varepsilon_s}{1-\nu_{dry}} \tag{5.28}$$

Where E_{dry} is the elastic modulus and ν_{dry} (about 0.25) is Poisson's ratio for dry stone. If the fully saturated block begins to dry, then the surface layer will tend to contract, but its shrinkage will be prevented by the larger volume of wet stone in the block. This will result in tension in the surface layer, which is also given by Eq. 5.28. Since stone is typically about 10 times stronger in compression than in tension, it is usual for damage to result from the tensile stress. Indeed the "mud-cracking" pattern on stone of the stones in House 1 appear to have been caused by tension (a short discussion on observations from House 1 is given in the conclusions section).

A different type of damage is expected on the surface of a building, because the swelling of the stone is largely inhibited by the volume of the adjacent dry stone. Therefore, when the surface of a building is wetted, the surface is under threat of buckling, which would be enhanced if there was a natural defect or salt crystallisation, which would allow the layer of stone to 'peal' off more easily. The compressive stress in the wet surface is equal to the strength required to compress a swollen stone back to its original length and that is given by Eq. 5.29.

$$\sigma_s = \frac{E_{wet}\varepsilon_s}{1-\nu_{wet}} \tag{5.29}$$

Where E_{wet} is the elastic modulus and ν_{wet} (about 0.25) is Poisson's ratio for the wet stone. This stress does not usually exceed the compressive strength, but it may be sufficient to cause buckling. That is, the saturated layer will detach at some depth below the surface of the building and will bend outwards; the detachment is peeled open by tensile stresses. When this occurs, the surface of the stone is smooth, but there are cracks parallel to the surface at a depth that depends on the nature of the stone and the severity of the exposure. For example, if salt crystallises inside the stone, the damage from the salt can create a weak spot that initiates buckling.

The calculated stresses for the Skara Brae stones are presented in table 5.12. The elastic modulus was obtained by cutting thin plates of the stone and subjecting them to three point bending, either after drying in an oven at 60 °C or after saturating in water at room temperature. The modulus is calculated using Eq. 5.30

Sample	Wet Modulus	Dry Modulus	Swelling strain		Swelling Stress (Mpa)		Drying Stress (Mpa)	
	(GPa)	(GPa)	parallel	normal	parallel	normal	parallel	normal
SK01-1	7.23	17.2	7.36E-04	1.24E-03	-7.10	-11.98	**16.88**	28.51
SK01-2	5.94	15.1	7.36E-04	1.24E-03	-5.83	-9.84	**14.82**	25.03
SK02-2	40.5	57.2	1.80E-04	1.39E-04	-9.72	-7.51	**13.73**	10.60
SK02-5	48.6	67.9	1.80E-04	1.39E-04	-11.66	-9.01	**16.30**	12.58
SK04-1	36.2	65.2	8.14E-04	3.48E-03	-39.29	-167.77	**70.76**	302.18
SK04-4	31.8	52.9	8.14E-04	3.48E-03	-34.51	-147.38	**57.41**	245.17
SK09-1	43.1	63.3	2.40E-04	7.27E-04	-13.79	-41.78	**20.26**	61.36
SK11-1	49.4	62.4	5.50E-05	2.68E-04	-3.62	-17.65	**4.58**	22.30
SK11-2	49.4	50.2	5.50E-05	2.68E-04	-3.62	-17.65	**3.68**	17.94
SK12-1	1.89	6.26	5.80E-05	5.80E-05	-0.15	-0.15	**0.48**	0.48
SK12-2	1.86	4.91	5.80E-05	5.80E-05	-0.14	-0.14	**0.38**	0.38

Table 5.12: The swelling and drying stress as calculated from Eqs. 5.28 and 5.29. The strain was measured parallel and normal to the bedding planes as shown. The resulting stress for the normal direction is over estimated as the modulus of elasticity used for the calculation was measured parallel to the bedding plane.

$$E = \frac{WL^3}{4bh^3\Delta} \tag{5.30}$$

Where W is the force on the sample, L is the distance between the supports, b is the width of the sample, h the thickness of the sample and Δ is the deflection from horizontal. For this test, the samples were cut such that the long direction was parallel to the bedding, which is the stiffest direction.

The strain produced on swelling and drying was measured using a Perkin-Elmer differential mechanical analyser (DMA) by mounting a sample about 15 mm high in the device, then surrounding it with water at room temperature. Samples were cut both parallel and perpendicular to the bedding, since the amount of swelling is usually not equal.

The drying stresses are calculated from Eq. 5.28; drying causes tensile (positive) stresses, while wetting causes compressive (negative) stresses. Wetting always reduces the stiffness of the stone, sometimes by more than a factor of two, so wetting stresses are lower. The drying stresses are more significant as the site rarely gets rained on due to the presence of the roof. Many of the stones in Skara Brae are face bedded, so the stresses develop parallel to the bedding; consequently, the elastic

moduli obtained in the bending measurements are appropriate. However, the stresses would be over-estimates for any stones with natural bedding.

The tensile strength of the stone is unknown, although the bending strength of the Caithness Flagstone (a comparable stone to the unweathered samples) is known to be 37.2 MPa (data from the Building Research Establishment website). It is difficult to say which SK stone most resembles the Caithness Flagstone, its low porosity value (0.3 %) would indicate that SK 11 (unweathered) or SK 4 are possibly the closest matches. The high bending strength value of the Caithness Flagstone indicates it is a very strong, competent material. It is likely that the tensile strength of the much softer rocks (SK 1 for example) is easily exceeded by the drying stress. The tensile strength, on average of many stones falls within the range of 3-9 MPa [29].

Although the tensile strength is not known, and viscoelastic relaxation effects on the stress produced have not been taken into consideration, the data suggest that expansion contraction cycles could produce significant damage. However, the largest stresses are for SK 4, which represents the most competent monuments in House 7. It is probably significant that tensile damage seems to have occurred in House 1, which is not covered, while similar stones show a different mode of deterioration in the glass covered House 7. It can be assumed that this mechanism cannot be ignored and that cyclical wetting and drying should be avoided.

5.7 Conclusions

In this section, the cause of the extreme damage and spalling is discussed in terms of the potential damage mechanisms at work.

5.7.1 Salt damage

There is no very clear cut answer, but the following points provide the logic behind the conclusions:

- Very few samples are available from the upper region of the stones. This is important because the visual evidence of salt crystallisation is mainly along

the bottom of the stones. Water transport modelling using HYDRUS 2D indicates that the water transport, under the given environmental conditions of the site does not reach the upper half of the stone. Modelling simulated the water transport process over the course of 694 days rather than the lifetime of the site, but indicated that steady state conditions were reached during this time. This means that salt crystallisation is not expected in the upper half of the stone, based on those results only, however, the site was buried (with no covering roof) for thousands of years. Therefore the stones could have been saturated with salt water during this time. A salt content of 0.5 – 2 wt % was found in brushing samples from further up the stone, however, this does not necessarily indicate a salt weathering problem as the samples taken were few and could possibly be the result of wind blown particles. Further sampling and modelling could help to clarify this issue.

- A field study by Ibrahim et al. on salt weathering of archaeological sites attributes the decay present to salt weathering. The salt content of samples of weathered stone samples seems to have been 2-3 wt % [30] which is quite close the salt content of samples from this study.
- A source of salt containing water is continually seeping into the site.
- The powdery surface suggests granular disintegration from salt weathering.
- However, there were no visible salt crusts behind fallen fragments, although there was often powdery residue behind the samples from the summer visit which when X-rayed had the same composition as the rock with a few % halite.
- The Caithness Flagstones are known to be salt resistant. (http://projects.bre.co.uk/ConDiv/stonelist/caithflag.html).
- The slabs showing severe decay are also iron stained. The non-iron stained stones are in much better condition.
- The weathered slabs are thought to contain pyrite. This is also a serious decay mechanism which results in the dissolution of carbonate cement and substantial secondary porosity.

- Flaking was also apparent in the damp, high humidity winter months. Salts would be expected to remain in solution in winter, although the flakes could have been loosened during the drier summer months.
- The area showing the worst decay (area 3) is the corner furthest away from the damp area as shown on figure 5.4, which points to a mechanism other than salts.

5.7.2 Most likely cause of damage

Pyrite inclusions have been found in some of the fallen spall fragments which show characteristic iron staining (the secondary iron mineral has not been identified by analytical methods), although it should be noted that the weathering of any iron rich cementing material, such as ankerite can also produce iron staining without pyrite oxidation. That being the case, SK 4 shows no iron staining and no obvious pyrite, but has a dolomite/ankerite peak on the XRD trace in the same place as the stones showing staining. Two pdf cards show a good fit to the peaks: dolomite (pdf card 073-2409), and ankerite (pdf card 084-2066). It is difficult to say which is present over the other. Perhaps more likely is that both are present. If ankerite were solely responsible for the iron staining, it could be expected that SK 4 would also show staining. This conclusion possibly points to pyrite oxidation being the main cause of the iron staining, but it cannot be certain.

The heightened levels of calcium and sulphate, plus the strong correlation between them, could indicate that carbonate dissolution from sulphuric acid is responsible for some of the gypsum present on site, but again restricted sampling means that this conclusion cannot be certain. Water transport testing indicates that leaching out the carbonate cement results in a significantly higher sorptivity and porosity, making the stone much more accessible to moisture and hence salts. It can only be theorised that the stones in excellent condition (SK 4 as a comparative stone) have little pyrite content. The sampling of background rock types from around the site shows that within a small area, there are a variety of lithologies found within the Upper and Lower Stromness Flagstones.

It has been proven that swelling/contraction can produce significant stresses in these materials, how damaging this could be is uncertain, but the mechanism cannot be overlooked and cyclical wetting and drying would be best avoided for this site. This is an important point, which might influence the conservation methods used for these stones.

As only the iron stained stones show severe decay, it is likely that carbonate weathering (naturally or through pyrite oxidation) is required before salts can act. The low porosity of the unweathered samples coupled with the BRE data and the observation that unstained stones on the site are in good condition leads to the conclusion that carbonate weathering opens up the stone to salt weathering. It is not clear exactly how important the role of salts is for this site, but they should be considered during any conservation treatments. The high humidity of the site, while good for keeping salts in solution, encourages the oxidation of pyrite.

Sampling was restricted to salt/surface brushings, soil, sand and fallen stone flakes. As such it is difficult to be certain of whether pyrite oxidation is primarily responsible for the loss of carbonate. Comparison between SK 4 and SK rocks containing pyrite suggests that pyrite oxidation is important, but certainty is not guaranteed without further sampling from inside the site.

It would seem that the atmosphere in House 7 is less prone to extreme cyclical conditions than House 1, which is generally considered less damaging. It would appear that the cyclical conditions in House 1 lead to swelling/drying "mud-cracking" (based on photographs of the site only) which does not appear to be the case in House 7. The colour of the damaged stones in House 7 would indicate that the consistently high RH might be causing pyrite decay, which is not as obvious (visually) from the House 1 stones. The stones in House 1 are covered with a layer of thick white growth, which is presumably an organism of some sort. This makes assessment of the stone type challenging and might also act as a protective barrier. That being the case, there are signs of decay in House 1 too, but it is less severe than House 7. No samples were taken from House 1, therefore any thoughts on the decay of this site are based on photographs only.

is less severe than House 7. No samples were taken from House 1, therefore any thoughts on the decay of this site are based on photographs only.

Figure 5.42: White covering (presumably organic although no samples were taken) of the stones in House 1.

Figure 5.43: Cracking and damage on stones in House 1. Small corner image is a magnification of the circled area, which is estimated to be 20 mm wide. The scale of the stone 'furniture' is very similar to House 7.

5.8 References

1. Fleming, L., *Skara Brae: Environmental monitoring of house 7, relevant background information. Private communication.* 2004, Historic Scotland: Edinburgh.

2. Dell, J.H., *Plan of village at Skara Brae.* 1930, H.M. Office of works, Ancient Monument Department: Edinburgh.

3. Hyslop, E.K., *Report of a site visit to Skara Brae, Orkney. Report EE04/0764.* 2004, British Geological Survey: Edinburgh.

4. Price, C., *An Expert Chemical Model for Determining the Environmental Conditions Needed to Prevent Salt Damage in Porous Materials. Report.* 2000, University College London, University of East Anglia, Universitat Hamburg.

5. Bionda, D., *RUNSALT.* 2002: Zurich.

6. Stumm, W. and J.J. Morgan, *Aquatic Chemistry: An Introduction Emphasizing Chemical Equilibria in Natural Waters.* 2nd ed. 1981, Toronto: John Wiley and Sons.

7. Parkhurst, D.L. and C.A.J. Appelo, *PHREEQC for windows: A hydrogeochemical transport model.* 1999: Amsterdam.

8. Andersen, S.O., F. Larson, and D. Postma, *Pyrite oxidation in unsaturated aquifer sediments. Reaction stoichiometry and rate of oxidation.* Environmental Science and Technology, 2001. **35**: p. 4074-4079.

9. Appelo, C.A.J., E. Verweij, and H. Schafer, *A hydrogeochemical transport model for an oxidation experiment with pyrite/calcite/exchangers/organic matter containing sand.* Applied Geochemistry, 1998. **13**: p. 257-268.

10. Ritsema, C.J. and J.E. Groenenberg, *Pyrite oxidation, carbonate weathering, and gypsum formation in a drained potential acid sulfate soil.* Soil Science Society of America Journal, 1993. **57**: p. 968-976.

11. Hercod, D.J., P.V. Brady, and R.T. Gregory, *Catchment-scale coupling between pyrite oxidation and calcite weathering.* Chemical Geology, 1998. **151**: p. 259-276.

12. Ludwig, B., P. Khanna, R. Balkenhol, G. Friedrich, and R. Dohrmann, *Pyrite oxidation in a sediment sample of an open-cut brown coal mine: mineral formation, buffering of acidity and modelling of cations and sulfate.* Journal of Plant Nutrition and Soil Science, 1999. **162**: p. 499-509.

13. Jerz, J.K. and J.D. Rimstidt, *Pyrite oxidation in moist air.* Geochimica et Cosmochimica Acta, 2004. **68**: p. 701-714.

14. Fritz, S.J., *A survey of charge balance errors on published analyses of potable ground and surface waters.* Ground Water, 1994. **32**(4): p. 539-546.

15. Matero, F.G. and A.A. Tagle, *Cleaning, iron stain removal, and surface repair of architectural marble and crystalline: The metropolitan club.* Journal of the American Institute for Conservation, 1995. **34**: p. 49-68.

16. Deer, W.A., R.A. Howie, and J. Zussman, *The rock forming minerals*. 2nd ed. 1992, Essex: Pearson Education Limited.

17. Dogan Paktunc, A. and N.K. Davé, *Formation of secondary pyrite and carbonate minerals in the Lower Williams Lake tailings basin, Elliot Lake, Ontario, Canada.* American Mineraologist, 2002. **87**: p. 593-602.

18. Fannin, N.G.T., *The sedimentary environment of the old red sandstone of western Orkney. PhD thesis*, in *Sedimentology Research Laboratory*. 1970, University of Reading.

19. Parnell, J., *Evidence for evaporites in the ORS of Northern Scotland: Replaced gypsum horizons in Easter Ross.* Scottish Journal of Geology, 1985. **21**(3): p. 377-380.

20. Hall, C. and W.D. Hoff, *Water Transport in Brick, Stone and Concrete*. 2002, London: Spon Press.

21. Parnell, J., *Hydrocarbon source rocks, reservoir rocks and migration in the Orcadian Basin.* Scottish Journal of Geology, 1985. **21**(3): p. 321-336.

22. Šimúnek, J., M. Sejna, and M.T. Van Genuchten, *The HYDRUS 2D software package for simulating the two dimensional movement of water, heat and multiple solutes in variably saturated media*. 1999: Version 2.0, US Department of Agriculture, Riverside, CA.

23. Marshall, T.J., J.W. Holmes, and C.W. Rose, *Soil Physics*. 3rd ed. 1996, Cambridge: Cambridge University Press.

24. Brönsted, J.N., *International Critical Tables of Numerical Data, Physics, Chemistry and Technology (1st Electronic Edition)*, ed. E.W. Washburn. 2003: Knovel. p216.

25. Gonzalez, I.J., M. Higgins, and G.W. Scherer. *Hygric swelling of Portland Brownstone*. in *Materials Issues in Art and Archaeology VI*. 2002. PA, USA.

26. Gonzalez, I.J. and G.W. Scherer, *Effect of swelling inhibitors on the swelling and stress relaxation of clay bearing stones.* Environmental Geology, 2004. **46**: p. 364-377.

27. Scherer, G.W., *Characterization of saturated porous bodies.* Concrete Science and Engineering, 2004. **37**: p. 21-30.

28. Scherer, G.W. and I.J. Gonzalez, *Characterization of swelling in clay-bearing stones.* Geological Society of America, 2005. **Special paper 390**: p. 51-61.

29. Flatt, R.J., *Salt damage in porous materials:how high supersaturations are generated.* Flatt, R. J., 2002. **242**: p. 435-454.

30. Ibrahim, H. and K. Gamal, *The negative effect of environmental geological conditions of some geo-archaeological sites of North Coast and Alexandria.* Environmental Geology, 2005. **49**: p. 179-187.

6. Introduction

Salts move through a porous material in aqueous solution, therefore to understand salt crystallisation damage in stone, water transport must first be understood. The previous chapter touched upon the importance of water transport in a real life example of stone decay and the novel use of HYDRUS-2D for modelling water transport through stone. One small set of flagstones were analysed, which exhibited very different water transport characteristics: SK 12 had what might be classed as, 'usual' porosity and sorptivity for sedimentary rocks whereas SK 4 and SK 11 (unweathered) had remarkably low porosity and sorptivity. These important material characteristics merit further discussion, which in this case is achieved through the analysis of three common building materials. The results are compared with another four laboratories, which provides a rare insight into the accuracy of water transport measurements and discusses in depth the porosity, sorptivity and to an extent the pore structure of these building materials, demonstrating how pore structure has an effect on water transport properties. This chapter goes into more detail than the previous and offers a more thorough explanation through example of water transport in porous materials. This project was carried out as part of a European Union initiated study to develop a platform for assessment of computational heat, air and moisture (HAM) modelling in building physics and was named HAMSTAD.

6.1 Water transport characteristics of HAMSTAD materials

Three very different materials were investigated in a round robin inter-laboratory comparison of their hygric properties [1]. Calcium silicate (CS), autoclave aerated concrete (AAC) and ceramic brick (CB) were investigated by the University of Edinburgh using a variety of techniques, including vacuum saturation, sorptivity testing with water and a hydrocarbon (decane), mercury intrusion porosimetry, isothermal adsorption and NMR amongst many other techniques that will be discussed in turn. The hygric characterisation methods discussed here will be the ones which were carried out, at least in part, by the author.

6.1.1 Open porosity, density and vacuum saturation water content

An understanding of the pore structure of a material is essential when trying to understand the physics of fluid transport through it. Vacuum saturation, sorptivity testing and mercury intrusion porosimetry were used to investigate the pore structure and basic water transport.

The open porosity, f_o, of a sample is defined as the ratio of the open pores to the total volume of the sample, the bulk density, ρ, is defined as the ratio of the dry mass of the sample to its volume and the matrix density, ρ_{mat}, is defined as the ratio of the dry mass to the volume of the solid matrix, including closed pores. The following equations are used to define these characteristics:

$$f_o = \frac{m_w - m_d}{V\rho_l} \tag{6.1}$$

$$\rho = \frac{m_d}{V} \tag{6.2}$$

$$\rho_{mat} = \frac{m_d}{V(1-f_o)} \tag{6.3}$$

If an irregular shaped sample is used, the volume can be calculated using the 'Archimedes mass' (the mass of the saturated sample suspended in the saturating liquid) from the following relationship:

$$V = \frac{m_w - m_a}{\rho_l} \tag{6.4}$$

Where m_w is the saturated mass, m_d is the dry mass, m_a is the Archimedes mass, V is the sample volume and ρ_l is the density of the saturating liquid. Vacuum saturation is the method used to obtain these property values: the samples are dried to constant mass and placed in an airtight vacuum chamber which is then evacuated to an absolute air pressure of no greater than 2 kPa. The chamber is typically evacuated for 5 h, before water is allowed to flow into the chamber and immerse the samples,

which are then allowed to saturate for at least 24 h before being removed and weighed [2] or 18 h immersion (in the case of clay bricks). The results from vacuum saturation of the three specimens are given in tables 6.1 – 6.3. The other laboratories listed are: NRC (National Research Council, Canada), KUL (Katholic University of Leuven, Belgium), TNO (TNO Building and construction research, The Netherlands) and TUD (Technical University of Dresden, Germany).

Sample	% open porosity	matrix density	bulk density
AAC1	80.33	2283.91	449.31
AAC2	79.91	2279.49	457.89
AAC3	80.76	2292.85	441.07
AAC4	80.96	2370.20	451.38
AAC5	80.72	2385.16	459.84
AAC6	81.00	2305.64	437.96
AAC7	79.88	2159.15	434.49
AAC8	80.08	2247.96	447.70
AAC9	80.39	2298.61	450.81
AAC10	80.35	2266.98	445.53
AAC11	80.96	2345.19	446.55
AAC12	80.07	2232.45	444.88
AAC13	80.47	2286.40	446.45
mean (this data)	**80.45**	**2288.77**	**447.22**
mean (TNO)	**82.81**	**2572.24**	**442.03**
mean (TUD)	**82.15**	**2435.37**	**432.24**
mean (KUL)	**82.21**	**2555.42**	**454.52**
mean (NRC)	**81.50**	**2497.92**	**461.72**
stdev (this data)	**0.40**	**58.97**	**13.63**
Minimum (this data)	**79.88**	**2159.15**	**434.17**
maximum (this data)	**81.00**	**2385.16**	**474.97**

Table 6.1: Shown above. Open porosity, matrix density and bulk density (kg/m^3) of the HAMSTAD autoclaved aerated concrete specimens. This is the final data presented to the workgroup and incorporated in [1]. This work was carried out by Ioannis Ioannou at the UMIST, Manchester, UK.

Sample	% open porosity	matrix density	bulk density
CS1	87.43	2130.46	267.82
CS2	87.80	2195.08	267.80
CS3	86.94	2043.03	266.82
CS4	88.54	2327.14	266.69
CS5	87.55	2144.66	267.01
CS6	87.43	2110.22	265.23
CS7	88.15	2242.11	265.69
CS8	88.04	2233.95	267.18
CS9	88.08	2235.40	266.46
CS10	88.27	2257.89	264.85
CS11	87.52	2127.32	265.49
CS12	87.65	2147.21	265.18
CS13	87.50	2129.92	266.24
CS14	87.46	2097.21	262.99
CS15	87.80	2182.79	266.30
CS16	88.11	2225.23	264.58
CS17	88.09	2202.52	262.32
CS18	88.14	2233.64	264.91
mean	**87.81**	**2181.43**	**265.75**
mean (TNO)	**89.44**	**2548.77**	**269.24**
mean (TUD)	**89.52**	**2539.66**	**266.06**
mean (KUL)	**89.40**	**2549.19**	**270.32**
mean (NRC)	**89.56**	**2527.80**	**263.97**
stdev (this data)	**0.40**	**70.18**	**1.50**
minimum (this data)	**86.94**	**2043.03**	**262.32**
maximum (this data)	**88.54**	**2327.14**	**267.82**

Table 6.2: Shown above. Open porosity, matrix density and bulk density (kg/m^3) of the HAMSTAD calcium silicate specimens. This is the final data presented to the workgroup and incorporated in [1].

Sample	% open porosity	matrix density	bulk density
CB1	23.20	2652.42	2037.06
CB2	22.17	2611.14	2032.25
CB3	23.23	2667.11	2047.54
CB4	22.13	2577.83	2007.36
CB5	23.03	2621.98	2018.14
CB6	23.22	2670.34	2050.29
CB7	22.59	2637.62	2041.78
CB8	23.50	2641.08	2020.43
CB9	23.95	2670.28	2030.75
CB10	22.42	2636.04	2045.04
CB11	22.26	2595.96	2018.10
CB12	22.67	2646.44	2046.49
CB13	21.89	2607.94	2037.06
CB14	22.53	2630.49	2037.84
CB15	21.64	2604.52	2040.90
CB16	22.45	2616.84	2029.36
CB17	23.11	2666.73	2050.45
CB18	21.60	2600.96	2039.15
CB19	21.67	2559.52	2004.87
CB20	23.01	2676.80	2060.87
CB21	24.43	2703.89	2043.33
mean	**22.70**	**2633.14**	**2035.19**
mean (TNO)	**23.78**	**2631.39**	**2005.60**
mean (TUD)	**23.73**	**2612.81**	**1992.81**
mean (KUL)	**23.98**	**2632.66**	**2001.19**
mean (NRC)	**23.64**	**2628.75**	**2007.33**
stdev (this data)	**0.76**	**35.94**	**14.54**
min. (this data)	**21.60**	**2559.52**	**2004.87**
max. (this data)	**24.43**	**2703.89**	**2060.87**

Table 6.3: Open porosity, matrix density and bulk density (kg/m^3) of the HAMSTAD ceramic brick specimens. This is the final data presented to the workgroup and incorporated in [1].

Comparing the values with the other labs listed with the results produced by the University of Edinburgh, it is clear that the values are consistently lower. The reason for this is thought to be due to the vacuum system not completely fulfilling the requirements of the test. This hypothesis was tested by a new vacuum system, as old samples were remeasured and the results compared in table 6.4 below:

Sample	% open porosity – new vacuum system	% open porosity – original vacuum system
CB2	23.70	22.17
CB6	23.72	23.22
CB7	24.19	22.59
CB9	24.71	23.95
CB10	23.48	22.42
CB11	23.83	22.26
CB12	23.68	22.67
CB13	23.70	21.89
CB14	23.90	22.53
CB15	23.82	21.64
mean (this data)	**23.87**	**22.53**
stdev (this data)	**0.35**	**0.66**
mean (TNO)	**23.78**	
mean (TUD)	**23.73**	
mean (KUL)	**23.98**	
mean (NRC)	**23.64**	

Table 6.4: Comparison results between the same set of samples done twice using the original vacuum system and a new system. Samples re-measured by Dr V. A. Pugsley at the School of Engineering and Electronics, University of Edinburgh.

The new chamber appears to have a better seal and was using a more appropriate pump (a pump designed for fluids work), which is reflected in the slight increase in porosity of ceramic brick results. For inter-laboratory comparison, this highlights the necessity of using very accurate equipment, preferably using equipment of the same model and manufacturer in each laboratory.

It is obvious from the results that the AAC and CS samples are extremely porous. A more detailed investigation of these materials is presented later in this chapter. The pore structure of these three materials was investigated using MIP (Mercury Intrusion Porosimetry). Defining a porous material leads to the obvious question of what size are the pores? MIP attempts to answer this. As mercury does not wet the pores of inorganic materials, it must be driven into the pore structure by applying a hydrostatic pressure. Increasing the pressure allows the mercury to pass into finer and finer pores. There is generally, a point of inflection on the volume-pressure curve which marks the breakthrough from the surface layers of the sample into the interior [3]. The breakthrough pressure (P_c) can be related to the percolation threshold. Percolation relates connectivity of the open pore space of the material, the threshold is the point at which the open pores would become isolated if the material was compacted. Therefore, below the percolation threshold, there can be only closed pores but above it, there can be open and closed pores. For each applied pressure, the diameter of the mercury pore space interface is determined by the Washburn equation: $P_c = -4\gamma\cos\theta/d$ where γ is the surface tension of the mercury, θ is the contact angle, P is the capillary pressure and d is the local diameter of the pore space [4]. Turning this around and using l_c for the diameter and P_c (called P_t in Katz et al.) as the pressure at the point of inflection, we get $l_c \geq -4\gamma\cos\theta/P_c$ and take l_c to be the pore width (or the diameter of the largest sphere capable of passing through the pore throats). The contact angle of the mercury is taken to be 140 ° and the surface tension is taken as 485 dyn/cm as given by MCA Services, Cambridge, UK who carried out the MIP measurements. Obviously this is only a rough estimate as the contact angle and surface tension of the mercury in a porous material will vary from these values depending on the surface energy of the solid. More importantly, the Washburn equation assumes cylindrical pore geometry and l_c corresponds to the radius of the largest sphere of mercury that can pass through the material, which is much more idealised than the pore structure of a porous material can ever be. However, l_c does provide an estimate of the diameter of the open pores.

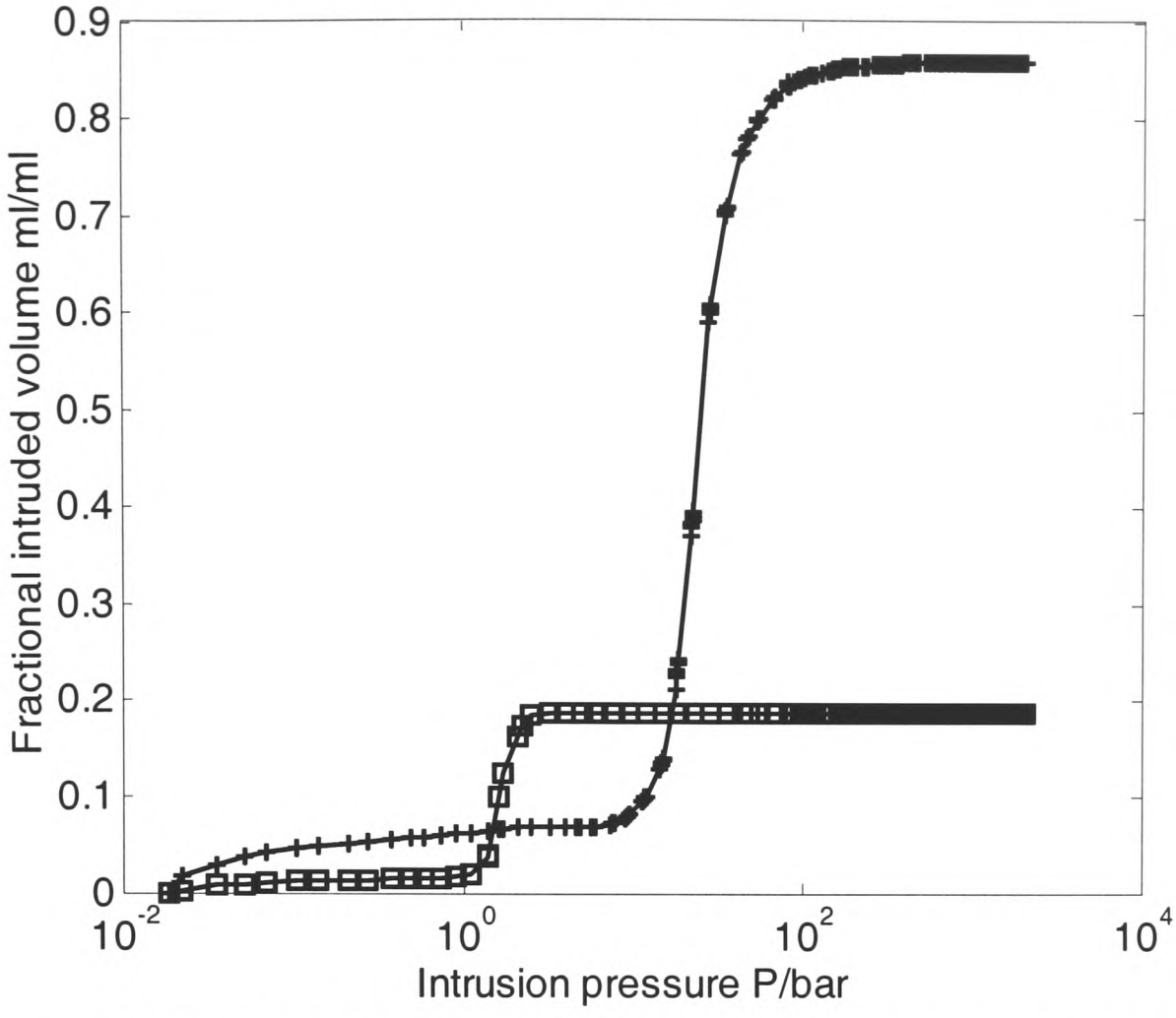

Figure 6.1: The MIP curves for CS (crosses) and CB (squares). The point of inflection (pressure in bar) is given as 1.42 bar for CB and 23.68 bar for CS.

The point of inflection corresponds to l_c values of 10.45 μm for CB and 0.63 μm for CS. This can be seen in figure 6.2. Clearly the CS is a much finer pored material with a good deal of open porosity resulting in a higher pressure and smaller sphere of mercury able to fully probe the open pores.

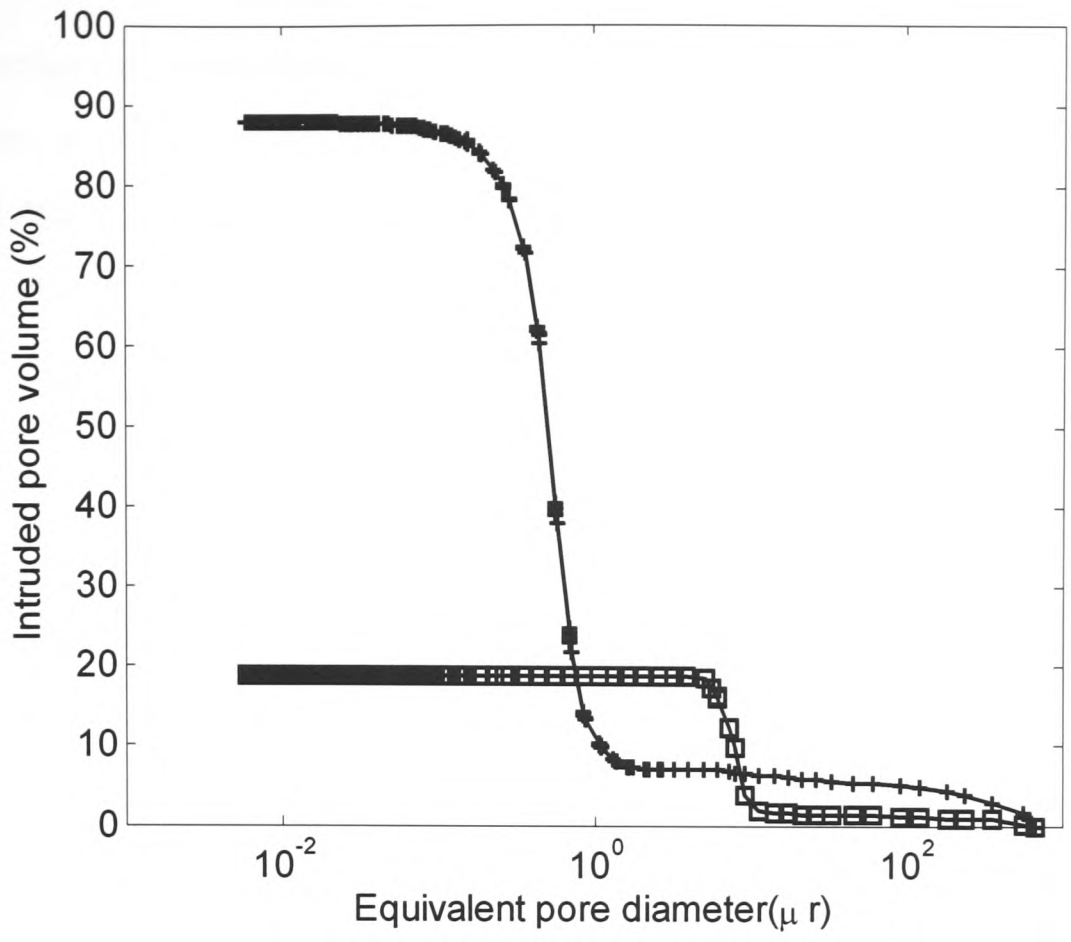

Figure 6.2: l_c is taken as the x axis while the intruded volume on the y axis represents the porosity of the sample as a percentage open porosity.

6.1.2 Sorptivity and capillary moisture absorption

While the previous section dealt with the characteristics of the material itself as described statically by fluid ingress methods, this section is primarily concerned with the fluid transport characteristics of the materials. Starting with the extended Darcy equation for unsaturated flow. The equations presented in this section are taken from [3]:

$$u = -K(\theta)F \tag{6.5}$$

where u is the velocity flow vector originated by the gradient of capillary potential in the material, K is the hydraulic conductivity function of the water content, θ and F is the capillary force [5]. F is identified with the negative gradient of the capillary potential ψ so that:

$$u = -K(\theta)\nabla\psi \tag{6.6}$$

Where $\nabla\psi$ is the gradient of the capillary potential [3]. Capillary potential is the suction of the material, which is known to be a function of the water content and is zero at complete saturation, increasing as water content falls [6]. K is also a function of the water content of the material. Combining Eq. 6.6 with a mass conservation equation leads to the well known Richards' equation:

$$\frac{d\theta}{d\psi}\frac{\partial\psi}{\partial t} = \frac{\partial}{\partial z}[K(\psi)\frac{\partial\psi}{\partial z} - K(\psi)] \qquad \textbf{(6.7)}$$

which is written as:

$$\frac{\partial\theta}{\partial t} = \nabla(K\nabla\psi) \qquad \textbf{(6.8)}$$

As the water content is a more easily measured quantity for rocks, we use the diffusivity to provide a connection. D =K(dψ/dθ). Therefore Eq. 6.8 becomes:

$$\frac{\partial\theta}{\partial t} = \nabla(D\nabla\theta) \qquad \textbf{(6.9)}$$

For one dimensional flow, this simplifies to:

$$\frac{\partial\theta}{\partial t} = \frac{\partial}{\partial x}(D\frac{\partial\theta}{\partial x}) \qquad \textbf{(6.10)}$$

$\theta = \theta_s$ at $x = 0$, $t \geq 0$

$\theta = \theta_0$ at $x > 0$, $t = 0$

using the Boltzmann transformation ($\phi = xt^{-1/2}$) Eq. 6.10 can be given in terms of ordinary differentials:

$$-\frac{\phi}{2}(\frac{d\theta}{d\phi}) = \frac{d}{d\phi}(D\frac{d\theta}{d\phi}) \qquad \textbf{(6.11)}$$

Integrating Eq. 5.11 between the limits $\theta = \theta_s$ (saturated) and $\theta = \theta_0$ (dry) leads to:

$$D(\theta) = -\frac{1}{2}\left(\frac{d\phi}{d\theta}\right)\int_{\theta_o}^{\theta}\phi d\theta \qquad \textbf{(6.12)}$$

The cumulative volume of water absorbed (per unit area) is given by:

$$i = t^{1/2}\int_{\theta_o}^{\theta}\phi d\theta = St^{1/2} \qquad \textbf{(6.13)}$$

Where the sorptivity is an integral function of the hydraulic diffusivity [5]. The theory states that water advances through the sample with a $t^{1/2}$ profile, which has long received practical confirmation. The sorptivity is measurable as a simple imbibition test, where a dry sample is allowed to absorb water through one face and the amount of water absorbed is determined by regular weighing. The sorptivity, *S*, is the gradient of the slope of *i* plotted against $t^{1/2}$, where *i* (cumulative absorption) in cm is the mass gain/density of the imbibing liquid/area of the imbibing face of the sample. The capillary absorption coefficient is essentially the sorptivity expressed in slightly different units ($kgm^{-2}s^{1/2}$). The capillary moisture content is equal to the moisture content of the sample at the transition from the first to the second stage of water absorption: The first stage represents the inflow of water into a dry sample while the second stage represents inflow into a capillary saturated sample. The inflow in the second stage is attributed to dissolution of trapped air as the sample and as such is minimal. The graphical appearance is that the inflow 'levels off'. At the turning point, where the graph appears to level off and the two fitted lines cross is the capillary moisture content (kgm^{-3}) and is equal to the moisture content of the sample at the transition from stage one to stage two. Tables 6.5 – 6.7 contain the data

Sample	Capillary moisture content, kgm^{-3}	Capillary abs. co. $kgm^{-2}s^{1/2}$
CB1	145.41	0.1396
CB2	145.77	0.1393
CB3	149.87	0.1394
CB4	144.31	0.1401
CB5	143.81	0.1423
CB6	147.71	0.1445
CB7	153.40	0.1534
CB8	155.14	0.1513
CB9	158.87	0.1569
CB10	145.59	0.1353
CB11	149.27	0.162
CB12	148.07	0.1405
CB13	148.09	0.1447
CB14	153.30	0.1393
CB15	151.01	0.1388
CB16		0.1434
CB17		0.1363
CB18		0.1434
CB19		0.1509
CB20		0.1405
CB21		0.1606
mean	**149.31**	**0.1449**
mean (TNO)	**146.27**	**0.1745**
mean (TUD)	**161.29**	**0.1476**
mean (KUL)	**149.59**	**0.1881**
mean (NRC)	**131.59**	**0.1328**
stdev (this data)	**4.34**	**0.0078**
min. (this data)	**143.81**	**0.1353**
max. (this data)	**158.87**	**0.1620**

Table 6.5: Capillary absorption coefficient and capillary moisture content data for ceramic brick – comparison data is given from the other laboratories.

Sample	Capillary moisture content, kgm^{-3}	Capillary abs. co. $kgm^{-2}s^{1/2}$
CS1	810.12	1.0797
CS2	813.54	1.1689
CS3	809.57	1.1831
CS4	812.88	1.1526
CS5	814.03	1.1778
CS6	815.99	1.1752
CS7	813.26	1.1428
CS8	811.47	1.1375
CS9	810.23	1.0874
CS10	812.28	1.1810
mean	**812.34**	**1.1486**
mean (TNO)	**801.48**	**1.2359**
mean (TUD)	**817.83**	**1.1842**
mean (KUL)	**811.14**	**1.3022**
mean (NRC)	**765.91**	**1.1618**
stdev (this data)	**2.02**	**0.0378**
min. (this data)	**809.57**	**1.0797**
max. (this data)	**815.99**	**1.1831**

Table 6.6: Capillary absorption coefficient and capillary moisture content data for calcium silicate plate – comparison data is given from the other laboratories.

Sample	Capillary moisture content, kgm^{-3}	Capillary abs. co. $kgm^{-2}s^{1/2}$
AAC1	261.74	0.0313
AAC2	304.70	0.0371
AAC3	301.58	0.0378
AAC4	310.13	0.0350
AAC5	270.57	0.0321
AAC6	262.62	0.0319
AAC7	240.45	0.0314
AAC8	272.03	0.0285
AAC9	284.38	0.0318
AAC10	245.20	0.0330
mean	**275.34**	**0.0330**
mean (TNO)	**240.64**	**0.0230**
mean (TUD)	**329.75**	**0.0398**
mean (KUL)	**305.81**	**0.0312**
mean (NRC)		**0.0282**
stdev (this data)	**24.38**	**0.0028**
min. (this data)	**240.45**	**0.0285**
max. (this data)	**310.13**	**0.0378**

Table 6.7: Capillary absorption coefficient and capillary moisture content data for autoclaved aerated concrete, carried out by Ioannis Ioannou, UMIST, Manchester, UK – comparison data is given from the other laboratories.

While the open porosity results obtained by vacuum saturation exhibited a very close comparison between laboratories, the spread of results is much greater for the imbibition test. The data is shown in table 6.8.

measurement	Average (from TNO, TUD, UE, NRC, KUL)	maximum – minimum (from TNO, TUD, UE, KUL)	% spread
Capillary absorption coefficient - AAC	0.0310	0.0111	35.76
Capillary absorption coefficient - CS	1.2065	0.1387	11.49
Capillary absorption coefficient - CB	0.1576	0.0468	29.71
Capillary moisture content - AAC	287.8850	88.3500	30.69
Capillary moisture content - CS	801.7400	17.7680	2.22
Capillary moisture content - CB	147.6100	20.6700	14.00

Table 6.8: Column two is the average of the average result of the group of participating laboratories for the measurement indicated in column one. Column three is the average of the maximum results minus the average of the minimum results. Column four is the % of spread in the results taken from the two preceding columns.

As table 6.8 shows, the imbibition test presented more of a problem to the participating laboratories than the vacuum saturation test. Clearly, the greatest spread in results can be found in AAC and the least in CS. The following factors have been identified as perhaps contributing to the spread:

1. The sorptivity test requires that the sample be weighed at regular intervals. The sensitivity and quality of the balance is a variable but more important is the method used for weighing the sample: it is standard practise to wipe the absorbing face of the sample with a damp cloth before weighing. This procedure could introduce some errors as it is very much dependant on the skill and experience of the experimentalist carrying out the measurement.

2. The fitting of sorptivity plots. How many points are included in the plot and what method is used to fit the points will determine the gradient. It is clear from the AAC capillary moisture content results that allocating a point of transition from first to second stage water uptake is difficult, as there is often no clear graphical distinction between the two stages. This is reflected in the large standard deviations reported by all laboratories carrying out this measurement.

3. The bimodal pore system of the AAC results in a slightly different sorptivity, but how the data is fitted is the most likely cause of error. It was this laboratory's policy to only fit the straight line segment and not force-fit a straight line through any curvature.

4. The HAMSTAD instruction document asks for the sides of the samples (i.e. all faces except the imbibing face and the face parallel to it) to be sealed. This was done (using epoxy resin) for AAC, but not for CS and CB as was reported with the results to the HAMSTAD co-ordinator.

It is clear that the sorptivity of AAC is the most interesting of the three sample types. A further observation on this point is the swelling of AAC samples in contact with water, which was investigated further and the results of which are presented in the next section.

6.2 AAC sorptivity

The trimodal pore structure of AAC is an important factor in the water transport characteristics of the material and is a direct result of the manufacturing method. AAC is usually manufactured from a mixture of finely ground silica sands, Portland cement, lime and water. Adding aluminium powder to the slurry before decanting the mix into a mould and allowing it to 'rise' in an oven develops its cellular or foaming character. After the slurry has obtained sufficient competence it is removed from the mould and autoclaved at 180 °C for 10 to 16 hours[7, 8]. The

trimodal pore size distribution consists of a fine pored matrix of high suction, within which are dispersed large aeration pores formed by foaming the wet slurry during manufacture. Some macro pores are also in evidence (figure 6.5) and have been described as connecting the coarse aeration pores (typical diameter of aeration pores is 0.1 -1.0 mm) to the finer matrix pores [9]. The connectivity of the pore structure was studied by Roels et al. who identified that 75 % of the aeration pores are accessible by the macro pores. The microstructure of the material can be seen from three SEM images of the sample, figures 6.3 – 6.5. The pore structure is assumed to be bimodal, since it is the water uptake into pores that exhibit classical $t^{1/2}$ sorptivity (both micro and macro pores) and the large aeration pores, which do not, that is being investigated.

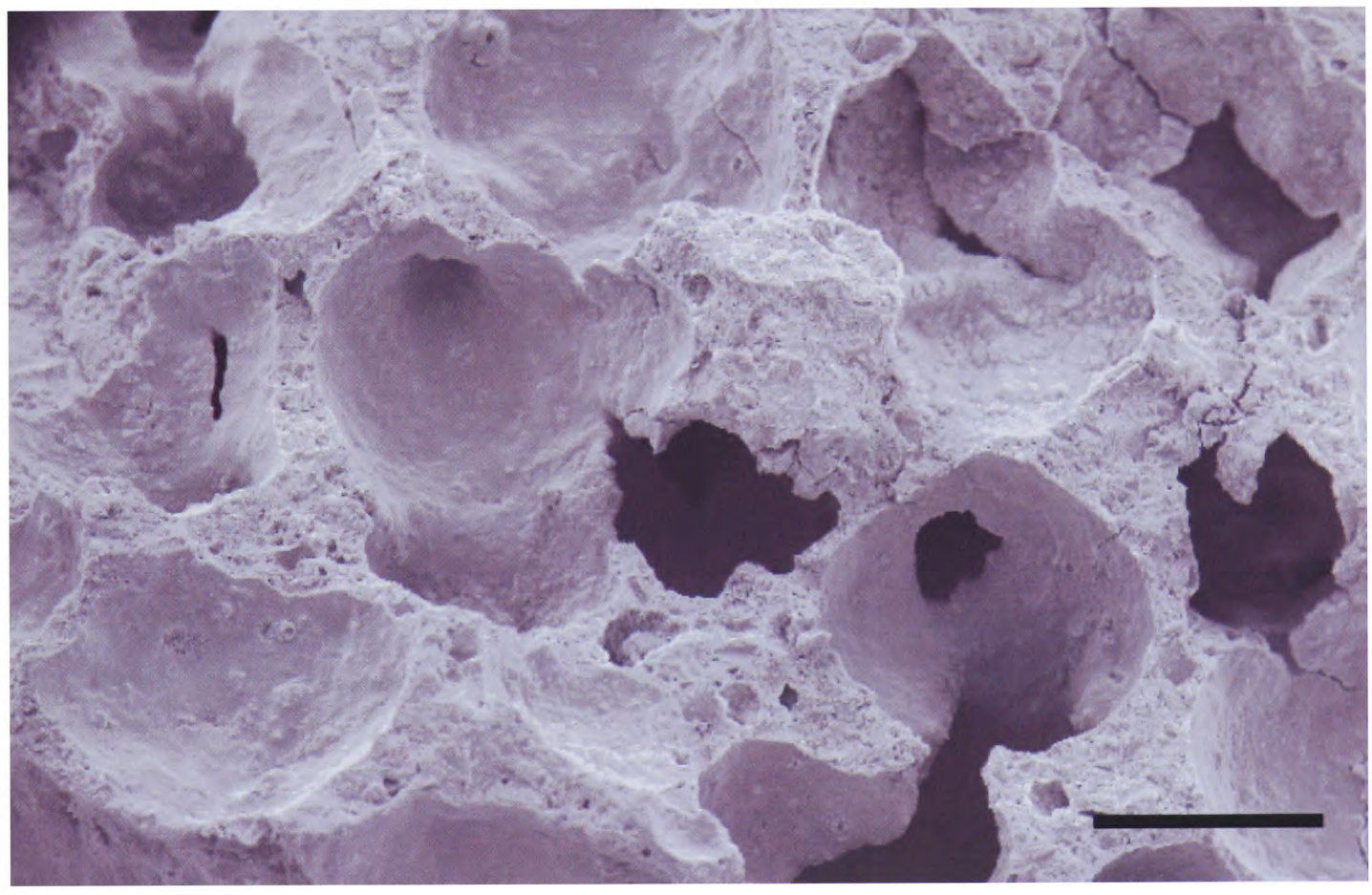

Figure 6.3: Low magnification SEM image of AAC microstructure: aeration pores. Scale bar represents 500 µm.

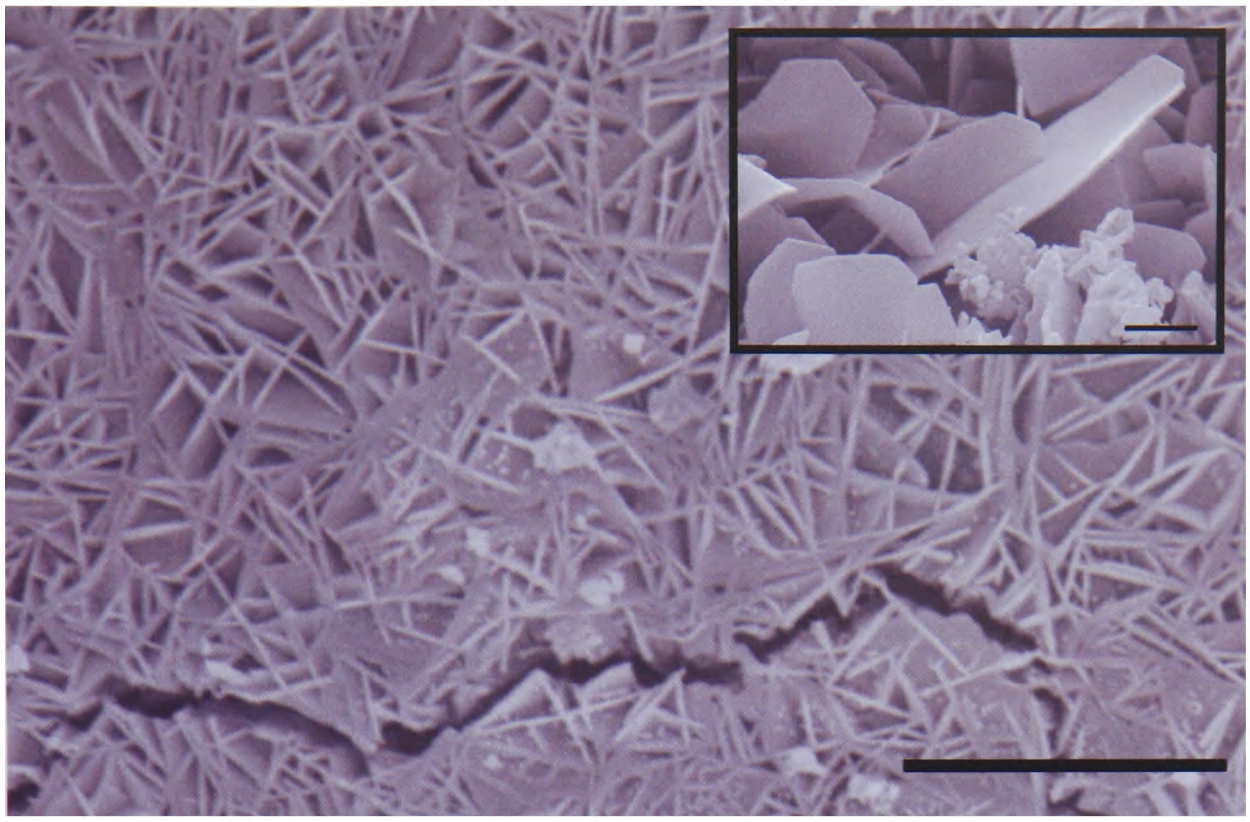

Figure 6.4: High magnification SEM image of AAC microstructure: micro capillaries. Scale bar in main image represents 10 µm. Smaller inset image is a slightly higher magnification of the platelet like pore structure. The scale bar represents 2 µm.

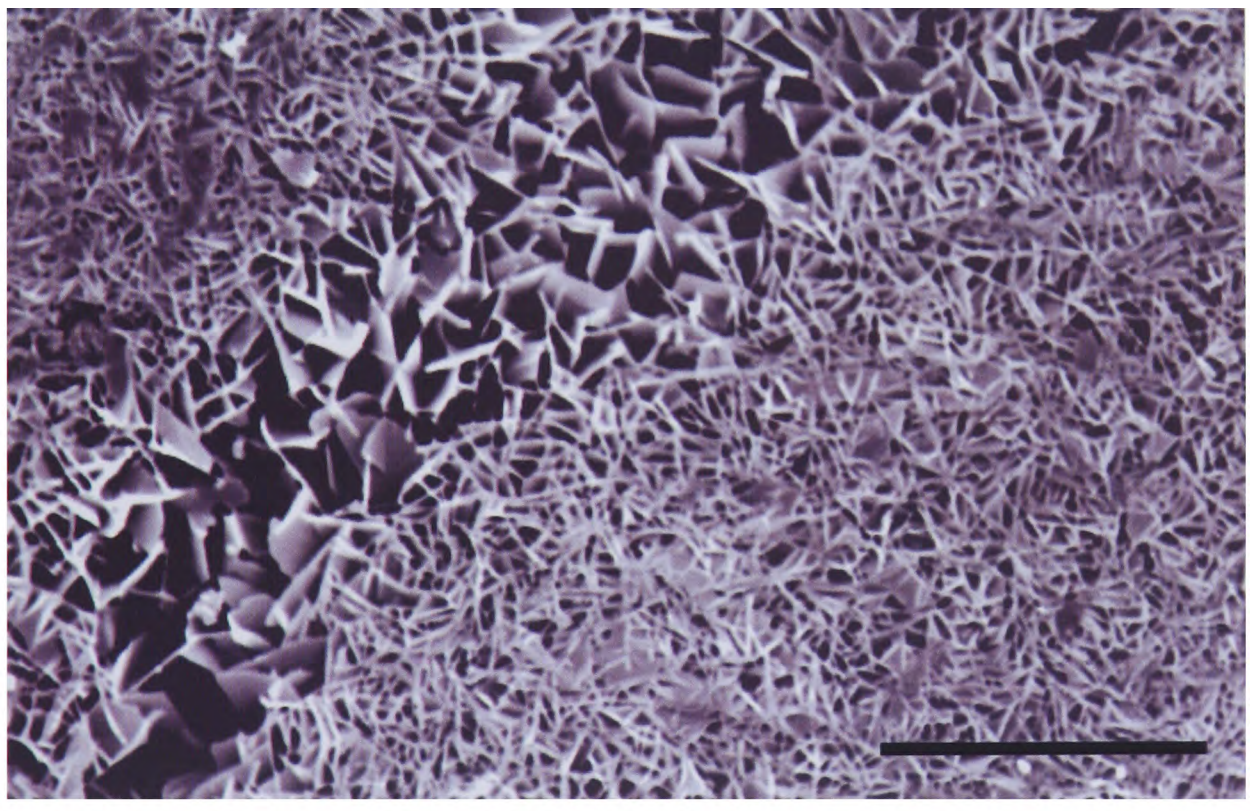

Figure 6.5: High magnification SEM image of AAC microstructure: macro pores. Scale bar represents 20 µm.

6.2.1 Capillary absorption of water

This experimental work was carried out by Dr Ioannis Ioannou (UMIST) and as such a summary of the work is given here and is discussed only because it sheds important light on the sorptive properties of AAC and why there is marked variation in the interlaboratory results.

Long term sorptivity studies on three samples indicate a marked deviation from classical $t^{1/2}$ behaviour indicating water absorption into the known, coarse aeration pores and the finer matrix material. An example sorptivity plot is given in figure 6.6a which shows this marked deviation. Analysis of the capillary moisture content leads to the conclusion that the aeration pores account for 59.49 % of the open porosity (aeration pore volume fraction porosity is 0.47, total volume fraction porosity is 0.79) and as such cannot be overlooked. Plotting the difference in cumulative water content, Δi, between the actual absorbed water content and the predicted water content from back interpolation of the matrix absorption gives the water content absorbed by the coarse aeration pores. Fitting this data with the sharp front model shows that gravity effects must be taken into consideration [3, 10-12], as illustrated in figure 6.6b.

The model has two parameters: i_∞ which is the cumulative water absorption of the coarse pores at capillary rise equilibrium; and S_a the sorptivity. The reduced variables are:

$$T = (\frac{S_a^2}{2i_\infty^2})t \qquad \textbf{(6.14)}$$

And

$$I = \frac{i}{i_\infty} \qquad \textbf{(6.15)}$$

The entire capillary rise process is described by the equation:

$$T = \ln(\frac{1}{1-I}) - I \qquad \textbf{(6.16)}$$

i_∞ is easily found as Δi at $t = 0$ (1.40 in the example shown here). S_a is defined as $S_e - S_m$, which is the early time sorptivity minus the matrix sorptivity. The data is fitted by back calculating i and t from I and T and plotting this on a semilog plot with the experimental Δi data. This proves that gravitational effects are strong in that region (early time) of the sorptivity plot.

The cumulative absorption which is attributed to the aeration pores is small, 1.40 mm for this sample. Using the estimate that the aeration porosity is 0.47 and that it is completely water filled during capillary rise, then the height of capillary rise in these pores is only about 2.98 mm. It is also possible to roughly estimate the expected equilibrium height of capillary rise from Z_e (in m) = 14.7 x 10^{-6} /(r in m) for water at 24°C [3] where Z_e is the equilibrium height of rise above the reservoir. For an aeration pore of 0.5 mm, radius Z_e = 29mm. Although there is no real quantitative information on the size of the aeration pores it is a fair assumption that few of them are larger than 1 mm diameter. The expected height of rise is therefore 10 times greater than the calculated height of rise. It is reasonable to tentatively conclude that the aeration pores are poorly interconnected (connected only through the matrix or through the few macro pores [9]) and that they are not efficiently filled because of trapped air. Loss of air from such pores is likely to be extremely slow.

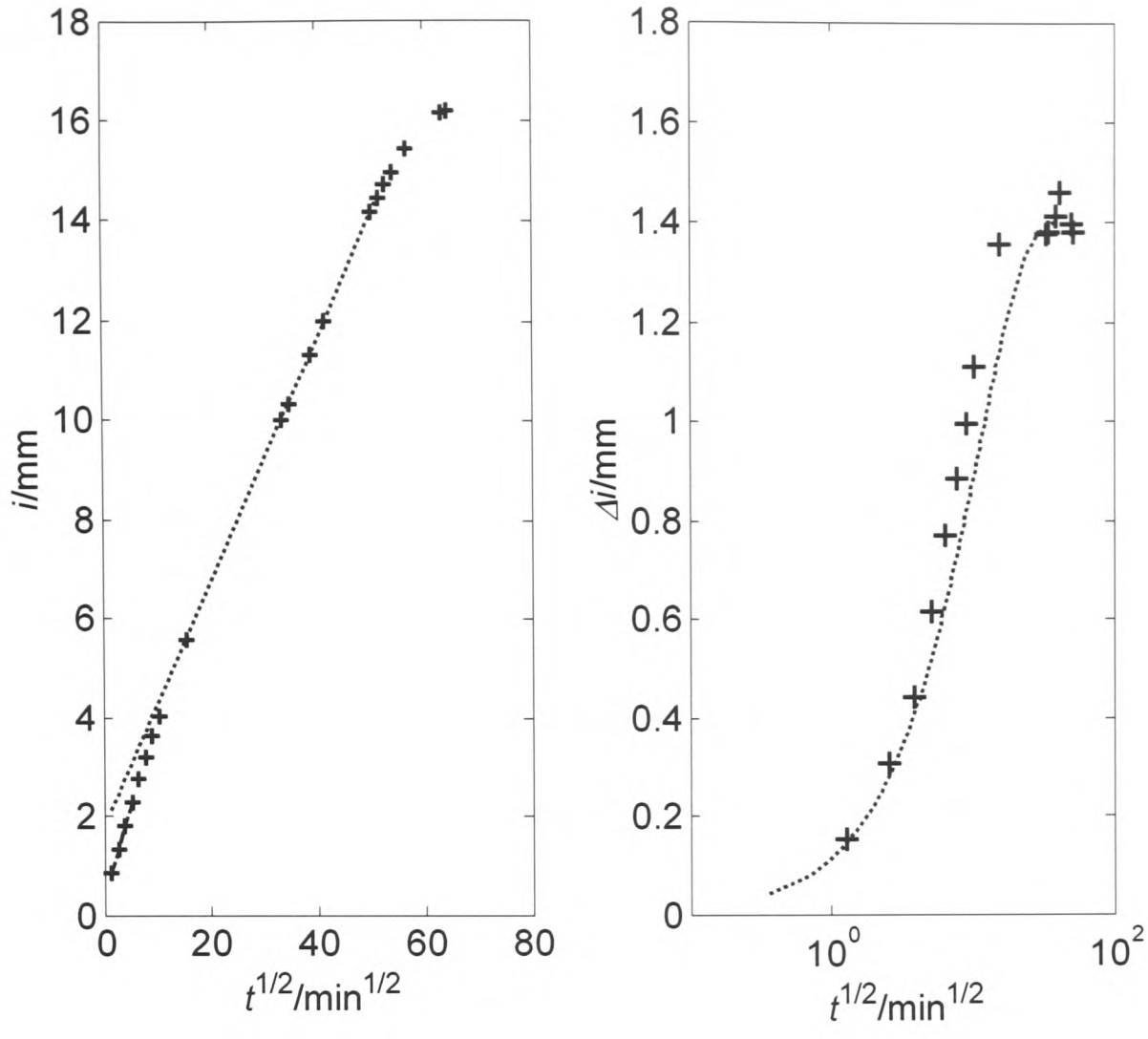

Figure 6.6a and 6.6b: Figure 6.6a is on the left hand side and 6.6b is on the right hand side. The cumulative water absorption is clearly split into three distinct areas of early time: heavy dashed line, matrix absorption: main segment, dashed line and late time: curving off at the end. Figure 6.6b is a plot of the difference between the actual absorption and the back interpolated absorption of the main segment. The experimental data points (crosses) are fitted to the sharp front theory as indicated by the dashed line.

In conclusion, the gravity effects of these large aeration pores are clearly a factor, but the curvature introduced into the plot as a result of these coarse pores is the most likely factor behind the spread of results reported by HAMSTAD.

6.2.2 Capillary absorption of *n*-decane

It was noted by several HAMSTAD researchers that there was some swelling of the AAC sample in contact with water. Therefore a simple sorptivity was carried out using an inert hydrocarbon, n-decane, to examine the effect of water on AAC. The

experimental work was carried out by Dr Ioannis Ioannou, UMIST, and as such is summarised here for completeness.

Sorptivity is a function of the suction of the material and the physical properties of the imbibing liquid. As such, the sorptivity can be defined as [3]:

$$S = (\frac{\sigma}{\eta})^{1/2} S \qquad \textbf{(6.17)}$$

Where σ is the surface tension of the liquid, η is the viscosity of the liquid and S is the intrinsic sorptivity, a property of the material that is independent of the characteristics of the imbibing liquid. As a result, the sorptivity using different liquids should scale as $(\sigma/\eta)^{1/2}$ therefore it is predicted that $S_{m\ (n\text{-decane})}/S_{m\ (water)} = 0.59$.

Instead experimental matrix sorptivity was found to be around 1.0 based on the water transport and *n*-decane transport through the same sample. The water sorptivity is some 40 % lower than expected on the basis of simple capillary scaling. This is another instance of a water sorptivity anomaly in a cementitious material, earlier examples of which have been reported. While the sorptivity is a well defined quantity for both liquids, the anomaly comes from the fact that the absorption rate is lower than expected for a simple capillary process. This can be interpreted in limestone as the result of partial wettability [13] but in cementitious materials it is thought to arise from an alteration of the pore structure produced by interaction with water [3, 14, 15], which does not happen with the inert *n*-decane.

The wide ranging sorptivity results for the AAC material in the final HAMSTAD report, can be attributed to the difficulty in fitting the data, fitting criteria used by the individual laboratories and the effect water has on the structure.

6.3 Calcium silicate (CS) characterisation

CS was the other interesting material studied as part of the HAMSTAD project. In this section it is characterised further with the intention of understanding its water transport properties in greater depth.

A large number of calcium silicate hydrates are formed as hydrothermal reaction products in lime, silica and cement systems under autoclave conditions [16, 17]. Some of these combine good mechanical properties with excellent thermal stability. Commercial calcium silicate [CS] products fabricated as sheet and other shaped forms are now becoming established in certain countries as insulation and moisture-control materials in construction and thermal engineering. Such a CS product (in the form of a low density board) has been investigated for water transport characteristics as described earlier in this chapter. This material was thought to merit further investigation due to the remarkably high porosity and sorptivity. Methods such as SEM, synchrotron and conventional XRD, CHN (carbon-hydrogen-nitrogen) analysis for organic material, helium pycnometry, and ^{29}Si NMR (nuclear magnetic resonance) were employed to understand more about this material. This section is taken from a publication by the author [18].

6.3.1 X-ray diffraction

An XRD powder pattern was obtained on the bulk material using techniques developed for inorganic building materials [19, 20]. The tests were carried out on the UK synchrotron at Daresbury Laboratory, using energy-dispersive powder diffraction. The measurements were carried out on station 16.4 using the high-energy white beam supplied by a 6-T wiggler. The method involves passing a beam of polychromatic X-rays through an intact sample (in this case through a cylindrical sample 20mm dia at right angles to the cylinder axis). Bragg scattered X-rays are collected by an energy sensitive solid state detector, set at a fixed diffraction angle, to record the diffraction pattern as a function of energy. All powder diffraction patterns were collected using a three-angle detector system [20]. The calcium silicate sample was clamped into a mechanical rig and rotated in the path of the beam. Shown in Figure 6.7 is the diffraction pattern of the CS sample, from which it can be seen that the observed diffraction peaks correspond almost exactly to the known diffraction pattern of the calcium silicate hydrate mineral, xonotlite [21]. A minor amount of calcite is detected. The crystalline material present in the calcium silicate board is therefore identified as almost pure synthetic xonotlite. It is noteworthy that

the diffraction pattern shows some diffuse background scattering, which indicates the presence of non-crystalline/amorphous material. It is known from the manufacturer that this CS board material is reinforced with cellulose fibres.

The crystallinity of synthetic xonotlite is often considered to be of poor quality [21], with the extent of crystallinity apparently being minimal in calcium silicate bricks. Crystallinity is thought to decrease during drying shrinkage and improve resistance to chemical attack. Naturally occurring xonotlite is found to have a higher degree of crystallinity. Xonotlite has a crystallographic (ideal) density of 2710 kg/m^3, and mineral specimens of good crystallinity are reported with density around 2700 kg/m^3

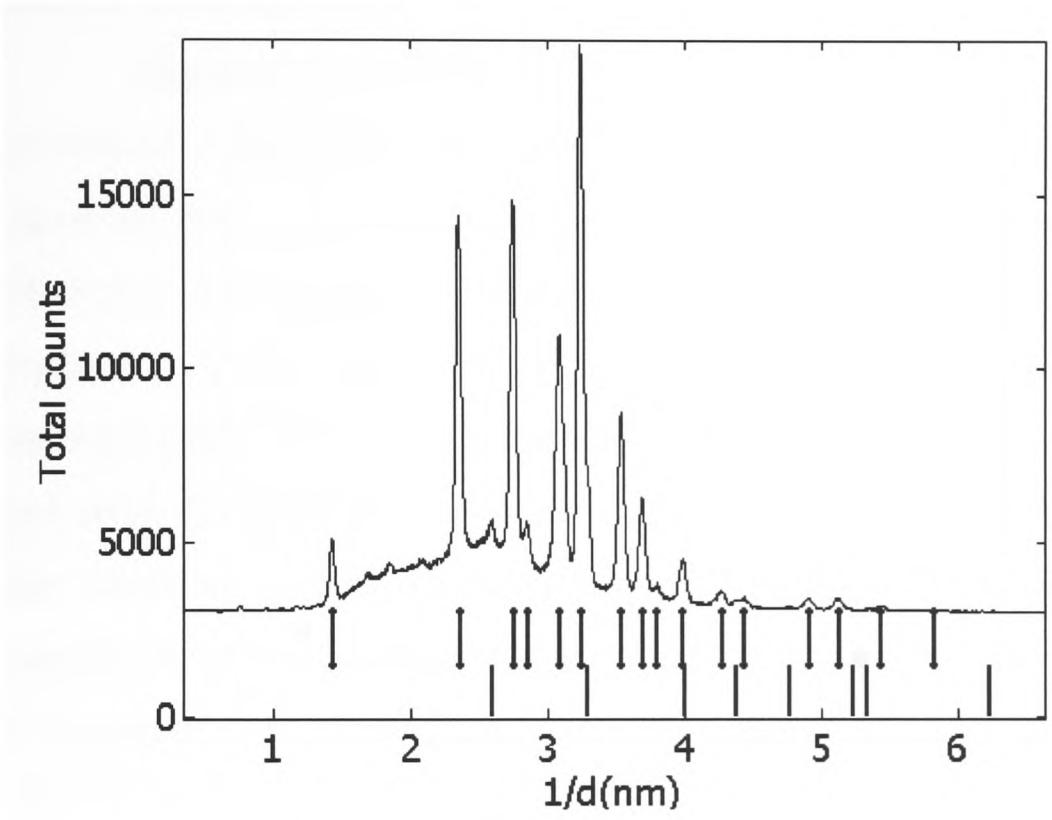

Figure 6.7: Synchrotron XRD analysis of calcium silicate sample: energy dispersive diffraction pattern measured in transmission through a 20 mm CS sample (continuous curve), with reference diffraction peak positions of xonotlite (upper row of tick lines) and calcite (lower ticks).

6.3.2 Helium pycnometry

Helium displacement (Quantachrome Pyknometer) was used to determine the solid density of a calcium silicate sample. Helium pycnometry generally produces good results for the matrix or solid density of porous materials [3]. The helium

pycnometric solid densities of three samples are: 2480, 2480 and 2490 kg/m^3 respectively, showing good reproducibility.

The mean solid density reported from vacuum saturation measurements in the HAMSTAD project is 2542 kg/m^3, which is about 2.5 per cent greater than the solid density value obtained from using helium pycnometry. Assuming the organic fibres are indeed cellulose (density 1580-1630 kg/m^3) and using a xonotlite solid density of 2700 kg/m^3, then the observed solid density of the calcium silicate board material corresponds to a volume fraction of cellulose fibres of about 0.14. However it is probable from the XRD patterns that the density of the inorganic component may be lower than that of crystalline xonotlite. Hence the cellulose fibre volume fraction may be lower than 0.14.

Organic CHN (Carbon-Hydrogen-Nitrogen) analysis showed that the material contained 2.00% (by mass) of carbon and 0.58% (by mass) of hydrogen. The observed H/C ratio (0.29) is considerably higher than expected for cellulose (0.14). However, it is possible that the hydrogen contains a contribution from the inorganic hydrates. Using the organic C value only, the calcium silicate material contains approximately 0.07 volume fraction of fibre. The NMR data presented below does not show the presence of any truly amorphous inorganic material but does show that the xonotlite is more disordered than the highly crystalline synthetic comparison sample. It can be assumed that the solid density of the xonotlite in the HAMSTAD CS material is probably lower than the ideal crystallographic value of 2700 kg/m^3.

6.3.3 Electron microscopy

Hitachi S4700 II cold field emission SEM analysis of the CS material showed it to be composed of fine, needle-like particles with a small amount of long, coarse fibres, which is understood to be cellulose. The organic fibres seem to be abundant. Xonotlite is visible as a network of long thin needles. The high aspect ratio of the xonotlite fibres favours open packing, as shown in figure 6.8 and is the main cause of the exceptionally high porosity of this material. Figure 6.9 shows several of the suspected cellulose fibres, which also appear to have fine, hair like growths. Figure

6.10 is a high magnification view of a xonotlite crystallite showing surface features and a fibrillar texture.

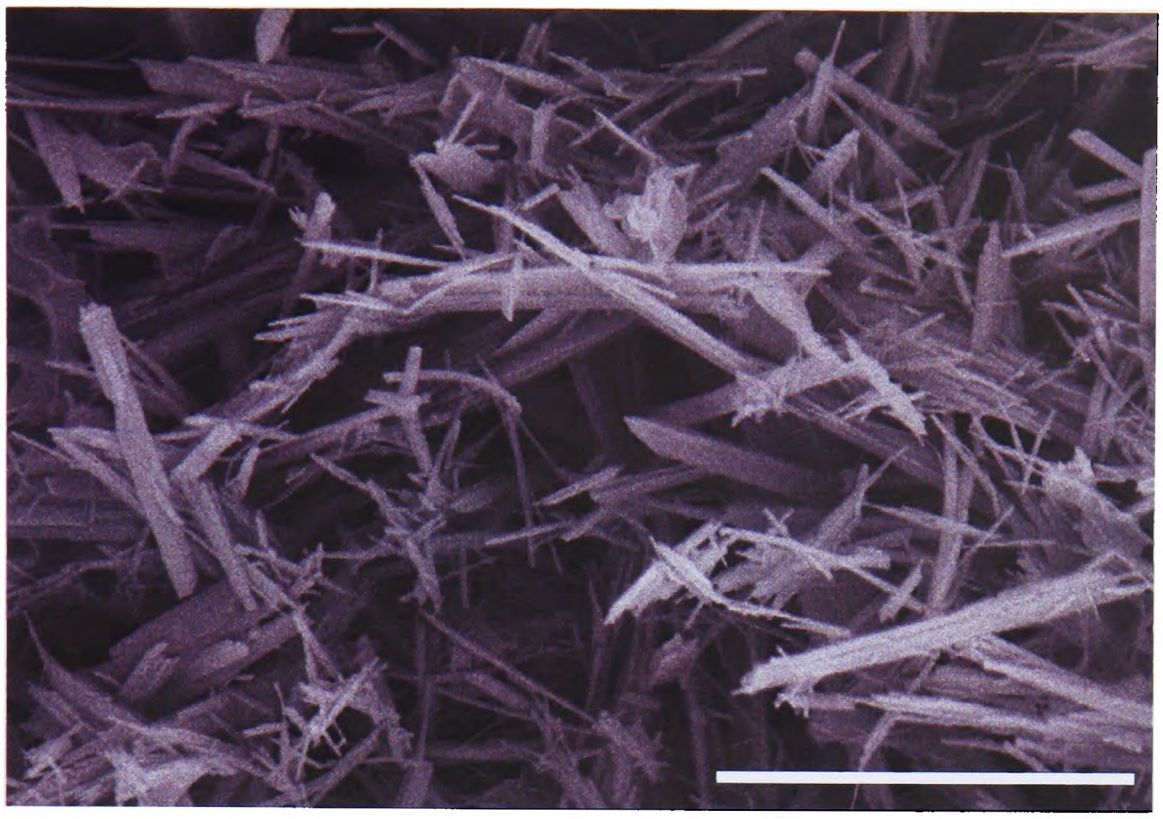

Figure 6.8: Shown above. High magnification SEM image of a fracture surface of a CS sample showing a porous microstructure formed from a loosely packed mass of needle-like xonotlite particles. Scale bar represents 3 μm.

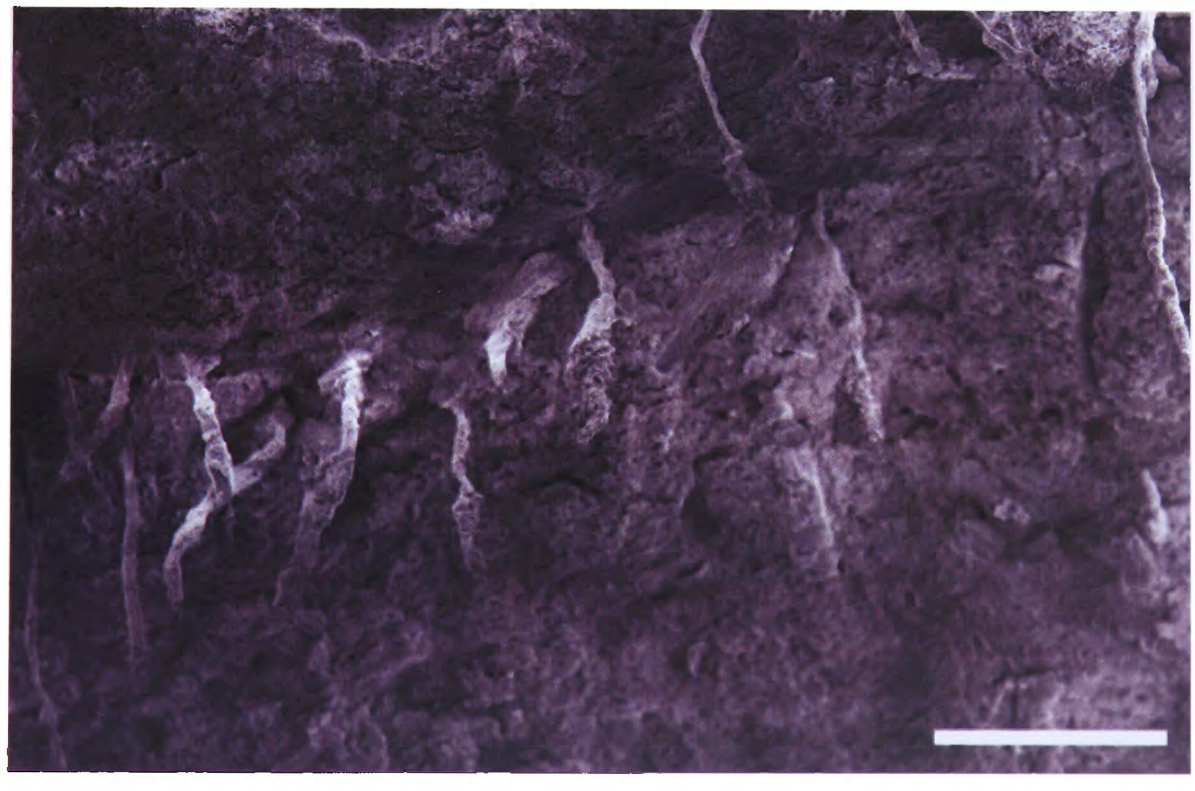

Figure 6.9: Shown above. Low magnification SEM image of a CS sample showing suspected cellulose fibres within the cementitious matrix. Scale bar represents 500 μm.

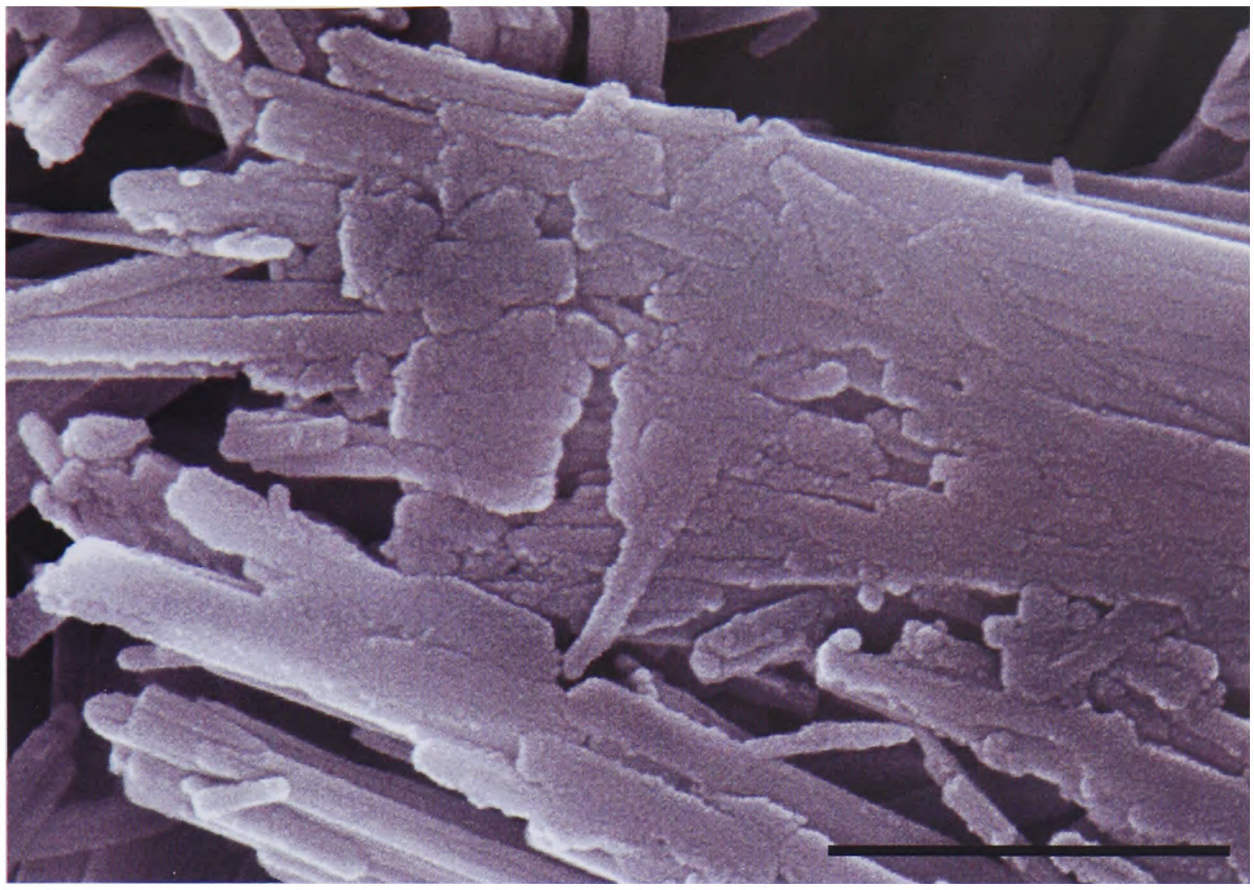

Figure 6.10: Shown above. High magnification SEM image of a CS sample showing surface features of an individual xonotlite particle. Scale bar represents 500 nm.

6.3.4 ^{29}Si MAS-NMR Spectra

NMR spectra were collected by J. Skibsted, University of Aarhus, Denmark, using high-resolution magic angle spinning techniques to observe ^{29}Si. The MAS method has proved valuable in characterizing many cementitious materials [22], including xonotlite [23-26]. This method was employed here to investigate the possible presence of an amorphous inorganic phase in the material. Two spectra were recorded from the sample of HAMSTAD xonotlite and one spectrum from a sample of highly crystalline synthetic xonotlite. The three spectra are shown in Figure 6.11. The following instrument parameters were used.

a) Single-pulse ^{29}Si MAS spectrum with ^{1}H decoupling of the HAMSTAD sample recorded using a spinning speed of 7000 Hz, a repetition delay of 30 s, and 7712 scans.

b) ^{29}Si(1H) cross-polarisation/MAS NMR spectrum of the HAMSTAD sample recorded with a spinning speed of 3000 Hz, a 8-s repetition delay, a CP contact time of 1 ms, and 2252 scans.

c) ^{29}Si(1H) cross-polarisation/MAS NMR spectrum of a sample of highly crystalline xonotlite recorded with a spinning speed of 3000 Hz, a 8-s repetition delay, a CP contact time of 2 ms, and 2190 scans.

The main features are strong resonances from the Q^2 and Q^3 silicate units of the main double chain of the xonotlite structure. In the HAMSTAD CS spectra, there is also a weak but distinct Q^1 resonance at -79.6 ppm, which indicates the presence of broken chains. This feature is absent in the highly crystalline synthetic sample The Q^2 peak in the highly crystalline synthetic sample is split, this splitting was previously observed by Noma et al. [26] in both natural and synthetic xonotlites, and arises from two crystallographically different non-bridging Si sites with different Si–O bond lengths. The fact that these two distinct Q^2 sites are not observed in the HAMSTAD CS material is further evidence of some degree of disorder or poor crystallinity, and is a probable reason for the somewhat less than ideal value of the solid density.

While an amorphous phase is not directly evident, it cannot be excluded since this would produce broad resonances from Q^1 and Q^2 units in the range -80 to -90 ppm. However there is no strong positive evidence for such amorphous material and all features of the ^{29}Si NMR spectrum can be explained in terms of a poorly crystalline xonotlite.

6.3.5 Conclusions

The inorganic component of the HAMSTAD CS board material is almost pure synthetic xonotlite, as indicated by synchrotron X-ray diffraction, conventional XRD and SEM. The XRD shows that a trace amount of calcite (calcium carbonate) is present. The CHN analysis indicates the presence also of organic carbon, possibly cellulose, which can be seen as the coarse fibres dispersed in the matrix on the SEM micrographs. The CS material has a fine pore structure, built of a randomly

orientated open packing of needle like crystals, rather than composed of tubiform pores in a sintered matrix as in fired clay brick. Unusually, the helium density is lower than the practical vacuum saturation density and markedly lower than the crystallographic density.

Xonotlite is known to have a variety of crystallographic polytypes based on stacking disorder [21]. The precise density of the individual polytypes is not known. In addition, there is evidence from the ^{29}Si MAS NMR spectra of the HAMSTAD CS material of broken chains and disorder in Q^2 sites. The less than perfect crystallinity of the major xonotlite component is the most probable explanation of the lower than expected matrix or solid density. The discrepancy between the vacuum saturation matrix density determined in the HAMSTAD round-robin tests and the helium pycnometric density remains unresolved, but further vacuum saturation testing with inert organic liquids (*n*-decane for example) might help provide an answer.

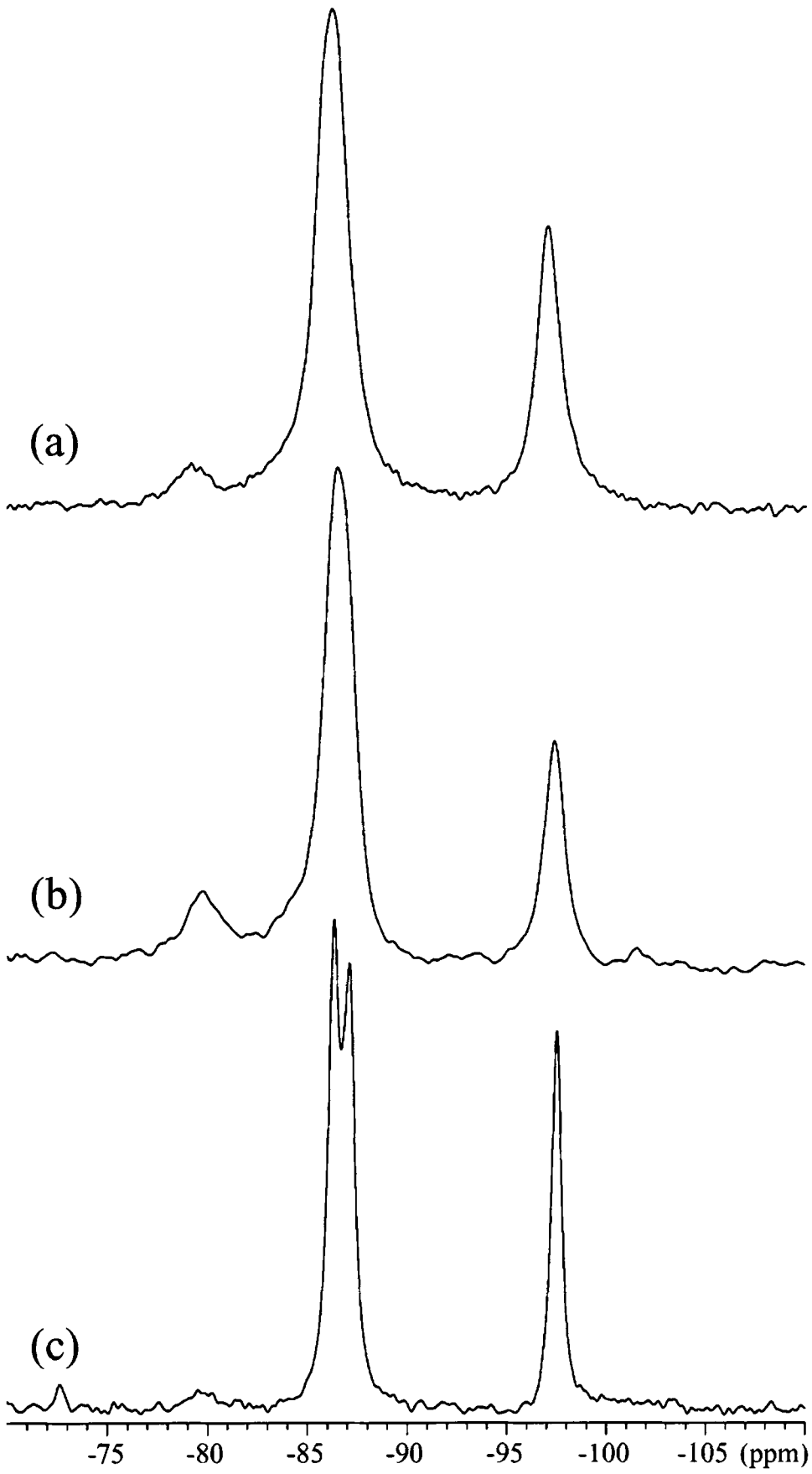

Figure 6.11: Three ^{29}Si MAS NMR spectra: (a), (b) HAMSTAD calcium silicate board material (see text); (c) synthetic xonotlite for comparison. The resonance at –87 ppm is from Q^2 silicate units and that at –97ppm is from Q^3 units; the weak feature at –79 ppm is from Q^1 units.

6.4 Conclusions

HAMSTAD WP1 was designed to compare interlaboratory results on the water transport testing of three different building materials using simple test methods.

Lab.	CB porosity	AAC porosity	CS porosity	CB capm	CB capabs	CS capm	CS capabs	AAC capm	AAC capabs
mean (UE)	22.7	80.5	87.8	149.3	0.15	812.3	1.15	275.3	0.03
mean (TNO)	23.8	82.8	89.4	146.3	0.17	801.5	1.24	240.6	0.02
mean (TUD)	23.7	82.2	89.5	161.3	0.15	817.8	1.18	329.8	0.04
mean (KUL)	24.0	82.2	89.4	149.6	0.19	811.1	1.30	305.8	0.03
mean (NRC)	23.6	81.5	89.6	131.6	0.13	765.9	1.16		0.03
mean	**23.6**	**81.8**	**89.1**	**147.6**	**0.16**	**801.7**	**1.21**	**287.9**	**0.03**
stdev	**0.5**	**0.9**	**0.7**	**10.6**	**0.02**	**20.9**	**0.06**	**38.6**	**0.01**

Table 6.9: The mean result from each participating laboratory is given (with the exception of CTU) with the standard deviation of the mean results.

It is clear from table 6.9 that the porosity results obtained from vacuum saturation exhibit very little spread but the results obtained from a simple uptake test have a much greater range. It is also clear that AAC presented the greatest challenge for the laboratories involved, which is most likely to be a result of the unusual pore structure introducing some uncertainty on fitting the data. This was proven by a sharp front analysis of the early time sorptivity leading to the conclusion that the two stage sorptivity results from filling of the coarse aeration pores and the finer matrix pores and as such the effects of gravity cannot be neglected [27]. Sorptivity testing with *n*-decane indicated that AAC is not inert in contact with water, which is another possible contributor to the spread in results. Although CS and AAC have a similar porosity value, the sorptivity, or rather capillary water content of the CS is much higher. The fibrous nature of the material allows it to act like a 'sponge' while the coarse aeration pores in AAC are subject to gravitational effects, and as such reduces the attainable capillary saturation. An investigation on the CS material [18] by the

the attainable capillary saturation. An investigation on the CS material [18] by the author shows the fine, packed nature of the fibres but opens some questions into the 'anomalous density' of the material which might benefit from some further experimental work using a hydrocarbon like *n*-decane.

6.5 References

1. Roels, S., J. Carmeliet, H. Hens, O. Adan, H. Brocken, R. Cerny, z. Pavlik, C. Hall, K. Kumaran, L. Pel, and R. Plagge, *Interlaboratory comparison of hygric properties of porous building materials.* Journal of Thermal Envelope and Building Science, 2004. **27**: p. 307-325.

2. Roels, S., J. Carmeliet, and H. Hens, *HAMSTAD WP1: Final report moisture transfer properties and materials characterisation*, in *Hamstad project*. 2003: KU Leuven, laboratory of building physics, Kasteel Park, Avenberg 51, B-3001 Heverlee, Leuven.

3. Hall, C. and W.D. Hoff, *Water Transport in Brick, Stone and Concrete*. 2002, London: Taylor and Francis.

4. Katz, A.J. and A.H. Thompson, *Quantitative prediction of permeability in porous rock.* Physical review B, 1986. **34**(11): p. 8179-8181.

5. Carpenter, T.A., E.S. Davies, C. Hall, L.D. Hall, W.D. Hoff, and M.A. Wilson, *Capillary water migration in rock: process and material properties examined by NMR imaging.* Materials and Structures, 1993. **26**: p. 286-292.

6. Hall, C. *Unsaturated flow*. in *International Conference on Ion and Mass Transport in Cement-Based Materials*. 1999. Toronto.

7. Narayanan, N. and K. Ramamurthy, *Structure and properties of aerated concrete: a review.* Cement and Concrete Composites, 2000. **22**: p. 321-329.

8. Grutzeck, M., S. Kwan, and M. DiCola, *Zeolite formation in alkali-activated cementitious systems.* Cement and Concrete Research, 2004. **34**(6): p. 949-955.

9. Roels, S., J. Sermijn, and J. Carmeliet. *Modelling unsaturated moisture transport in autoclaved aerated concrete: a microstructural approach.* in *Proceedings of the 6th Symposium on Building Physics in the Nordic Countries*. 2002. Norwegian University of Science and Technology, Trondheim, Norway.

10. Gummerson, R.J., C. Hall, and W.D. Hoff, *Capillary water transport in masonry structures: building construction applications of Darcy's law.* Construction papers, 1980. **1**: p. 17-27.

11. Hall, C., *Water sorptivity of mortars and concretes: a review.* Magazine of concrete research, 1989. **41**: p. 51-61.

12. Hall, C. and T.K. Ming Tse, *Water movement in porous building materials - VII. The sorptivity of mortars.* Building and Environment, 1986. **21**: p. 113-118.

13. Taylor, S.C., C. Hall, W.D. Hoff, and M.A. Wilson, *Partial wetting in capillary liquid absorption by limestones.* Journal of Colloid and Interface Science, 2000. **224**: p. 351-357.

14. Taylor, S.C., W.D. Hoff, M.A. Wilson, and K.M. Green, *Anomalous water transport properties of Portland and blended cement based materials.* Journal of Materials Science Letters, 1999. **18**: p. 1925-1928.

15. Taylor, S.C., *A study of liquid transport properties of cement based materials*, in *Manchester Centre for Civil&Construction Engineering.* 1998, UMIST: Manchester.

16. Shaw, S., S.M. Clark, and C.M.B. Henderson, *Hydrothermal formation of the calcium silicate hydrates, tobermorite ($Ca_5Si_6O_{16}(OH)_2.4H_2O$) and xonotlite ($Ca_6Si_6O_{17}(OH)_2$): an insitu synchrotron study.* Chemical Geology, 2000. **167**: p. 129-140.

17. Taylor, H.F.W., *Cement chemistry*. 2nd ed. 1997, London: Thomas Telford.

18. Hamilton, A. and C. Hall, *Physicochemical characterisation of a hydrated calcium silicate material.* Journal of Building Physics, 2005. **29**: p. 9-19.

19. Hall, C., J.K. Cockcroft, S.D.M. Jacques, X. Turrillas, M. Hanfland, and D. Hausermann, *Rapid whole-rock mineral analysis and composition mapping by synchrotron X-ray diffraction.* Analytical Communications, 1996. **32**: p. 245-248.

20. Hall, C., S.L. Colston, A.C. Jupe, S.D.M. Jacques, R. Livingston, A.O.A. Ramadan, A.W. Amde, and P. Barnes, *Non-destructive energy-dispersive diffraction imaging of the interior of bulk concrete.* Cement and Concrete Research, 2000. **30**: p. 491-495.

21. Hejny, C. and T. Armbruster, *Polytypism in xonotlite $Ca_6Si_6O_{17}(OH)_2$.* Zeitschrift fur Kristallographie, 2001. **216**: p. 396-408.

22. Skibsted, J., C. Hall, and H.J. Jakobsen, *Nuclear magnetic resonance spectroscopy and magnetic resonance imaging of cements and cement based*

materials. 2nd ed. Structure and performance of cements, ed. J. Bensted and P. Barnes. 2002, London: Taylor and Francis.

23. Bell, G.M.M., J. Bensted, F.P. Glasser, E.E. Lachowski, D.R. Roberts, and M.J. Taylor, *Study of calcium silicate hydrates by solid state high resolution ^{29}Si nuclear magnetic resonance.* Advances in Cement Research, 1990. **3**: p. 23-37.

24. Cong, X. and R.J. Kirkpatrick, *Si-29 and O-17 NMR investigations of the structure of some crystalline calcium silicate hydrates.* Advanced Cement Based Materials, 1996. **3**: p. 133-143.

25. Lippmaa, E., M. Magi, A. Samoson, G. Engelhardt, and A.R. Grimmer, *Structural studies of silicates by solid-state high resolution silicon-29 NMR.* Journal of the American Chemical Society, 1980. **102**: p. 4889-4893.

26. Noma, H., Y. Adachi, Y. Matsuda, and T. Yokoyama, *^{29}Si and ^{1}H NMR of natural and synthetic xonotlite.* Chemistry Letters, 1998. **3**: p. 219-220.

27. Hall, C., I. Ioannis, and A. Hamilton, *Capillary absorption of water and n-decane into autoclaved aerated concrete.* unpublished data.

7. Conclusions

The general aim of this work was to come to a greater understanding of the factors behind stone decay by soluble salts, in particular, sodium sulphate. This was broken down into three main component parts: investigation of sodium sulphate crystallisation, on its own and in the presence of other commonly occurring cations, as is more likely in natural conditions. Secondly an analysis of a site showing stone decay, which was examined for soluble salt damage with an aim to understanding how this site was decaying and if soluble salts were primarily responsible. It was felt that examining a real site showing signs of decay would be invaluable since laboratory tests rarely mirror the real world accurately and previous visits to the site by Historic Scotland had yielded information, in the form of visible efflorescence, that salts were at least present. This route was chosen in preference to laboratory testing of rocks with sodium sulphate and other salts because it was felt to be more 'real world' and unique. Of course, given more time, both routes would ideally be taken and compared. The final component part was a study on water transport properties of three building materials. The importance of water transport in the movement and deposition of solutes was touched upon during the analysis of House 7 and was discussed more rigorously with respect to common building materials in chapter 6 where the pore structure of the materials (AAC in particular) was shown to have a strong effect on its water transport properties.

The general aim of the thesis was broad but the individual components were examined thoroughly, resulting in a greater understanding of the individual facets of stone decay, ranging from the transport of water to the crystallisation of sodium sulphate. However, the overall aim could be further investigated, with a view to understanding how sodium sulphate causes the obvious damage it does to stone. Many authors have investigated which factors (temperature, RH, stone type, solution concentration etc) result in the most amount of damage to stone from sodium sulphate crystallisation. Important experimental work by Scherer and Rodriguez-Navarro et al. [1, 2] highlights which factors they consider lead to greater damage to the stone. The comparison of sodium sulphate crystallisation and sodium chloride crystallisation in a limestone at conditions of set RH and constant temperature

indicates that conditions of low RH (fast evaporation conditions) leads to greater damage. Salt is forced to crystallise under the surface of the stone, as the solution concentration is driven up faster than ions in solution can be transported to the surface of the stone, leading to surface scaling as pictured in chapter 2. Sodium sulphate was found to cause much greater damage than the "little" damage caused by sodium chloride even under low RH conditions. Interestingly it was also noted, through an MIP investigation that halite crystals were capable of blocking the pores, preventing further damage through a "cementing action" [1] which did not occur with sodium sulphate. In the case of wetting and drying cycles, Scherer [2] notes that damage is found to occur during the wetting cycle rather than the drying cycle under conditions of cyclical wetting and drying with a sodium sulphate solution. As discussed in chapter 2, this damage is attributed to the particular solubility of sodium sulphate. Much investigation involving laboratory testing has already been carried out, but this does not fully answer how or rather why this damage is caused. Scherer's discussion and theory of crystallisation pressure resulting from a repulsive interaction between a growing salt crystal and the confining pore is an attempt to answer this. Further experimental work in this direction would be useful.

7.1 Sodium sulphate phase transitions

Chapter 3 presented new information on the dynamic phase transitions of mirabilite – thenardite. It has long been suspected that aqueous sodium sulphate solution can sustain a high supersaturation before crystallisation occurs and this has been quantified in chapter 3 by dynamic XRD measurements and PHRQPITZ analysis. Further confirmation of this via more powerful synchrotron radiation is necessary. As the beam in a laboratory instrument does not penetrate to the bottom of the sample holder, as calculated in chapter 3, there is always the possibility that mirabilite forms at higher temperatures during the cooling cycle than the results suggest. This can be investigated using synchrotron radiation as the full sample can be probed and scanned vertically. The obscuring effects of preferred orientation can be circumvented by rotating the sample in the path of the beam, as indicated by preliminary experiments at Daresbury Laboratory. Preferred orientation effects can

only be reduced by grinding the sample to a fine powder and carefully packing the holder when using a laboratory instrument. For publication, a synchrotron radiation experiment would clarify the data obtained using the laboratory instrument.

7.2 Sodium sulphate and metal cation crystal growth

A novel synchrotron radiation experiment designed to investigate the effect of mirabilite dehydration in a 'closed' system with gypsum present was carried out. As mirabilite dehydrates to form thenardite crystals in contact with a sodium sulphate solution, gypsum progressively dissolves precipitating as labile salt (eugsterite), which results in the dissolution of the solid thenardite crystals (at least in part, if not completely) as discussed in chapter 4. There is no strong evidence or very convincing X-ray pattern for thenardite during the experiment, but literature sources indicate that labile salt ($Na_4Ca(SO_4)_3.2H_2O$) only forms rapidly in the presence of solid thenardite, therefore it must form initially when mirabilite loses its water of crystallisation and either dissolves if one assumes all gypsum is converted to labile salt, or some remains, isolated from solution along with any unreacted gypsum. This is assuming the system is at equilibrium and obeys the phase rule. Further work would include investigating the effect of varying amounts of gypsum present in the system as part of a synchrotron radiation study. Some alterations could be made to the experimental method such as scanning the sample vertically and rotating it. Scanning and rotation are easily achieved at ambient temperature, but to do this while heating and cooling the sample would require a stage to be designed (or an existing one re-designed) to carry out the synchrotron experiments proposed as the heating/cooling stage is not fitted with a rotation device and has only a slit for the beam to access the sample.

The second half of chapter 4 presents novel results on the crystallisation (by evaporation) of sodium sulphate in the presence of calcium, with some attention given to other cations, providing evidence that phase III (one of the five polymorphs of Na_2SO_4) is stabilised by cation substitution. This is the first work that investigates sodium sulphate cation substitution from aqueous solution and indicates that increasing amounts of calcium in solution leads to greater amounts of phase III

forming. Phase V (thenardite) always forms and a sample of pure phase III is never obtained as the calcium concentration reaches a threshold value which results in the precipitation of labile salt and consequently less phase III is formed. Literature sources discuss the stabilisation of a complete sample in phase III or I but these samples are usually formed from the melt and always at very high temperatures (>800 °C) before being quenched to room temperature. Clearly, in the case of aqueous solutions, solubility of hydrated double salts, such as labile salt, becomes important and prevents the formation of a complete sample of phase III. Phase I was never found, which is not unexpected given the temperature of the experiment is low (40 °C) and phase I is a high temperature phase stable at temperatures in excess of c. 240 °C, whereas phase III is known to be metastable, without substitution, at room temperature. Also, literature sources state that a larger amount of substituting cation is required to stabilise phase I than was present in these experiments. Further work includes expanding the series of experiments reported to include work at temperatures within the mirabilite stability regime (i.e. <32.4 °C) and controlled RH. Experimental investigations into the position of the cation defect would be useful. So far, the experimental work has assumed that the defect cations sit in phase III, but it would be useful and interesting to investigate phase III and V crystals to ascertain if this is true. Theoretical modelling indicates that for certain faces in both phases, all three cations can substitute, although Mg^{2+} substitution was largely unfavourable for either phase. With this in mind, the experimental work and theory could be further compared.

Further modelling and theoretical work would also help in understanding the cation substitution of phase III from aqueous solution at a deeper level and single crystal diffraction studies on phase III and V grown under these conditions would provide information on changes to the crystal lattice as a result of substitution. Theoretical modelling work on this project has been carried out by Drs N. H. de Leeuw and T. G. Cooper, the results of which are reported in this work. Further modelling work, incorporating Al^{3+} and Cu^{2+} defects into sodium sulphate (bulk and surface) would provide further comparison between experimental work and theory.

7.3 Skara Brae field investigation

House 7, Skara Brae was investigated for signs of salt decay using a variety of techniques such as XRD, ICP-OES, Swelling/contraction analysis, water transport testing, thin section analysis and novel use of modelling package, HYDRUS 2D to understand water transport through the stones. The end conclusion was that a number of decay mechanisms are present, but especially carbonate cement weathering and salt decay. Restricted sampling meant much of the analysis was carried out on background samples from outside the site, with no way of sampling the interior of the stone articles in House 7. Core samples from some of the furniture pieces on site would allow salt content analysis through the stone and an investigation of the stones pyrite content, which could provide more definite answers. Further work would also include extending the modelling work in terms of accuracy and range for publication. This would require accurate cataloguing of the soil type present at the site, an indication of the water table position and a measure of the evaporation rate of the site, which could be obtained by using an evaporimeter. This data would improve the accuracy of the model, but without it much can be done in terms of varying the input parameters and geometry of the soil region to produce a more comprehensive analysis of the water transport.

7.4 Fluid transport and materials characterisation

Water transport testing on three different building materials was carried out as part of an E.U. funded, round robin exercise. The general trend was more spread in the water uptake experiments with AAC than any other material. Long term testing with water and *n*-decane revealed the complex pore structure of AAC which was discussed as being the reason for the noticeable range in the results produced by the contributing laboratories. Further work would include *n*-decane uptake testing for the CS material to investigate if there is any alteration of the material on contact with water.

7.5 References

1. Rodriguez-Navarro, C. and E. Doehne, *Salt weathering: Influence of evaporation rate, supersaturation, and crystallization pattern.* Earth Surface Processes and Landforms, 1999. **24**: p. 191-209.
2. Scherer, G.W., *Stress from crystallization of a salt.* Cement and Concrete Research, 2004. **34**: p. 1613 - 1624.